Time-Resolved Properties and Global Trends in dMe Flares from Simultaneous Photometry and Spectra

Adam F. Kowalski

A dissertation submitted in partial fulfillment of
the requirements for the degree of

Doctor of Philosophy

University of Washington

2012

Reading Committee:

Suzanne L. Hawley, Chair

Rachel A. Osten

Eric Agol

Program Authorized to Offer Degree:
Astronomy

University of Washington

Abstract

Time-Resolved Properties and Global Trends in dMe Flares from Simultaneous Photometry and Spectra

Adam F. Kowalski

Chair of the Supervisory Committee:
Dr. Suzanne L. Hawley
Astronomy

We present a homogeneous survey of near-ultraviolet (NUV) /optical line and continuum emission during twenty M dwarf flares with simultaneous, high cadence photometry and spectra. These data were obtained to study the white-light continuum components to the blue and red of the Balmer jump to break the degeneracy with fitting emission mechanisms to broadband colors and to provide constraints for radiative-hydrodynamic flare models that seek to reproduce the white-light flare emission. The main results from the continuum analysis are the following: 1) the detection of Balmer continuum (in emission) that is present during all flares, with a wide range of relative contribution to the continuum flux in the NUV; 2) a blue continuum at the peak of the photometry that is linear with wavelength from $\lambda = 4000 - 4800$Å, matched by the spectral shape of hot, blackbody emission with typical temperatures of $10\,000 - 12\,000$ K; 3) a redder continuum apparent at wavelengths longer than Hβ; this continuum becomes relatively more important to the energy budget during the late gradual phase. The hot blackbody component and redder continuum component (which we call "the conundruum") have been detected in previous $UBVR$ colorimetry studies of flares. With spectra, one can compare the properties and detailed timings of all three components. Using time-resolved spectra during the rise phase of three flares, we calculate the speed of an expanding flare region assuming a simple geometry; the speeds are found to be $\sim$5 – 10 km s^{-1} and 50 – 120 km s^{-1}, which are strikingly consistent with the speeds at

which two-ribbon flares develop on the Sun. The main results from the emission line analysis are 1) the presentation of the "time-decrement", a relation between the timescales of the Balmer series; 2) a Neupert-like relation between Ca II K and the blackbody continuum, and 3) the detection of absorption wings in the Hydrogen Balmer lines during times of peak continuum emission, indicative of hot-star spectra forming during the flare. A byproduct of this study is a new method for deriving absolute fluxes during M dwarf flare observations obtained from narrow-slit spectra or during variable weather conditions. This technique allows us to analyze the spectra and photometry independently of one another, in order to connect the spectral properties to the rise, peak, and decay phases of broadband light curve morphology. We classify the light curve morphology according to an "impulsiveness index" and find that the fast (impulsive) flares have less Balmer continuum at peak emission than the slow (gradual) flares. In the gradual phase, the energy budget of the flare spectrum during almost all flares has a larger contribution from the Hydrogen Balmer component than in the impulsive phase, suggesting that the heating and cooling processes evolve over the course of a flare. We find that, in general, the evolution of the hot blackbody is rapid, and that the blackbody temperature decreases to $\sim$8000 K in the gradual phase. The Balmer continuum evolves more slowly than the blackbody – similar to the higher order Balmer lines but faster than the lower order Balmer lines. The height of the Balmer jump increases during the gradual decay phase. We model the Balmer continuum emission using the RHD F11 model spectrum from Allred et al. (2006), but we discuss several important systematic uncertainties in relating the apparent amount of Balmer continuum to a given RHD beam model. Good fits to the shape of the RHD F11 model spectrum are not obtained at peak times, in contrast to the gradual phase. We model the blackbody component using model hot star atmospheres from Castelli & Kurucz (2004) in order to account for the effects of flux redistribution in the flare atmosphere. This modeling is motivated by observations during a secondary flare in the decay phase of a megaflare, when the newly formed flare spectrum resembled that of Vega with the Balmer continuum and lines in absorption. We model this continuum phenomenologically with the RH code using hot spots placed at high

column mass in the M dwarf quiescent atmosphere; a superposition of hot spot models and the RHD model are used to explain the anti-correlation in the apparent amount of Balmer continuum in emission and the U-band light curve. We attempt to reproduce the blackbody component in self-consistent 1D radiative hydrodynamic flare models using the RADYN code. We simulate the flare using a solar-type nonthermal electron beam heating function with a total energy flux of 10^{12} ergs cm^{-2} s^{-1} (F12) for a duration of 5 seconds and a subsequent gradual phase. Although there is a larger amount of NUV backwarming at log $m_c/(1g\ cm^{-2})\sim0$ than in the F11 model, the resulting flare continuum shape is similar to the F11 model spectrum with a larger Balmer jump and a much redder spectral shape than is seen in the observations. We do not find evidence of white-light emitting chromospheric condensations, in contrast to the previous F12 model of Livshits et al. (1981). We discuss future avenues for RHD modeling in order to produce a hot blackbody component, including the treatment of nonthermal protons in M dwarf flares.

TABLE OF CONTENTS

Page

LIST OF FIGURES

ACKNOWLEDGMENTS

I owe thanks to many individuals who directly and indirectly contributed to this dissertation over the past six years. I thank Suzanne Hawley for all the amazing opportunities as a graduate student, the travel experiences to the edges of the world, and this extremely interesting dissertation project. I want to thank Suzanne for all the interesting discussions and for all the expert advice along the way. I want to thank John Wisniewski, Mark Giampapa, and Henny Lamers for extremely fruitful conversations that contributed to several ideas developed in this work. I thank Petr Heinzel for interesting discussions about Ellerman bombs on the Sun. I thank Petr Heinzel and Eugene Avrett for useful discussions on radiative transfer. I want to thank Rachel Osten and Mihalis Mathioudakis for useful discussions on a wide variety of topics pertaining to solar and stellar flares. I thank Tom Ayres for useful discussions about the interpretation of stellar spectra (*there is no such thing as absorption!*). I thank Jeremiah Murphy, Ellen Zweibel, and Ben Brown for useful discussions that improved my theoretical and modeling insight. I thank Sean Matt for discussions on relevant physical scenarios. I thank Jeff Valenti for discussions on T Tauri spectra. I thank Joel Allred for the use of his RADYN model results and for useful discussions and insight; also for IDL code used for the analysis of RADYN results. I thank William Abbett for IDL code used in the analysis of RADYN results. I thank Han Uitenbroek for the use of the RH code and for being extremely helpful in adapting RH for our uses (including writing and implementing a version of RH that calculates n_e from NLTE ionization). I thank Mats Carlsson for teaching me how to use the RADYN code, for many IDL tools used in the analysis of the RADYN results, and for helping me along the way with the modeling. I thank the International Space Sciences Institute (ISSI) "Solar Chromospheric Flares" team, including Lyndsay Fletcher, Hugh Hudson, Gianna Cauzzi, Petr Heinzel, Mats Carlsson, Bill Abbett, Jana Kasparova, Fatima Rubio da Costa, Ryan Milligan, Arek Berlicki, and Mingde

Ding, for opening my eyes to and teaching me about solar flares. I thank Ben Williams for very useful discussions about differential atmospheric refraction. I thank Andrew C. Becker for discussions on Principal Component Analysis. I thank my collaborators – Eric Hilton, James Davenport, Sarah Schmidt, John Wisniewski, and Jon Holtzman – for many useful discussions and for tremendous and generous help with obtaining observations. I thank Nick Ule for helping obtain observations. I would like to thank Jon Holtzman for the generous and frequent use of the NMSU 1-m telescope at the Apache Point Observatory. I would like to acknowledge the incredible staff at the Apache Point Observatory and especially the Observing Specialists at the 3.5-m for assistance with data acquisition and data calibration feedback. Their flexibility and knowledge allowed us to diagnose several calibration aspects that were very important to the final results presented in this dissertation. In particular, I thank Russet McMillan, Bill Ketzeback, Joe Huehnerhoff, and Jack Dembicky. I thank my reading committee – Rachel Osten, Eric Agol, Suzanne Hawley – for excellent feedback on this dissertation. I thank all my professors at the University of Washington for the excellent classes and graduate education. Finally, I thank my loving and supportive family, Gerald, Ruby, Alison, Andy Kowalski, and Grandma K, for the constant and unrelenting encouragement that empowered me through the last six years.

DEDICATION

I dedicate this dissertation to my parents, Gerald and Ruby Kowalski.

Chapter 1

INTRODUCTION

Optical and near-ultraviolet (NUV) continuum radiation during stellar flares is a commonly observed phenomenon, yet its origin remains unknown despite decades of investigation. This emission is known as the white-light continuum because it is detected in broadband filters, such as the TRACE white-light filter during solar flares and Johnson $UBVR$ bands during stellar (especially M dwarf) flares. Broadband color investigations suggest that the white-light energy distribution peaks within the U band ($\lambda \sim 3250 - 3950$Å) or just shortward of the U-band at $\lambda \sim 3000$Å. Accurately flux-calibrated, time-resolved spectra in the blue and NUV are important for understanding the emission processes that produce the white-light, which encode information about the depths, temperatures, and densities where it is formed, and ultimately the heating mechanism. Understanding white-light emission therefore also necessitates radiative-hydrodynamic (RHD) flare model atmospheres that are produced self-consistently with a realistic flare heating mechanism, with the goal of reproducing the observed NUV/optical spectrum.

Magnetically active M dwarfs are those with a persistent chromosphere as seen by significant Hα line emission even outside of flares. This is attributed to strong magnetic fields ($\sim$few thousand Gauss) covering $\sim$50% or more of the stellar surface (Saar & Linsky, 1985; Johns-Krull & Valenti, 1996). These active M dwarfs regularly produce flare emission across the electromagnetic spectrum, from soft X-rays ($1-10$ keV) to the radio ($\sim 1-10$ GHz). Due to the low photospheric background in the blue and NUV, white-light flares on M dwarfs produce a large contrast which facilitates flare detection and reduces the contribution of quiescent (non-flare) emission. The contrast of the flare emission against the quiescent background is known as the "flare visibility" (Gershberg, 1972) and makes the Johnson U-band filter preferred for flare studies (Moffett, 1974). Active M dwarfs with spectral sub-

types dM3e-dM6e[1] have been found to flare most frequently with good visibility and thus are the main targets for flare monitoring. Earlier M subtypes produce higher energy but less frequent flares (Lacy et al. 1976, Hilton et al. 2011). In particular, stars with spectral subtype ∼dM4e have both a large flare visibility and the tendency to produce energetic flares with small/moderate-size flares ($E_U \sim 10^{31}$ ergs) occurring several times per night of monitoring; extremely large flares (E> 10^{34} ergs) occur perhaps monthly or several times per year and have been observed on more than one occasion (Andrews et al., 1969; Hawley & Pettersen, 1991; Cully et al., 1994; Christian et al., 2003; Osten et al., 2010; Kowalski et al., 2010).

Stellar flares produce greatly enhanced emission in chromospheric lines, such as the Hydrogen Balmer series, Ca II H and K, and He I. These lines are typically associated with chromospheric temperatures ranging from 6000 – 20 000 K. The Hydrogen lines have a fast rise phase but peak several minutes after the peak of the (U-band) continuum emission (Kahler et al., 1982; Hawley & Pettersen, 1991; García–Alvarez et al., 2002). The energy budget in the emission lines is only a small fraction of the total flare energy, ∼4% in the impulsive phase and 17% in the gradual phase (Hawley & Pettersen, 1991), although some flares produce lines that contribute a larger percentage, ∼30 – 50%, of the total energy (Hawley et al., 2007). Broadening of the line profiles has been observed, with full widths (at zero-max) that approach ∼20Å for large flares (Hawley & Pettersen, 1991; Fuhrmeister et al., 2008). The broadening of Hydrogen (and Helium) lines has often been interpreted as an indication of mass motions of tens to several hundred km s^{-1} (Doyle et al., 1988; Eason et al., 1992; Fuhrmeister et al., 2008) or Stark broadening due to increased electron densities on the order of $10^{13} - 10^{14}$ cm^{-3} (Švestka, 1972; Worden et al., 1984). Broadening of the Ca II lines is not observed (Paulson et al., 2006), but the total flux exhibits a characteristic late peak after the Balmer lines at the beginning of the continuum gradual phase (Hawley & Pettersen, 1991). In most previous studies, the entire Balmer series has not been captured simultaneously in order to achieve wavelength coverage in the blue, usually at the expense of Hα. Eason et al. (1992), Crespo-Chacón et al. (2006), Fuhrmeister et al. (2011) have

[1] "e" indicating that in quiescence Hα is in emission.

provided data covering most of the Balmer series (the Hβ line was not included in the studies of Eason et al. (1992) and Fuhrmeister et al. (2011)), but with the red and blue data obtained at significantly different cadence. Measuring the relative flux in each Hydrogen line (the Balmer decrement) over the duration of the flare is an important diagnostic for the evolution of electron densities (Drake & Ulrich, 1980).

Whereas the first possible record of a flare on another star was reported in Hertzsprung (1924), white-light flare radiation was first discovered on the Sun during the famous "Carrington" event of 1859 (Carrington, 1859). During the largest X-class flares on the Sun, approximately 10^{32} ergs is released in the entire bolometric flare spectrum (Emslie et al., 2005), of which $> 70\%$ is emitted at wavelengths longer than $\lambda = 2000$Å (Woods et al., 2004; Kretzschmar, 2011). Butler et al. (1988) showed a scaling relation between the Hγ and soft X-ray energies, establishing the solar-stellar connection and also an energy scaling difference of about an order of magnitude between typical solar flares and small M dwarf flares, which was extended to the U-band for several more stellar flares by Hawley & Pettersen (1991). This has led to the generally accepted idea that dM flares are "scaled-up" versions of solar flares (Eason et al., 1992; van den Oord et al., 1996). However, white-light data are rarely available for solar flares, which makes direct comparisons difficult. To date, the best white-light spectra during solar flares were obtained by Don Neidig in the 1980s, primarily using the Universal Spectrograph and the multiband polarimeter at Sacramento Peak Observatory. One of the largest white-light flares on the Sun occurred on 24 April 1984 ($\geq$X13), and the total NUV and optical ($\lambda = 2000 - 9500$Å) energy for this flare was estimated as 1.2×10^{32} ergs and areal coverage of the typical two-ribbon flare structure at $\lambda = 3610$Å of 2×10^{19} cm^2, or $\sim$0.13% of the visible solar disk area (Neidig et al., 1994)[2]. The largest solar flares produce a very small relative increase in white-light, due at least partly to the small flare visibility. The X17, 28 October 2003, flare was the first detected flare in the total solar irradiance (SORCE/TIM spacecraft), producing a relative increase of 270 parts-per-million and an estimated white-light energy ($\lambda > 2000$ Å) of $3.5{\times}10^{32}$ ergs (Woods et al., 2004).

[2]The value from Neidig et al. (1994) is 6×10^{31} ergs. On the Sun, one can assume a half hemisphere of emission, whereas stellar fluxes are multiplied by 4π. Here, we multiply by 2 for direct comparison.

Although comparable to moderately large stellar flares, these flares are exceptional for the Sun. In contrast, the largest M dwarf flares can produce more than 10^{34} ergs in the U-band alone (Kowalski et al., 2010). An energy budget of 3×10^{34} from $\lambda = 1200 - 8000$Å was calculated for one such flare (hereafter, the Great Flare) on the dM3e star AD Leo in Hawley & Pettersen (1991). The peak flux occurred in the U-band, and a significant fraction (27%) was also emitted from $2000 - 3260$Å.[3]

Candidates for the emission mechanism that produces the white-light continuum have been described by Cram & Woods (1982), Giampapa (1983), and Nelson et al. (1986), and include blackbody (BB), Hydrogen free-free (ff), Hydrogen bound-free (bf), and H^- bound-free. Inverse Compton scattering of quiescent infrared radiation from relativistic electrons has also been proposed (Gurzadian, 1988), but this "fast-electron hypothesis" does not hold ground with X-ray observations (Mullan, 1990). The observed spectral peak in the NUV supports a model of the white-light continuum whereby the radiation originates from a source that emits with the general shape of a blackbody with $T = 8500 - 9500$ K (Mochnacki & Zirin, 1980). Similar temperatures have been found from Johnson broadband photometry (hereafter, "colorimetry") of flares ranging from $E_U \sim 10^{31}$ ergs to $E_U \sim 10^{34}$ ergs (Hawley & Fisher, 1992; Hawley et al., 2003, see also de Jager et al. (1989) for a determination of 13 000 K). Hawley & Pettersen (1991) and Hawley & Fisher (1992) used UBVR photometry and IUE SWP/LWP data to study the continuum shape evolution during the Great Flare, finding a peak flux in the U band and a broadband distribution that was fit very well by a blackbody with $T = 9500$ K and $T = 9000$ K in the impulsive phase and $T = 8400$ K and $T = 8800$ K in the gradual phase. The reddening of the continuum in the gradual phase was suggested to be the result of the presence of two (or more) competing emission mechanisms, including a contribution from Hydrogen (Paschen continuum) recombination radiation. Other studies have similarly concluded from colorimetry that flare radiation consists of a combination of the hot blackbody emission and optically thin Balmer continuum recombination radiation, while speculating that the blackbody is short-lived and the Balmer

[3]Hawley & Pettersen (1991) characterized the detailed energy budget of this flare, finding that 17% of the energy at $\lambda > 1200$Å is emitted in the $\Delta\lambda = 700$ Å of the U-band. Therefore a $E_U \sim 2 \times 10^{31}$ erg stellar flare may be roughly comparable in total energy to the largest solar white-light flares, such as the one discussed in Neidig et al. (1994).

continuum becomes more dominant in the gradual phase (Abdul-Aziz et al., 1995, see also Abranin et al. (1997); Zhilyaev et al. (2007)). A two-component model was first proposed using simultaneous colorimetry and spectra of dMe flares by Kunkel (1970) – see also Moffett & Bopp (1976) – who concluded that a single, isothermal ($T_e = 3000 - 30\,000$ K) optically thin hydrogen emission (bf+ff) model was too blue to explain the observed flare colors, nor could it account for the spread of colors among a sample of flares. Instead, they proposed a model consisting of a dominant component of Hydrogen bf (recombination) radiation with a secondary contribution from a heated photosphere, which increases in relative contribution over time during the flare decay. However, Allred et al. (2006) recently showed that continuum constraints using colorimetry are fraught with degeneracies; a model spectrum that has a large Balmer jump (due to Hydrogen bf radiation) may exhibit the shape of a hot, blackbody with $T_{\rm BB}\sim$9000 K when convolved with broadband filters.

Previously, spectra of the Balmer jump ($\sim$1000Å near 3646Å) have been obtained during several large flares on dMe stars: AD Leo (Hawley & Pettersen, 1991), UV Ceti (Eason et al., 1992), Gl 866 (Jevremovic et al., 1998), AT Mic (García–Alvarez et al., 2002), and CN Leo (Fuhrmeister et al., 2008) and (Doyle et al., 1988). These spectra covered about 1000Å around the Balmer jump ($\lambda = 3646$Å). None of these studies showed conclusive evidence of a component that could be attributed to Hydrogen (Balmer) recombination radiation, in contrast to the findings of Kunkel (1970). Interestingly, Eason et al. (1992) noted that the Balmer continuum appeared in *absorption*[4].

Constraining the emission mechanism from flux-calibrated spectra at wavelengths redder than the Balmer jump has been done in several previous studies, revealing blackbody temperatures consistent with those inferred from colorimetry. Mochnacki & Zirin (1980) used a multichannel spectrophotometer to map the evolution of the hot blackbody component, which they speculated may be dominant at flare maximum. They found that the rise phase could be caused by increasing area coverage of the hot component while the decay phase is explained by both rapidly decreasing temperature (from 9500 K at peak to $5500 - 7000$ K in the decay) and relatively constant area. They were unable to accurately observe the

[4]Although, the authors gave the caveat that the observations were obtained at high airmass.

Balmer continuum due to spectral vignetting, but they did note a smaller Balmer jump than predicted by Kunkel (1970) and found the decay of NUV emission was slower than in the optical, perhaps indicating two components in action. Kahler et al. (1982) observed a flare on YZ CMi in the optical, radio, and X-ray and found a similar temperature of 8500 K at peak by fitting to $\lambda = 4200 - 5900$Å. Katsova et al. (1991) also found an optical continuum consistent with $T = 10\,000$ K blackbody in a flare on YZ CMi. Hawley & Pettersen (1991) obtained spectra during the Great Flare showing that the flux distribution increases toward the blue with little (if any) observed Balmer jump; Hawley & Fisher (1992) suggested that the peak lies somewhere between $\lambda = 3000 - 3500$Å. Paulson et al. (2006) found a temperature of 8000 K in long-integration optical echelle spectra of a flare on an inactive dM4 star.

Accurately flux-calibrated spectra showing the peak of the blackbody component do not exist; spectra obtained around the Balmer jump and bluer indicate the possibility that it peaks outside the atmospheric window, $\lambda < 3250$Å; the blackbody fits from colorimetry suggest a peak at $\lambda \sim 3000$Å with the largest observed flux emitted within the U band. Fuhrmeister et al. (2008); Schmitt et al. (2008); Fuhrmeister et al. (2011) measured the NUV shape of the flare continuum down to the atmospheric limit at $\lambda \sim 3250$Å with VLT/UVES and found a temperature of 11 300 K; the fits were not very good and only certain to ∼4000 K, possibly due to the long integration times, narrow wavelength range ($\lambda = 3250 - 3800$Å), and lack of a robust flux calibration (without standard stars) for these echelle data. These authors also measured the continuum shape in red, higher cadence spectra and found temperatures inconsistent with the NUV: $20\,000 - 27\,000(\pm 5000)$ K at peak and $5600, 3200$ K during the decay. Fuhrmeister et al. (2011) observed a flare on Proxima Centauri with a similar VLT/UVES setup and could not find a good blackbody fit to the flare spectrum. de Jager et al. (1989) determined a temperature of 16 000 K from (non-flux calibrated) spectra of a 5-magnitude flare on UV Ceti. During a different 5-magnitude event on UV Ceti, Eason et al. (1992) concluded that an optically thick thermal-bremsstrahlung (Hydrogen ff) model with $T \sim 13\,000$ K gave the best fit to their spectrum.

The origin of the possible $T \sim 10\,000$ K blackbody component is currently unknown, and indeed its existence has been contested by van den Oord et al. (1996) and Nelson et al.

(1986) on grounds that it requires very high heating fluxes from a solar-type flare heating beam of $\sim 5 \times 10^{11}$ ergs / s / cm^2. However, we know today that these fluxes are possible on the Sun (Neidig et al., 1993; Krucker et al., 2011). The inferred areal coverages are small, $\leq 0.5\%$, for even the largest stellar flares (e.g., Hawley & Fisher, 1992), supporting the idea that this hot, blackbody emission component originates from a compact source at locations of intense and focused heating, perhaps at the footpoints of converging magnetic loops.

The blackbody has been reproduced in static phenomenological models. In Cram & Woods (1982), their model atmosphere #5 features extreme heating from the chromosphere through the deep photosphere and results in a $T_{\rm BB} \sim 14\,000$ K emission component and an Hα line with a central absorption; they note that this atmosphere most closely matches the continuum observations of stellar flares and could represent the stellar-analog of solar flare kernels where there is deep and concentrated atmospheric heating. Houdebine (1992) also produced model spectra that rise into the NUV like a hot blackbody but with a sizeable Balmer jump; their models employ very large electron densities of 10^{16} cm^{-3}. They vaguely suggest that hydrogen recombination radiation and blackbody continua contribute in varying proportions depending on the various parameters of the flare atmospheres. Phenomenological models of an energetic flare in the extreme-ultraviolet on a dM4 star gave a very small Balmer jump and peak in the NUV (2400Å; Christian et al., 2003). Kowalski et al. (2011a) showed that placing a Gaussian temperature "hot spot" below the temperature minimum in a quiescent M dwarf atmosphere produces an optical spectrum with $T_{\rm BB} \sim 11\,000 - 18\,000$ K and strong absorption in the Hydrogen Balmer features (discussed in Chapter 7).

Self-consistent models that use realistic flare heating mechanisms typically result in a white-light continuum that is dominated by a strong Hydrogen recombination component (Hawley & Fisher, 1992). The sophisticated one-dimensional RHD models of Abbett & Hawley (1999) and Allred et al. (2005, 2006) used the RADYN code (Carlsson & Stein, 1994, 1995, 1997) to simulate flares on an M dwarf and on the Sun using moderate (10^{10} ergs s^{-1} cm^{-2}, F10) and large (10^{11} ergs s^{-1} cm^{-2}, F11) fluxes of mildly relativistic electrons injected at the top of a semi-circular flare loop. The RADYN models employ the thick-target formulae of Emslie (1978), Ricchiazzi & Canfield (1983), and Hawley & Fisher (1994) that

describe how the nonthermal electron beam deposits energy throughout the atmosphere. The accelerated electron distribution in the Allred et al. (2006) models employs a double power-law energy distribution of beam electrons with a minimum cutoff energy, E_c, which is assumed to be 37 keV (inferred from solar flare hard X-ray observations with RHESSI (Holman et al., 2003). The energy from the electrons is deposited in the chromosphere, which explosively evaporates into the corona, illustrating the chromospheric evaporation scenario developed by Fisher et al. (1985). The Allred et al. (2006) F10 and F11 models represent *impulsive* heating, and they were run with constant beam fluxes for 230 sec and 16 sec, respectively. Gas-dynamic modeling has employed higher heating fluxes for an M dwarf flare, between 3×10^{11} and 10^{12} ergs cm^{-2} s^{-1} (Livshits et al., 1981; Katsova et al., 1997). Their models produced a sufficiently blue continuum from a high density ($10^{15} - 10^{16}$ cm^{-3}), hot ($T \sim 9000$ K), high velocity (100 km s^{-1}) condensation front. Although radiation losses were included, detailed radiation processes were not calculated in those simulations.

The Allred et al. (2006) RHD predictions of Hydrogen Balmer line emission, such as line broadening and flux decrements, are generally consistent with observations. However, a severe shortcoming of these predictions is the lack of hot blackbody emission which is clearly present, and in fact dominant, in the spectra of stellar flares. Instead, the dominant continuum components at $\lambda > 2000$Å are a large spectral discontinuity at the Balmer jump and optical emission from the Paschen continuum and the moderately heated photosphere. The photospheric heating is at most ~ 1000 K and results from incident NUV backwarming radiation; direct beam heating contributes relatively little to the heating of deep layers, and cannot reproduce the heating or densities implied by phenomenological models. The ultimate problem in the physically self-consistent models is therefore not enough heating at high densities. However, as mentioned previously, the broadband colors of the model flare spectrum produce a continuum distribution with the general shape of a blackbody with $T \sim 9000$ K and also appear to match the observed broadband $UV, UBVR$ fluxes quite well (e.g., flare 8 of Hawley et al., 2003).

The last study of a large flare sample with simultaneous spectra and photometry was that of Moffett & Bopp (1976), who revealed several global trends in the spectroscopic characteristics of flares. Their sample consisted of five flares with low-resolution spectral

coverage from $\lambda = 3700 - 5700$Å and high cadence U-band photometry. The exposure times were between 30 sec and 3 minutes, with most > 1 minute. Their main result was the demarcation of flares into "spike" and "gradual" phases according to the relative contribution of line and continuum emission; they also suggested a two-component model with Hydrogen recombination to explain these phases. Other results were shown for the He Iλ4026, He I λ4471, and Mg Ib lines, indicating no apparent relation between flare properties and their detection/non-detection. They found a longer time delay in the time of emission line maxima for higher luminosity stars, but their use of equivalent widths for line diagnostics makes interpretation difficult. The continuum shapes were not analyzed and the lack of blue wavelength coverage did not allow for an assessment of possible Balmer continuum radiation.

1.1 Proposed Project

For my dissertation project, we have obtained high signal-to-noise spectral observations in the blue/NUV, including the Balmer jump, of a homogeneous survey of flares for detailed line and continuum analysis. These data are necessary to break the degeneracy of fitting emission types to broadband photometry and to determine which continuum processes contribute (and how much) to the white-light. In the past, colorimetry was preferred in order to achieve a high signal-to-noise at good time resolution, but the U-band is difficult to interpret because it straddles the Balmer jump. Modern, 4-m class telescopes now provide good blue/NUV sensitivity and allow time-resolved spectra to be used to characterize faint levels of flare flux varying on short timescales. A large, systematic study of blue/NUV flare emission will reveal if hydrogen recombination (Balmer continuum) radiation is present in flares. Including a range of flare types (e.g., fast vs slow) could be useful to assess why this continuum component doesn't obviously appear in some flares. For example, perhaps the disappearance of the Balmer continuum is a phenomenon that only occurs during large impulsive flares, which coincidentally are the only ones that have yet been studied in detail with blue spectra.

We have interpreted the observations with new phenomenological and RHD models in order to understand the origin of the continuum properties. The RHD modeling uses

a higher beam flux of 10^{12} ergs cm^{-2} s^{-1}, similar to that employed in the gas-dynamic simulations of Livshits et al. (1981). An important new component of the RHD models is the inclusion of a gradual phase to study how an M dwarf atmosphere relaxes after the end of impulsive flare heating.

We have obtained simultaneous broadband photometry to connect with decades of single-filter and colorimetric flare studies. Most importantly, simultaneous observations allow us to relate the spectral continuum characteristics to the diverse types of light curve morphology observed. Through many studies of broadband optical photometry, a canonical fast-rise-exponential-decay ("FRED") light curve morphology has been invoked to explain the general morphology of a flare. The details of this "classical" morphology for dMe flares consists of a fast rise typically lasting tens of seconds, which is followed by a fast decay and a break to a gradual exponential decay lasting minutes to hours (Moffett, 1974). Coincidentally, the largest flares which have been studied with NUV spectra have time-profiles in the U-band that deviate from the canonical model and include a secondary, (usually lower) amplitude continuum enhancement following the fast decay phase of the first peak (Hawley & Pettersen, 1991; García–Alvarez et al., 2002; Fuhrmeister et al., 2008). Some flares have three or more continuum spikes in the impulsive phase (Kahler et al., 1982; Eason et al., 1992), while other flares have low-amplitudes but gradually emit a large amount of energy over a longer time period (Hawley et al., 1995).

A basic phenomenological question therefore is, "How do the continuum properties evolve through the different phases of the U-band evolution, and can we ultimately use these properties to create a flare continuum model that can explain the gamut of flare light curves that are observed?" For example, Osten et al. (2005) studied two U-band flares on the dM3.5e star, EV Lac: their durations were 4.5 and 7 minutes, yet their peak amplitudes were a factor of twenty different: how is the physics (i.e., flare heating) different between these two flares? With a large sample of flares that have simultaneous time-resolved spectra and photometry, we can constrain the detailed continuum parameters over a range of flare characteristics.

The most general aspect of this question is how the continuum components compare between the impulsive and gradual phases, and therefore how their respective "fast" and

"slow" evolution are related to the dominant flare heating mechanism and atmospheric cooling response acting at those times. In addition to identifying the differences between the individual phases of flares, we also seek to identify similarities between the same phases of different flares, to clarify important phenomena that must be reproduced by RHD models.

This dissertation is organized as follows. In Chapter 2, we discuss the data reduction and the basic line and continuum measurements. In Chapter 3 we present the observational parameters, an overview of the properties of the flare sample, and a short description of each of the twenty flares. Chapter 4 contains the emission line analysis. In Chapter 5, we present the ApJL Kowalski et al. (2010) which presents the first bona-fide detection of the Balmer continuum and establishes the two-component continuum framework for the decay phase of the "Megaflare". We improve upon and apply this continuum analysis to all flares in the sample in Chapter 6. In Chapter 7 (drawn from Kowalski et al. (2012)), we use phenomenological modeling to reproduce the detailed continuum properties of the data in Chapter 5. In Chapter 8, we present results from a 10^{12} ergs cm^{-2} s^{-1} RHD flare simulation that includes a gradual phase. In Chapter 9, we summarize our findings. There are several Appendices which discuss details of the data reduction and error analysis.

Chapter 2

OBSERVATIONS AND DATA REDUCTION

In September 2008, we began a three-year, simultaneous spectroscopic and photometric flare-monitoring campaign of nearby, dMe flare stars. Low-mass stars provide ideal hosts to study near-UV flare radiation due to the high contrast against the quiescent background. We chose to monitor the M dwarf flare stars that had the highest optical/NUV flare rates ($\sim$ 1 / hour, Lacy et al. (1976); Pettersen et al. (1984)), and we limited our sample to five bright, nearby stars (EV Lac, YZ CMi, AD Leo, EQ Peg, Gl 644) to allow for short exposure times. The multiwavelength properties of the flares on these stars have been studied extensively (Kahler et al., 1982; Hawley et al., 1995; van den Oord et al., 1996; Osten et al., 2005, 2010). The targets and basic stellar parameters are given in Table 2.1.

The sixth target star GJ 1243 is a star that hasn't had its flare rate previously measured. It is known to be an active star (Gizis et al., 2002) of spectral type dM4e, and its long baseline photometric starspot activity was recently measured by (Irwin et al., 2011). This star is in the Kepler field and part of our GO program with observations at 1 minute cadence. Therefore, this star was added to our ground-based monitoring program. The Kepler flare properties will be presented in Hawley et al. 2012.

From the light curves, we selected eighteen flares, from five different stars, to analyze in detail. These flares occurred over fourteen separate nights and totaled 75 hours of spectral monitoring with 7780 spectra[1]. In addition, we consider the data obtained during the large flare of 27 Oct 2009 on EV Lac, which has been presented in Schmidt et al. (2012). The blue spectra were obtained at the Dominion Astrophysical Observatory (DAO) and have much lower time resolution (200 – 300 sec) and only cover the wavelength range $\lambda = 3550 - 4700$Å with $R \sim 750$, but these data encompass an unusually fast and large amplitude flare. We

[1]There are several more nights and several more (small-amplitude) flares and other types of variability in the data that were not analyzed in this study; these nights are listed in the observing logs below the horizontal line and are also available online.

also calculate relevant quantities from the Great Flare on AD Leo on 12 April 1985 (Hawley & Pettersen, 1991, hereafter, HP91) for comparison.

2.1 Spectral Data

Spectra were obtained with the Dual-Imaging Spectrograph (DIS) on the ARC 3.5-m at the Apache Point Observatory (APO). We employed the low-resolution B400/R300 gratings, which provided continuous wavelength coverage from $\sim 3400 - 9200$Å, except for a dichroic feature that affected the flux calibration from $\sim 5200 - 5900$Å. The CCD was binned by 2 and windowed to $130 - 150$ pixels along the spatial axis ($\sim$100"), thereby reducing the readout time from 40 sec to ~ 10 sec. Integration times ranged from 1 second to 45 seconds (most were between 10 and 20 seconds). Short ($1 - 8$ second) spectra were occasionally interspersed in the observing sequence in order to avoid non-linearity and saturation in the red during the longer integration times that were necessary to obtain visible counts on the 2D image at $\lambda = 3450$Å ($x \sim 300$ on the chip). This typically provided an adequate signal to noise of ~ 10 at 3600Å in quiescence. We obtained data with the 1.5" slit for the first two years and primarily with the 5" for the last year (if the conditions were clear). The wide slit facilitated absolute flux calibration (so that we could check the scaled spectra against the original flux-calibrated spectra; see below) and allowed the exposure times to be reduced. The slit was automatically rotated to the parallactic angle (perpendicular to the horizon) in order to account for atmospheric differential refraction (Filippenko, 1982). Care was taken to ensure the star stayed centered on the slit through the course of the observations, but in some instances slight deviations may have affected the observations. The observations were taken under moderate to good weather conditions; the seeing was estimated with each spectrum, but rarely exceeded the slit width by more than $\sim$0.5".

The spectra were reduced using standard IRAF[2] procedures via a customized PyRAF[3] wrapper, developed from the reduction software of Covey et al. (2008). Initial processing

[2]IRAF is distributed by the National Optical Astronomy Observatories, which are operated by the Association of Universities for Research in Astronomy, Inc., under cooperative agreement with the National Science Foundation.

[3]PyRAF is a product of the Space Telescope Science Institute, which is operated by AURA for NASA.

included bias, overscan, and flat-field corrections. Aperture extraction and background subtraction were performed and a wavelength solution was applied using HeNeArHg and HeNeAr lamps. The resulting dispersions were 1.82 Å per pixel for the blue and 2.3 Å per pixel for the red. The spectral resolutions were determined from the He I λ4471 arc line taken at the beginning of the night. For the 1.5" slit, the resolution at this wavelength was $5.5-7.3$Å and ~ 18Å for the 5" slit. For the very wide (5") slit width, the profiles of arc lines are wider and less gaussian than for point sources, and measuring the quiescent emission line profiles of the M dwarfs reveals an actual resolution closer to $13-15$Å. Although broad, the line profiles for the spectra of M dwarfs taken with the wide slit were in general nearly gaussian and allowed line fluxes to be measured. Observations of spectrophotometric standard stars (white dwarf or sdO stars) were obtained every night and were used to convert from counts to an energy scale. An airmass correction was applied to the spectra using the atmospheric extinction curve of APO, published with the SDSS project.The spectral shape accuracy across the $\lambda = 3400-5200$Å range was usually better than 10%, which we calculated from observations of multiple spectrophotometric standard stars. Synthetic U, u, and g absolute magnitudes obtained from the spectra were accurate to within $20-25\%$. The spectrophotometric standard star fluxes were obtained from Oke (1990); second order corrections to the APO atmospheric extinction curve were not applied to the data. Further details about the data reduction and flux accuracy are given in Appendix A.

The observing log for each target star is given in Tables $2.2-2.5$. The monitoring time / night, number of exposures, exposure times, spectral resolutions, and available simultaneous photometry are also provided. For the number of exposures given, the three values indicate the number used for blue analysis, the total number of spectra recorded, and the number of spectra obtained at a shorter exposure time for red analysis: (nB, nT, nR). For a spectrum to be considered in the analysis (and be counted in nB), the standard deviation divided by the flux just blueward of the Balmer jump was required to be less than 20%. This allowed us to select spectra that were (mostly) unaffected by weather and cosmic rays. Note, some short-exposure spectra were excluded by this requirement; these are analyzed independently.

2.2 Photometric Data

Photometry was obtained from the NMSU 1-m telescope and/or the ARCSAT 0.5-m telescope at the Apache Point Observatory. The 1-m is operated robotically (Holtzman et al., 2010), and in almost all cases provided continuous Johnson U-band photometry. Observations were reduced as part of the standard 1-m pipeline (and in some cases by hand using standard IRAF procedures). We used the Flarecam instrument (Hilton et al. 2011) on the 0.5-m, which was remotely operated. Flarecam has enhanced UV sensitivity, a fast readout ($\sim$ 1 second), and rapid filter wheel rotation among the available SDSS *ugri* filters. A variety of imaging sequences were employed during the campaign in order to determine the optimal balance of duty cycle and wavelength coverage. The data were reduced using standard IRAF procedures with the *ejhphot* reduction wrapper (Hilton et al., 2011). By comparing the times in the spectra and photometry headers, we determined that the timing of the Flarecam images was not always synched with UTC. This offset ranged between 7 – 30 seconds, and we adjusted the center times of the measurements accordingly. This precision is all that is necessary for our study, since the spectra have a cadence no better than 11 seconds.

Differential aperture photometry was performed using nearby bright stars, and a quiescent window was chosen to normalize the count flux for the night[4].

Tables 2.2 – 2.5 contain information about the photometry used for each night.

2.2.1 Measured Quantities

In each spectrum we measured the average flux in thirteen $\sim$30Å - wide continuum windows across the DIS spectral range. The continuum windows are listed in Table 2.6, and were chosen to correspond to spectral windows free of major (and most minor) emission lines that appear during flares. We used the peak flare spectrum from 24 Feb 2011 and a decay spectrum from 16 Jan 2009 (both from flares on YZ CMi) to guide our selection of line-free regions. We also used quiescent M dwarf spectra to select relatively flat (small slope)

[4]Airmass and color corrections were not applied to the data; differential photometry provides the necessary accuracy for this study.

regions of the quiescent continuum (away from large molecular feature variations) so that intra- and inter-night wavelength shifts would not affect the average continuum flux. The fluxes at wavelengths near those of several important solar filters were also calculated at $\lambda \sim$ 4300Å, 4500Å, 6200Å. In addition to these narrow-band fluxes, we also calculated synthetic U, B, V, u, g, r, i, K_p[5] and custom filters designed for the stellar instrument ULTRACAM (Dhillon et al., 2007), which has been used to study flares in the NBF3500, NBF4170, RedCont#1 and Hα (Kowalski et al., 2011b). A large data paper containing flare light curves in these filters will be presented in a future work.

The two continuum measures that we use to characterize the blue are the average flux in the wavelength region from $3600-3630$Å (C3615) and the average flux in the wavelength region from $4155-4185$Å (C4170). The C3615 region was chosen to be blue of the Balmer jump at 3646Å, while also red enough to obtain a reasonable signal to noise in small to moderate-size flares. The C4170 region was chosen to emulate the NBF4170 continuum filter, which is a custom continuum filter that is also employed on the solar camera ROSA (Jess et al., 2010b).

The value C3615 / C4170 gives a Balmer jump ratio, and can be used to distinguish flares from grey slit loss. The continuum ratios contain quiescent emission and therefore can only diagnose *if* the continuum was changing and on what timescales. Removal of quiescent emission is described in Section 2.2.3 below. The quantity $\mathrm{C3615_{total}}$ will be used to indicate a flux that includes quiescent emission, whereas the use of C3615 without subscripts will indicate that quiescent emission has been subtracted. Note that in previous papers (Kowalski et al., 2012, in Chapter 7), a prime symbol was used to indicate that quiescent emission had been removed.

2.2.2 Emission Line Fluxes

Line fluxes were calculated for hydrogen Balmer α, β, γ, δ, ϵ + Ca II H, Ca II K, several Helium I lines (λ4026, λ4386, λ4471), He II λ4686, and several prominent lines with ambiguous identifications that possibly represent a combination of Helium I, Fe II, or Mg Ib

[5]Johnson filter curves obtained from Maíz Apellániz (2006), SDSS filter curves obtained from the SDSS website, Kepler filter curve obtained from the Kepler web site.

lines ($\lambda \sim 4920$Å, $\lambda \sim 5015$Å, $\lambda 5167$Å+$\lambda 5173$Å, $\lambda \sim 5184$Å)[6]. A line flux can be calculated by measuring the equivalent width of the line and multiplying by the nearby continuum (Reid et al., 1995). If the continuum is normalized to absolute photometry or if the observations are spectrophotometric, this method accounts for the effects of weather and slit-loss. However, the continuum changes dramatically during flares, especially in the region of the blue lines. Alternatively, one could look for a region of the continuum with an accurate calibration whose value doesn't vary during flares and use this to calculate the equivalent width and flux normalization. After close inspection, we found that the entire optical continuum (3400 – 9200Å) experiences significant flux variations during the largest flares. The red continuum near λ =8650Å is most nearly constant, but the flux calibration here is not always reliable.

The calculation of line fluxes during flares is further complicated by the increasing widths of the line wings (Doyle et al., 1988; Hawley & Pettersen, 1991). During flares, the apparent full width of the wings can increase dramatically to $\Delta\lambda \sim 60$Å (see Chapter 4). Wide wavelength windows are used for integration limits to account for the extreme broadening of the line wings. The integration limits and continuum ranges are given in Table 2.7, and were chosen to be wide enough to account for the maximum amount of broadening observed in the flare sample; the same windows were used for all spectra of all flares in the DIS sample to be consistent. An example peak flare spectrum with significant broadening is shown with the integration windows in Figure 2.1.

The measurement of line fluxes employed in this paper is as follows. Starting with the total (flare+quiescent) flux in each spectrum, we define local continuum regions and determine a linear fit between regions on either side of each emission line. The linear fit allows us to estimate a first-order change in the continuum beneath the line (as is important during flares). We then compute the flux in the line region (Table 2.7). Measurements of the line fluxes in Hγ, Ca II K, and He I λ4471 can be reliably calculated before subtracting a preflare spectrum; flare-only emission is obtained after calculating the line fluxes. However, for the other lines, it was necessary to subtract the quiescent spectrum before calculating the

[6]There is a Fe II (42) triplet at λ = 4924, 5018, and 5169Å have been identified in previous flare spectra (Abdul-Aziz et al., 1995).

line flux because the lines were either at very low-level and were not readily visible (e.g., the other He I lines) or the surrounding continuum is poorly modeled by a linear function due to "jagged" quiescent molecular features (as is the case for Hα, Hβ, Hδ). For these lines, the line flux was calculated after subtracting a quiescent spectrum (see Section 2.2.3), allowing for a more precise fit of the line to the local continuum. For Hα, and for flare-emission in faint lines, this method resulted in negative features away from line-center if the quiescent lines were not aligned precisely with the flare features (e.g., due to occasional single pixel jumps from wavelength instabilities); therefore, we summed the positive and negative flux values over the Hα line.

The local continuum near important features such as Hδ, Hγ, Hβ and Hα also contains numerous photospheric molecular features which present an additional complication for defining line and continuum regions. Because we integrate over a large wavelength window, we include some molecular features in the line flux (for Hγ, He I λ4471; see above); however, the molecular flux is hypothetically removed by subtracting the quiescent spectrum. The line calculations are done with an automatic routine, and they were examined by eye to ensure that we accounted for all of the excess flare flux. The line windows given in Table 2.7 were adjusted by a small amount for every spectrum depending on the centroid of the line, which was determined initially for the Balmer Hα, Hβ, Hγ, and Hδ lines; the wavelength shifts for the Ca II K and He I λ4471 lines were forced to be the same as for the Hγ line. The wavelength centroid stability is typically < 1Å but can vary by about a pixel ($\Delta\lambda = 1.83$Å/pixel) from one spectrum to the next.

In Table 2.8, we present the quiescent properties derived for master non-flaring spectra of each star. The quiescent Hγ line flux (and Balmer decrements) are listed in this table and were calculated using a 16Å width window around each line. The local continuum regions were chosen closer to the base of the line than for the flare measurements. For the Hγ line, there is a molecular feature (a "pedestal", see Figure D.1 for the case of AD Leo) which is visible in inactive templates of the same spectral type as our target stars ($\sim$dM4) and which blends with the base of the line at the resolution of DIS. However, even if molecular flux is included in our measurements of the line flux, subtraction of the quiescent flux effectively accounts for this (since the molecular flux is included in both the quiescent and flare values).

Obtaining precise quiescent fluxes is only important in this study for comparing quiescent to flare decrements (Chapter 4)[7].

2.2.3 The Determination of Absolute Fluxes

An additional step in flux calibration was necessary to correct for exposure-to-exposure grey variations in the level of flux, due to variable seeing, variable transparency, and imperfect centering of the star in the slit. In Kowalski et al. (2010) (see Chapter 5), we used simultaneous U-band photometry to apply a single scaling factor to each spectrum. Since then, we have developed an improved method to scale the spectra (detailed below) which minimizes the subtraction residuals in the molecular features in the red continuum. Importantly, this new technique allows us to independently compare the spectra and photometry, as the integration time of the photometry (especially during the fast impulsive phase of a flare) may differ from the spectra.

For each night, a master quiescent (or pre-flare) spectrum was found by identifying non-variable times from the photometry and the Hγ line. The spectra during the non-flaring interval were scaled to a common flux at $\lambda = 4500$Å in order to account for the weather or slit-loss variations over the course of the spectra within this time window. Synthetic Johnson B and V fluxes were compared to the accepted magnitudes (in Table 2.1, obtained from Reid & Hawley (2005)), using the Johnson (1966) flux zeropoints. The observed fluxes were scaled so that the synthetic fluxes were equal to the accepted fluxes. This initial scaling is important for placing all nights (for a given star) on the same baseline flux level.

A scaling for each flare spectrum relative to the master quiescent spectrum is then performed as follows. For each spectrum during the flare, we multiplied by a range of scale factors $(0.2 - 4.0)$, subtracted the quiescent spectrum, and calculated the sum of the standard deviation of the subtraction residuals in three spectral regions (outside of features from the Earth's atmosphere which can change over time) from $\lambda = 6600 - 6800$Å (excluding

[7]More precise line fluxes were estimated for the Hγ and Hδ lines of AD Leo by subtracting an inactive template to account for the molecular flux; the line flux was found to change by 0.7 and 1.2 times (respectively) the value obtained without subtracting an inactive template. Therefore, the range of possible "true" quiescent flux decrement, Hδ / Hγ, is 0.4 – 0.7 for AD Leo

the region around He I 6678Å), $\lambda = 7000 - 7100$Å, and $\lambda = 7350 - 7550$Å[8]. These regions correspond to strong flux changes in the quiescent spectrum due to the presence of molecular bandheads; therefore, errors in flux scaling appear as significant over- or under-subtractions at these wavelengths. The best scale factor minimized the sum of the standard deviation of the subtraction residuals. We tested this procedure using a *gedanken* experiment (Appendix B). Essentially, we generated a model flare spectrum and multiplied by an arbitrary scale factor to simulate flux loss (from weather or slit-loss). We found that our simple algorithm determines the correct scaling factor for all but extremely high amplitude flares, which aren't in our sample. A similar scaling method was employed by Abdul-Aziz et al. (1995). The principle behind the scaling method is analogous to PSF subtraction in imagery of protoplanetary disks, where the optimal subtraction is found by minimizing the subtraction residuals in the background (e.g. Wisniewski et al., 2008).

Ultimately, a single scaling value was determined for each spectrum, and we refer to this scaling factor as R_i. The final stage in flux calibration was to multiply the flux density, line fluxes, continuum fluxes, and synthetic filter fluxes by R_i during the flare times. The flare-only fluxes were then obtained by subtracting the quiescent values. Figure B.1 in Appendix B demonstrates the recovery of flare variations during times of variable cloud cover.

[8]The data on 10 Oct 2009 had highly non-linear or saturated flux values in the red, and the data on 01 Oct 2008 did not have red data. For these spectra, we scaled using molecular features in the blue from $\lambda = 4745 - 4770$Å, $4947 - 4960$Å, and $5159 - 5172$Å. On nights with good red data, this gave scalings that were consistent with the red windows. For the DAO spectra from 27 Oct 2009 presented in Schmidt et al. (2012), we used windows: $\lambda = 4572 - 4589$Å, $4621 - 4630$Å, and $4660 - 4673$Å.

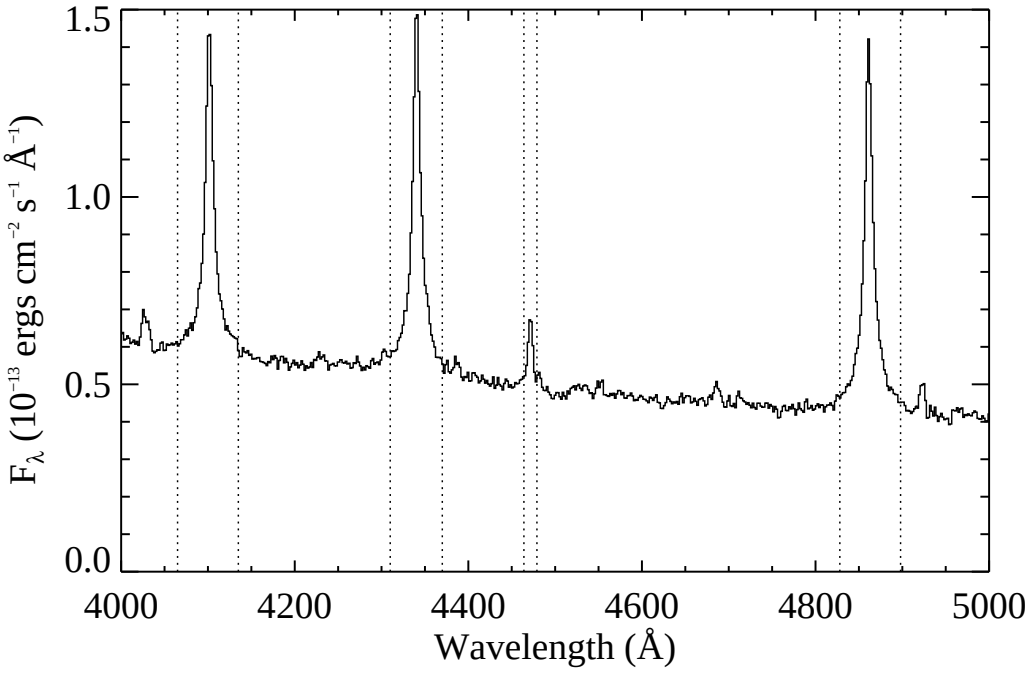

Figure 2.1 The peak spectrum from the flare on 14 Feb 2010 on YZ CMi showing the windows of line flux integration for the Hδ, Hγ, He I λ4471, and Hβ lines. These data were obtained with the 1.5" slit.

Table 2.1. Target Star Basic Parameters

Star	Spectral Type	U Mag	B Mag	V Mag	dist (pc)	R (R_{Sun})	log L_U (erg / s)	$F_{U,q}$ (10^{-14} erg / s / cm^2 / Å)
YZ CMi (Gl 285)	dM4.5e	13.77	12.80	11.19	5.97	0.30	28.6	1.35
EV Lac (Gl 873)	dM3.5e	12.96	11.86	10.28	5.05	0.36	28.8	2.85
AD Leo (Gl 388)	dM3e	11.91	10.85	9.32	4.89	0.43	29.2	7.49
EQ Peg A (Gl 896 A)	dM3.5e	13.18	12.12	10.41	6.34	0.36	28.9	2.33
GJ 1243	dM4e	∼15.5	14.47	12.83	12	0.36	∼28.5	0.27
Gl 644 AB	dM3e	11.65	10.60	9.02	6.45	0.43	29.52	9.52

Note. — Magnitudes are obtained from Reid & Hawley (2005); magnitudes for GJ 1243 and Gl 644 are obtained from SIMBAD. The U-band magnitude for GJ 1243 assumes that $U - B = 1$.

Table 2.2. YZ CMi Observing Log

UT Date (MJD)	Monitoring Time (Hrs)	Exp time (# exp)	Slit	Photometry
16 Jan 2009 (54847)*	1.3	10 (157B,163T,0R)	1.5 (6,13)	1m (U)
26 Jan 2009 (54857)	6.183	20-45, 60, 300 (485B,524T,0R)	1.5 (5.7,11,6)	n/a
14 Feb 2010 (55241)	4.856	5,10,30,45,150 (332B,424T,83R)	1.5 (5.9,12)	1m (U), 0.5m
11 Dec 2010 (55541)	5.028	18,30 (438B,468T,0R)	5 (17,30,12.5)	1m (U), 0.5m
13 Dec 2010 (55543)	5.191	15, 18, 90 (574B,606T,0R)	5	1m (U), 0.5m
08 Feb 2011 (55600)	5.5804	8,12,15,20 (610B,703T,0R)	5 (18,31,13)	1m (U), 0.5m (ugri)
24 Feb 2011 (55616)	3.988	7,10,12,15 (437B,462T,0R)	5 (19,32,13.5)	1m (U), 0.5m (ugri)
2 Mar 2011 (55622)	3.9209	20 (235B,403T,32R)	1.5 (7.3,19,7.4)	1m (U), 0.5m
04 Mar 2011 (–)	–	20, 60	5	0.5m
15 Dec 2009 (55180)	2.868	30, 240	1.5	0.5m
13 Jan 2012 (–)	–	–	5	1m (U), 0.5m

Note. — *Does not include two spectra that were found to to have spurious flux values, does not include the four spectra at the beginning of the night that had 30 sec exposure times (and saturated red flux values). Next to the slit width, we have indicated the (FWHM of arc line He I λ4471, full width at 0.1 max of arc line He I λ4471, and the FWHM of Hγ for a sample target spectrum). The flare event on 14 Feb 2010 exclude the short exposure data from the B total.

Table 2.3. EV Lac Observing Log

UT Date (MJD)	Monitoring Time (hrs)	Exp time (# exp)	Slit	Photometry
10 Oct 2009 (55114)	8.202	6, 15, 20, 30 (572B,626T,0R)	1.5 (5.5,12,5.5)	1m (U) 0.5m
11 Oct 2010 (55480)	4.868	3, 5, 9, 10 (621B,686T,108R)	1.5 (7.3,18,6.5-7)	1m (U) 0.5m (ugri)
24 Sep 2009 (55098)	9.6602	30 (481)	1.5	1m (U), 0.5m
10 Oct 2010 (55479)	4.518	9, 7 (813)	1.5	1m (U), 0.5m

Note. — The flare event on 11 Oct 2010 excludes the short exposure red spectra from the B total.

Table 2.4. AD Leo Observing Log

UT Date (MJD)	Monitoring Time (hrs)	Exp time (# exp)	Slit	Photometry
03 Apr 2010 (55289)	3.973	1,2,10 (431B,581T,145R)	1.5 (6.5,15,6-6.5)	0.5m (g)
08 Feb 2011 (55600)	2.8562	2,5 (409B,446T,109R)	5	0.5m (ug)
13 Mar 2010 (55268)	4.231	1,10 (537B, 743T,206R)	1.5 (6.8,16.5)	1m (U), 0.5m (ugri)
15 Dec 2009 (–)	–	2,4,10,20	1.5	0.5m
05 Mar 2009 (–)	–	10-45 (130)	1.5	0.5m (ug)
21 Apr 2009 (–)	–	3,8,5,10 (700)	5	0.5m
29 Feb 2009 (–)	–	5,7+ (1300)	1.5	0.5m (ug)
27 Dec 2009 (–)	–	15,20,45 (300)	1.5B1200/R1200	1m (U,B)
24 Apr 2009 (–)	–	5,15,10,300 (–)	1.5	0.5m (ug)
07 Apr 2010 (–)	–	10,2,10,12,120 (650)	1.5	1m, 0.5m
12 Apr 2010 (–)	–	8,2 (800)	1.5	1m, 0.5m -
08 Apr 2011 (–)	–	3,8,10,12 (540)	1.5	1m, 0.5m
09 Apr 2011 (–)	–	2,5 (1000)	5	1m, 0.5m

Note. — Of the nights below the horizontal line (not included in this study) 8 Apr 2011 and 9 Apr 2011 have small flares. The 3 Apr 2010 date excludes the short R exposures from the B total. The 13 Mar 2010 date excludes the short R exposures from the B total.

Table 2.5. EQ Peg, GJ 1243, Gl 644 Observing Log

Star	UT Date (MJD)	Monitoring Time (hrs)	Exp time (# exp)	Slit	Photometry
EQ Peg A	01 Oct 2008 (54740)	9.2153	20, 30, 40 (722B, 786T,0R)	1.5 (6,12)	1m (U), MRO (B)
GJ 1243	20 Oct 2011 (55854)	2.830	45, 60 (135B, 159T, 0R)	5 (20,31,14)	n/a
GJ 1243 (nr)	06 Oct 2011	–	–	5	n/a
Gl 644 (nr)	2009 Feb 29	5-12 (50)	1.5	0.5m (ug)	

Table 2.6. Continuum Windows

Name	Window ($\AA$)	Comments
$C3615$	$3600 - 3630$	blueward of Balmer jump, does not include blue chip contaminant
$C4170$	$4155 - 4185$	similar to ULTRACAM NBF4170 filter
$C4285$	$4270 - 4300$	similar to Hinode SOT 4305Å G band
$C4505$	$4490 - 4520$	near SDO/AIA 4500Å filter
$C4720$	$4705 - 4745$	···
$C4930$	$4926 - 4942$	···
$C5080$	$5055 - 5105$	near classic 5000Å continuum window, not affected by dichroic
$C6010$	$5990 - 6030$	emulates ULTRACAM RC#1
$C6200$	$6170 - 6200$	similar to SDO/HMI
$C6435$	$6420 - 6450$	···
$C6815$	$6800 - 6830$	just blueward of atmospheric B? band
$C8100$	$8083 - 8130$	blueward of Paschen jump
$C8575$	$8562 - 8592$	between Ca II IR triplet lines, affected by fringing

Table 2.7. Spectral Windows for Line Fluxes

Line	Integration Window (Å)	Continuum Region (Å)
Hα	$6520 - 6610$	$6465 - 6484, 6610 - 6665$
Hβ	$4828 - 4898$	$4813 - 4825$, $4895 - 4912$
Hγ	$4310 - 4370$	$4260 - 4305$, $4375 - 4420$
Hγ (DAO)	$4321 - 4361$	$4260 - 4305$, $4375 - 4420$
Hδ	$4065 - 4135$	$4040 - 4064$, $4137 - 4167$
Hδ (DAO)	$4084 - 4122$	$4040 - 4064$, $4137 - 4167$
Hϵ+ Ca II H	$3944 - 3997$	$3914 - 3923$, $4000 - 4017$
Ca II K	$3923 - 3945$	$3914 - 3923$, $3946 - 3955$
He I 4471 (1.5" slit)	$4464.6 - 4481$	$4380 - 4461$, $4488 - 4554$
He I 4471 (5" slit)	$4464.6 - 4481$	$4380 - 4461$, $4488 - 4554$

Table 2.8. Selected Quiescent Properties

Star	Date	$F_{U,q,spec}$	$C3615_{\rm quiescent}$	$C4170_{\rm quiescent}$	Hγ (10^{-13} ergs/cm^2/s)	Decrements (Hδ, Hβ, Hα)
YZ CMi*	24 Feb 2011	1.9	1.47	3.34	6.24	0.4, 1.1, 4.1
YZ CMi	14 Feb 2010	1.78	1.41	3.25	5.36	0.6, 1.5, 5.6
AD Leo	03 Apr 2010	9.67	7.78	22.7	1.35	0.4, 1.3, 4.5
EV Lac	10 Oct 2009	3.75	3.04	8.34	7.03	0.5, 1.3, 4.6
EQ Peg A	01 Oct 2008	3.38	2.81	7.01	5.5	0.5, 1.4, n/a
GJ 1243**	30 Aug 2011, 20 Oct 2011	0.31	0.27	0.70	0.63	0.4, 1.3, 4.4

Note. — The $F_{U,q,spec}$, $C3615_{\rm quiescent}$, and $C4170_{\rm quiescent}$ fluxes have units 10^{-14} ergs cm^{-2} s^{-1} Å^{-1}. $F_{U,q,spec}$ is the quiescent Johnson U-band flux estimated from the spectra. Note that $C3615_{\rm quiescent}$ is closer to the accepted U-band flux, likely because the filter curve that we use does not weight the U-band correctly.

*The data on 24 Feb 2011 were obtained with the 5" slit; the data on 14 Feb 2010 were obtained with the 1.5" slit.

**Line fluxes of GJ 1243 obtained from 30 Aug 2011 as part of another program (with 1.5" slit); continuum fluxes obtained from 20 Oct 2011 with 5" slit.

Chapter 3

THE FLARE ATLAS

In this Chapter, we introduce several basic observational parameters and measurements that are used to describe the flares, and then briefly describe each of the 20 flares in the Atlas.

3.1 Basic Observational Parameters

In this section, we will refer to Figures 3.1, 3.2, 3.3, 3.5, and 3.6.

3.1.1 Photometry Parameters

In Figure 3.1, we show a light curve from 01 Oct 2008 of a large flare on EQ Peg A. We use this figure to illustrate the following empirical values that can be directly measured.

1. τ

   We use a decay time constant to describe the decay phase light curves that are well-fit by an exponential function. τ measures the time it takes for the flare to decay from peak emission to 37% of peak emission. Exponential fits are calculated with a 5-parameter least-squares routine that employs the IDL routine *mpcurvefit*. For the example flare in Figure 3.1, a single exponential fit with $\tau = 2.8$ minutes (green line) does not account for the entire decay phase due to the complexity in the light curve. Considering sections of the decay phase separately usually results in better fits.

2. $t_{1/2}$

   To describe the time-evolution of a light curve, we use $t_{1/2}$, which is the full width of the light curve at half-maximum. This measures the 'timescale' of the flare, including both rise and decay times and provides an alternative to τ. The measure of $t_{1/2}$ does

not assume a functional form for the decay, which can be complex, as seen in the example. We also measure $t_{1/2}$ for the light curves of spectral components (Section 3.1.2). In some cases, the rise time is fast compared to the photometric/spectral cadence; in these cases we must interpolate between data points to obtain $t_{1/2}$.

3. I_f, $I_f + 1$

The measure I_f is a familiar quantity in flare studies (Gershberg, 1972). It is the ratio of flare-only count flux (photons cm^{-2} s^{-1}) in a given band, to the quiescent count flux in that band. $I_f + 1$ is the flux enhancement, or the *total* count flux relative to quiescence. In solar physics, I_f is used to express the *intensity contrast*[1]. If $C(t)$ is the total relative count flux (counts$_{\rm target}$/counts$_{\rm comp}$) normalized to 1 during quiescence, then

$$I_f(t) = C(t) - 1; I_f(t) + 1 = C(t) \tag{3.1}$$

In Figure 3.1, $I_{f,U}(t_{\rm peak}) = 20.4$.

4. ED

The equivalent duration (ED) in a given bandpass is the integral of I_f over the duration of a flare (Gershberg, 1972). The units are *seconds* and multiplying by the quiescent luminosity in the band gives the energy of the flare.

5. $\mathcal{I}$

To characterize the shape of the light curve, we use an "impulsiveness index", $\mathcal{I}$, which is defined as

$$\mathcal{I} = I_{f,peak}/t_{1/2} \tag{3.2}$$

The quantity $\mathcal{I}$ is a measure of the peak relative flux of a flare weighted by how fast it rises to peak and decays. Both a more luminous-at-peak flare and a smaller

[1] I_f has traditionally been used in stellar flare work also, although we realize that it is not the intensity, but the count flux that we are measuring in that case.

$t_{1/2}$ can give rise to larger values of $\mathcal{I}$. We find that this measure provides a way to quantitatively sort the flares by their light curve evolution.

The impulsiveness index provides the main classification scheme employed in the remainder of the paper. For our flare sample, $\mathcal{I}$ ranges from $0.02 - 100$. The *impulsive flares (IF)* are those that have $\mathcal{I} > 1$, whereas the *gradual flares (GF)* have $\mathcal{I} < 1$, as can be seen easily by visual inspection in Figures 3.3, 3.5, and 3.6. For flares that are close to this dividing line ($\sim 0.6 - 1.8$), we assign the classification *hybrid flares (HF)*, as these flares have a prominent impulsive phase (or several impulsive phases) but also share properties with the gradual flares.

We also considered the *fast* and *slow* flare classification scheme from Dal & Evren (2010), but this grouping employs a total decay time measurement; in some cases, poor weather, a standard star sequence, or secondary flares interrupted the decay measurements. Using $t_{1/2}$ bypasses the ambiguities with measuring precise start and stop times (Hilton et al., 2011), and also allows a better determination of the contribution of secondary flares to the decay emission (Kowalski et al., 2010, Chapter 5).

6. $\mathcal{L}$, $\mathcal{E}$

The specific luminosity ($\mathcal{L}$, units of ergs s^{-1} Å^{-1}) and specific energy ($\mathcal{E}$, units of ergs Å^{-1}) are more useful for characterizing the spectral energy distribution (SED) without the ambiguity of using a spectral window of width, $\Delta\lambda$. For example, U-band energies (and luminosities) assume $\Delta\lambda = 700$Å whereas B-band energies (and luminosities) assume $\Delta\lambda = 900$Å, making total energies in the two bands not directly comparable. In some cases, we present the integrated (over wavelength) quantities L, E in bandpasses that are directly comparable to previous studies. However, when comparing measurements from the spectra, we use $\mathcal{L}, \mathcal{E}$. All measures (L, E, $\mathcal{L}, \mathcal{E}$) assume an isotropically-emitting source, and employ the distances given in Table 2.1.

3.1.2 Spectral Parameters

We now refer to Figure 3.2 to describe the measured parameters from the spectra. This spectrum shows the peak flare-only emission during a simple, moderate-amplitude flare on AD Leo from 03 April 2010.

1. Spectral Zones:

   For reference, and throughout the rest of the thesis, we divide the spectrum into four zones: the *near-UV zone* ($\lambda = 3400 - 3646$Å), the *intermediate zone* ($\lambda = 3646 - 4000$Å), the *blue-optical zone* ($\lambda = 4000 - 5200$Å), and the *red-optical zone* ($\lambda = 5800 - 6800$Å).

2. C3615

   The average flare-only flux from $\lambda = 3600 - 3630$Å (see Section 2.2.1). This filter covers the approximate central wavelength of the U-band, which is much broader.

3. C4170

   The average flare-only flux from $\lambda = 4155 - 4185$Å (see Section 2.2.1).

4. $\chi_{\rm flare}$

   To describe the flare color across the blue and near-UV wavelengths in (mostly) line-free continuum bands, we use the quantity:

$$\chi_{\rm flare} = \mathrm{C3615/C4170} \tag{3.3}$$

   The error of this quantity is obtained by propagating the standard deviation of the fluxes in C3615 and C4170. Formally, the uncertainty of C3615 and C4170 is the standard error of the mean, but some emission line features (e.g., Fe I, Fe II) appear in this spectral region; therefore, a better estimate of the uncertainty in the continuum level in each window is given by the standard deviation. We calculate $\chi_{\rm flare}$ for each

spectrum. We analyze $\chi_{\rm flare,peak}$ and $\chi_{\rm flare,decay}$ (at times indicated in Tables 4.2), which are given in Table 3.2 (columns 4 and 5). The errors on $\chi_{\rm flare,peak}$ are 0.01 – 0.12, but some flares have significantly larger errors. $\chi_{\rm flare,decay}$ has larger errors. We exclude the flares with $\sigma_{\chi_{\rm flare}}/\chi_{\rm flare} > 0.2$ from the $\chi_{\rm flare,decay}$ analysis (IF5, IF6, GF3, IF8, GF5, GF4, and GF2). GF4 is also excluded from the $\chi_{\rm flare,peak}$ analysis due to large uncertainties.

$\chi_{\rm flare}$ is similar to the Balmer jump ratio, which has been employed to describe the Balmer jump strengths (J) in T Tauri stars (Valenti et al., 1993; Herczeg & Hillenbrand, 2008) and also in previous M dwarf flare studies in the blue to derive electron temperatures assuming an isothermal, isodensity slab of Hydrogen (Kunkel, 1970).

5. BaC3615

   The quantity C3615 is the *total flare-only* continuum emission from $\lambda = 3600 - 3630$ Å consisting of Balmer continuum emission from Hydrogen recombination and other possible components that contribute toward the continuous emission throughout these wavelengths such as Paschen continuum and blackbody continuum. Our estimate for *only* the flare Balmer continuum emission at 3615Å, BaC3615, is obtained by extrapolating and subtracting the continuum that is fit to the blue-optical zone. In particular, we fit a line to the wavelength windows listed in Table 3.1 from $\lambda = 4000 - 4800$Å (BW1-BW6), extrapolate to $\lambda = 3600$Å, and subtract this estimate from the flare-only flux in the 3615 window ($3600 - 3630$Å) to obtain BaC3615. This procedure is shown for an example flare spectrum in Figure 3.2. In all cases, BaC3615 $\leq$C3615.

6. BaC

   The estimate for the wavelength-integrated Balmer continuum energy from $\lambda = 3420 -$ 3646Å. The BaC is estimated using the same fitting & extrapolation procedure as for BaC3615.

7. PseudoC

The intermediate zone contains the higher order Balmer lines (Hϵ (H7) and greater) in addition to the Ca II H and K lines ($\lambda = 3934, 3968$Å). Although Ca II H is blended with Hϵ in these low resolution data, Ca II K is resolved. Within this zone, we integrate the flare flux from $\lambda = 3646 - 3914$Å (from the Balmer jump through H8) and refer to this as the "PseudoC" because many of the Hydrogen lines blend together (are partially or completely unresolved) at these wavelengths to form a pseudo-continuum. Again, as with the BaC, we use an extrapolation of the line-fit to the blue-optical to estimate the underlying continuum.

8. S#

   We refer to the time-sequential spectrum number (starting at 0 at the beginning of each night) with an S#. These numbers are also the IDL indices of the flux and time arrays available in the online data.

9. Times

   The times given on the light curves indicate the number of hours elapsed on the respective MJD from Table 2.2 – Table 2.5. The times for IF1 are given in "elapsed hours from flare start", as used in Kowalski et al. (2010) (Chapter 5).

10. Spike

    A "spike" is a type of impulsive event with a local maximum in the light curve and a fast drop soon thereafter. The impulsive phase can be comprised of several spikes, such as in HF1. We define a spike as any increase in the U-band by more than 33% of the quiescent level which also drops to at least 33% of the increased amount within two data points after the increase. A spike may not include the entire rise or impulsive phase of a flare.At least two data points must be elevated above the pre-spike level for us to consider it as a real event. In short-duration spikes with only two light curve points, we check the PSF profile in the reduced image for cosmic ray contamination. Other terms that refer to similar morphology used in this thesis are "burst" and "peak". We hope to construct more precise, physically significant

definitions for "spike", "burst", and "impulsive" emission using future data sets (e.g., according to the derivative of the light curve) which have complete time coverage of fast events.

11. Stall

    We define a "stall" as a break in the fast decay phase of a light curve. A stall occurs during a time when the emission is slowly decreasing or nearly constant, preceded and followed by times of fast decay.

12. Gradual Phase

    Gradual emission is observed during times of slowly rising or slowly decreasing emission. Following Hawley & Pettersen (1991), the "extended gradual phase" is defined as the turnover from fast to slow decay. The light curve in this phase is usually well-represented by an exponential decay function. The extended gradual phase spectra are chosen from the section of the light curve as near to the break from fast decay to slow decay as possible. We select three spectra around a time when C3615 is not changing rapidly so that the spectra can be coadded to increase the signal-to-noise without largely affecting the interpretation of atmospheric parameters. Appendix C details the times chosen for each phase of the flares in the flare atlas. The red vertical dashed lines in Figures C.1 – C.19 indicate the time that we selected to represent the extended gradual decay phase.

13. "Peak or maximum continuum emission"

    "Peak continuum" or "maximum continuum" emission always refer to the maximum value of C3615 during a flare.

3.2 Overview of the Flare Sample

The bluest available photometry (SDSS u, Johnson U, or SDSS g) for the flares in our sample are shown in Figure 3.3 (the nine impulsive IF flares), Figure 3.5 (the four hybrid

HF flares), and Figure 3.6 (the five gradual GF flares[2]). IF0 and IF10 are shown in Figure 3.4. IF0 on AD Leo from Hawley & Pettersen (1991) is known as the "the Great Flare", and the IF1 on YZ CMi (Kowalski et al., 2010, Chapter 5) is known as "the Megaflare". In the decay phase of IF1, we refer to the sub-peak at $t = 2.13$ hours as the "megaflare decay secondary peak #2" or "MDSF2". It is apparent that our sample contains a diverse set of peak amplitudes, total durations, and light curve morphologies. The naming convention (IF, HF, and GF) is based[3] on the value of $\mathcal{I}$ as detailed in Section 3.1.1. The IF flares generally have a classical, simple shape: a fast-rise, a fast decay, and a more extended decay beginning at a low level, $\sim 20\%$ or less, relative to the peak. Durations range from several minutes (e.g., IF6, IF8) to several hours (e.g., IF1, IF3). The IF flares have a large spread of amplitudes from low ($I_{f,peak} + 1 \sim 2.5 - 3$) to very large ($I_{f,peak} + 1 > 10$). Some IF events have secondary flares but are usually dominated by a single prominent peak. The HF flares also have fast rise components, but they exhibit marked deviations from the classic flare shape, such as multiple spikes of comparable amplitude during the impulsive phase (e.g., HF1) and an elevated or prolonged decay phase (e.g., HF2). These flares are low to moderate amplitude ($2 < I_{f,peak} + 1 < 5$) and usually longer lasting than the IF flares (> 1 hour). The GF flares are low-amplitude ($I_{f,peak} + 1 < 2.2$) except for GF1 which has $I_{f,peak} + 1 \sim 8$. The rise phases are notably slower, although they can have distinct periods of faster and slower emission; and may be accompanied by intermittent spikes (e.g., GF1 and GF3). However, these spikes do not dominate the overall timescales, which can be several hours for even the low amplitude flares.

Table 3.3 summarizes the key properties of the U-band photometry: flare ID (col 1), star name (col 2), date (col 3), time of peak continuum emission (col 4), $I_{f,U} + 1$ at peak photometry (col 5), equivalent duration in U (col 6), U-band energy (col 7), peak U-band luminosity (col 8), $t_{1/2,U}$ (col 9), and $\mathcal{I}$ (col 10). All properties are calculated only over the time over which spectra were obtained, except for peak amplitude in U, $t_{1/2,U}$, and $\mathcal{I}$. In Figure 3.7, we show the peak luminosity of the U-band and the $t_{1/2,U}$, which illustrates the

[2]Plus an extra gradual flare, GF6, for Hα study in Section 4.8.3

[3]IF10 is actually the most impulsive flare in the sample, but it is excluded from several areas of this study due to low cadence and a lack of complete spectral coverage.

large range of photometric properties.

In the Appendix C, we show figures of each flare with the integration times of the spectra indicated (Figures C.1 – C.19) and the spectrum numbers (S#'s) indicated.

In Figures 3.8, 3.10, and 3.11, the flare-only spectra at maximum continuum emission are presented in the same order as the photometry in the previous figures. The quiescent levels are shown in light grey for comparison. Table 3.2 gives the $I_{f,\mathrm{C4170,peak}}$ for each spectrum for reference. A detailed analysis of the continuum will be discussed in Chapter 6; here, simply a Planck function has been fit to the blue optical ($\lambda = 4000 - 4800$Å; BW1 – BW6 in Table 3.1) to parameterize the slope of the continuum (light blue line). The best-fit temperatures and χ_{flare} values are shown in parentheses. There are varying amounts of the excess continuum at $\lambda < 3640$Å in the IF flares, but the spectral trend into the NUV is similar to the underlying blackbody curve (the blackbody is scaled to the flux at $\lambda = 3600 - 3630$Å and shown in yellow). The HF and GF flares have large amounts of excess continuum at $\lambda < 3640$Å. Except for GF1 (and possibly GF5), the gradual flares are generally too faint for an accurate continuum fit. The IF flares have the lowest $\chi_{\mathrm{flare,peak}}$ values, mostly < 2, but with a few that have ~ 2.2 (IF5, IF6). The HF flares have intermediate values, $2.3 - 3$, and the GF flares have the larger and (besides GF1) more uncertain values, $\sim 3+$. The values of $\chi_{\mathrm{flare,peak}}$ and the errors are given in Table 3.2. The errors on the $\chi_{\mathrm{flare,peak}}$are typically $3 - 10\%$, with the GF events having larger errors. Using standard error propagation, we determine how well-separated the IF, HF, and GF flares are by the $\chi_{\mathrm{flare,peak}}$ parameters. We find that IF9 and HF1 are separated by 4.5σ, HF4 and GF1 are separated by $<1\sigma$, HF1 and GF1 are separated by 5σ, and IF5 and IF9 separated by almost 4σ.

In Figure 3.12 (top panel), we plot the flare peak properties, using our main spectral continuum diagnostic ($\chi_{\mathrm{flare,peak}}$; y-axis) and our main photometric continuum diagnostic ($I_{f,peak}+1$, x-axis). Flares with $I_{f,peak}+1 > 10$ have low $\chi_{\mathrm{flare,peak}}$ values, but $I_{f,peak}+1 < 10$ can have a large range of $\chi_{\mathrm{flare,peak}}$ values. Generally the lower amplitude flares have the largest $\chi_{\mathrm{flare,peak}}$. Column 4 of Table 3.2 gives the $\chi_{\mathrm{flare,peak}}$ of each flare.

The instantaneous continuum shape at maximum photometric amplitude appears to be linked to the overall evolution of the flare. In Figure 3.12 (bottom panel) we show $\chi_{\mathrm{flare,peak}}$

vs. the impulsive index, $\mathcal{I}$. A stronger trend appears here, compared to amplitude. Basically, the most impulsive flares have the lowest $\chi_{\rm flare,peak}$. IF5 and IF6 are exceptions that are quite impulsive flares (see Figure 3.3) but that have $\chi_{\rm flare,peak} \sim 2.2$. Interestingly, both flares occurred on EV Lac[4].

Impulsive flares with a "slow-down", or "stall", in their fast decays (e.g., IF5, IF6) show different continuum properties compared to impulsive flares that do not stall. In contrast, IF8 may have a stall[5] but a much lower value of $\chi_{\rm flare,peak} \sim$ 1.6. IF4 and HF3 are flares with "stalls" but with extremely different $\chi_{\rm flare,peak}$, $\sim$1.3 and 2.8, respectively. Flares that have multiple peaks can have a range of $\chi_{\rm flare,peak}$ values and $\mathcal{I}$ values. For example, IF0 ($\chi_{\rm flare,peak} \sim 1.4-1.9$), HF2 ($\chi_{\rm flare,peak}$2.6), and GF2 ($\chi_{\rm flare,peak} \sim$4.3) show multiple peaks in the impulsive phase but produce a range of peak continuum ratios.

In Figure 3.13 (top panel), we show the Hγ line flux divided by the continuum C4170 flux (both taken at peak C4170; essentially this is the equivalent width of the C4170 flare continuum in units of Å). There is a strong relationship with $\chi_{\rm flare,peak}$: flares with larger line-to-continuum ratios show larger Balmer jumps. This implies a connection between the amount of Balmer line radiation and the amount of Balmer continuum radiation at flare maximum. In the inset, IF2, IF3, IF7 , IF8, IF9, and IF10 cluster together, at $\chi_{\rm flare,peak} \sim 1.6-1.8$. The first and second peaks of the Great Flare (IF0) are also included in the inset. Note that IF8 and IF3 are the smallest and largest amplitude impulsive flares (with full coverage) on YZ CMi, yet they show very similar peak characteristics. The first and second peaks of IF4 are shown in purple and blue respectively; this flare has an extremely low $\chi_{flare,peak}$ and also line-to-continuum ratio.

The bottom panel of Figure 3.13 shows the maximum flux enhancement in the U band against the maximum enhancement for Hγ flux (they need not coincide to the same time). Generally, the impulsive flares produce larger relative continuum flux enhancements than the line flux enhancements (1:1 line shown). The flares IF2, IF3, IF4, IF7 and IF8 stand out as the most continuum dominated at peak; they are classical flares in many respects,

[4]Note that we also found an impulsive flare on EQ Peg A that had $\chi_{\rm flare,peak} \sim 2.2, I_f + 1 \sim 5$ in ULTRACAM data (Kowalski et al., 2011b).

[5]The stall is only apparent in one point during variable conditions; it may be suspect.

and all but one (IF4) occur on YZ CMi. Flares that lie on the 1:1 line are IF5 and IF9.

3.3 Descriptions of the Flares

In this section, we describe in detail the observational quantities about each flare. First we show figures that can used to guide the reader through the description of each flare; these are sorted by alternative characteristics in addition to the basic "impulsive", "hybrid", and "gradual" classification schemes.

In Figures 3.14 - 3.18, we show the light curves around each flare, for the photometry (blue or green line) and several important spectral components: the C4170, the Hγ line flux, and the BaC3615. All quantities are presented by the relative evolution of each component compared to its peak emission. The normalized flux is useful for qualitatively comparing rise and decay timescales between components in the same flare.

Simple, impulsive flares (Figure 3.14)

These flares all have moderately large amplitudes ($I_{f,U,\mathrm{peak}} + 1 \sim 5 - 12$) and energies ($E_U \sim 2 \times 10^{31} - 2 \times 10^{32}$ ergs). A defining characteristic is that the U-band (or bluest photometry) follows the evolution of the C4170. In fact, this holds for most of the flares. The different timescales of decay between the spectral components are evident: although the C4170, BaC3615, and Hγ vary from fastest to slowest, there is a spread of relative $t_{1/2}$ values, with IF9 having the smallest ratio of $t_{1/2,\mathrm{C4170}}/t_{1/2,\mathrm{BaC3615}}$. Except for IF7, these flares don't have obvious secondary flares in the decay.

Low amplitude flares (Figure 3.15)

The low amplitude flares have $I_{f,U,\mathrm{peak}} + 1 \sim$2 (GF) and $\sim$3 (IF). There are both complex and simple events in this group. These flares have lower energies: the low-amplitude short flares have $\sim 5 \times 10^{30}$ ergs and the low-amplitude long-duration flares have $\sim 10^{31}$ ergs (in their first main peaks). The durations range from minutes to hours.

Multiple-peaked, medium amplitude flares (Figure 3.16)

The multiple-peaked, medium amplitude flares have $I_{f,U\,\mathrm{peak}}+1 \sim 2.5-5.5$. These flares are all hybrid flares (HF type). Generally, in the HF flares, the evolution of the U-band closely matches the evolution of the BaC3615, whereas typically in the IF flares, the evolution in the U-band matches the evolution in C4170. In these flares, the $\chi_{\mathrm{flare,peak}}$ is $2.3-3$.

High Energy Flares (Figure 3.17)

The high energy flares have $E_U > 3\times10^{32}$ ergs. IF3 and GF1 are shown over the same time window of 1 hour. IF9 is also a high energy flare, shown over 1 hour duration in Figure 3.14. The C4170 and photometry track each other well in the high energy flares, whereas the BaC3615 is closer to the Hγ line. We caution against over-interpretation of the panel for IF10, which had long integration times compared to the fast photometric evolution in the early stages of the flare. Therefore, normalizing to the peak spectral quantities gives too much weight to the gradual phase quantities.

Low-amplitude, simple gradual flares (Figure3.18)

These flares have a moderate amount of energy ($E_U \sim 1-10\times10^{31}$ ergs) for their low peak-amplitudes. Interestingly, they lack a prominent fast decay phase after the peak emission. In GF5, short impulsive events are observed later in the flare decay.

The MDSF2 during the IF1 decay phase is included in this group. The bottom two panels are MDSF2: the left, bottom figure shows the normalized quantities of the MDSF2 after subtracting the emission at $t = 2.03$ hours and the bottom, right figure shows the normalized quantities of the total emission. Note that the Hγ and BaC3615 decrease in this sub-peak relative to the emission at $t = 2.03$ hours (their values are negative because absorption forms on the star; see Section 6.6.1); therefore, the normalized values in the bottom, left figure are positive. It is interesting that the normalized quantities of MDSF2 follow a similar general trend as other high-energy flares (IF3, IF9, GF1): approximately equally fast times to the maximum continuum / minimum line emission, but the C4170 faster than the BaC3615, which is faster than the Hγ line flux in the decay. Note that the

normalized values Hγ and BaC3615 peak after the peak of C4170 and the U-band. It is interesting that here the U-band decays faster than the C4170.

3.4 Individual Flare Descriptions

We present short descriptions of each flare, referring to Figures 3.14 - 3.18. When describing the light curve morphologies, we use the following terminology: *spike* to refer to the times of fastest evolving continuum emission, *fast decay* refers to the decay of the spike phase, and *gradual* phase to the times after the spike phase has ended, the emission has slowed to a slow exponential decrease, whereby the second derivative of the light curve does not noticeably change sign for many spectra. A *stall* is referred to an interruption in the fast decay phase when the derivative of a light curve changes to $\sim$0 before resuming a fast decay. The *impulsive* phase is the time covering the initial fast rise, peak, and fast decay phases of the flare. We investigated the use of a *first derivative* for a quantitative demarcation of the phases of the flare, but we found that the gradual phase emission of one flare (e.g., IF4) could be considered the impulsive phase emission of another flare (e.g., HF3). Therefore, we use the qualitative terms described above.

3.4.1 IF0: The Great Flare

The data for this flare are presented in Hawley & Pettersen (1991). IF0 released $> 10^{34}$ ergs of energy in U and had a rise time of $\sim$5 minutes. A clear demarcation between impulsive and gradual phases is evident. The initial spike is followed by a small gradual phase that precedes a secondary flare 6.3 minutes after the first peak. The gradual phase begins at 12% of the peak flux and the secondary flare occurs at 46% of the peak.

3.4.2 IF1: YZ CMi, 16 Jan 2009 (The Megaflare)

In this dissertation, we extensively analyze and model the spectral and photometric data for IF1: the light curves and a two-component continuum analysis are presented in Kowalski et al. (2010) (Chapter 5): the newly-formed flare emission during a secondary peak revealing

a Hydrogen Balmer features in absorption[6] is presented in Section 6.6.1. Phenomenological modeling and the solar-stellar analogy of this flare are presented in Kowalski et al. (2012) (Chapter 7). A detailed characterization of the temperature and areal coverage evolution during the secondary flare is given in Section 6.7. A new way to detect absorption in flares using the wing profiles and Balmer decrements of the *total* flare emission is illustrated in Section 4.5.4. We compare the light curve morphology of the impulsive phase of IF1 to the RHD model light curve in Chapter 8.

In IF1, there were several secondary flares during the decay phase, with typical separations of ∼30 minutes. Throughout the dissertation, we focus our analysis on the secondary flare, "MDSF2" . At the onset of MDSF2, there was decaying line and continuum emission. We estimate the energy of this event as $E_U \sim 1.4 \times 10^{32}$ ergs, which is less than 1% of the energy in the entire flare event (Kowalski et al., 2012). The MDSF2 has a rise time of 5.2 minutes and a total duration of 18.5 minutes, a $t_{1/2,U} = 9.22$ minutes, and $I_{f,U} + 1 = 6.9$. Although MDSF2 is a *gradual* flare with $\mathcal{I} \sim 0.6$, we classify this flare event according to the properties of the main peak (IF1), because the decaying emission from the main peak is present within our spectral observations.

Since IF1 did not have spectral coverage of the main peak event, we cannot compare it to the other flares in every regard. Instead, the "peak" properties are taken from the peak of MDSF2 (S#113). The decay phase properties correspond to S#24, immediately before the first secondary flare. For reference, the mid rise-phase of the secondary flare corresponds to S#108-109.

3.4.3 IF2: YZ CMi, 08 Feb 2011

This large-amplitude flare ($I_{f,U} + 1 = 12.2$, $E_U \sim 2.8 \times 10^{31}$ ergs) is the most impulsive flare in the DIS sample, and exhibits a strictly simple fast-rise/slow-decay shape with no obvious secondary flares. The peak of this flare followed the peak of HF1 by 11.2 minutes. The U-band reaches the pre-flare level about 8.5 minutes after the peak, but the quiescent level does not appear to be obtained, presumably due to the underlying, slow decay of HF1. At

[6] We use the term absorption throughout to refer to "less emission than the neighboring spectral regions."

peak the $I_{f,H\gamma} + 1 \sim 4.4$, quite low for the large amplitude enhancement in the continuum. When fit by an exponential function, the Hγ decay is well-fit for limited windows of time; the decay constant appears to lengthen as the prolonged decay from HF1 likely becomes increasingly important.

We will compare the peak spectral properties of IF2 and HF1 in Section 6.7.3.

3.4.4 IF3: YZ CMi, 24 Feb 2011

This incredible flare is a classical, impulsive flare that is characterized by a large peak luminosity ($I_{f,U} + 1 = 78$) but with a remarkably long rise time of ∼2.7 minutes. At 22% of the peak flux, the u-band shows a low-amplitude secondary flare, followed by an exponential decay giving a total duration of nearly 3 hours.

The spectral observations cover the first 1.7 hours of this flare. The Hγ line increased by nearly 22 times at peak and released $\sim 9 \times 10^{31}$ ergs (during which the U-band released 1.8×10^{33} ergs). We obtained eight spectra during the rise phase (with 15-second exposure time), and after maximum continuum emission switched to 7-second exposures, giving a total of twenty-four spectra covering the impulsive phase. The brightness of the flare, the relatively slow evolution, and a combination of good observing conditions (despite high dust levels) while using a wide slit have allowed us to obtain the fastest cadence and shortest exposure times ever achieved with optical spectra during a stellar flare.

IF3 is a flare that we will study in detail throughout this dissertation.

3.4.5 IF4: EQ Peg A, 01 Oct 2008

This flare is a large-amplitude, fast flare with a well-defined impulsive/gradual phase demarcation and was presented in Figure 3.1 to illustrate observational parameters of the photometry. The impulsive phase consists of a rise time of 80 seconds of an initial spike (with peak amplitude, $I_{f,U} + 1 \sim 21$). After the spike, there is a gradual decrease to 55% of the peak flux, when there is a secondary event or "stall" that occurs $\sim$ 2 minutes after the first peak. The ratio of impulsive to total energy is 0.62, similar to IF0 (Hawley & Pettersen, 1991). In many ways, this flare is similar to IF0 except that it occurs on shorter

timescales.

The Hγ evolution is remarkably different from the continuum evolution (Figure 3.16), as Hγ reaches maximum near the start of the gradual phase in the continuum. Of the other flares in the sample, IF0 and HF2 show a secondary event that appears to produce an apparently large time lag in the maximum amount of line emission. The rise and peak spectra from this flare have notably little (or no) BaC3615 emission with the BaC3615 appearing later in the flare. The lack of BaC3615 at peak continuum has been noted by Hawley & Pettersen (1991) for IF0, a flare on UV Ceti studied by Eason et al. (1992), and for the peak of the secondary flare in the decay phase of IF1 (Kowalski et al., 2010, 2012).

Only blue spectral data ($\lambda = 3420 - 5200$Å) are available for this flare and for HF4. It should be noted that IF4 occurred at high airmass (≥ 1.9) without orienting the slit at the parallactic angle. Additional flux calibration procedures were taken to attempt to account for the loss of blue light (see Appendix A).

3.4.6 IF5: EV Lac, 11 Oct 2010

This fast, classical flare has a peak amplitude of $I_{f,u} + 1 \sim 5.37$, and $I_{f,g} + 1 \sim 1.25$. There is a "stall" in the fast decline which occurs in the SDSS u-band at 57% of the peak emission. The energy in the SDSS u is 2.8×10^{31} ergs, and there are well-defined impulsive and gradual phases, especially evident in the g band.

The Hγ light curve also has defined impulsive and gradual phases with an exponential (well-fit by $\tau = 0.096$ hours) beginning at $\sim$50% of the peak flux. Of the IF events, this flare has the largest $\chi_{\rm flare,peak}\sim$2.2 and H$\gamma$/C4170 $\sim$50 (Figure 3.13). We hypothesize that like IF4, the stall is responsible for generating increased Hydrogen Balmer emission; but unlike IF4, the stall occurred on shorter timescales than the spectral integrations; hence we did not resolve it completely.

3.4.7 IF6: EV Lac, 10 Oct 2009

This is a low-energy ($E_u \sim 4.6 \times 10^{30}$ ergs), low-amplitude ($\Delta u \sim -1$), fast flare. Very little extended decay emission is visible, and the total duration appears to be < 5 minutes. This

flare is similar to IF5, but with ∼3x smaller peak amplitude. This flare also has the same $\chi_{\rm flare,peak}$ and Hγ/C4170 ratio as IF5. Note that this flare has the same peak amplitude as HF4 but occurred much faster; there are also indications of a possible pre-flare enhancement in the photometry and a stall during the fast decline, resulting in two periods of fast decline (as for IF0, IF4, and IF5).

The flare appears in C4170 for just a single (peak) exposure, whereas the C3615 flux is elevated for the peak and initial decay phase over about four spectra. Radio VLA (3.6 and 6 cm) data are available during this flare and will be presented in a future paper. There are larger uncertainties in the calibration for this night because the star was found systematically off the slit center; furthermore, excellent seeing conditions cause the red data to be highly non-linear or saturated; therefore, the scaling factor, R, was determined from the blue molecular features.

3.4.8 IF7: YZ CMi, 14 Feb 2010

This classical flare with $I_{f,U} + 1 = 6.6$ appears during a complex flare event spanning 1.5 hours. The flux nearly reaches the preflare level before a slow-rise secondary flare occurs, 14.7 minutes after the peak of IF7. The energy over the $\sim$ 12 minute duration is $E_U \sim 3.3 \times 10^{31}$ ergs. It is instructive to compare IF7 to the more impulsive IF2, which has a $t_{1/2,U}$ about 2.5x shorter but a peak amplitude nearly twice as large. Despite the timescale differences, the relative evolution of C4170 follows the same trend, decreasing to 40% of the peak in the subsequent spectrum after the peak (Figure 3.14), followed by gradual decay of C4170. Curiously, both flares have the same $\chi_{\rm flare,peak}$∼1.74 and nearly the same $\chi_{\rm flare,decay}$.

The exponential decay constant of Hγ for IF7 is about 5.9 minutes, twice as long as for the continuum (U), and the $t_{1/2}$ of Hγ is shorter by a factor of 3-4 than for U. The flare was observed with 45 second exposure times, but interspersed shorter (8 second) exposures were also obtained.

We will use the gradual decay spectrum of this flare to compare to the gradual phase properties observed in IF1 in Chapter 6, as both observations have higher spectral resolution than most of the sample.

3.4.9 IF8: YZ CMi, 11 Dec 2010

The U-band of this flare is dominated by very fast evolution, and a short duration decay phase: four data points sample the impulsive phase and four data points sample the gradual phase. This flare is one of the lowest energies, $E_U = 5 \times 10^{30}$ ergs in the sample; the peak amplitude is $I_f + 1 = 3$ (it is possible that the "true" peak occurred during readout), and the short-duration decay phase begins at 20% peak emission.

There may have been a preflare enhancement and/or rise in Hγ. The ratio of U-band energy to Hγ energies is the highest for this flare, ~ 37. The $\chi_{\rm flare,peak}\sim$1.6 is one of the lowest in the sample. There is one peak spectrum and one fast decay spectrum for this flare; the gradual phase spectra are very near quiescent values.

3.4.10 IF9: AD Leo, 03 Apr 2010

The peak spectrum from this large, classical flare was used in Figure 3.2 to illustrate spectral parameters and continuum decomposition. This flare is set apart from the other IF flares by exhibiting a higher amplitude gradual phase. Although U-band photometry is not available for this flare, the extended decay begins at $\sim$40% relative to peak amplitude in a synthetic U-band, and at 25% in C4170. High-cadence (2 sec) SDSS g-band data are available, giving a rise time of $\sim$21 sec. The peak amplitude is $I_{f,g} + 1 \sim 1.28$, and we estimate the peak U-band amplitude as $I_{f,U} + 1 \sim 4 - 6$ The estimated U-band flare energy is high, $2 - 4 \times 10^{32}$ ergs[7], and the photometry doesn't return completely to quiescence until about 2.6 hours after the flare start.

There are four spectra covering the rise, peak, and initial decline (three spectra with 10-second integration times, one spectrum with 1-second integration time). An interesting feature of this flare is how fast the C4170 is compared to the Hγ line (Figure 3.14), with ratio of 0.1 for their $t_{1/2}$ values. We will study the emission line properties in detail in Chapter 4. Because intermittent clouds were present (during the peak spectra), we use these data to test the accuracy of continuum fitting in Chapter 6; we also use these data to

[7]We estimated it two ways: one using spectrophotometry and also by scaling from the observed g-band energy ($E_u \sim 3.3 \times E_g$ derived from IF3).

illustrate the scaling applied to the spectra in Appendix B and Figure B.1.

3.4.11 IF10: EV Lac, 2009 Oct 27

The most impulsive flare in the sample with $I_{f,u} + 1 = 44$; blue spectra were obtained at the DAO 1.85-m with long, 200 – 300 sec integration times. The spectrum covering the peak also integrated over a large amount of quiescent time; therefore, the absolute energies from the spectra are significantly lower than what the photometry indicate. We choose to analyze the SDSS u-band photometry (other, Ug data are also available).

Light curves and modeling of the Hδ, Hγ, He I 4471, and Ca II K lines were presented with infrared emission line data in Schmidt et al. (2012).

This flare has a rise time of ∼45 seconds, a prominent first peak, two smaller secondary peaks, and an exponential decay of ∼1 hour. The $\chi_{\rm flare}$ changes rapidly from 1.7 in the first spectrum to $\chi_{\rm flare}$∼2.4 in the three subsequent spectra. From Figure 3.17, the C4170 is elevated at peak emission for the first two spectra, whereas the BaC3615 and Hγ line clearly reach their peaks in the second spectrum.

3.4.12 HF1: YZ CMi, 08 Feb 2011

This low-amplitude flare consists of three peaks ($I_{f,g} + 1$ ∼1.2, 1.35, 1.3, $I_{f,U} + 1$ ∼ 3.5, 5.3, 5.1) spaced by ∼35 seconds. There is also a slow "ramp-up" in this flare, in contrast to IF2, which occurs without warning. The entire impulsive phase lasts 3.6 minutes, and an extended gradual phase lasts 8 minutes until the onset of IF2. The decay phase appears to consist of three phases: a fast, medium, and slow decay. Three peaks may be a pattern among some flares, including IF10. This flare is morphologically similar to HF4 on EQ Peg A, a low-amplitude flare with only two peaks. The energies of these two flares are $E_U \sim 4 \times 10^{31}$ ergs.

As is evident from Figure 3.16, the C4170 peaks first (S#520) before the BaC3615 and Hγ line (S#522)[8], which reflects the different decay timescales of the C4170 and the Hydrogen Balmer components. In contrast to IF9, the ratio $t_{1/2,C4170}/t_{1/2,H\gamma} = 0.5$. The

[8]The C3615 and U-band peak at the time of S#521, Figure 3.16.

peak Hγ flux is only 75% of the peak in IF2, but the rise times are vastly different and the C4170 flux in HF1 is 25% the C4170 flux in IF2. The decay constant of Hγ is fit well with a single exponential for all points in the decay ($\tau = 2.3$ minutes).

In Section 6.7.3, we compare HF1 and IF2 in order to determine whether a large-amplitude fast flare has a different continuum shape than a low-amplitude hybrid flare showing multiple bursts.

3.4.13 HF2: GJ 1243, 20 Oct 2011

We did not obtain simultaneous photometry during this flare. However, the 5" slit was used during photometric conditions. The integration times for this night were longer than usual (45 seconds) due to the faintness of the star. The signature of this flare is a double-peaked continuum light curve, similar to IF0 and IF4, but with a relatively high amplitude onset of the decay phase, as will be seen is also present in HF4. We estimate that $I_{f,U}+1 \sim 4.5-6.5$ and $E_u \sim 9 \times 10^{31}$ ergs. Observations were terminated before the end of the flare.

The Hydrogen line emission is similar to IF0 and IF4, with the peak occurring after the second continuum increase: the maximum Hγ emission occurs nearly 3 minutes after the peak in the continuum. The decay is on average a linear function, but can also be represented by an exponential with a large (0.35 hours) decay constant. The line emission for this flare will be studied extensively in Chapter 4.

3.4.14 HF3: YZ CMi, 13 Dec 2010

HF3 is the largest amplitude flare within a complex event. The flare persists for 8.5 minutes until it is interrupted by a slow-rise secondary flare. The energy of the main event is 1.8×10^{31} ergs[9]. This flare has an initial spike phase with peak amplitude $I_{f,U} + 1 = 3.2$. After the peak, the flux returns to 55% of the maximum and has an extended stall phase lasting 1.5 minutes. The gradual decay begins at 40% the peak flux after a second, short and fast decay phase. Apparently, this flare has many qualitative light curve features in common with IF4 but with a more pronounced gradual phase relative to peak.

[9]As with IF2 and IF7, the integrations used for energy calculation do not include the secondary flares.

3.4.15 HF4: EQ Peg A, 01 Oct 2008

This is a low-amplitude ($I_{f,U} + 1 = 2.4$), double peaked flare. The two peaks are noticeable in both the Hγ line and continuum measures; however, the peaks are equal in Hγ whereas the first peak is larger in the continuum. This flare released 4×10^{31} ergs, 5.5 times the amount released in the Hγ line. This is the lowest ratio of U-band to Hγ energy in the sample. Kahler et al. (1982) found a similar small ratio ($\sim$4) for a U-band flare (on YZ CMi) that had a low amplitude and several peaks in the photometry.

3.4.16 GF1: EV Lac, 11 Oct 2010

This flare has a very complex light curve morphology, with the defining feature being a very broad, slowly evolving emission peak ($t_{1/2,U} = 13$ minutes). and the $\chi_{\rm flare,peak}$= 3.2, in stark contrast to any IF event with the same peak amplitude. The blue photometry for this flare is a combination of SDSS u (peak) and Johnson U (rise, decay) measurements. Before a secondary flare occurs 1.18 hours after the flare starts, the u-band energy is estimated as 6.2×10^{32} ergs. The rise phase ($t_{rise,U}$ is 11.3 minutes, the rise time of the Hγ is 16.4 minutes) consists of three intervals of fast emission. The decay consists of a slow decay interval followed by an even slower decay, breaking at $\sim$55% of the peak flux. We will analyze this flare in detail and address the differences in the continuum properties between the fast and slow phases.

3.4.17 GF2: YZ CMi, 02 Mar 2011

This complex, low-amplitude flare has a U-band energy of $8{\times}10^{31}$ and a duration of 1.6 hours until the observations were interrupted by clouds. There are two prominent peaks, separated by 19 minutes, with approximately equal amplitudes of $I_{f,U} + 1 \sim 2.2$. A prolonged, slow rise phase connects the two peaks. Throughout, GF2 refers to the first event, which has $E_U \sim 1.4 \times 10^{31}$ ergs and a rise time of 4.2 minutes and decay time of 8 minutes. The rise phase appears as a superposition of several events.

Whereas the two main peaks are equal in the U-band, the maximum Hγ emission is obtained in the second peak, where the peak emission is 1.5 times greater than in the first

peak (the net change in line emission during the rise phase of the two main peaks is about the same). The $t_{1/2}$ value of Hγ is poorly defined for the first event, because of the onset of the second event.

As can be seen from Figure 3.15, the C4170 value responds strongly around the peak times. This flare has one of the largest $\chi_{\rm flare,peak}$ values of $\sim$4.3 and also the largest Hγ/C4170 ratio of $\sim$160.

3.4.18 GF3: EV Lac, 10 Oct 2009

This low-amplitude ($I_{f,U}+1=1.9, E_U=3.5\times10^{31}$ ergs), complex flare consists of three main peaks in the U band. As for GF2, we concentrate the analysis on the first peak, which has a rise time of 3.3 minutes, a decay time of 8.1 minutes, and $E_U=1.5\times10^{31}$ ergs. GF2 shows similar properties in these parameters. There is an emission spike in the rise phase of GF3 (also similar to GF2) which has $I_{f,U}+1=2.2$.

The changes in the C4170 during this event are very small and C3615/C4170 traces the U-band well. In the first peak, the U-band reaches maximum emission whereas the Hydrogen lines reach their maxima in the second event. As in GF2, the net amount of Hydrogen line emission is about the same between the two peaks. There are larger uncertainties in the calibration for this night because the star was found systematically off the slit center; furthermore, excellent seeing conditions cause the red data to be highly non-linear or saturated; therefore, the scaling factor, R, was determined from the blue molecular features.

After the main peak, there is a gradual decay followed by a break to even more gradual decay at $\sim$55% of the peak value - precisely similar to the decay morphology of the larger amplitude, high energy event GF1.

3.4.19 GF4: AD Leo, 08 Feb 2011

This is a low-amplitude flare has with $I_{f,u}+1=1.32$, and $E_u=1.2\times10^{31}$ ergs. This flare has a slow rise of 1.5 minutes and a $t_{1/2,u}=2$ minutes, with a total duration of about 10 minutes.

The Hγ stalls at 80% the peak flux, followed by a fast decay and a possible change to

an extended decay in the light curve at about 50% peak flux. The $C3615_{total}/C4170_{total}$ exhibits a change from 0.34 to 0.43 indicating a bona-fide continuum change during this small flare.

3.4.20 GF5: YZ CMi, 26 Jan 2009

Approximately three and a half rotations after the Megaflare (IF1), a remarkably long, gradual flare occurred on YZ CMi. Simultaneous photometry is not available for this flare; we estimated the U-band amplitude to be $I_f + 1 \sim 1.5$, a duration of 1 hour, and energy $\sim 3 \times 10^{31}$ ergs. There is a noticeable peak phase in the Hγ and continuum light curves; four spectra are averaged to give the peak values and ten spectra are averaged immediately afterward to give the gradual phase values. We will compare the line and continuum properties of this high signal-to-noise spectrum to larger amplitude flares in Chapter 6.

The $\chi_{flare,peak}$ value is $\sim 4.3 \pm 1.3$, giving one of the largest values along with GF2. The $C3615_{total}/C4170_{total}$ changes from 0.4 in quiescence to a peak value of 0.6.

3.4.21 GF6: EV Lac, 11 Oct 2010

This flare occurred 110 minutes after the peak of GF1 (during the GF1 decay phase). This flare is a low-amplitude event consisting of a spike event followed a slow, flat-topped event, which constitutes GF5. The slow event perhaps consists of several individual events. This flare is morphologically similar to GF6. Because the amplitude of this flare is very small and is superposed on the decay of the much larger flare, GF1, we do not include this flare for detailed analysis, except in the analysis of the Hα line evolution (Section 4.8.3). This flare is therefore not included in any tables or any other figures. This flare has $\mathcal{I} \sim 0.04$ and therefore it is slightly less gradual than GF5 ($\mathcal{I} \sim 0.02$); but for the sake of continuity, we refer to this flare as GF6.

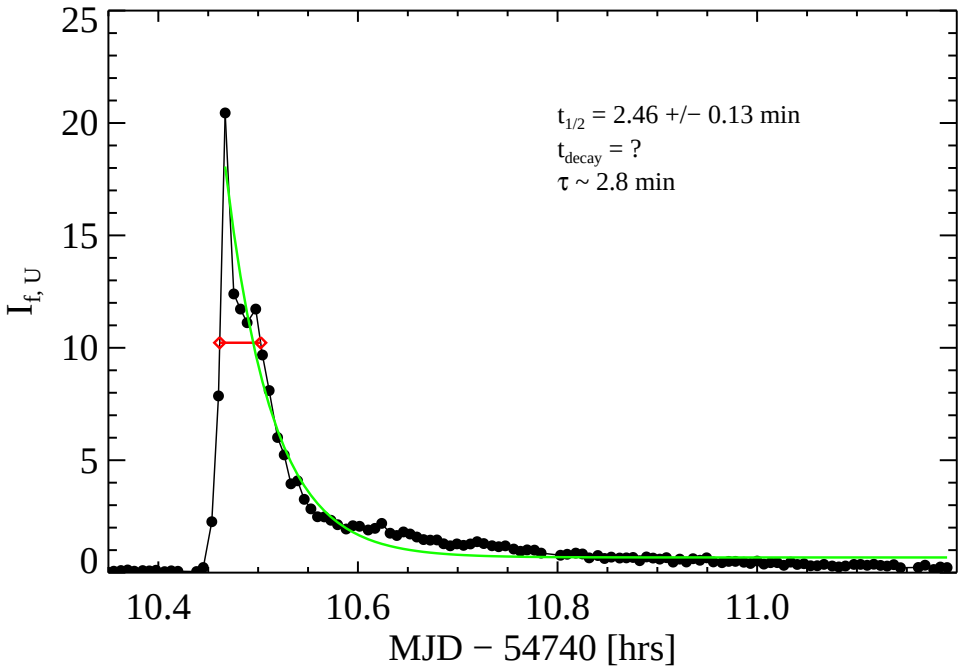

Figure 3.1 An example calculation of $t_{1/2}$ for a U-band light curve of a flare on EQ Peg A (01 Oct 2008). The time between observations ranges from $24 - 31$ sec. The $t_{1/2}$ is the FWHM of the light curve, illustrated in red. An exponential fit ($\tau = 2.8$ minutes) to the entire decay is shown in green, which does not account for substructure. The observations ended before the flare finished, not allowing a total decay time to be determined.

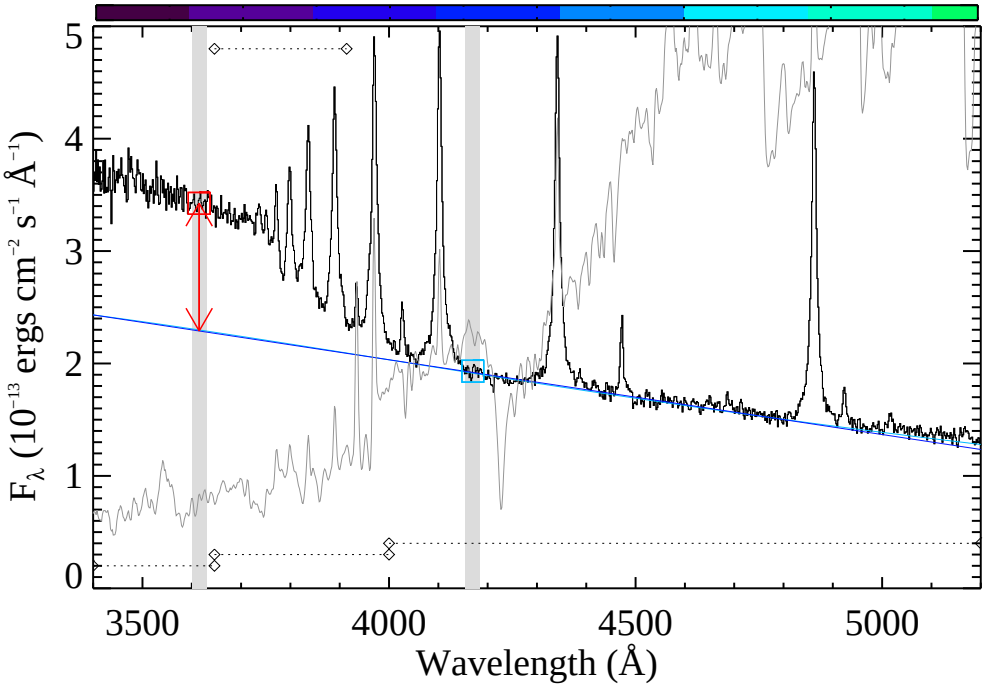

Figure 3.2 The flare-only emission from the peak of a flare on AD Leo from 03 April 2010 (IF9) showing the important terms from Section 3.1.2 used in this work. The coverage of the near-UV, intermediate, and blue-optical zones are indicated at the bottom with diamonds; the coverage of the PseudoC is indicated at the top with diamonds. The quiescent is shown in grey, the best-fit line shown in dark blue. The best-fit blackbody ($T_{\rm BB}$= 10 250 K, $X_{\rm BB}$= 0.00046) is shown in light blue (see Chapter 6). The blackbody and linear fits are nearly identical for this spectrum. Vertical grey bars indicate the wavelength regions used to calculate C3615 and C4170; squares denote the flare-only flux values in these regions. The $\chi_{\rm flare}$ (or Balmer jump ratio) is the flux of the red square divided by the flux of the blue square ($\chi_{\rm flare}$= 1.8 in this spectrum). The red arrow indicates excess emission, BaC3615, above the extrapolation of the linear fit to the blue-optical zone. Although U-band photometry was not available during this flare, the $I_{f,SDSSg}+1 \sim 1.28$ and $I_{f,{\rm C3615}}+1 \sim 5.4$. For reference the visible colors for this wavelength range are indicated with the colorbar.

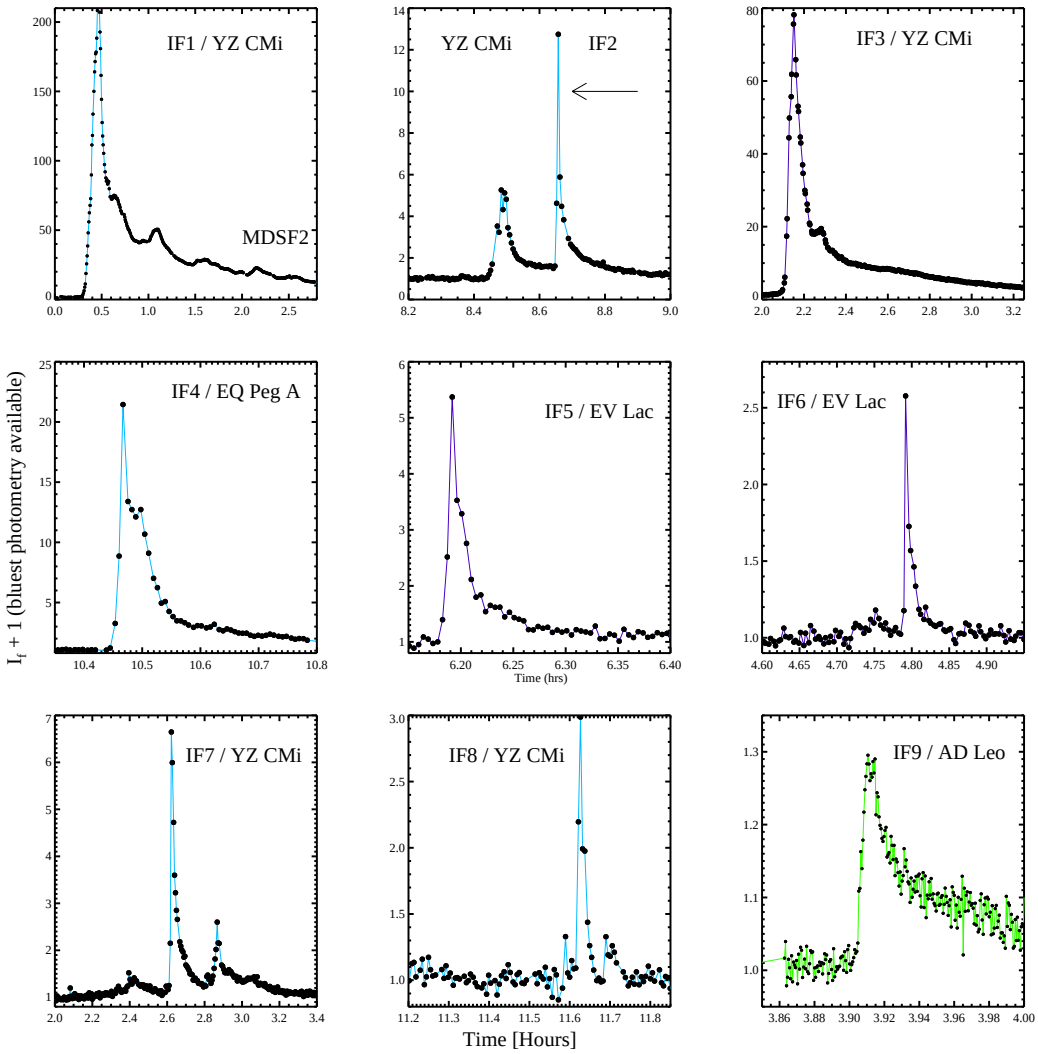

Figure 3.3 The impulsive flare photometry. The purple lines show photometry from the NMSU 1m (Johnson U), the light blue shows photometry from ARCSAT/Flarecam (SDSS u), and the green shows photometry from ARCSAT/Flarecam (SDSS g). Open circles show spectrophotometry estimations of the Johnson U band.

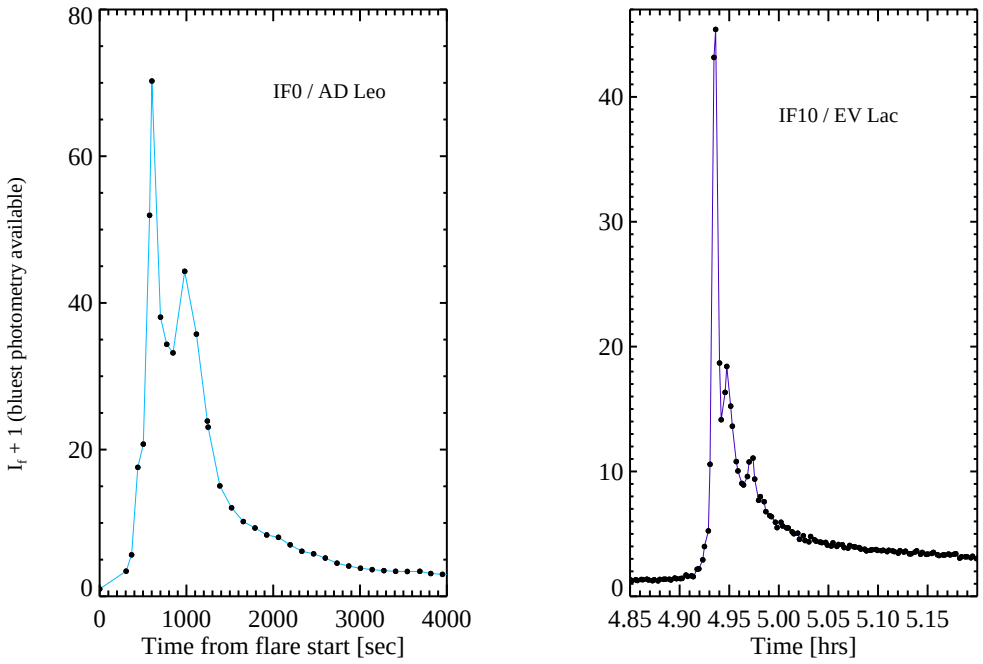

Figure 3.4 Same as in Figure 3.3, for the impulsive flares with lower time-resolution and limited wavelength coverage in the near-UV and blue-optical.

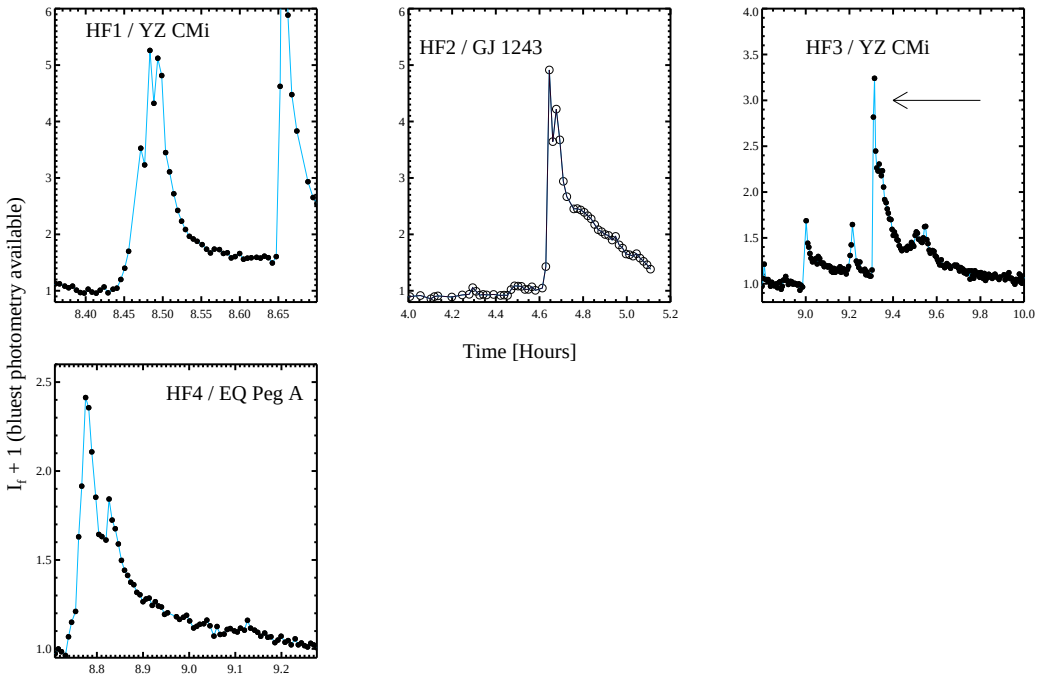

Figure 3.5 Same as in Figure 3.3, for the hybrid flares.

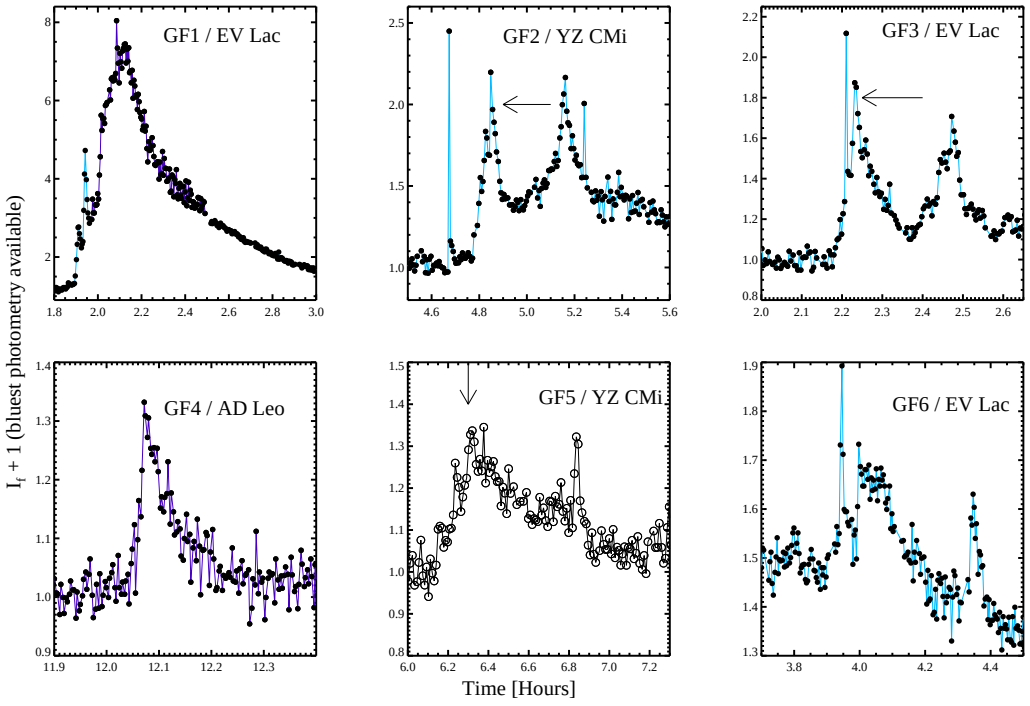

Figure 3.6 Same as in Figure 3.3, for the gradual flares.

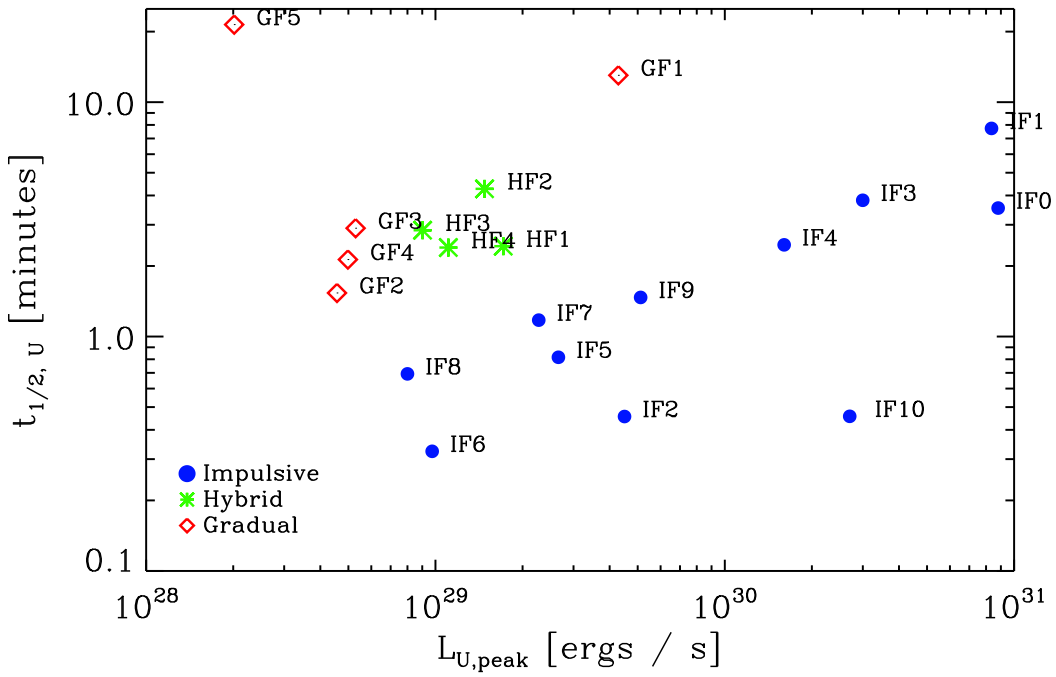

Figure 3.7 The range of the U-band properties for the flares in our sample.

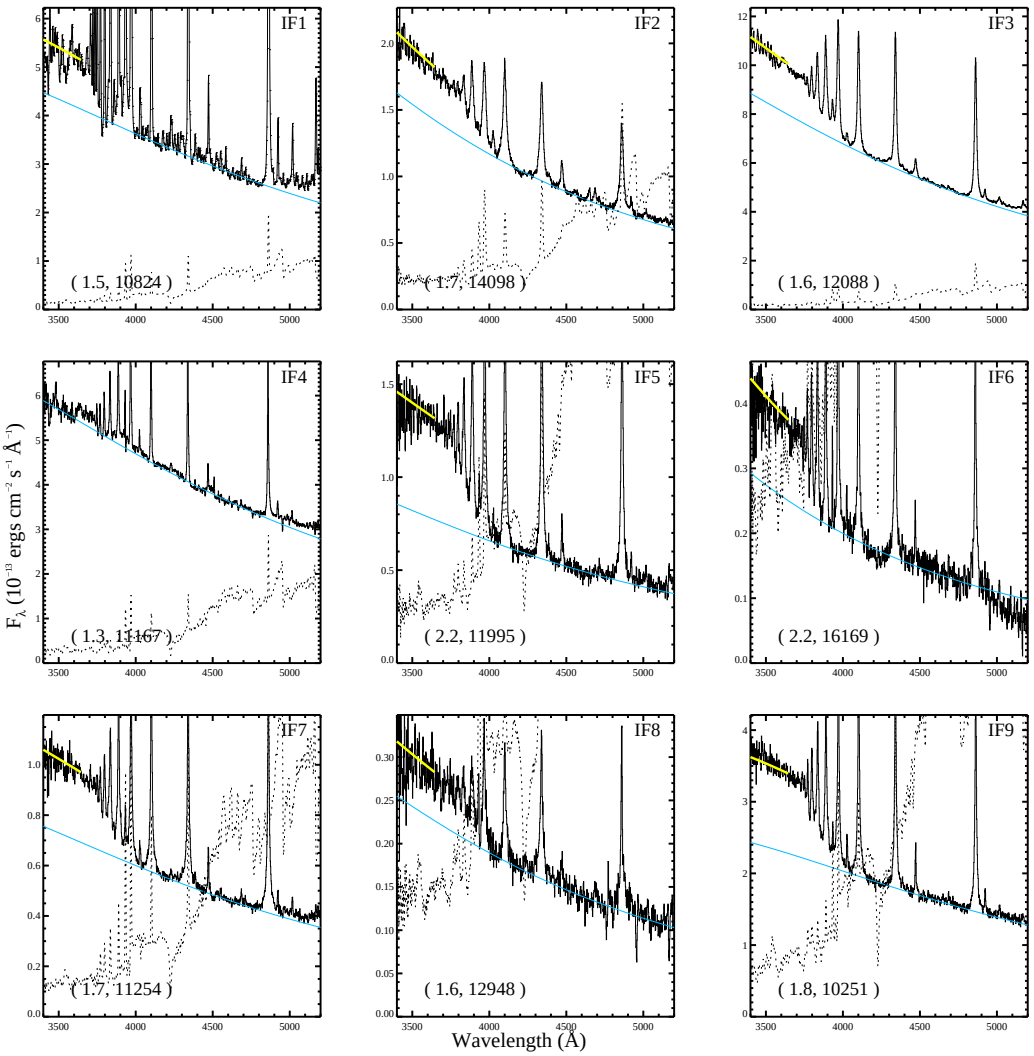

Figure 3.8 The spectra at maximum continuum emission. The black is the flare-only emission, the dotted line is the quiescent spectrum. The best-fit Planck function to the blue-optical region is shown in light blue. The yellow curve at $\lambda < 3646$Å is the best-fit Planck function *scaled* to the C3615 flux. In parentheses, we have the $\chi_{\rm flare,peak}$ and the best-fit color temperature. See Chapter 6 for more details.

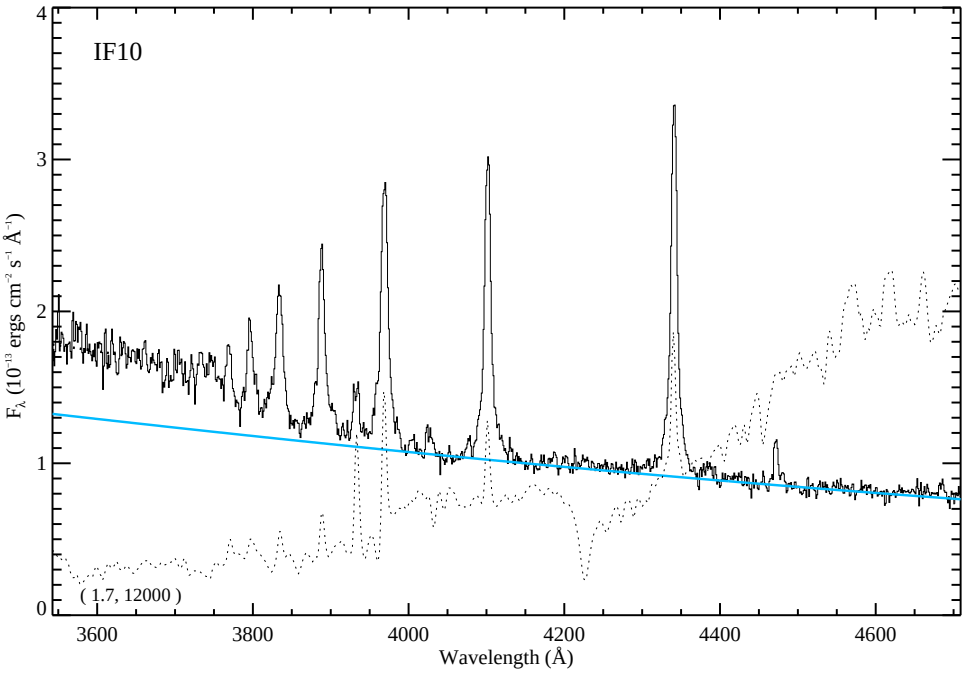

Figure 3.9 Peak spectrum (S#31) from IF10. For peak spectra of IF0, see Hawley & Pettersen (1991). Note the integration time in Figure C.15.

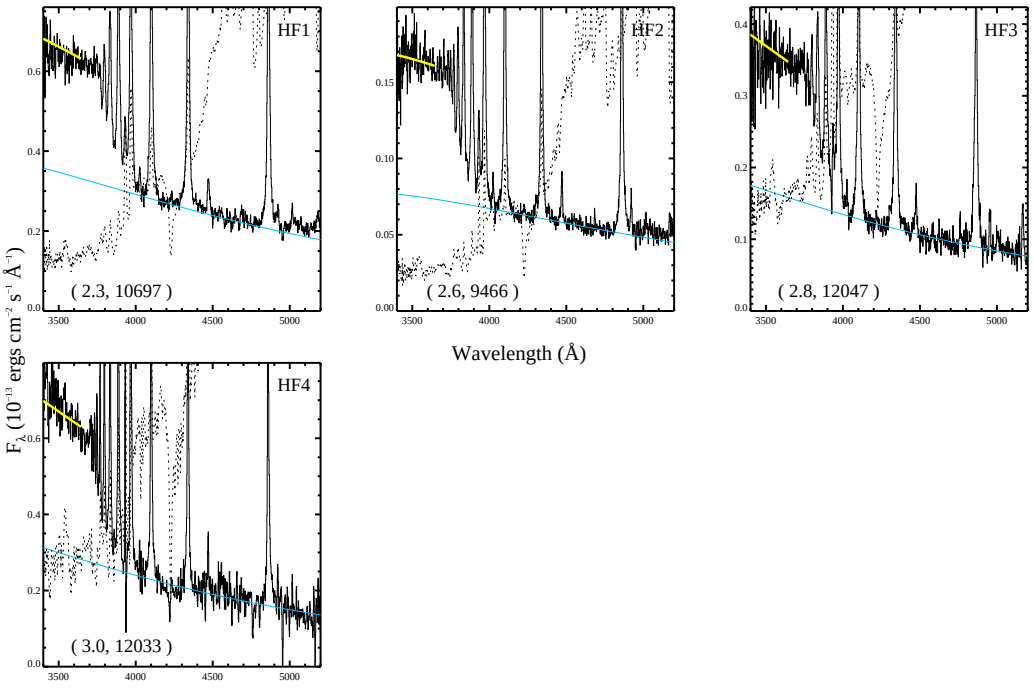

Figure 3.10 Same as in Figure 3.8.

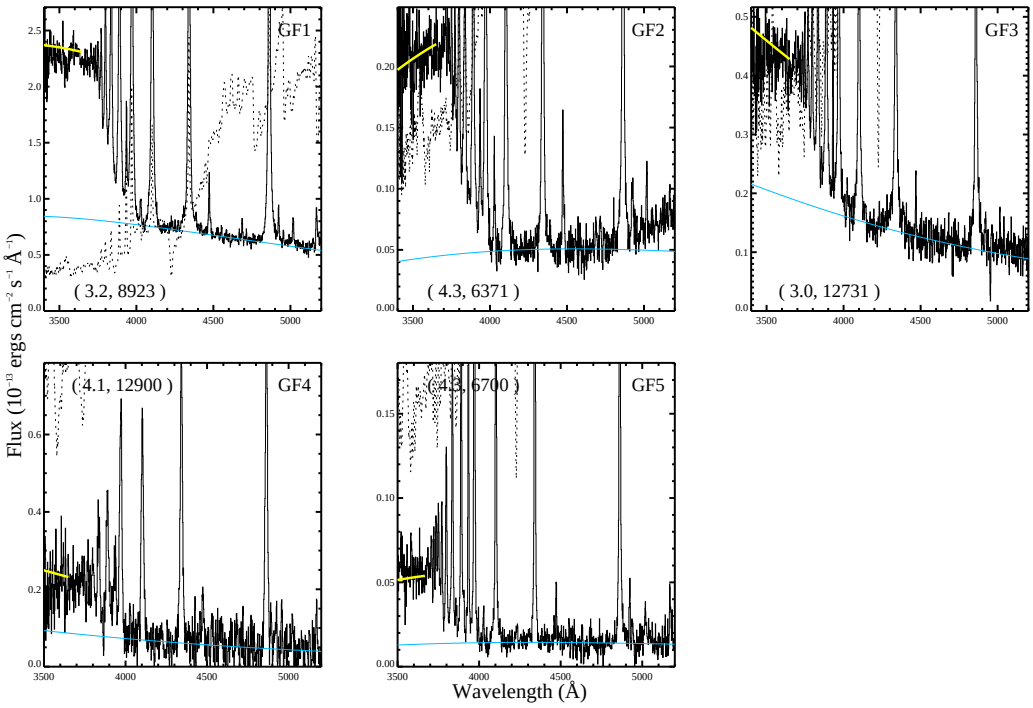

Figure 3.11 Same as in Figure 3.8.

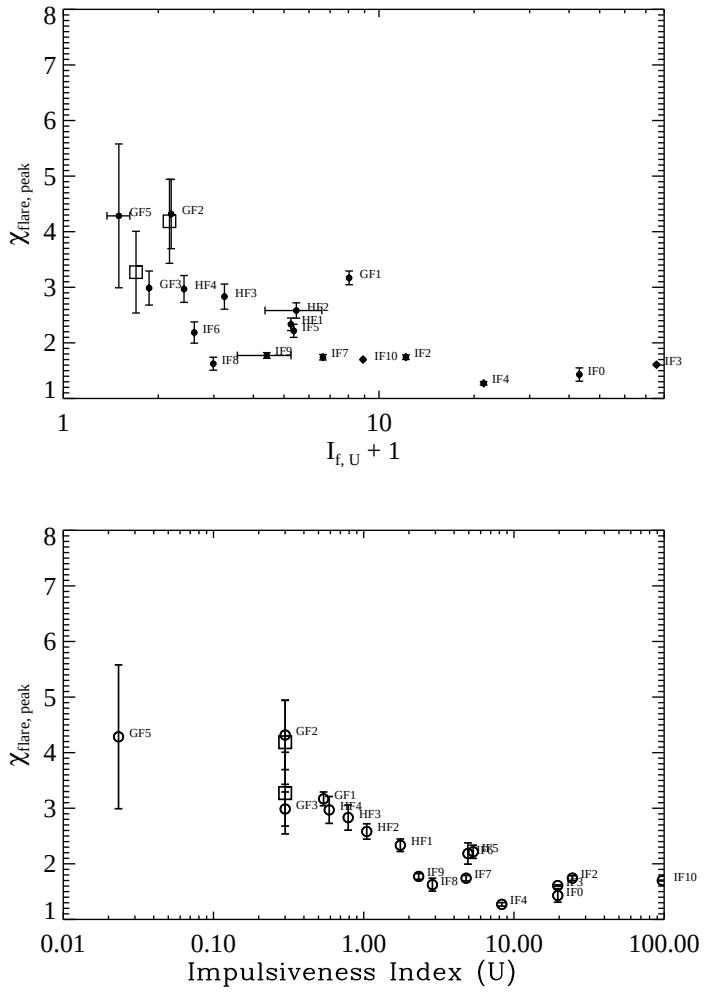

Figure 3.12 (Top panel) The peak properties of the flare sample: the $\chi_{\rm flare,peak}$ vs peak U-band flux enhancement. The error bars for $\chi_{\rm flare}$ were determined from propagating the standard deviation of the flux in C4170 and C3615. The horizontal error bars represent 25% uncertainties in the U-band peak amplitudes that were estimated from the spectra. (Bottom panel) The peak properties, continued: $\chi_{\rm flare,peak}$ shows a stronger trend with the impulsiveness of the flare. For GF3 and GF2, we show the properties of the second peaks in the events also (3.3 and 4.2 respectively) as square symbols, in both figures.

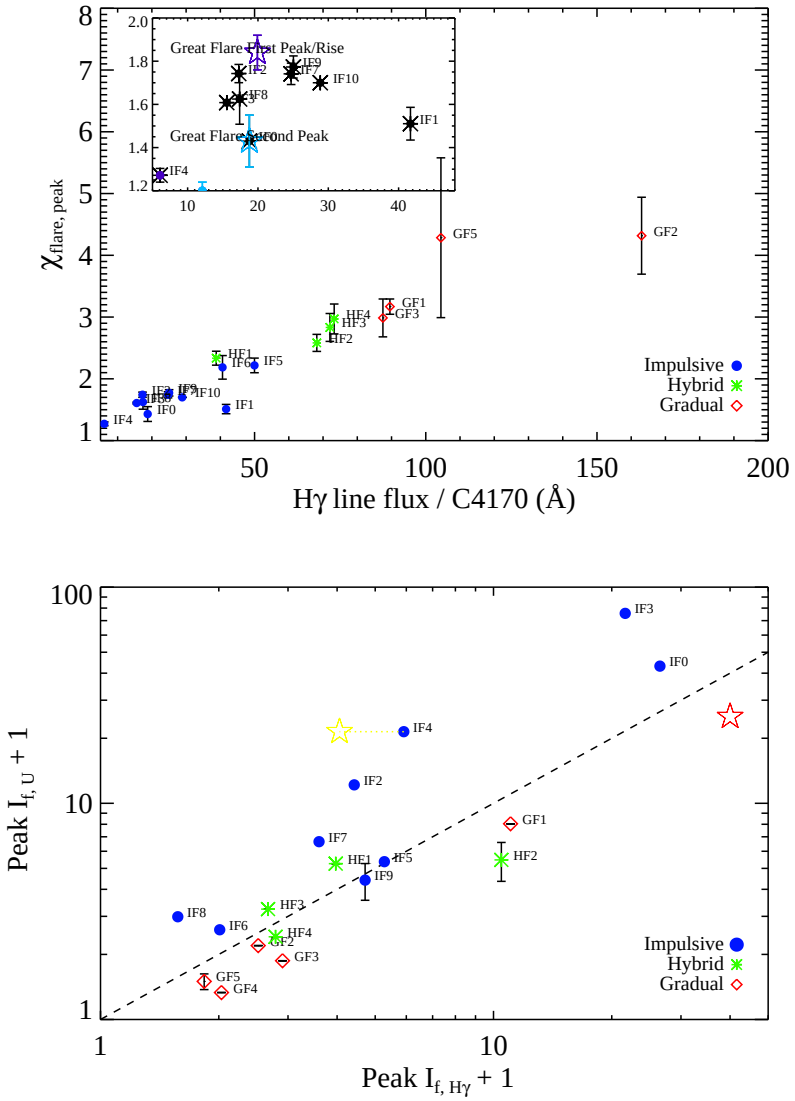

Figure 3.13 (Top panel) The $\chi_{\rm flare,peak}$ vs the equivalent C4170 width of Hγ at peak. There is a strong, rather linear relationship; IF1 is the largest outlier with a large Hγ line flux to C4170 ratio for the $\chi_{\rm flare,peak}$, likely due to having Hγ line flux present from the highly elevated decay phase of previous flares. GF2 and GF3 have significantly different relative amounts of Hydrogen at peak. IF7 and IF9 have similar properties. The inset zooms on the low values and shows subpeaks that belong to the same flare in the same color. (Bottom panel) Flux enhancement in Hγ and U-band at peak continuum emission. IF1 is not shown because of the ambiguity resulting from the large amount of absorption in the line at the peak of MDSF2. The red star indicates the value for the decay phase (S#24) of IF1. The 1:1 line is shown (dashed); the impulsive flares lie above it, wheres the gradual flares lie below it. The yellow circle is the value of the Hγ flux increase at the time of maximum continuum for IF4.

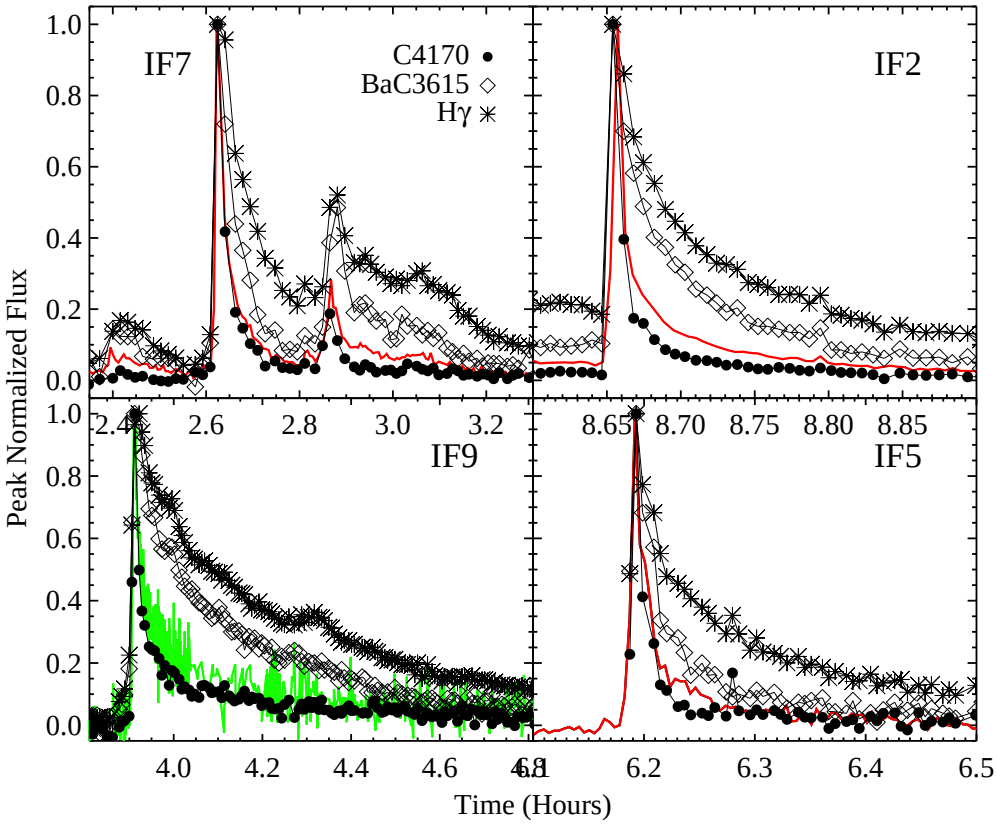

Figure 3.14 Flares with classical shapes, medium-amplitude ($I_{f,U}+1 \sim 5$), medium-energies in U or u band. Red line is the U or u-band photometry. Green line is the g-band photometry.

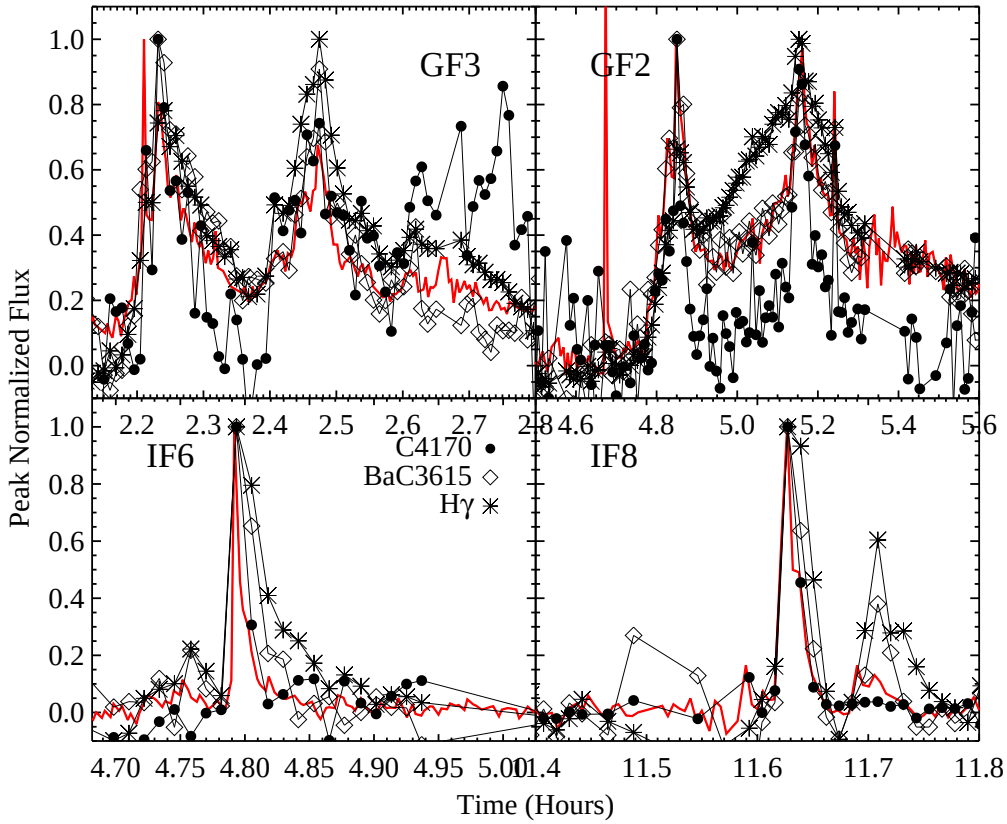

Figure 3.15 The low-amplitude flares, both complex, medium energy in U or u-band (top) and simple, low energy in U or u band (bottom). The complex flares are more than 10 times as energetic as the simple flares, even though the simple flares have three times the peak amplitude in U (or u). Red line is the U or u-band photometry.

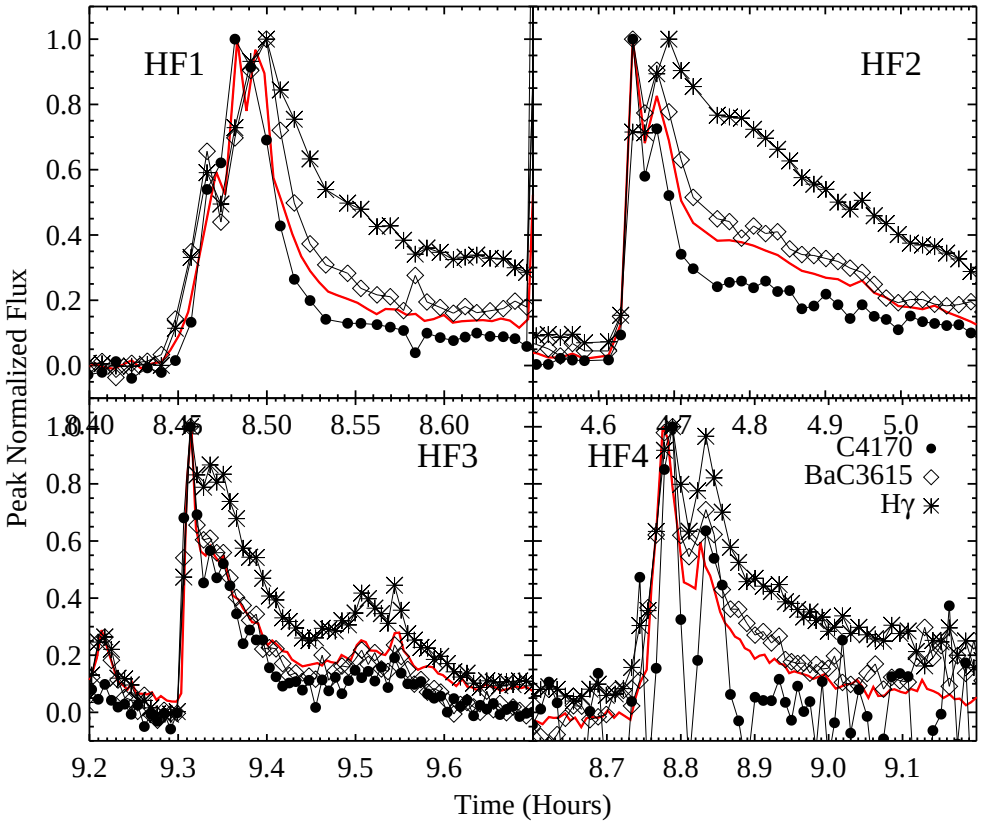

Figure 3.16 The HF flares have moderate U-band amplitudes and show multiple spikes in the impulsive phase. Red line is the U or u-band photometry, except in HF2, where the red line is a synthesized U-band using the spectra.

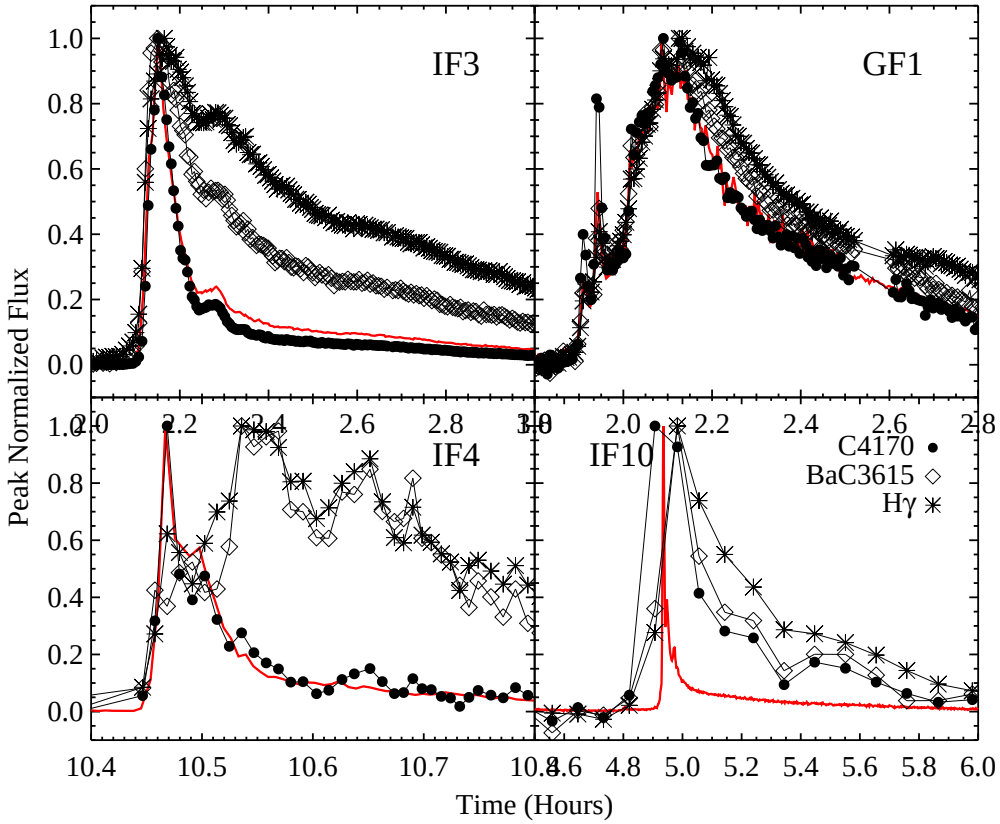

Figure 3.17 The high energy, large amplitude flares in U (or u) band. The top two flares are shown over 1 hour. Red line is the U or u-band photometry.

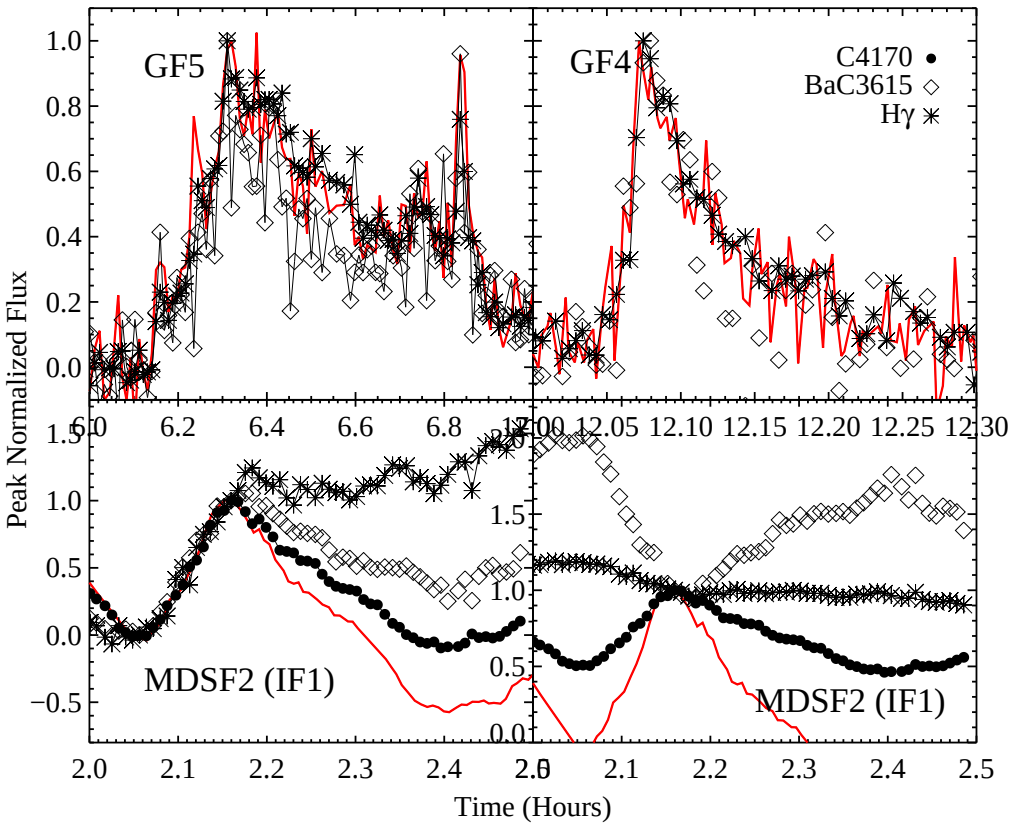

Figure 3.18 The low-amplitude gradual flares with relatively simple light curve morphology. Red line is the U or u-band photometry. The bottom two panels are MDSF2 during the decay phase of IF1: the left, bottom figure shows the normalized quantities of the sub-peak after subtracting the emission at $t = 2.03$ hours (before the rise of the secondary flare) and the bottom, right figure shows the normalized quantities of the total emission. Note that the Hγ and BaC3615 decrease in this sub-peak relative to the emission at $t = 2.03$ hours; therefore, the normalized values in the bottom, left figure are positive.

Table 3.1. Continuum Windows for Blackbody and Line Fitting

Name	Window ($\AA$)	Comments
BW1	$4000 - 4015$	$n\lambda = 8$
BW2	$4040 - 4057$	$n\lambda = 9$
BW3	$4152 - 4210$	$n\lambda = 31$, weighted by 0.97
BW4	$4495 - 4520$	$n\lambda = 13$
BW5	$4562 - 4630$	$n\lambda = 37$, line at 4584Å in IF1 decay
BW6	$4731 - 4800$	$n\lambda = 37$, not used for fitting spectra from DAO
RW1	$5920 - 6120$	$n\lambda = 71$
RW2	$6360 - 6470$	$n\lambda = 39$
RW3	$6705 - 6845$	$n\lambda = 50$
RW4	$7812 - 8115$	$n\lambda = 108$
RW5	$8562 - 8648$	$n\lambda = 30$

Note. — For the Great Flare (IF0), the higher resolution data (and limited wavelength range) allowed fitting in BW1, BW2, BW3 and also in the windows, $3915 - 3922$Å $4242 - 4287$Å, and $4400 - 4420$Å. $n\lambda$ is the number of wavelength points within each spectral window.

Table 3.2. Flare Summary Table (1): Key Continuum Observables from Spectra

ID	Peak $I_{f,C4170,\mathrm{peak}}+1$	$t_{1/2,C4170}$ (minutes)	$\chi_{\mathrm{flare,peak}}$	$\chi_{\mathrm{flare,decay}}$
IF1	11.5 (6)	8.8	1.51 (0.08)	2.65 (0.20)
IF2	4.1	0.6	1.74 (0.04)	2.67 (0.18)
IF3	20.1	3.6	1.61 (0.01)	2.66 (0.16)
IF4	7.3	1.1	1.27 (0.03)	2.28 (0.09)
IF5	1.8	0.5	2.22 (0.11)	4.39 (1.01)
IF6	1.2	0.9	2.19 (0.20)	3.94 (4.13)
IF7	2.7	1.3	1.74 (0.05)	2.40 (0.19)
IF8	2.9	1.0	1.62 (0.11)	2.44 (1.38)
IF9	1.8	1.0	1.77 (0.05)	2.74 (0.12)
HF1	1.8	2.4	2.33 (0.11)	3.60 (0.51)
HF2	1.9	3.5	2.58 (0.13)	3.40 (0.38)
HF3	1.4	1.4	2.83 (0.23)	3.20 (0.46)
HF4	1.3	1.5	2.97 (0.24)	···
GF1	1.9	15.0	3.17 (0.12)	3.46 (0.23)
GF2	1.15	0.7	4.32 (0.62)	···
GF3	1.87	2.2	2.99 (0.31)	···
GF4	1.03	0.5	4.11 (2.87)	···
GF5	1.04	0.9	4.28 (1.29)	4.26 (1.63)
IF0	8.7	11.7	1.4 – 1.9 (0.08 – 0.12)	2.4 (0.8)
IF10	1.3	–	1.7 (0.12)	2.4 (0.2)

Note. — Peak $I_{f,C4170,\mathrm{peak}}+1$ for IF1 obtained at S#113, but this value includes decay emission; the value for MDSF2 obtained by subtracting the emission at S#102 is given in parentheses. The $t_{1/2,C4170}$ of IF1 is given for MDSF2. Errros on χ_{flare} values are given in parantheses. No values are given for those with large errors ($\sim$100%) on χ_{flare}. Due to the low cadence, the spectra for IF10 could not be used to determine the value of $t_{1/2,C4170}$.

Table 3.3. Flare Summary Table (2): Key U-band Properties

ID	Star	Date	t_{peak}***	$I_{f,U,\mathrm{peak}}+1$	ED (s)	E_U (10^{32} ergs)	$L_{U,peak}$ (10^{29} erg/s)	$t_{1/2,U}$ (min)	$\mathcal{I}$
IF1†	YZ CMi	16 Jan 2009	6.3924	208	93 690	38	84.63	7.73	27.0
IF2	YZ CMi	08 Feb 2011	8.6540	12.2	690	6.2	4.50	0.48	23.3
IF3	YZ CMi	24 Feb 2011	2.1500	78.2	45 810	18.5	29.98	3.82	20.2
IF4	EQ Peg A	01 Oct 2008	10.4686	21.4	4710	3.7	16.04	2.46	8.3
IF5	EV Lac	11 Oct 2010	6.1929	5.4	460	0.28	2.7	0.84	5.2
IF6	EV Lac	10 Oct 2009	4.7934	2.6	70	0.04	0.97	0.32	5
IF7	YZ CMi	14 Feb 2010	2.6245	6.4	810	0.33	2.19	1.18	4.6
IF8	YZ CMi	11 Dec 2010	11.6274	2.9	130	0.05	0.78	0.69	2.8
IF9	AD Leo	03 Apr 2010	3.9120	4.4	–	2-4	5.11	1.47	2.3
HF1	YZ CMi	08 Feb 2011	8.4909	5.3	920	0.37	1.72	2.43	1.8
HF2	GJ 1243	20 Oct 2011	4.6452	5.4*	–	0.85	1.29	4.19	0.93
HF3	YZ CMi	13 Dec 2010	9.3138	3.2	440	0.18	0.88	2.84	0.77
HF4	EQ Peg A	01 Oct 2008	8.7889	2.4	530	0.41	1.11	2.40	0.58
GF1	EV Lac	11 Oct 2010	2.1265	8.04	10 180	6.20	4.29	13.02	0.54
GF2	YZ CMi	02 Mar 2011	4.8504	2.1	2020	0.81	0.43	3.68	0.3
GF3	EV Lac	10 Oct 2009	2.4744	1.87	570	0.35	0.38	2.88	0.3
GF4	AD Leo	08 Feb 2011	12.0746	1.32	80	0.12	0.48	2.13	0.15
GF5	YZ CMi	26 Jan 2009	6.3106	1.3-1.5*	–	0.36	0.13	21	0.02
IF0	AD Leo	12 April 1985	1038 (sec)	70.2 (43**)	–	–	88.06	3.53	19.6
IF10	EV Lac	27 Oct 2009	4.9069	45.4 (9**)	8720	5.3	27.0	0.46	96

Note. — *Estimated from spectra (no U-band photometry available). $t_{1/2}$ estimated by smoothing the lightcurve over three spectra. **Estimated from spectra with longer integration time; ***Time in hours from the beginning of the MJD obtained from spectra using the mid exposure of maximum C3615. †All properties pertain to spectral window except peak amplitude of U, $t_{1/2,U}$, and $\mathcal{I}$.

Chapter 4

EMISSION LINE ANALYSIS

Current radiative-hydrodynamic (RHD) models predict line flux decrements and profiles that are in agreement with the observations (Allred et al., 2006). Emission lines are used to probe the temperatures and densities, and therefore different heights, of a flaring atmosphere by matching the models to the observations. Since the line decrements are reproduced well by models, their heights of formation (Magain, 1986; Carlsson & Stein, 1997, via the contribution function) constrain the time-evolution of heating at different layers in the atmosphere. Ultimately, whatever heating mechanism we use to explain the continuum must also be consistent with the observed emission line properties. For example, Cram & Woods (1982) found that the model atmosphere which best matched continuum observations did not match the corresponding properties of Hα. As a result, they suggested a combination of several models to explain the observations.

The emission line analysis is divided into several sections. First, we summarize the properties of flares in Hγ for comparison to the U band to show that the BaC3615 component of the U-band is better correlated with the properties of Hγ than the U band. Then, we present the detailed energy budgets of hot, warm, and cool lines. The hydrogen line flux budgets are presented at two times (peak and decay) in each flare, demonstrating how all flares become more dominated by Hydrogen Balmer radiation in their decay phases. The flux budget of IF1 is studied in detail to illustrate how $\chi_{\rm flare}$ relates to Balmer radiation. We examine the detailed line properties of IF3, IF9, GF1, and HF2 which are high energy ($> 10^{32}$ erg) flares that have time-resolved data; using these flares, we present a new Hydrogen line relation, the "time-decrement", which will be a useful constraint for models. We investigate line broadening and flux decrements, which are important for RHD models. The Balmer continuum flux decrement is introduced. Moreover, we will show how these line measures can be applied to study transient absorption phenomena during flares. For

the first time, we have simultaneous high-time resolution data of Hα, Ca II K, the Ca II IR triplet, and Helium I, which can be used to study in detail the evolution of cool, warm, and hot regions of the flare atmosphere. We will show a Neupert relation between the Ca II K evolution and the time-integral of C4170.

In Appendix D, we show additional line properties, such as the properties and flux budget of faint metal lines, the Helium I lines, and the evolution of the feature at $\lambda = 5161 - 5192$Å, which may be attributed to Mg I b, Fe II, or a blend. In Appendix D.2, we present a detailed line comparison between the two peaks in HF2.

4.1 The relations between Hγ and U band

The Hγ line is a useful diagnostic because it is a strong, well measured line, in both high and low flaring states. This line is also the highest order Hydrogen line calculated in most RHD models to date. Furthermore, its properties have been studied extensively in the past for dMe flares. The U-band is widely used for flare monitoring (Moffett, 1974), and it is a diagnostic of the continuum flux and energy, since colorimetry studies have shown the peak of the white-light occurs in the U-band or at shorter wavelengths (Hawley & Fisher, 1992). The U-band contains higher order Balmer lines and Ca II H and K, but $> 92\%$ of the U-band energy is due to continuum (Doyle et al., 1988, see also Hawley & Pettersen (1991), hereafter HP91). It is a well-established property that the Balmer lines are slower than the continuum, staying elevated longer (Kahler et al., 1982) and sometimes peaking as late as the end of the impulsive phase (HP91 García–Alvarez et al., 2002). However, the time-integrated energy in the components scale over approximately 4.5 orders of magnitude with $E_U \sim 25 \times E_{H\gamma}$ (HP91). In this section, we find a stronger connection between the Hγ and the BaC component of the U-band according to their total energies, peak luminosities, and time evolution. We will address these three parameters individually.

4.1.1 Total Energy

First, we use the compiled results from HP91 and examine the global trend of total flare energies in our sample in the top panel of Figure 4.1. The energies were calculated over the same time window for U and Hγ, but in some cases they did not include the entire

decay (e.g., due to a secondary flare or an interruption in the observations). Although the same general trend is apparent as in HP91, we find a large scatter in the distribution of the energies when our flares are included. Lines indicating the median ratios of $E_u/E_{H\gamma} = 12.7$ and $E_{\rm BaC}/E_{H\gamma} = 3.1$ are shown to guide the eye with the trends. The flares, IF5, HF2, HF4, GF2, and GF3 have energies between $E_U = 10^{31.4}$ and $E_U = 10^{32}$ ergs and show a large amount of Hγ energy for their U-band energies, compared to the median ratio of energies. In Figure 4.1 (bottom panel), we show the ratio of the energies, which better visualizes the scatter about the trend. The aforementioned medium energy flares have $E_u/E_{H\gamma} < 10$ in this plot. Eighteen of the flares in our sample have a relation $E_U = 5 - 20 \times E_{H\gamma}$ (IF2 and IF8 have higher ratios), whereas 4 out of the 6 flares compiled in HP91 show ratios of > 20. Including additional decay would presumably bring down our ratios further because Hγ is slower to decay.

We find a tighter correlation between the Hγ energy and the energy in the Balmer continuum component (BaC, $\lambda = 3420 - 3646$Å; see Section 3.1.2) of the U-band than with the total U-band energy. The energies in the BaC contributing to the U-band are shown as red points in Figure 4.1. The ratio of the BaC to Hγ energies are shown in red in the bottom panel. The standard deviation is 0.25 for the red points (BaC), whereas the standard deviation for the U-band ratio is twice that at 0.5.

We find a large amount of energy is contained in the PseudoC (the flux in the higher order Balmer lines $\geq$H8; see Section 3.1.2). In Figure 4.2 (right panel), we compare the ratio of the energy of the PseudoC to the energy in the combined Hδ+Hγ+Hβ lines. Note that the PseudoC contains numerous other metallic and Helium lines, but most of the energy is undoubtedly from Hydrogen in this zone. The 1:1 line is shown for comparison in the left panel, indicating that the energy in the BaC is approximately equal to the combined energy of the Hδ, Hγ, and Hβ lines. Adding the PseudoC energy approximately doubles the energy in the hydrogen Balmer component at wavelengths > 3646Å. The ratio ranges from $0.8 - 1.8$. This gives a useful relation that $E_{BaC} \sim E_{\delta,\gamma,\beta} \sim E_{\rm PseudoC}$. The energy of the PseudoC is not accounted for in most RHD models that employ a Hydrogen atom having 6 levels with continuum, but we find that an important amount of cooling is contained in these transitions.

However, we have not accounted for Hϵ or Hα for the entire flare sample. For the case of IF3, the ratio of $E_{BaC} : E_{\delta,\gamma,\beta} : E_{PseudoC}$ changes from $1 : 0.98 : 1.3$ to $E_{BaC} : E_{\epsilon,\delta,\gamma,\beta,\alpha} : E_{PseudoC} = 1 : 1.6 : 1.3$. The inclusion of H$\alpha$ and Hϵ in the energy budget of IF3 increases the relative energy contribution from the resolved Balmer lines within this flare by a factor of $\sim$60% (with the energy in the Hα line over twice the energy in the Hϵ line), and increases the energy of the total Hydrogen Balmer component by $\sim$20%.

Using Balmer decrements, Butler et al. (1988) estimated the total energy in Balmer radiation in flares to be $\sim 11 E_{H\gamma}$. For three high-energy flares with Hα data (IF3, IF9, and GF1) we find strikingly similar ratios for the total energy in Balmer radiation ($\alpha, \beta, \gamma, \delta, \epsilon$, PseudoC, BaC) divided by the energy in the Hγ line: 12.6, 12.7, and 13.4, respectively. Johns-Krull et al. (1997) found a ratio of $E_{H\alpha,\beta,\gamma,\delta,\epsilon,H8} = 9.6 E_{H\gamma}$ for a solar flare.

4.1.2 Peak Luminosity

The peaks are determined for the light curves of Hγ, BaC3615, U-band, and C4170. In Figure 4.3 (top), we show the ratio of the peak luminosities in the U-band and in Hγ[1]. We observe first the large range of ratios, $10 - 90$, and also a large range at any given peak luminosity of Hγ (e.g., at $\log L_{H\gamma} \sim 28.2$). Second, the points are colored according to the $\chi_{\rm flare,peak}$ value, and the flares with $\chi_{\rm flare,peak} < 2$ (which are also the IF flares) have a large continuum to line ratio, a trend that was shown in Figure 3.13 for the C4170 measure of the continuum. The HF and GF flares, in contrast, have a much smaller ratio, < 30. The flares IF2, IF3, and IF8 (all are flares on YZ CMi) have the same ratio of $\sim$60. The GF, HF1, and HF3 events show a similar ratio of $10 - 20$. There is a transition point that is physically interesting. First, IF7 and IF9 have about the same ratio of $L_U/L_{H\gamma} \sim 35$[2]. They also share other similar properties, such as equal $\chi_{flare,peak}$ and $t_{1/2,C3615}$ values. IF9 and IF3 have very similar relations among their Hydrogen components (see the energy ratio scaling in Section 4.1.1, also the "time-decrement" in Section 4.4), but they have different relative amounts of U-band to Hγ at peak. Below a ratio of $L_U/L_{H\gamma} \sim 35$, the flares generally

[1]Which may correspond to different times in the flare evolution.

[2]Recall, the U-band of IF9 was estimated from the spectra, and therefore has $\sim$20% uncertainty

produce $\chi_{\rm flare,peak} > 2$ values. The highest values of $L_U/L_{H\gamma} \sim 75-85$ are produced by IF0 and IF4, which also have very low $\chi_{\rm flare,peak}$ values (< 1.5; Table 3.2).

There is a much more ordered relation with the ratio of the peak luminosities of BaC and Hγ, as shown in Figure 4.3 (bottom panel). The large scatter apparent with the U-band reduces to a tighter relation around a ratio of $L_{\rm BaC,peak}/L_{H\gamma,\rm peak} \sim$5, and the IF flares (IF3, IF7, IF8, IF9) are very close to this value. In summary, the IF, HF, and GF flares show a common trend between the BaC and Hγ peak emission, whereas they are widely differentiated by $\chi_{\rm flare,peak}$ and the ratio of $L_U/L_{H\gamma}$ at peak.

4.1.3 Timing

In Figures 3.14−3.18, we showed the light curves of Hγ and the U-band for the flares in our sample, illustrating the well-known property that Hγ generally stays elevated for much longer than the continuum, meaning that either the cooling timescale is much longer for the Balmer lines or that a persistent heating mechanism slows the decay of the Balmer lines and not the continuum. Some flares exhibit large delays of $2.5-10$ minutes between the times of maximum continuum and maximum line emission, suggesting a large difference in the heating and cooling timescales of the continuum and lines during the impulsive phase. We find that these large lags result when secondary continuum spikes lag the primary events by $\Delta t \sim 2-10$ minutes, as in IF0, IF4, and HF2. For most classical flares without a large secondary event, however, there is a difference of less than one minute between the peak times of the continuum and Hγ line. The short delay in peak times of < 1 minute gives insight into the impulsive flare heating mechanism of high energy flare events with relatively simple morphology, such as IF3 and IF9. We posit that the heating mechanism that produces the line emission during the rise phase and peak also produces the continuum emission because a large disconnect in timing is not observed. Time delays between Hydrogen line emission and continuum emission provide important constraints for flare simulations; delays of Balmer line emission have been studied with non-thermal heating in RHD models of solar flares (Kašparová et al., 2009).

In order to illustrate the connection in the timing between Hγ and the BaC3615, we

show the relations for the $t_{1/2}$ values between U-band and Hγ in Figure 4.4 (top panel) and between BaC3615 and Hγ (bottom panel). These figures are qualitative representations of the timing differences that are obvious in Figures 3.14−3.18. Equal times are indicated with the dotted lines. The inset of each panel shows the four short duration (IF2, IF5, IF6, IF8) classical flares in more detail. There is a range of amplitudes for these flares, $I_{f,U} \sim 2.5-12$, and total durations of $5-24$ minutes. The total durations are much longer than the $t_{1/2,U}$ values, < 1 minute, which reflects that $t_{1/2}$ is primarily a measure of the impulsive phase of these flares. The ratios of the $t_{1/2}$ values for U-band and Hγ against $L_{U,\mathrm{peak}}$ for all of the flares are given in Figure 4.5. The IF flares have the lowest ratios, < 0.4. The five flares with $L_{U,\mathrm{peak}} > 5 \times 10^{29}$ ergs s^{-1} have the smallest ratios, < 0.2. In all cases, the U band is faster than the Hγ line (ratio < 1), but the U band does not correlate strongly with the Hγ evolution as given by the $t_{1/2}$ index. The ratio does have a general decreasing trend towards higher U-band peak luminosities. It may become ubiquitously < 0.2 for high luminosity flares, which provides important constraints for modeling continuum and line evolution time-profiles.

The bottom panel of Figure 4.4 shows the relation between $t_{1/2,H\gamma}$ and $t_{1/2,BaC3615}$. We find a relation among the IF and HF flares *without multiple peaks* (crosses). The fit to these flares is shown as a light blue line, with parameters $0.54(\pm0.01) \times t_{1/2,H\gamma} + 0.4(\pm0.1)$. The GF flares (shown in open circles) follow a different trend with approximately equal timescales in Hγ and BaC3615. The flares with multiple peaks are shown with red squares: IF4 and HF2 are double-peaked flares and are apparent outliers (the red squares with $t_{1/2,H\gamma} \sim 16$ minutes). IF4 falls closer to the GF distribution, and HF2 has a much faster BaC3615 timescale given the Hγ timescale predicted by the light blue line. The timescales for this flare are discussed further in Section 4.4 and Appendix D.2. IF0 is a double-peak flare but has little BaC3615; GF1 can be considered a double-peaked flare, and it produces copious BaC3615 with a long timescale. The other multiple-peaked flares, HF1 and HF4, fall on either the single-peak distribution or the GF distribution. Clearly, characterizing the different timescales between Hγ and BaC3615 in double-peaked flares would benefit from a larger sample. Figure 4.5 gives the ratio of $t_{1/2,BaC3615}/t_{1/2,H\gamma}$ in red asterisks. The ratios are near 0.6 and 0.8. These are important values for modeling the time-evolution of Balmer

line and continuum emission.

In summary, we have shown that the Hγ line follows the U-band properties over several orders of magnitude in flare luminosity, but that its energy, peak emission, and time-evolution are related more closely to the BaC3615 component of the U-band. The differences between the U-band and Hγ line, which are most striking in the peak luminosity, are caused by the faster, hotter continuum component that contributes to U-band emission (Chapter 6). We speculate that at high U-band luminosities, this component causes the time-evolution of the U-band to diverge significantly from the Hγ line, with a ratio of $t_{1/2,U}/t_{1/2,H\gamma} < 0.2$ (Figure 4.5).

4.2 Line Energy Budgets

Line fluxes are calculated according to Section 2.2.2, and are grouped into *hot*, *warm*, and *cool* categories. The designation comes from our basic understanding of the formation temperatures of He I lines (*hot*, He I λ4026, λ4471 in the transition region, $T > 20\,000$ K, (Lites et al., 1986; Johns-Krull et al., 1997)), Hydrogen Balmer lines (*warm*, Hδ, Hβ, and Hγ; high chromospheric, $T \sim 10\,000$ K), and Ca II K (*cool*, low chromospheric, $T \sim$ 6000 K, Abbett & Hawley (1999)). There are three lines that appear prominently at $\lambda \sim \lambda4923, \lambda5018, \lambda5170$ in the flare spectra; these may be blends of Mg I b (cool), He I (hot), and Fe II (undetermined origin).

We will see that the designation approximately correlates with the timing properties: hot lines are the most impulsive, warm lines have an impulsive rise but stay elevated, and the cool lines reach their peak later in the flare. Some lines appear to have both a well-defined hot (impulsive) and cool (gradual) component such as the He I lines; the amount that the nearby features at 4481Å (possibly Mg II) and 4030Å (possibly Mn I; Doyle et al. (1988)) contribute to the Helium lines cannot be accurately determined from our low-res spectra.

In the Table 4.1, we show the line energy budgets for all flares, sorted according to the basic morphological classification. The impulsive flares generally have hot : warm energies of $0.03 - 0.05$, and the HF and GF events have ratios of $0.025 - 0.035$. HF2 has the lowest hot : warm ratio and IF2 has the largest. IF5 has a low hot : warm ratio for an IF event.

The ratio of cool : warm is often found to be ∼0.15. Surprisingly, IF3 has a relatively small hot : warm ratio and relatively large cool : warm ratio for an impulsive flare. A larger sample of flares and a suite of models is necessary for determining how line energy budgets vary according to flare heating.

4.3 Hydrogen Balmer Flux & Energy Budgets

We next study in detail the properties of the Hydrogen Balmer lines. Since the models accurately predict chromospheric properties of flares – Balmer flux decrements and broadening amounts (also Balmer continuum shapes, see Chapter 5)– we can use the models for understanding important parameters about the flares, such as chromospheric electron densities and temperatures. We will use flares IF1 (time-resolved flux budgets), IF3 (line broadening characteristics), IF9 (line broadening characteristics), and GF1 for detailed analyses of the Hydrogen lines.

We establish a relationship between the Hydrogen Balmer flux and $\chi_{\rm flare}$. The energy budget of Balmer emission to the total emission quantifies the amount of unaccounted energy in model predictions (Allred et al., 2006). Ultimately, we seek to model the unaccounted (white-light) energy. We find that more impulsive flares have a larger amount of unaccounted energy, peak flux, and decay flux. We analyze the energy budgets at peak and decay phases of each flare, and we study the time-resolved flux budget of IF1, in order to show that the relative amount of Hydrogen Balmer flux varies with the shape ($\chi_{\rm flare,peak}$), and therefore formation parameters, of the NUV/blue continuum. Models especially fail to reproduce $\chi_{\rm flare,peak}$ (Chapter 8); therefore, knowing the amount of Hydrogen Balmer emission present at this time helps modeling efforts. Any model that reproduces the blue continuum must be consistent with the Hydrogen line properties (Cram & Woods, 1982).

In Table 4.1, we show the fraction of flux radiated in the Hydrogen Balmer (HB) component relative to the total flux in $\lambda = 3420 - 5200$Å. The HB component is a sum of the fluxes in Hδ, Hγ, Hβ, the PseudoC, and the BaC. For a comparative energy budget among these components, please refer to Figure 4.2. Note, Hϵ and Hα are not included in the HB component. The total energy from $\lambda = 3420 - 5200$Å (assuming isotropic emission) is shown in the last column for comparison. The fraction of HB generally increases according

to our IF/HF/GF ordering. In the IF flares, this fraction is 25 – 35%, whereas in the GF flares, it is > 40%. Most (sixteen) flares show the majority of the $3420 - 5200$Å energy (> 60%) is emitted in non-HB component emission. Flares that have <60% of their energy in the non-HB component are IF5, HF2, HF4, GF2, GF4, and GF5. The flare IF5 is an exception, being an impulsive flare with an unusually large fraction of HB emission (42%). Among the impulsive flares, this flare also has an unusually high value of $\chi_{\rm flare,peak}\sim 2.2$ and the largest Hγ/C4170 ratio $\sim$50.

In IF1, we sample 1.3 hours of the gradual phase, yet it is still one of the flares that is least dominated by the HB component. The high spectral cadence ($\sim$30 sec) allows us to calculate a detailed flux budget evolution during the decay phase and secondary flares. IF1 illustrates the detailed evolution of the percentage of HB emission and the connection to $\chi_{\rm flare}$ evolution. In Figure 4.6 (top), the $\chi_{\rm flare}$ evolution is compared to the U-band evolution. The trends are anti-correlated during the secondary flares with U-band peaks at $t \approx 1.6$ hours and $t \approx 2.15 - 2.16$ hours (MDSF2), and will be explained in Chapter 7 as the combination of effects resulting from increasing C4170 (blackbody) continuum and the formation of absorption in the Balmer continuum. In Figure 4.6 (bottom panel), the HB flux ratio is shown, and it varies significantly with time. The anti-correlated behavior with the U-band (light grey) is the same as between the U-band and $\chi_{\rm flare}$. The maximum ratio is 35%, but the contribution from Hydrogen drops to a minimum of 15% at $t \approx 2.17$ hours just after the U-band peak of the MDSF2 (note, including Hϵ, Ca II K and Ca II H changes these values to 37% and 17%, respectively, but does not change the trends).

Now, we investigate the coarse time-evolution of the fraction of HB flux in the flare sample. We calculate the fraction of HB flux at the time of maximum continuum emission and near the beginning of the extended gradual phase; these times (and spectrum numbers) are given in Table 4.2 and are indicated by red vertical lines in Figures C.1 – C.19. The decay phase measurements are averaged over three spectra, and the peak measurements are averaged in several of the GF flares to increase signal to noise. The HB component does not include Hϵ in the blue-optical because it is blended with Ca II H. Including Hϵ in the HB energy budget (by subtracting Ca II K as an estimate for Ca II H) increases the peak percentages by $\sim$1% and the gradual phase percentages by $\sim$2%. One can multiply columns

2, 3, and 4 by column 5 of Table 4.1 to obtain the fraction of either the *hot*, *cool* or $H\alpha$ for comparison with the HB values.

The results are shown in Figure 4.7 (left panel) for the impulsive, hybrid, and gradual flares. The values in this figure are also given in Table 4.3. The spectra S#23-25 (gradual) and #113 (just before peak of MDSF2) measurements are shown for IF1 as light blue star symbols and the IF0 peak and decay spectra are shown as dark purple star symbols. The peak value of IF1 is for the secondary flare (MDSF2) peak and coincidentally falls on the same curve as the other IF flares; however, it's difficult to determine the percentage of the newly formed Balmer *emission* due to all the Hydrogen Balmer *absorption* (Section 6.6.1). Figure 4.7 indicates a ubiquitous evolution to a higher percentage for all flares in their decay phase[3]. The ratios increase by ∼20% for most flares; larger changes by ∼30% occur during IF0, IF4, IF5. These flares also have very sudden breaks from impulsive to gradual phases. IF3 also has a large change by about 30%. Significantly smaller changes, <20%, occur during HF3, GF1, and GF5 likely because the gradual phase of these flares begins at a relatively high amplitude compared to the peak.

There is also an increasing percentage of Hydrogen Balmer emission during both the peak and decay phases according to the IF/HF/GF sequence. The impulsive flares show a tight clustering between 10% and 18% at the peak in the ratio of HB flux to total, and changing to either $30-36\%$ or $43-52\%$ (IF0, IF10, IF5, IF6) during the gradual phase. Comparing to column 4 of Table 4.1 shows that the time-integrated energetics are weighted toward the values of the gradual phase flux percentages. The HF flares are scattered around $25-35\%$ Hydrogen contribution during the peak phase and the GF flares are scattered around $35-50\%$. There is generally an increasing scatter of percentages going from the IF flares to the GF flares; we attribute this effect to the spectral component that gives rise to the spike phase in these flares. The spike phase is particularly strong in IF2, IF4, and IF10; of these IF4 produces an extremely low amount of HB component in the rise and peak phases. Note that in GF1, there is a stand-alone impulsive phase prior to the major, broad

[3]Except for GF5 which shows equal HB percentages in peak and decay; for this flare, the decay phase time was chosen immediately after the impulsive phase time in order to increase the S/N in this low-amplitude event.

emission peak; the percentage is 25% for the peak.

The evolution of $\chi_{\rm flare}$ from the peak to the gradual phase times is shown in the right panel of Figure 4.7 and the values are given in Table 3.2. Both $\chi_{\rm flare}$ and the percentage of HB component increase during the flare decay phases, implying a connection between these measures. The $\chi_{\rm flare}$ of IF1 for peak and decay times (Figure 4.6) are shown in light blue star symbols; these are consistent with the other IF events, even though a large amount of decay emission was present at the start of the secondary flare. The IF events have very ordered trends: they all increase by ∼20% in the HB contribution in the decay phase and have $\Delta\chi_{\rm flare}\sim1$.[4]

Anomalous IF events are IF5 and IF6. They stand out as IF flares that have an unusually large amount of HB ($>$ 20%) and large $\chi_{\rm flare}$ (∼2.2) at peak. We already noted that IF5 has a large amount of HB total energy (∼ 40%) for an IF event. These two flares have HB fluxes that rise to large percentages ($42-52\%$) and $\chi_{\rm flare}$ values that rise to ∼4 in the extended decay phase, further strengthening the connection between these two measures ($\chi_{\rm flare}$, HB fraction) even for just the two flares that are not as similar as the other flares in the (IF) grouping.

The fractions in Table 4.3 will be directly compared to RHD models in Chapter 8 in order to understand the contribution from backwarming and Paschen continuum emission to the total flare emission. The non-HB flux ((1-HB)/Total) is largely due to flux from the underlying continuum that extends from the near-UV through the optical and which we measure using C4170. This accounts for $82-90\%$ of the total flux during the peak phase. For the first time, we have included the Balmer continuum ($\lambda > 3420$Å) energy budget with the budget of the other Balmer features and shown that the Balmer component is not the dominant source of flux in flare emission in the blue. At most, the Balmer contribution accounts for 50% of the blue-optical flux. Throughout the rest of this thesis, the continuum

[4]We note that it is striking that the largest amplitude flares have ∼40% HB at the beginning of the extended gradual flares. The data for IF1 is far into the decay; extrapolating back to $t = 0.8351$ hours at the beginning of extended decay phase (when there were no spectra) and using a fit of $\%{\rm HB(t)} = 0.429-0.06\times t$, we predict 38% HB contribution for this flare. IF3 has an HB contribution of 37% at the beginning of the extended gradual phase. The large amplitude flares IF0 and IF10 have ∼44% of HB emission in the extended decay; however these flares did not have spectra as blue as $\lambda = 5200$Å to allow a directly comparable energy budget to be calculated.

component that accounts for the excess flux is represented by C4170. In Chapter 6, we will model this non-HB emission using blackbody and hot-star continua.

HP91 presented an energy budget analysis of IF0 from the FUV through the optical, and compared to a smaller, similar morphology flare from Rodono et al. (1984). The energy breakdown from HP91 showed that 4% of the impulsive energy and 17% of the gradual phase energy is radiated in the lines. We must comment on why the measures presented here are different. The first reason is that the values here – 12% (peak) & 44% (gradual) – are only for select times (they represent the fraction of the luminosity as opposed to the fraction of the total energy) during the flare. Second, if we take the hydrogen lines divided by the U and B bands only (which gives similar coverage as the HP91 spectra, see values from Table 6 of their paper), we obtain 7% and 38% of the impulsive and gradual luminosity radiated in the lines. The remaining apparent discrepancy occurs because we include the PseudoC and the BaC in the HB component while HP91 included these in their "continuum" rather than "lines" component. Therefore, our analysis is consistent with values presented in HP91, but is simply a presentation of the instantaneous values to be consistent with the time-resolved analysis of our flare sample.

4.4 Hydrogen Balmer Time Evolution

We study the time-evolution of the Hydrogen lines in flares IF3 (Figure 4.8), IF9 (Figure 4.9), HF2 (Figure 4.10), and GF1 (Figure 4.11). In addition to Hα, Hβ, Hγ, and Hδ, we show the evolution of the PseudoC, BaC3615, and C4170. The fluxes are normalized to their peaks to illustrate the different decay trends (left axes; the C4170, Hγ, BaC3615, and the U-band are shown for their normalized evolution for all flares in Figures 3.14 - 3.18). The Ca II K and He I λ4471 normalized fluxes are also shown. Figure 4.8 (bottom panel) also shows the rise phase in detail for the absolute fluxes of Hα, Hβ, Hγ, and Hδ. In this section, we connect the components of the Hydrogen Balmer time evolution in each flare using a new measure, the *time-decrement*.

From these figures it is evident that the higher order Balmer lines have a faster decay time compared to the lower order lines, attaining a lower relative flux by the end of the impulsive phase. This effect was noted by Doyle et al. (1988) and HP91. According to $t_{1/2}$,

the ordering of the components, from fastest to slowest, is C4170, He I λ4471, BaC3615, PseudoC, Hδ, Hγ, Hβ, Hα, and Ca II K. Ca II K is discussed further in Section 4.8.1. Hγ and Hδ have rather similar decay rates, but the Hγ is slower[5].

To connect the timescales across the Balmer series, we analyze the $t_{1/2}$ values of each line. We plot the $t_{1/2}$ against the wavelength of the transition in Figure 4.12 (black symbols). The $t_{1/2,\mathrm{C4170}}$ values are also shown as light blue symbols. An estimate of the H10 line (using an extrapolation from the blue-optical as the underlying continuum) from the PseudoC component is included as well as the flux of BaC3615. This "time decrement" is displayed for the four flares. Remarkably, the relationship among the Balmer spectral components appears nearly linear in wavelength space for the two IF flares in the figure. The time-decrement for IF3 is shown in red and is fit with a linear relation to show the trend[6]. The flare IF9 has a similar time-decrement as IF3 but on $\sim$1.7 times shorter timescales (the fit is shown as a black dashed line)[7]. GF1 has a much flatter time decrement, likely due to the slow rise of each emission component. GF1 has the same $t_{1/2}$ for Hγ and Hδ as IF3, but the lower order lines are faster and the higher order lines are slower: the time decrement for GF1 is shallower, which we hypothesize is a feature of gradual flares. The time-decrement of HF2 is apparently flat for the lower order lines and steep for the higher order lines, consistent with its *hybrid* classification. HF2 has two continuum peaks and a highly elevated decay phase relative to its peak; its emission line and continuum properties are studied in detail in Appendix D.2. Recall that in Figure 4.4 and Figure 4.5, we compared the $t_{1/2}$ of Hγ and the BaC3615 between all flares, and found a general relation for the simple events while complex events, such as HF2, behaved differently. Figure 4.12 elucidates this difference.

4.4.1 Discussion

Drake & Ulrich (1980) discuss how densities and the difference in energy levels among Hα,

[5]We hypothesize that $t_{1/2}$ is affected by the amount of A-star absorption at peak, as during IF3 (see Section 4.5.4), causing the 0.5 level to slightly overestimate the $t_{1/2}$ for Hδ, more so than for Hγ.

[6]Conversely, the time-decrement follows a $1/E$ trend, where E is the energy of the transition

[7]The two, classical flares IF3 on YZ CMi and IF9 on AD Leo have a ratio of $\sim$8 in their SDSS g-band energies, yet the time-decrements follow a scaling relationship with a factor of $\sim$1.7 in the parameters of the best-fit line. The ratio of the $t_{1/2,\mathrm{C4170}}$, however, is 3.8, which does not follow the same relationship.

Hβ, Hγ, and Hδ affects the relative flux in each line: larger densities preferentially populate the higher levels via collisional excitation, due to the larger energy difference between their upper levels and a given lower level. The time-decrement is therefore a result of each transition's individual sensitivity to decreasing density during the flare decay. Due to the larger optical thickness, the lower order lines are less sensitive to the decreasing electron density of the flare chromosphere in the late phase. We have measured the Balmer continuum's time-evolution for the first time (from flare start to finish) and have shown that it is the fastest Hydrogen Balmer component. Moreover, its timescale is consistent with the timescale extrapolated from the bound-bound Hydrogen Balmer transitions. Hydrogen bound-free cooling is related to electron density according to n_e^2 (recombination is a collisional process); if the Balmer continuum originates from a higher column mass, and therefore a higher density, than the bound-bound transitions, the Balmer continuum will radiate energy away quicker.

In addition to density, the time decrement is also likely dependent on several other important flare parameters in the decay phase: the change in chromospheric temperatures, the sustained levels of nonthermal particle bombardment in the gradual phase, the incident XEUV radiation field and overpressure from the superheated corona. In a future work, we will study the influence of each of these effects on the decay phase emission with our new RHD models (see Chapter 8).

4.5 Hydrogen Balmer Line Broadening

In this section, we first study the Hydrogen Balmer line broadening for the entire sample of flares, finding a new relation at peak times between the broadening in Hγ and the value of the BaC3615 / Hγ line flux ratio. We then look in detail at the line broadening evolution in IF3 and IF9, which are two classical flares with lower and higher spectral resolution data, respectively. An important finding is that the maximum line broadening occurs during the mid rise phase of a flare, but more time-resolved data will be required to understand how ubiquitous this correlation is. A second important finding in this section is direct evidence for wing absorption during times of extreme C4170 continuum production in IF1 and IF4. These absorption features are seen as depressions in the line wings at $\pm$15Å from line center.

4.5.1 Line Broadening Background

Balmer line broadening has been studied extensively in stellar flares (Doyle et al., 1988; Hawley & Pettersen, 1991; Jevremovic et al., 1998; García–Alvarez et al., 2002; Hawley et al., 2003; Paulson et al., 2006; Fuhrmeister et al., 2008, 2011). The cause of line broadening remains an open question, as it has been attributed to both Doppler and Stark effects (see discussion in Kurochka & Maslennikova, 1970). The Doppler effect may contribute to broadening through mass motions and thermal velocities in the flare atmosphere (Eason et al., 1992). Understanding the broadening of Hydrogen lines is important because the higher order members (in the PseudoC) likely blend together, leading to the apparent lack of a Balmer discontinuity in stellar flare spectra (Hawley & Pettersen, 1991, also see the high spectral resolution decay phase spectrum in Schmitt et al. (2008); Fuhrmeister et al. (2010)). The Stark effect is an important broadening mechanism in RHD models, which have been matched to the widths of observed Hydrogen lines (Allred et al., 2006; Paulson et al., 2006), but have failed in others (Doyle et al., 1988; Eason et al., 1992). The Stark effect is also thought to generate line broadening (and consequently blending) in solar flares (Švestka, 1972; Donati-Falchi et al., 1985; Johns-Krull et al., 1997). On the other hand, echelle data of Hα during flares have been interpreted in terms of thermal and Doppler broadening (Eason et al., 1992; Fuhrmeister et al., 2008, 2011), indicating either tens to several hundreds km s^{-1} mass motions or very high temperatures. However, sometimes these long-integration exposures (as is typical for the echelle observations) are difficult to interpret because they average over many phases of changing flare evolution. Moderate resolution data (R$\sim$ 2700) have also been obtained for the higher order lines ($\geq$Hγ) with poor fits to Stark profiles (Doyle et al., 1988). The broadening was connected to directed or turbulent mass flows with velocities of $\sim 250-300$km s^{-1}. However, these authors explained how the interpretation of such large symmetric, broad wings could be complicated by a succession of spatially distinct upflows and downflows occurring within the integration time (60 seconds) of their spectra.

4.5.2 Line Broadening Measurements

The broadening of the Hγ line in IF0 was presented in HP91 and was discussed in relation to the predictions of the Stark effect (however, it was ultimately inconclusive due to low spectral resolution). The width of the line reached a maximum of $\sim$15Åat 10% line profile maximum[8], which approximately matched the F11 peak spectrum Hγ profile (width of 13Å) from (Allred et al., 2006).

For the DIS sample, we calculate the full width at 10% of the maximum line profile flux, which we refer to as simply the "width"; the full width at 10% maximum avoids nearby metal lines in the wings of Hydrogen, and it is a commonly employed measure in past studies. The lowest width that we can measure with our low-resolution data is $\sim$15Å for the 1.5" slit and $\sim$31Å for the 5" slit, determined from an arc line (see the observation logs, Tables 2.2-2.5). See Appendix D.1 for more details on calculating line widths.

Despite the low resolution of our data, we do observe line broadening in the wings during the flares. The widths of Hγ at peak emission for all flares are shown in Figure 4.13. The line broadening plotted against the value BaC3615 divided by the Hγ line flux, which effectively gives a "Balmer continuum decrement", and the resolution limits are indicated by horizontal lines. It appears that the broadening is dependent on the value of BaC3615/Hγ, and $\sim$0.02 is a limit at which measurable broadening occurs for the 1.5" data. In other words, flares with larger relative amounts of BaC3615 show more broadening. The maximum broadening observed is $\sim$35Å for the 1.5" data (Figure 2.1). Due to the lower spectral resolution of the 5" data, the peak-normalized line profile biases the 0.1 width measure towards larger values (e.g., compare the horizontal lines depicting the limits). Therefore, the 0.1 width is not directly comparable between 5" data and 1.5" data. One should consider the *excess* broadening above the limits as representing the bona-fide broadening.

A few of the flares deserved discussion. IF10 and IF4 show about the same amount of broadening as the maximum broadening in the Great Flare from HP91. The very small amount of BaC observed during this flare is consistent with having a smaller amount of line broadening. Also note that IF1 is shown for the continuum peak of MDSF2 (not for the

[8]Note that HP91, Figure 9, shows that the *full width at 0 maximum* reached 21Å.

Hγ peak like the others), and the broadening is just at the resolution limit. A tentative trend is that IF0, IF4, HF2, GF2, GF3 show a smaller amount of broadening than the other flares; it is interesting that they also have multiple continuum peaks and delays in the peak of Hγ relative to the continuum peak. These flares with more than one *resolved* flare events support the argument in Doyle et al. (1988) that the superposition of unresolved flare events affects line width measurements.

4.5.3 Time-Resolved Line Broadening Measurements

The Stark effect results from the perturbation of atomic energy levels from ambient electric fields, hence increasing the widths of the absorption/emission profiles from a given level (Mihalas, 1970). The linear Stark effect in particular results in larger broadening of the higher order lines compared to the lower order lines (Sutton, 1978) because the higher levels are less bound by the nuclear charge. In this section, we study the time-evolution of IF3, IF9, and GF1 broadening of the Hδ line because we have a better chance of observing the Stark effect, if present. We demonstrate the connection between broadening and the Balmer continuum flux, which manifests in different ways between the IF3 and IF9 flares. The IF3 event had many spectra during the impulsive phase, thereby allowing us to investigate the time-evolution of line broadening during this event. IF9 is a classical, simple high energy flare that allows a comparison to IF3; GF1 is high-energy flare with time-resolved data. Ultimately though, more time-resolved, high spectral resolution data will be required to study this effect in detail.

In Figure 4.14 (top panel), we show the line profiles of Hδ over the impulsive phase of IF3. The line profiles are color-coded to the BaC3615 flux light curve, which is shown in the inset panel. Also in the inset, we plot the width of the Hδ line. The quiescent profile of Hδ is shown as a dark solid line in the figure, to illustrate the large amount of broadening present during the flare. The maximum width of the line occurs in the middle of the rise phase, at the time when there is the fastest change in the Balmer continuum. The quiescent profile is shown in black, the red profile is at flare maximum, and the profile with maximum broadening is in green. Several other flares have a maximum line width

that does not occur at maximum continuum (e.g., IF4). Note that the trend in IF3 may not be significant, considering the formal systematic errors of 9Å for the 5" slit data; the correlation between the time-derivative of BaC3615 and maximum line broadening requires further investigation.

We also looked for this relation in the high energy flare GF1, which has smaller systematic errors (∼3.5Å) and line broadening is detected at ∼4 σ. The time-evolution of Hδ broadening is shown in the Appendix D.1 (Figure D.2). Although not entirely clear precisely when the maximum line broadening occurs during the final fast ascent to peak, the maximum broadening precedes the maximum BaC3615 and Hδ emission. The difference between the broadening in the rise phase and at peak is still only suggestive considering the errors.

IF9 is also a classical high-energy flare; in contrast to IF3, the maximum broadening occurs at (or near) maximum continuum peak whereas the maximum derivative of BaC3615 (within our time resolution) occurs during the rise phase. For this flare, we demonstrate that the time-evolution of the broadening follows the BaC3615 flux. In Figure 4.15 we show the BaC3615 flux (red), the Hγ line flux (asterisks) and the Hγ width profile (squares). The relative evolution of the Hγ broadening follows the relative evolution of BaC3615 more closely than the Hγ line flux.

4.5.4 Hydrogen Balmer Wing Absorption

We now present individual cases of line broadening in larger flares that exhibit absorption in the wings. This finding will be used to connect to the previous findings of the time-evolution of broadening and to the flux decrements in the next section. Wing absorption signifies heating in deep layers of the atmosphere, which is an important constraint for flare heating models.

In Figure 4.16, we show Hδ, Hγ, Hβ, and He Iλ4471 profiles for IF4, at maximum continuum emission (black, S#665) and at maximum Balmer line emission (S#672, turquoise/grey). The profiles are plotted with the local continuum subtracted with a straight line and then are normalized to the peak of the line. The striking effect here is a "depression" in the line wings in the black profile (maximum continuum) between ±10 to 30Å from line center.

Furthermore, the amount of wing depression increases from Hβ to Hδ. The differences in the widths between maximum continuum flux and maximum line flux times are $\sim$6Å for Hδ and Hγ and $\sim$2Å for Hβ. The change in the line widths for Hδ and Hγ are $\sim 2\sigma$ (given 3Å uncertainty in widths). During the rise phase (S#664 at $\sim$40% of the peak continuum emission), the Balmer lines are narrow (the widths are 1Å less for Hδ and Hγ but 3Å less for Hβ), and there is less evidence for wing depressions. In the spectrum following peak, the Balmer lines have begun to broaden significantly.[9]

A similar wing absorption effect is seen in the Megaflare (IF1) spectra. In Figure 4.17, we show the profiles for the IF1 flare immediately before the secondary flare (turquoise) and at the peak of MDSF2 (black). The amount of wing depression is less than in IF4. Over the course of the MDSF2 rise phase (going from the turquoise to the black in Figure 4.17), the change in widths is only about 1Å for each line, while the total line flux *decreases*. As in IF4, the amount of wing depression increases for the higher order Balmer lines.

We interpret these wing depressions as a direct signature of Balmer line absorption forming during these flares. The absorption wings in model hot star spectra with $\log g = 5$ are very broad (Castelli & Kurucz, 2004), and the superposition of chromospheric emission lines and increasing amount of absorption in the wings leads to the net decrease in the wings. The chromospheric Balmer emission veils the (presumably, photospheric) Balmer absorption in the total flare spectrum. See Johns-Krull et al. (1997) for a phenomenological illustration using quiet-Sun Hα absorption and superimposed chromospheric Hα emission. For IF1, the newly formed flare emission during the MDSF2 was found to have a spectrum like a hot star, with the Balmer lines in absorption (see Section 6.6.1). The effect we see here is a technique of directly detecting hot star signatures without needing to isolate newly formed emission. This analysis can be employed with other flares that have non-flux calibrated data, or for flares with limited spectral range.

We search for wing depressions in the flares with the largest continuum enhancement in the DIS sample, at the peak of IF3. We find depressions only during the newly formed emission at peak. In Figure 4.18, we show the SDSS u-band photometry during the rise and

[9] As an aside, we note a curious red wing enhancement at $\lambda = +5 \mathrm{to} + 10$Å in the H$\beta$ line, which is present in the rise and at the times of peak continuum and line emission.

peak emission. The black circles are the original data points, and the asterisks represent the derivative of the light curve. The derivative is useful for diagnosing changes in a light curve with an irregular cadence (like for these data). At $t = 2.14$ hours ($\sim$75% of the maximum emission) the derivative has decreased, indicating the presence of a transient maximum in the photometry; we interpret this as evidence of the end of a fundamental"burst" of emission during the rise phase. Afterwards, the derivative increases again, signifying a new burst of emission leading to the peak. The red squares represent the photometry interpolated (using a spline function) and rebinned to fifteen seconds, illustrating the same effect as the derivative.

In Figure 4.19 we show evidence of wing depressions at the time of the IF3 peak for the newly formed emission in the peak emission "burst". We assume that this burst corresponds to a different flare region on the star (in Chapter 6 we show that the rise phase corresponds to increasing flare area, suggesting that our assumption is valid), allowing the first burst spectrum to be subtracted from the second burst spectrum. The green profiles show the normalized total flare emission at S#29 (this corresponds to the rise phase when the continuum flux is at 80% of the maximum – before the second flare burst), the turquoise profiles show the normalized total flare emission at S#31 (at maximum continuum emission), and the black profiles show the difference (using the unnormalized spectra) of S#31 - S#29. The integration times of these spectra are indicated with green and turquoise shaded bars in Figure 4.18. There is line emission formed during the second burst; however, the wings are certainly depressed relative to the total flare emission. The apparent amount of depression increases from Hβ to Hγ to Hδ, as in IF4 and IF1.

4.6 Hydrogen Balmer Flux Decrements

We now analyze the Hydrogen Balmer decrements. Similar to the broadening, we will look at the whole sample, and then focus on several flares in particular. We will show that the decrements reach their maximum departure from the quiescent value early in flares and only some secondary flares within complex flare events produce a response in the decrement. Then, we will jointly discuss the decrements and broadening.

4.6.1 Background on Balmer Decrements

The Balmer decrement (BD) for a given line is the ratio of the line flux to a fiducial Balmer line, usually Hγ or Hβ. The BD is an indicator of changing plasma conditions during flares, and has been used to infer an increase in chromospheric electron density during dMe flares (Kunkel, 1970; Katsova, 1990; Jevremovic et al., 1998; García–Alvarez et al., 2002). In quiescence, the decrements are typically "steep" with more flux in the lower order Balmer lines and Hα being the strongest line and contributing the most to the radiative cooling (see Table 2.8). In flares, the decrement "flattens" (or becomes "shallow") such that the flux emitted in the higher order lines (H5 – H8 (Hawley & Pettersen, 1991; García–Alvarez et al., 2002)) becomes comparable with the flux in the lower order lines (H3 – H4). This effect has been studied and explained by Drake & Ulrich (1980) and is attributed to a combination of the higher optical depths in the lower order lines coupled with increasing electron densities during the flare. According to these calculations, the Balmer decrement (relative to Hβ) follows a complicated trend, reaching a maximum at a relatively high value of electron density but decreasing at higher densities. The RHD models from Allred et al. (2006) predict this general behavior, with the medium flare heating (F10) model predicting 1.28 and 0.96 and the large flare heating (F11) model predicting 1.19 and 0.89 for the Hβ and Hδ decrements (using Hγ as the fiducial) respectively, which well match the observed decrements from the Great Flare in HP91. Interestingly, the larger beam heating model produces an Hγ line flux that relatively stronger than both Hβ and Hδ compared to the moderate heating model. . Observed Hδ decrements in the literature have ranged from $0.69 - 1.05$ (Rodono et al., 1984; Phillips et al., 1988; Doyle et al., 1988; Jevremovic et al., 1998; Eason et al., 1992; Hawley & Pettersen, 1991; García–Alvarez et al., 2002), with most ≤ 0.96. Kunkel (1970) observed reversed decrements of ~ 1.2 for Hδ/Hγ in the early stages of a flare. Recently, Hilton et al. (2010) studied the decrements with fifteen minute integration time spectra from SDSS, and found that of the Hydrogen lines only the Hα to Hβ ratio changes (decreasing during the rise phase and increasing in the decay phase) over the evolution of the flare; the other decrements stay flat. Similarly, Schmidt et al. (2012) found a low and relatively constant flux decrement of ~ 0.8 for Hδ/Hγ during IF10 (and

possibly decreasing slightly into the gradual phase).

Atmospheric conditions change on short timescales during the impulsive phase, and time-averaged decrements may average out important constraints for RHD models. The unique aspect of our data is that we can study the time resolved characteristics of the decrement, and unlike past studies (except for Hilton et al. (2010)) we can calculate the Hα decrement simultaneously.

4.6.2 Decrements at Flare Peak

As for the broadening analysis, we examine the distribution of the decrements at flare peak. We concentrate our analysis on this time because ultimately we are most interested in the atmospheric parameters at the time when the non-HB flux (Section 4.3) is most important. These data will be used to guide flare models that produce extremely high electron densities in Chapter 8, as decrements do not become increasingly flat at extremely high densities (Drake & Ulrich, 1980). In other words, the white-light formation mechanism must produce an electron density that is consistent with the observations.

In Figure 4.20, the Hδ and Hβ decrements are presented relative to Hγ at the time of maximum continuum emission. As in Figure 4.13, we plot against the Balmer continuum decrement, BaC3615/Hγ line flux. There are remarkably similar values of the Hδ decrement ($0.85-1$) over $\sim$2 orders of peak Hγ luminosity. We also show the Hδ decrements at peak line emission, to show they are often times different; in some cases, such as IF2, they are equal because the maximum continuum and maximum line emission occurred in the same spectrum (possibly not time-resolved). There is a trend of shallower Hδ decrement as the BaC3615 decrement becomes shallower. The Hδ decrements become flat ($\sim$1) at a BaC3615 decrement of $\sim$0.022. IF2 is one of the most impulsive (time-resolved) flares, and its decrements reverse.

The horizontal lines correspond to the RHD predictions from the impulsive phases of the F10 flare model (dotted line) and F11 flare model (dashed line). The predictions are in general agreement, producing a better match for the Hδ decrement than for the Hβ decrement. The decrements for IF0 (HP91) are shown as green and black open circles; as noted

by Allred et al. (2006), the RHD models are consistent with these data points. However, at higher values of BaC3615/Hγ, the F11 is closer to the observations for Hβ decrement (but not too good of a match) and the F10 model best matches the observed Hδ decrements. Therefore, the range of beam fluxes (F10 – F11) are not accurately constrained by the observations; more investigations with the models would be helpful to understand what flare conditions cause the decrements to approach 1 for larger values of BaC3615/Hγ. The BaC3615/Hγ ratio from models will be a measure that we will test against the observations in future work with RADYN (see Chapter 8).

4.6.3 A-Star Decrements

The decrements for a log $g \sim 4$ main sequence A star are steep, with Hδ : Hγ : Hβ : Hα = 1.10 : 1.0 : 0.72 : 0.22 using the spectrum of Vega from Bohlin (2007)[10]. Figure 4.21 demonstrates the formation of A-star decrements during IF1 (the Megaflare). In Section 4.5.4, we showed that this flare produced wing depressions during MDSF2. In this figure, we plot the Hδ, Hβ decrements. The Hδ decrement starts as ~ 0.9 and is generally decreasing whereas the Hβ is $\sim$ 1.3 and overall increasing, as expected if these lines were settling back to the quiescent state. The time-evolution of the BD has been suggested to flatten at flare maximum and steepen back toward the quiescent value after flare maximum (Katsova, 1990). Just following the peak of the secondary flare (MDSF2), the decrement drops to a minimum of $\sim$0.75 for Hδ and increases to a maximum of $\sim$1.5 for Hβ at $t \approx$2.18 hours. This is opposite to what is seen at the maxima of other flares (Figure 4.20), where decrements approach $\sim$1.0. We attribue this effect to A-star decrements forming during the flare: the absorption in an A-star is relatively stronger in the higher order lines. Thus, when flare absorption features with the A-star decrement add to the flat decrements already present in the flare decay, the observed decrements changes are explained. We also note that the most extreme "A-star decrements" occur at the minimum value of χ_{flare} (Figure 4.6, top), after the maximum U-band is reached.

We also examined the distribution in decrement against the luminosity in C4170, to

[10]Quiescent dMe emission decrements are also steep but in the opposite sense (e.g., flux in Hδ< flux in Hα).

test the hypothesis that more luminous (non-Balmer) continua would generate hot-star decrements, thereby causing the total decrement to decrease for Hδ and increase for Hβ. We found only a very slight trend in the opposite direction of increasing Hδ decrement and decreasing Hβ decrement as the C4170 luminosity increases, which is not what we would expect from hot-star decrements. With future RHD models we will address which combination of flare parameters (e.g., temperature, areal coverage) and heating processes give rise to A-star decrements (and absorption wings) in some flares but not in others.

4.6.4 Decrement Evolution of IF3

We study the detailed line decrement evolution for IF3, for which the detailed line and continuum evolution is shown in Figure 4.8. In the right panel, the absolute flux level evolution for the Hδ, Hγ, and Hα line during the impulsive phase of this flare is exhibited. In Figure 4.22, the decrements as a function of time are plotted. First, there is a ~ 5 minute duration gradual rise phase, from $t = 2.02 - 2.10$ hours. In quiescence H$\alpha \sim 5\times$Hγ, while in the early fast rise period the Hγ line produces an equal amount of flux compared to Hα. By the early-to-mid rise phase spectrum (S#27, $\sim$ 80sec into the fast rise of the line), Hγ exceeds the Hα flux and the largest departure from the quiescent decrement is produced. After the mid rise phase, there is a slowdown in the increase of Hγ (also for Hδ, generating the "S-shape" described in the Flare Atlas, Chapter 3), whereas the Hα line continues a steady ascent, until the Hα and Hγ fluxes become equal at peak line emission for both lines. The peak continuum times are indicated with vertical lines (S#31), with the Hγ and Hα decrements at this time ~ 1 (Figure 4.20). At peak line emission (S#33; ~ 1 minute after maximum continuum emission) the Hδ decrement has started decreasing towards the quiescent value. The Hγ evolution near the peak continuum emission is complex, but there is an apparent stalling of the line flux followed by a final jump in emission to the peak, consistent with the assumption in Section 4.5.4. The decrements are also quite complex during the fast decline. The Hα remains elevated near its peak value for three spectra and the initial fast decline is apparently faster, and then becomes slower, than the Hγ line. The Hγ eventually decreases much quicker whereas the Hα continues to stay elevated, leading

to the fast rise toward the quiescent decrement. In Figure 4.22 (left panel), note that the Hα and Hδ decrements are still far from the non-flaring values at $t = 3.4$ hours, since the line emission is still greatly enhanced.

The lines reach the maximum departure of the BD from its quiescent values during the early to mid rise phase of a time-resolved flare. We concentrate our analysis on this observation. The BD$\sim$ 1 is reached for Hδ and Hβ and BD$\sim$ 0.82 is reached for the Hα line by S#27. Hβ and Hα then undergo a fast decrement increase from mid rise phase to peak continuum phase while the Hδ decrement undergoes a decrease from S#29-31. Recall from Section 4.5.3, we found that the largest line broadening also occurred near the mid-rise phase (S#27; Figure 4.14), with a subsequent decrease to the flare maximum. Furthermore, suggestive evidence of wing absorption at maximum continuum was presented in Figure 4.19. In the rise phase of this extraordinary flare, we see a change from the typical BD$\sim$1 to a hot-star decrement as the widths decrease and hot star Balmer absorption forms by the time of peak continuum. More time resolved spectra during the impulsive phases and higher spectral resolution observations (so that BD(λ) over the line can be measured) would allow for a more rigorous understanding of the relation between wing absorption, hot-star decrements, and line broadening.

4.6.5 Decrement Evolution of Other Flares

We study the decrement evolution of a representative sample of flares in Figure 4.23. The Hγ flare-only emission is shown in grey for comparison. As in IF3, large BD departure is achieved very early in each flare, before the maximum continuum emission is reached. This maximum departure results in a very flat value of $\sim$1 for both the Hδ and Hβ decrement in all of these cases. Several key times have been indicated with a vertical line, and a BD of 1 is shown as a horizontal line. In the larger flares, it may take longer for the decrement to reach the preflare level, as can be seen by comparing IF9 and GF1 to HF1 and GF2. The return of the BD in all flares occurs gradually after the maximum departure is achieved, with a faster return for Hβ than for Hδ, also an effect that we saw for IF3 in Figure 4.22.

The decrements respond in varying degrees to the secondary events in these flares, which

may provide important insight to the spatial distribution of flares in complex events. For example, if we compare the flare at $t = 5.15$ hours in GF2 to IF2 we see the decrements respond very little in the former, although the line emission has substantially increased by the peak time. In contrast, the decrements and line flux respond strongly in IF2. Note also the lack of response to the main peak event in GF1, when most of the line emission is released.

We speculate why the decrements during complex events respond differently. The first possibility is that the gradual events that produce a small response in the decrement simply fail to produce high electron densities due to a diffuse and slow input of flare heating over a large area. For GF1, this would be consistent with a large amount of additional line emission that is produced. A second scenario that we envision is that the decrements respond to a secondary flare as a result of new regions being heated; the decrements that don't respond represent a particle bombardment of stellar surface area that has already been heated and therefore has become saturated so that extra heating goes into emission with an already flat decrement. Under a beam heating scenario, any additional particle bombardment would be stopped by the large densities and would only be able to heat the top of the chromosphere. Therefore, IF2 is a new flare region (distinct from the preceding flare, HF1) and the main peak of GF1 originates from an area that has already been impulsively heated, such as during the initial spike events at $t = 1.95$ hours. More observations and modeling of repeat bombardment of flare regions are required to determine if the decrement response can be used to spatially resolve flare regions as we have envisioned. Spatially resolved observations of the Balmer decrement in solar flares (e.g., Johns-Krull et al., 1997) would also provide useful insight into the different types of atmospheric response.

We are investigating these phenomena with the new generation of RADYN models, and we are in the process of obtaining solar flare spectra from 350nm - 450nm in order to study this behavior. The response of the chromospheric lines to flare heating in new and previously heated regions has been studied by Hawley & Fisher (1994). Kašparová et al. (2009) found that the intensity decrement (Hα/Hβ) does not respond in certain beam models using a periodic bombardment function; in particular the model using a low beam flux (F10) with a hard electron energy spectrum showed little response to the secondary flare heating pulses.

4.7 Broadening & Decrement Discussion and Summary

We find that wing depressions are indicative of hot-star (absorption) spectra forming during flares. This occurs during times of large continuum production in IF1, IF4, and possibly at the peak of IF3. We speculate that the chromospheric radiation may completely veil the wing absorption in other, smaller flares. There must be a threshold in a certain parameter (or combination of parameters) of the flare atmosphere at which absorption appears in the Balmer wings. We considered the ratio of Hγ to C4170 (Figure 3.13); this seemed promising for a value of $\sim 15 - 20$, but IF1 – the strongest case for the formation of absorption – has a large value of 40 due to the large amount of previously decaying emission present in the flare. We hypothesize that the threshold is a combination of filling factor and temperature of the source that produces emission in C4170 (Chapter 6). Determining this threshold would be invaluable to understanding the impulsive release of energy in flares; however, Balmer absorption is currently not produced in RHD models, except in the continuum dimming in the very early stages (< 0.1 sec) of flares (Abbett & Hawley, 1999).

We find that the evolution of the broadening is similar to the time evolution of the BaC3615, and we found suggestive evidence that during the time-resolved impulsive phases of IF3 and GF1, the maximum broadening occurs near the time of *maximum time-derivative of BaC3615* - during the rise phase, proceeding the maximum emission. For IF3, we connected the formation of wing depressions to the decrease in line widths, as was shown for IF4.

In addition to absorption features, electron density variations could cause the broadening and decrement changes that we observe. In fact, until the threshold heating for absorption is attained, electron density is likely the dominant factor for broadening and decrement variations in flares. Therefore, the influence on Hydrogen Balmer lines shifts from chromospheric parameters ($n_e, T_{\rm chrom}$) to photospheric parameters ($T_{\rm phot}$) as the threshold for absorption is reached. The filling factor of each component also determines the relative importance: a flare that has a large chromospheric network (e.g., ribbons) and a small amount of absorption kernels would have absorption features that are probably undetectable.

We now discuss the relation between decrements and line broadening, if Stark broad-

ening is the source of the observed trends. Both Stark broadening and the formation of Balmer continuum are dependent on the electron density, as both recombination and pressure broadening are collisional processes. In future work with our new RADYN models (see Chapter 8), we will investigate how they can be used to understand the relation between electron densities, broadening, and decrements in our flare sample. Here, we make a few preliminary predictions.

We are able to measure enhanced broadening in the wings of Hydrogen during flares, but due to the low spectral resolution, we cannot differentiate between mass motions, thermal broadening, and Stark pressure broadening contributions. The widths that we measure, 15 – 50Å, are much higher than measured previously, $\sim$ 15Å at 0.1 maximum (Allred et al., 2006); we attributed this to larger Balmer decrements occurring during some of the flares in this sample.

The Inglis-Teller relation (Kurochka & Maslennikova, 1970) relates the last member of the Hydrogen series that is resolved to the electron density that induces the Stark broadening. HP91 used this technique to deduce $n_e \sim 3 \times 10^{13}$ cm^{-3} in the Great Flare on AD Leo, whereas Worden et al. (1984) used the FWHM change in flares to deduce $n_e \sim 3 - 4 \times 10^{13}$ cm^{-3} in flares on YZ CMi, and Paulson et al. (2006) use the Inglis-Teller and RHD models to constrain the n_e to $n_e \sim 1.3 - 15 \times 10^{13}$ cm^{-3} in a flare on Barnard's Star.

According to the formula for linear Stark broadening (Sutton, 1978, see also Johns-Krull et al. (1997)), the amount of line broadening (in Å) is proportional to

$$\Delta\lambda \propto \frac{(n_u \times n_l)^4}{n_u^2 - n_l^2} \times n_e^{2/3} \tag{4.1}$$

This formula predicts that the Hδ broadening is 1.36 times the broadening in Hγ if they originate from regions with the same electron density. In future work with dynamic and static modeling, we will investigate the Stark effect in flares while considering the contribution function of the wings.

The highest order Balmer line observed in flares is H16 (HP91) in low-resolution time-resolved spectra and H13 (Paulson et al., 2006) and H19 (Fuhrmeister et al., 2011) in high spectral resolution, low time-resolution spectra. The highest Balmer line that is at least partially resolved in our data is typically H14 (H15 and H16 are possibly present,

but they are highly blended with a Helium I line). Assuming that H16 is the last line in the spectrum, the Inglis-Teller relation predicts that the H16 line experiences nearly $9x$ the broadening as the Hγ line; this is nearly 300Å width at 0.1 flux level! It is not known if (and how) the wings of these high order Balmer lines influence the emission at $\lambda < 3646$Å. Then, one must ask if the extreme high order lines contribute to the measured BaC3615, *what, precisely, is Balmer continuum?* The energy levels of the highest orders are significantly perturbed by the inferred electric fields, forming a continuum of emission that may be indistinguishable from recombination radiation from electrons which recombine with energies near the recombination energy edge. The Stark broadening of the Balmer edge has been considered for solar flares by Donati-Falchi et al. (1985).

Changes of the BD to non-flat values during flares are consistent with the presence of hot-star spectra absorption decrements that are veiled by the emission flux. These produce BD$\sim$ 1.5 and BD$\sim$ 0.7 in Hβ and Hδ respectively. During most other flares, a BD$\sim$1 is produced early in the impulsive phase of the flare.

We examined the broadening and decrements of IF3 in detail. The maximum decrement departure, the maximum line broadening, and the maximum time derivative of the BaC3615 light curve occur around the mid rise phase. Perhaps the optical thickness of the BaC is also increasing during the rise phase and the fast timescale to saturation is why we always see it match the RHD model spectrum (see Chapter 5). We note that the BaC3615 decrement evolution is similar to the Hδ decrement evolution, with a peak at S#28. Although the flare may have spatial evolution and therefore the radiation we see may come from a variety of atmospheric conditions with different beam fluxes, our observations are likely biased to the flare areas that are heated by the highest beam strengths. We will investigate 1.5D RHD models of flares in a future work.

Increasing electron densities provide a natural tie between the decrements, broadening, and time-derivative of the BaC3615 light curve. First, the BaC3615 flux is dependent on n_e^2. The linear Stark effect is dependent on $n_e^{2/3}$. Therefore, higher electron densities cause larger BaC flux and more blending of the higher order lines, whose wide wings may contribute to the BaC flux that we observe.

Drake & Ulrich (1980) connected the Stark broadening with decrement changes, which

we elaborate upon here. The increase in electron density in the chromosphere and the larger optical thickness of Hα leads to more energy being able to escape in higher order, more optically thin, Balmer transitions. The increased collisions from a larger density of electrons generate larger amounts of Hα radiation via collisional excitation and radiative de-excitation. Depending on the temperature of the plasma and energy distribution of the electrons, collisions also excite neutral Hydrogen atoms in $n = 2$ to higher energy levels, giving rise to Hγ, Hδ and higher order lines. Since Hα (and Lyα) are already very optically thick, those photons quickly photoionize electrons in $n > 2$ levels, which are then able to recombine to higher levels and cascade down to the $n = 2$ state giving enhanced emission in the $n \geq 4$ to $n = 2$ (Balmer) lines. The high n_e can also increases recombination to higher levels followed by a cascade. In this first scenario, energy is preferentially lost through the higher order lines because the lower order lines are more optically thick. In addition, energy is preferentially lost through the higher order lines because of enhanced Stark broadening in these transitions. In particular, the increased electron densities in the atmosphere generate a larger broadening in the higher order lines. This broadening leads to increased escape probabilities for photons, which can leak out through the wider wings at greater depth of the atmosphere. Since Hα has a smaller amount of Stark broadening, the photons can escape only near line center, which is very thick. The Hα photons are therefore produced only at the top of the flare chromosphere.

Finally, we must not dismiss directed mass motions or turbulence with velocities of hundreds of km s^{-1} as a possible source of broadening that we see during flares. These velocities are easily produced in RADYN models with low beam strengths (Allred et al., 2006), and gas dynamic simulations predict chromospheric condensations with velocities of $\sim$100 km s^{-1} (Livshits et al., 1981). Recently, Fuhrmeister et al. (2011) did not find evidence of Stark broadening in the higher order lines of high spectral resolution data during a moderate flare on Proxima Centauri. Eason et al. (1992) and Doyle et al. (1988) did not find satisfactory fits with Stark broadening profiles to their flare data for Hα and Hδ, respectively. High-cadence data with higher spectral resolution is necessary for understanding the origin of the Balmer line broadening during flares.

4.8 Individual Line Properties

In this section, we discuss a Neupert-like relation for Ca II K, and we show the Hα data for the flare sample. Appendix D.4 contains our analysis of Helium I emission, Appendix D.3 contains our analysis of Mg I / Fe II.

4.8.1 Ca II

The Ca II K line constitutes the *cool* component contributing about 15% of the flare energy contained in the *warm* component (Table 4.1). The Ca II K is the most gradual line in the intermediate and blue-optical wavelength zones (see Section 3.1.2). There is typically a fast rise and a slow rise period (e.g., blue points in Figure 4.8). The Ca II K line has the largest $t_{1/2}$ and peaks latest in the flare. Often at the peak of Ca II K, there is a low-level "hump" in the Hydrogen Balmer line light curve (e.g., at $t = 2.7$ hours in Figure 4.8).

We examine the Ca II K line evolution during the decay phase of IF1 (the megaflare) in Figure 4.24. The decrement evolution in Figure 4.21 shows substructure, but in Figure 4.24, the gradual nature is evident, and the substructure in the decrement is seen to be due to the relatively rapid flux changes in the Balmer line. Ca II K was emitting between 10 and 20 times the quiescent level, and the total energy during the decay was 53% of the Hγ energy. In contrast, during other flares, the Ca II K energy is about 25% the Hγ energy. Despite the limited timing window of the spectral observations, the evolution of the Ca II K line is obviously gradual, peaking at ~ 1.75 hours and decaying to 80% of that peak by the end of the spectral observations. The flux of the Ca II λ8542 line is about 42% the Ca II K flux, and the evolution is quite similar but slightly more gradual than Ca II K. Their light curves are shown in Figure 4.24, with the λ8542 line scaled to the peak of Ca II K. At the peak of the Ca II K line at $t = 1.7$ hours, the flux in the IR triplet is approximately 1.02 times the flux in the K line; the ratio among the four Ca II lines is $1 : 0.3 : 0.42 : 0.3$ in the order of the bluest (Ca II K) to reddest. Ca II H is blended with Hϵ in our low-resolution spectra and therefore not considered.

The energy budget of Ca II K in IF1 is consistent with gradual phase emission. We cannot determine whether the peak at 1.7 hours is the peak from the primary flare event

or whether it is associated with another flare event. Comparing to IF3, the second largest amplitude event in the sample, the peak Ca II K flux and the total energy (within the spectral observations) are 6.5 times greater in IF1 than in IF3. The U-band flux values at the peak Ca II K fluxes are 25 and 7 for IF1 and IF3, respectively. However, the *integrated* energy of the U-band, integrated to the approximate time of peak flux of Ca II K, is 7.5 times that in IF3, which is very close to the ratio of 6.5 for the peak flux ratio of Ca II K. In summary, if the peak in the spectral observations of the IF1 event is the bona-fide peak of Ca II K for the entire event, the integrated energy in the U-band divided by the peak flux of Ca II K is similar to that same ratio in IF3. In Figure 4.24, we show the cumulative distribution of the U-band compared to Ca II K (black dashed line). We will explore this Neupert relation in Section 4.8.2.

For IF3, the Ca II K has a gradual rise in the first part of the flare, and an apparent fast rise to 0.5 maximum emission from S#28 to S#32, then beginning a gradual rise to its maximum emission (see blue points in Figure 4.8). The peak of Ca II K is very broad (like the broad Hγ peak in GF1) and occurs about 30 minutes after the continuum peak. The Ca II K flux also appears to have substructure but it is unclear how accurately we are able to measure the fine details of this line considering the blending of the extreme wings of the nearby Hydrogen lines. The Ca II K and Ca II λ8542 line share similar peak times and a dual component rise phase in this flare. However, Ca II 8542 has a longer fast rise phase (ending at S#35, whereas the Ca II K line fast rise ends at S#32). Ca II K has the largest jump at the maximum continuum, whereas Ca II 8542 stalls. At maximum, the Ca II 8542 flux is 0.67 the flux of Ca II K, and the Ca II K has faster decline phase like what is seen in the megaflare (IF1, below). However, in the megaflare decay, the ratio of Ca II 8542/Ca II K is significantly lower, 0.42. Comparing the maximum fluxes in the Ca II K and Ca II 8542 between IF1 and IF3, both of which are sampled in the far gradual phase: the ratio of Ca II K line fluxes is 6.5, whereas the ratio of Ca II 8542 line fluxes is 4.3; IF1 has relatively more Ca II K during the time it was sampled.

In GF1 (Figure 4.11), the peak in Ca II K at approximately the same time as the break in the C4170 precedes from fast to slow decline phases ($t = 2.25$ hours). We draw attention to the rolling "hump", conspicuous in the emission lines, particularly, Ca II K, Hα and Hγ

in both flares IF3 and GF1, and strongly evident also in the He I lines in IF3. This hump occurs during the decay phase at $t = 2.6-2.8$ hours in GF1 compared to IF3. Coincidentally, this hump occurs at ~ 0.6 hours after the peak in both flares, and is slightly evident in the u-band and g-band photometry for IF3 (and hard to tell in GF1). It is much more the case in this flare compared to IF3 that the Ca II K resembles the Hα line morphological characteristics, however, the Hα has a faster rise phase and a more predominant first peak.

In IF9 (Figure 4.9), there is a slow "hump" in the line emission at $\sim$0.4 hours after the peak in the line emission, which is a common feature to the other two flares discussed above. The Ca II K evolution in this flare is similar to the the larger classical flare, IF3: at peak continuum, it is low (~ 0.5 relative to maximum, like in IF3) relative to the maximum emission that occurs ~ 14 minutes after the maximum continuum. This line may have a short fast rise component like for IF3 but the evolution is mostly gradual. This flare has a factor of two shorter "time-decrement" in the Balmer lines and also a factor of two shorter time delay in the Ca II K line.

The Ca II K line is extremely interesting in HF2 (Figure 4.10). Like GF1, the fast rise phase is not as evident as in the IF flares, and ends by rounding off to a peak at precisely the time when the impulsive phase of the continuum (and PseudoC) ends. The Ca II K line flux stays at the peak level for approximately 0.2 hours before beginning a slow descent. Hα and Ca II K both reach 0.5$\times$peak value at the end of the spectral observations. We calculate the time integral of the C4170 and show it as a grey dashed line in Figure 4.10. The growth of the integral of the blue continuum is approximately proportional to the instantaneous line flux of Ca II K during the rise phase of Ca II K. This effect has already been shown for IF1, and now we discuss evidence for it during the other flares in the following section.

4.8.2 A Neupert-like relation between Ca II K and C4170

In Figure 4.25 - 4.26, we show the flux of Ca II K (blue diamonds), the flux of C4170 (crosses) and the cumulative integral of C4170 (red lines). We calculate the cumulative integral up to the time of Ca II K maximum, which in some cases occurs at the end of the impulsive phase (HF1, HF2, GF1) and in some cases occurs deep into the gradual phase

(IF3, IF9, GF2). There is a varying degree of match between the Ca II K line and the integral of the continuum, with typically a much closer match in the HF and GF flares than in the IF flares. Note that in HF2, if the Ca II K preflare line flux is subtracted, there is a much closer match to the continuum integral. In some flares, especially IF3, HF1, and IF4, the Ca II K line evolution is ambiguous during the first part of the impulsive phase, having a potential delay. In other cases, e.g., IF9 and IF5, the Ca II K *decreases* relative to the previous spectrum at maximum C4170.

The formation and time-evolution of the Ca II K line has long been a mystery, including why it responds slowly in flares and peaks after the Balmer lines. It has been associated with formation in the lower chromosphere in RHD models (Abbett & Hawley, 1999; Allred et al., 2006), implying deep heating of the atmosphere, and also been suggested as coming from a hotter, higher region of the flaring chromosphere (Schmidt et al., 2012). The timing has suggested a scenario in which hot flare loops cool down in the late phase to the temperature of Ca II K formation of about 6000 K, but this remains inconclusive. In solar flares, million degree low-lying loops form late in the gradual phase, as seen in e.g., AIA 171Å and perhaps these are an example of low-lying loops which also excite the Ca II K line (in situ in hot loops or through backwarming).

The Neupert relation (Neupert, 1968) is an observed relation between the signatures of impulsive phase nonthermal particles and gradual phase coronal heating. The Neupert relation has been observed in solar (Dennis & Zarro, 1993) and stellar (Hawley et al., 1995; Guedel et al., 1996; Osten et al., 2004; Fuhrmeister et al., 2011) flares, and is a fundamental aspect of the standard flare model. It is usually interpreted in terms of the chromospheric evaporation process (Fisher et al., 1985), whereby the nonthermal particles impact the chromosphere, which then ablates into the corona and emits at millions of degrees well into the gradual phase of emission associated with nonthermal particles. The Neupert relation is usually reported as the proportionality between the integral of impulsive phase emission (e.g., microwave, hard X-ray, or white-light emission) and the instantaneous luminosity of coronal plasma (soft X-rays). If the Neupert relation is behind the behavior presented here, then the gradual evolution of Ca II K is related to the chromospheric evaporation process. Under this interpretation, regions of the chromosphere (perhaps even in distant

regions away from the main flare loops) are heated to ∼6000 K from, e.g.,, incident XEUV backwarming radiation originating from ten million degree coronal plasma. A connection between the fastest component, the C4170, and the slowest component, Ca II K provides important constraints for RHD models that seek to produce a consistent picture of the flare process whereby the C4170 can be incorporated into the standard model (e.g., Martens & Kuin, 1989).

The degree by which the Ca II K Neupert relation holds between impulsive, hybrid, and gradual flares may lend important insight into how the flare mechanism differs among these flare types. Osten et al. (2005) found an apparent violation of the Neupert effect from soft X-ray diagnostics during a U-band flare, suggesting that the relation may break down in some heating scenarios. Several possible explanations were given for this violation in Osten et al. (2005) (see also Doyle et al. (1988)). We note that this flare had an impulsive morphology, which is consistent with our finding that the relation generally holds better for gradual flares. Delayed rise phases in Ca II K are also consistent with a causal relation with C4170. The Neupert effect in Ca II K during very impulsive flares should be investigated with higher time resolution spectra.

There may be a connection between the gradual phase BD evolution and the gradual rise component in Ca II K evolution, such as in IF3. In this flare and in IF9, the Ca II K flux gradually increases to maximum and the BD gradually returns to quiescent values starting during or at the end of the impulsive phase of the C4170 continuum. If the Ca II K ascent is caused by non-local heating from the corona, then perhaps the gradual return of the decrement is also influenced by incident coronal radiation from superheated (∼10 MK) coronal plasma. The connection between *quiescent* X-ray luminosity and non-flaring decrement has been established by Katsova (1990), with dMe stars with larger L_X having a flatter quiescent decrement. Hawley & Fisher (1992) successfully reproduced the BD in the Great Flare with a X-ray heating flux of $\sim 2 - 4.5 \times 10^8$ ergs cm^{-2} s^{-1} from a coronal source having apex temperatures of $8-10$ MK; however, Ca II K emission was overproduced compared to the Hγ line flux.

We are seeking to understand the formation of Ca II K with the RADYN models that include a gradual phase (Chapter 8). Hawley & Fisher (1992) suggested that a corona with

$T > 20$MK or heating from nonthermal particles would help model the Ca II K line flux more accurately. We are investigating the physical processes of XEUV backwarming, coronal overpressures, chromospheric condensations, coronal heat conduction, and prolonged nonthermal particle heating. These processes have been investigated for chromospheric emission processes during solar flares in Hα (e.g., Canfield et al., 1984). 1D solar flare models have shown that condensations are important in generating Ca II K emission in the lower chromosphere (Abbett & Hawley, 1999).

4.8.3 Hα

Hα is the most important Balmer line energetically. Most recently, this line has been investigated at moderate time resolution ($\geq$ 90 seconds) with high spectral resolution (R= 45 000) by Fuhrmeister et al. (2011). Eason et al. (1992) studied high-spectral resolution (R$\sim$ 41 000) data of Hα during a large flare, but the cadence was $\sim$6 minutes. Crespo-Chacón et al. (2006) studied flares on AD Leo using $R \sim 6000$ spectra on timescales of seconds to minutes with coverage of the entire Balmer series; Hα was included in the red data but was obtained with a different cadence. Most previous high time resolution spectra of dMe flares did not include Hα, while optical flare data of the Sun has been taken in Hα (e.g., Canfield et al., 1993; Leka et al., 1993; de La Beaujardiere et al., 1993). Therefore, the Hα light curves for our sample can be used to test the solar-stellar connection.

We see a significant response in all of the flares in our sample that have red data. In Figure 4.28 – 4.29, we plot the Hγ and Hα light curves for twelve flares with Hα data. The large amplitude flares in the figures show the same trend: a reverse decrement for the majority of the impulsive phase with Hγ line flux exceeding Hα line flux (BD$\sim$ 0.8), while at the end of the impulsive phase the Hα and Hγ light curves cross over so that Hα flux exceeds the Hγ flux for the duration of the flare[11]. Whereas both lines have an explosive rise phase, they differ most strikingly in their fast and extended decay phases whereby Hγ has a well-defined fast decay after the peak spectrum and Hα remains at maximum emission level over the course of several spectra (see e.g., IF2, IF3, IF5, IF9) followed by a

[11]For HF1 and GF1, the reverse decrement is seen during the entire long rise phase of the line and they have equal fluxes near the beginning of the first descent period before the end of the impulsive phase.

slower decay. The general trends in their time evolution were shown in Figure 4.12, with $t_{1/2,H\alpha} \sim 2.5 \times t_{1/2,H\gamma}$. Overall, the difference in the line evolution can be attributed to Hγ's larger variance in emission levels between different stages (initial rise or the quick jump to reverse decrement in the beginning of the flare such as in IF9 and IF3 and the faster decay after the peak is reached). Even in the largest flares, we do not find a delay in the time to reach maximum, within our time resolution, except possibly in GF1. Oftentimes, the preflare of Hα is highly elevated due to slowly decaying emission from a previous flare; the preflare must be subtracted from the peak to compare absolute emission levels.

The smaller GF flares do not show the pronounced reverse decrement but instead produce more Hα emission at the peak. We are investigating the threshold conditions (possibly, n_e) at which the reverse decrement occurs.

The cause of the Hα line's prolonged decay is not well-understood in dMe flares. Figure 4.12 shows that Hα is connected with the higher order lines through the "time-decrement". Apparently, because the line has a significantly lower energy than the other Balmer lines, it has a proportionally different timescale. This effect possibly originates from late phase coronal pressure, coronal conduction, or direct particle heating (as outlined in Canfield et al., 1993). The larger optical thickness – and therefore decreased sensitivity to electron density in the chromosphere – may preferentially sustain this line over higher order Balmer lines (Drake & Ulrich, 1980, see also discussion in Section 4.4). We are investigating the response of Hα to local beam heating and nonlocal coronal conditions, as done in Hawley & Fisher (1994) and Kašparová et al. (2009) for solar flares.

4.9 Low-Level Fe and Ti Lines in the Megaflare Spectra

We analyze the low-level features in the blue optical spectrum of the decay phase of IF1. The high signal to noise blue-optical IF1 decay spectra are shown in Figure 4.30. The black spectrum is S#102 (before the MDSF2 rise) and the medium-shade grey is the peak of the MDSF2 (S#113). The dotted spectrum is the quiescent. Many "features" are visible in the continuum; there are likely blends of Fe I, Fe II, Ti I, and Ti II lines that are in sustained emission in the late phase. These lines are typically observed only during the impulsive phase of smaller flares (Paulson et al., 2006). We compare the wavelengths of

these features to the low-flux level line identifications from the flare echelle observations of stellar flares from Paulson et al. (2006) and Fuhrmeister et al. (2011). We find good matches to many of the features, and we have overplotted several of the more conspicuous ones. We calculate the flux budget of these low-level lines relative to the flux in $\lambda = 4000 - 4800$Å. To model the underlying continuum, a Planck function is fit to the overall trend to the continuum (light blue), however the fit (determined in Chapter 6) is not representative of the underlying continuum in the troughs between the small metal lines. We find that scaling the Planck fit by ∼94% better matches the continuum between the low-level features. The wavelength-integrated (λ =4000 – 4800Å) flux in the Planck function is 72.6% of the total flux from λ =4000 – 4800Å. The Hγ flux is 10.3% and the Hδ is 8.75%. The two major Helium lines, λ4026 (+ Mn I) and λ4471 are included and total 1.5%. Thus, $\sim$ 7% of the total 4000 – 4800Å flux presumably belongs to the low-level features seen superposed on the Planck continuum fit. This is an important fraction of energy. Therefore, at least in the gradual phase of an extraordinarily powerful flare, 10% ($\approx 0.07/0.726$) of the bona-fide white-light continuum is made up low-level metallic emission lines. Using the fluxes from the flare on Proxima Centauri from Fuhrmeister et al. (2011), we estimate that the flare flux from one hundred Fe I, Fe II, Ti I, and Ti II lines in the blue-optical (λ =4000 – 4800Å) constitutes 30% of the flux in Hδ. This is lower than what the calculation for IF1 gives (see above, 7% in the metals compared to 8.75% in Hδ implies the metals are 80% relative to Hδ). In NUV ($\lambda = 2000 - 2850$Å) flare data of YZ CMi, Hawley et al. (2007) found that the total flux in seventy-eight Fe II lines was equal to the flare flux in Mg II h and k. See Appendix D.3 for a discussion of the time-resolved properties of Fe II emission in our flare sample.

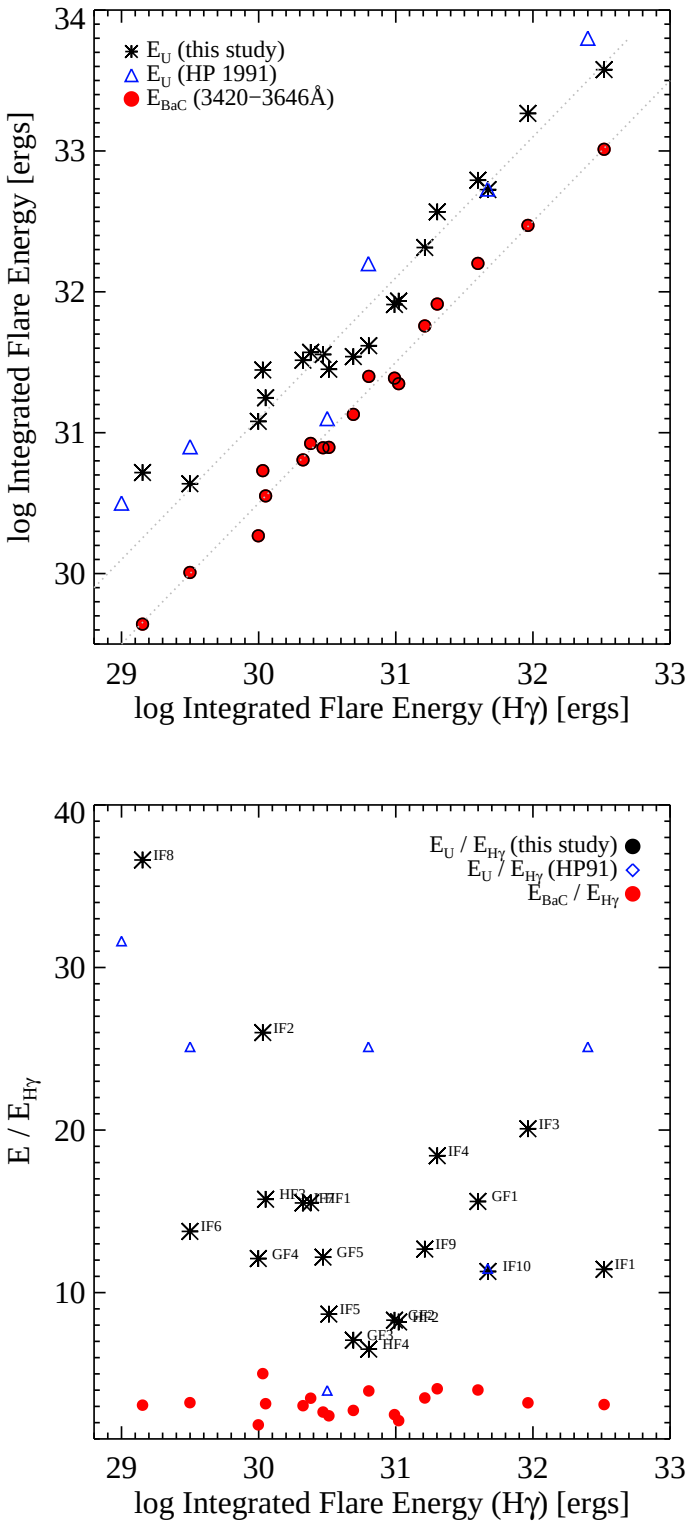

Figure 4.1 (Top panel) Total energy in U band vs total energy in Hγ. The dotted lines are shown to indicate the median ratios of the sample, $E_u/E_{H\gamma} = 12.7$ and $E_{\rm BaC}/E_{H\gamma} = 3.1$, and therefore show equal percentage increase in both quantities. The scatter is best visualized by the bottom panel which is the ratio of the energies. The triangles represent the flares studied by Kahler et al. (1982), Rodono' et al. (1989), Doyle et al. (1988), Phillips et al. (1988), and Hawley & Pettersen (1991).

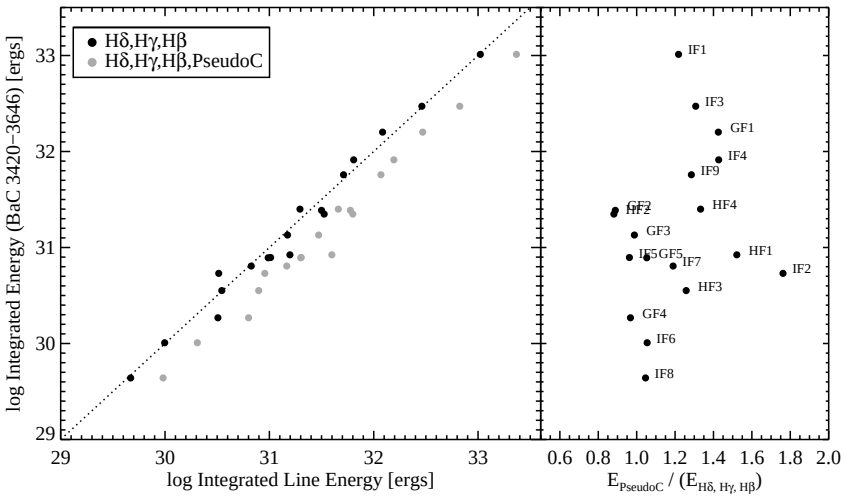

Figure 4.2 (Left panel) The energies in the Hydrogen lines indicated and in the PseudoC within the intermediate zone are compared to the BaC energy. (Right panel) Ratio of the PseudoC energy to the sum of the three blue-optical hydrogen lines.

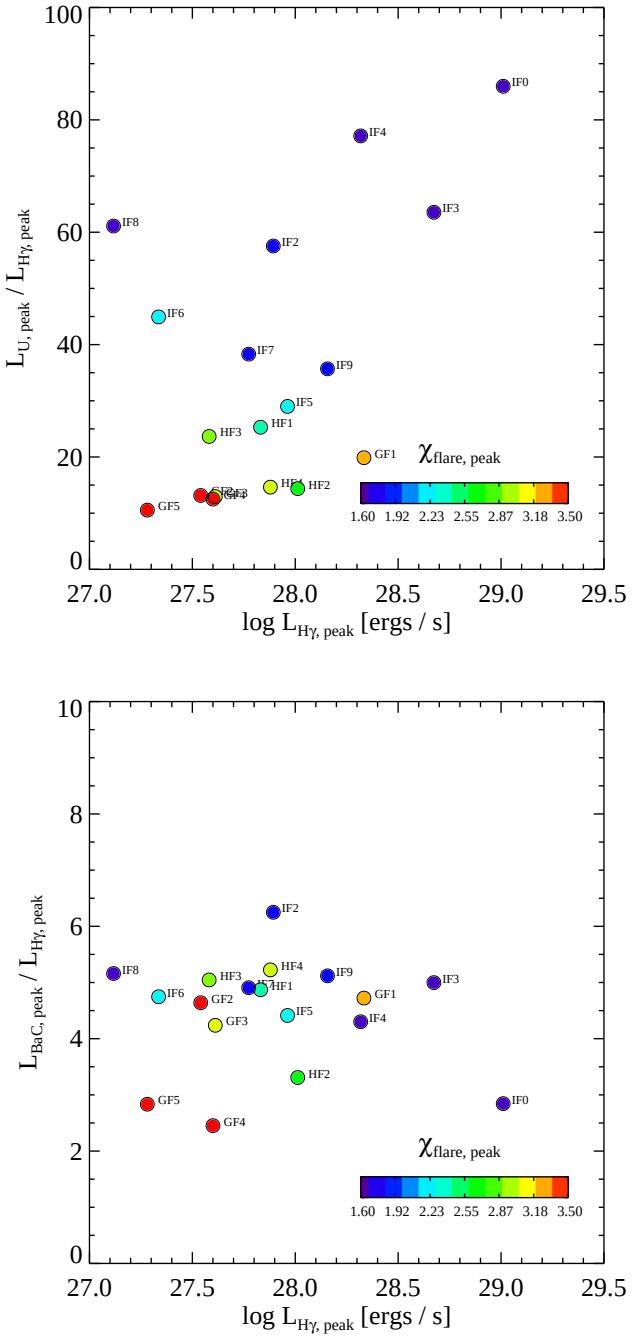

Figure 4.3 (Top) Peak luminosity in U band divided by the peak luminosity in Hγ; plotted against the luminosity in Hγ. The points are color-coded by the $\chi_{flare,peak}$ (colorbar). There are two distributions, one for the impulsive flares (larger $\chi_{\rm flare}$) and one for gradual flares (smaller $\chi_{\rm flare}$). (Bottom) The ratio of peak BaC luminosity to peak Hγ luminosity is more uniform among the sample.

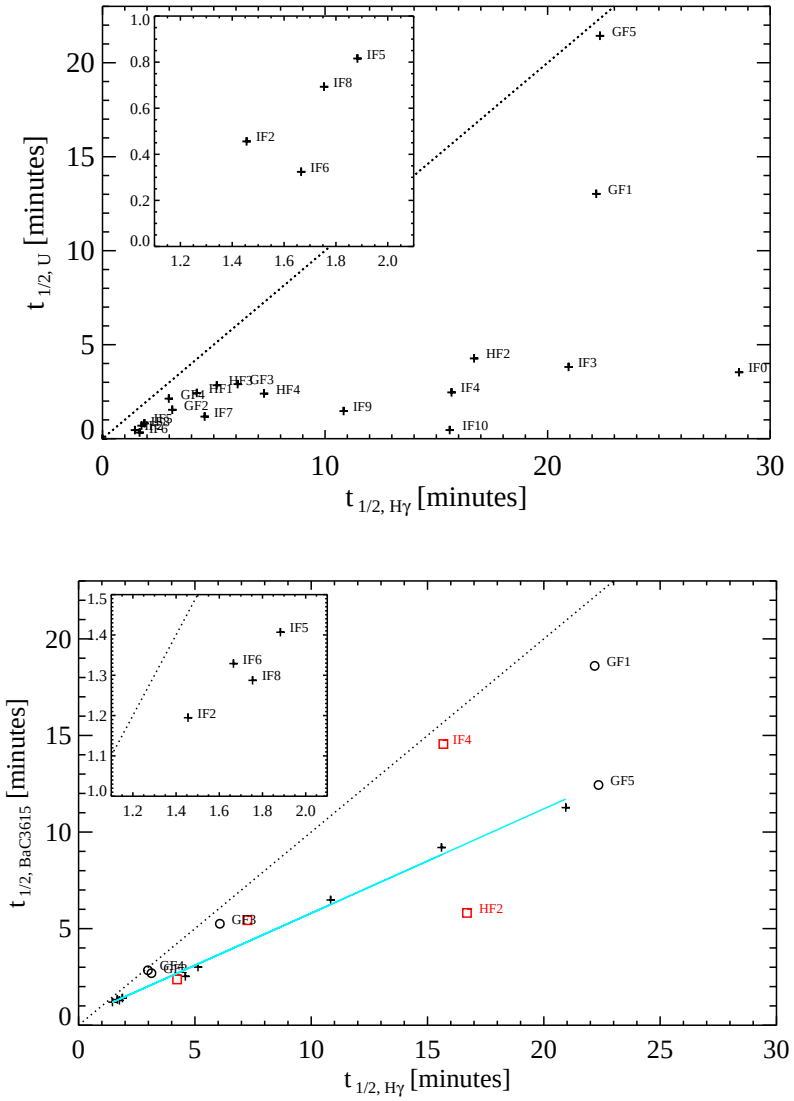

Figure 4.4 (Top Panel) $t_{1/2}$ for U-band and Hγ with 1:1 line shown as dotted. (Bottom) The $t_{1/2}$ values of the BaC3615 versus the values of the Hγ line. The insets in both panels have the same axes, showing the flares with the smallest values of $t_{1/2}$. The red squares represent impulsive flares with multiple peaks, the crosses are flares with single peaks, and the open circles are gradual flares. The light blue line is a fit to the flares with single peaks.

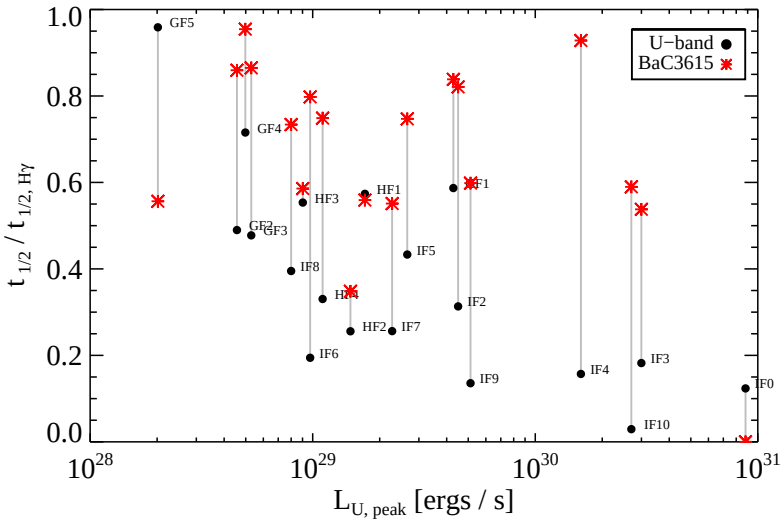

Figure 4.5 The ratio of $t_{1/2}$ to $t_{1/2,H\gamma}$ for the U band and BaC3615 versus $L_{\mathrm{U,peak}}$. Grey lines connect the points that correspond to the same flare. In order to determine if the larger ratio corresponds to smaller Hγ or larger U band, the reader must consult Figure 4.4. For example, the $t_{1/2,U}$ for IF8 is twice as large as for IF6 yet the $t_{1/2,H\gamma}$ values are the same.

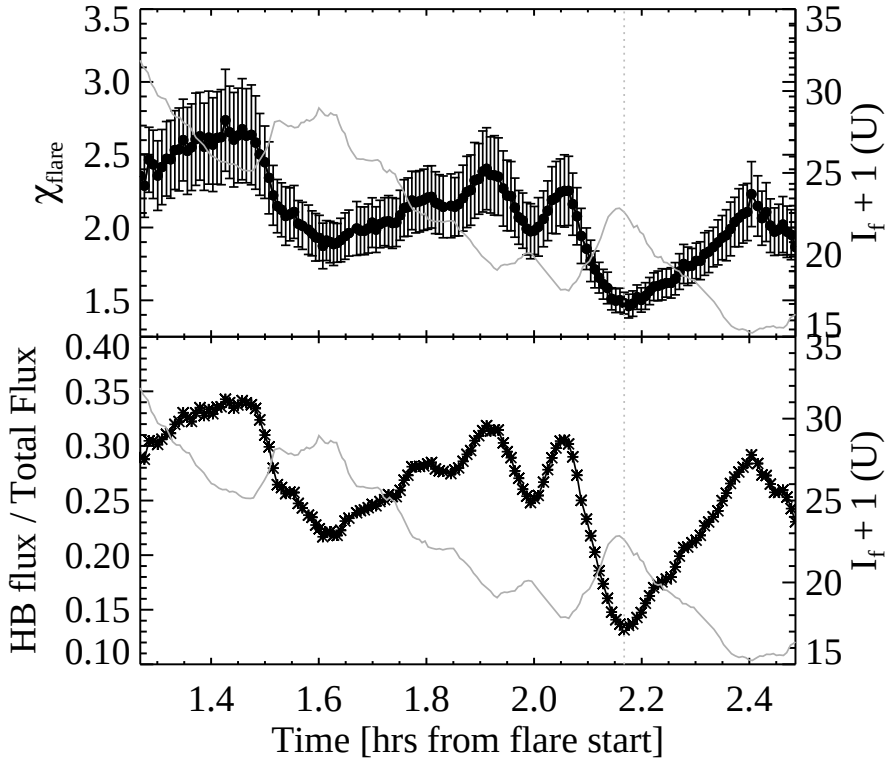

Figure 4.6 (Top Panel) The $\chi_{\rm flare}$ as a function time (black circles); the U-band evolution is shown in grey. (Bottom Panel) The time-evolution of the ratio of HB flux to total flux (dark asterisks). The ratio varies significantly and is anti-correlated with the U-band, strikingly similar to the evolution of $\chi_{\rm flare}$. The vertical line in both panels denotes the time of minimum HB flux ratio (at S#116), which occurs just before the minimum $\chi_{\rm flare}$ and just after the maximum U-band enhancement. The secondary flare, MDSF2, begins at $t = 2.072$ hours and peaks in the U band near $t = 2.15$ hours.

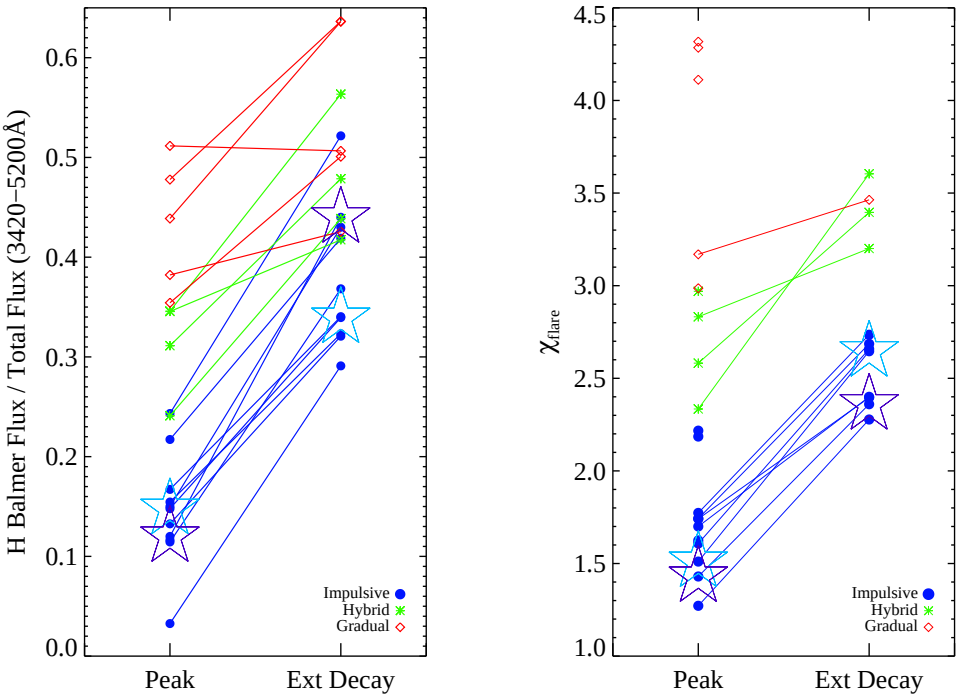

Figure 4.7 (Left panel) The relative contribution from the Hydrogen Balmer component during the peak and gradual phases. Light blue stars show the decay phase (S#23-25) and secondary flare (S#103) values for IF1; purple stars are the peak of the secondary spike ($t = 1038$s, S#40) and the beginning gradual phase for the Great Flare. (Right panel) The evolution of $\chi_{\rm flare}$ from peak to gradual phases, calculated at the same times as in the panel to the left. The $\chi_{\rm flare,decay}$ values are not included if they have >20% errors (due to very low levels of emission in the decay phase). This cut excludes IF5, IF6, GF3, IF8, GF5, GF4, and GF2.

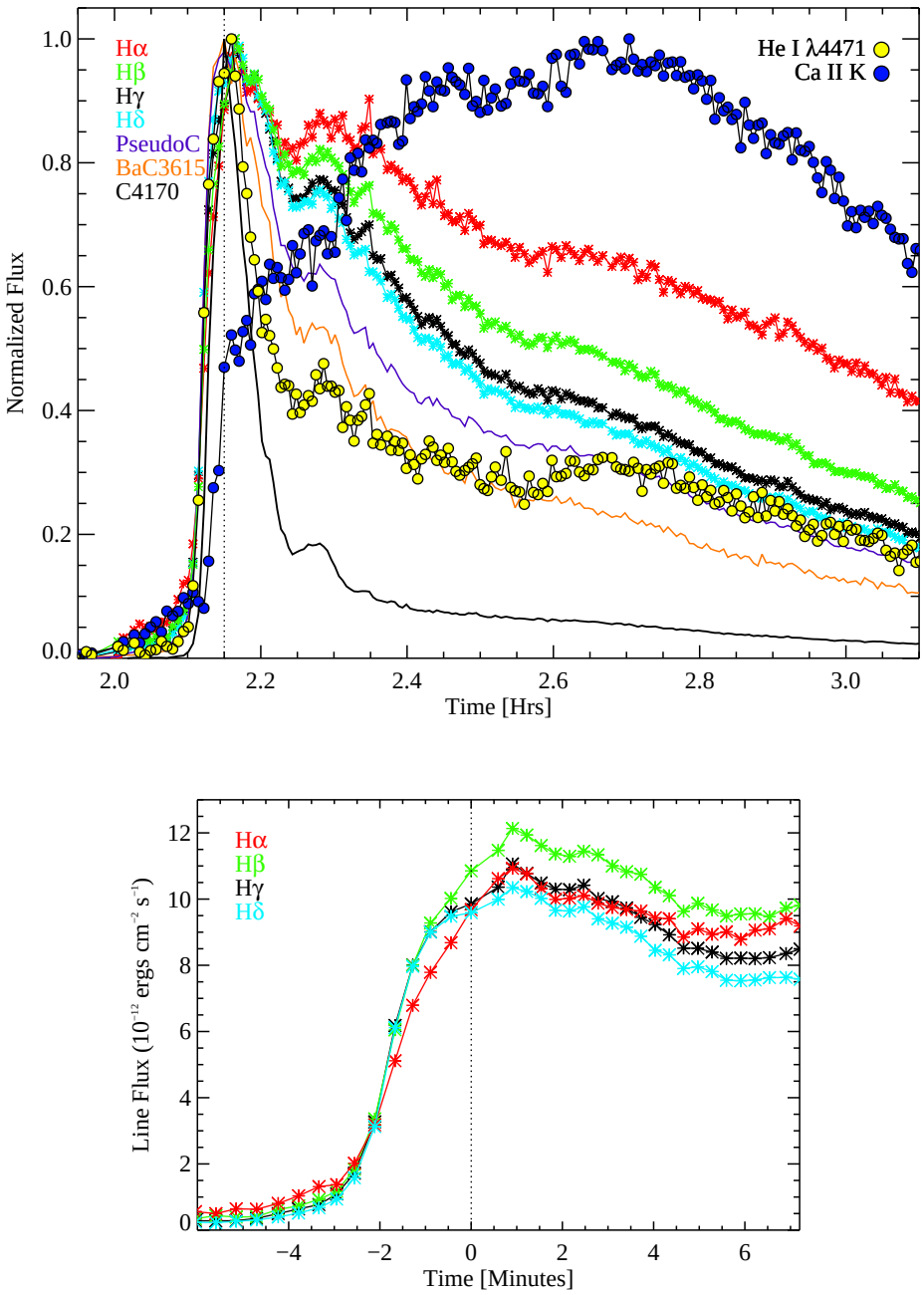

Figure 4.8 (Top) Line and continuum evolution for IF3. The C4170, BaC3615, PseudoC, Hα, Hβ, Hγ, Hδ, Ca II K, and He Iλ4471 are plotted according to their fluxes normalized to the peak flux (left axis). The vertical dotted line corresponds to peak continuum (S#31). (Bottom) Zoom of the rise phase, peak, and initial decay of IF3 for the Hα, Hβ, Hγ, and Hδ line fluxes. Note the "S"-shape in the rise phase morphology of Hβ, Hγ and Hδ. All four lines reach maximum in the same spectrum. Note, that the Hβ, Hγ and Hδ lines diverge from a common flare flux at S#29.

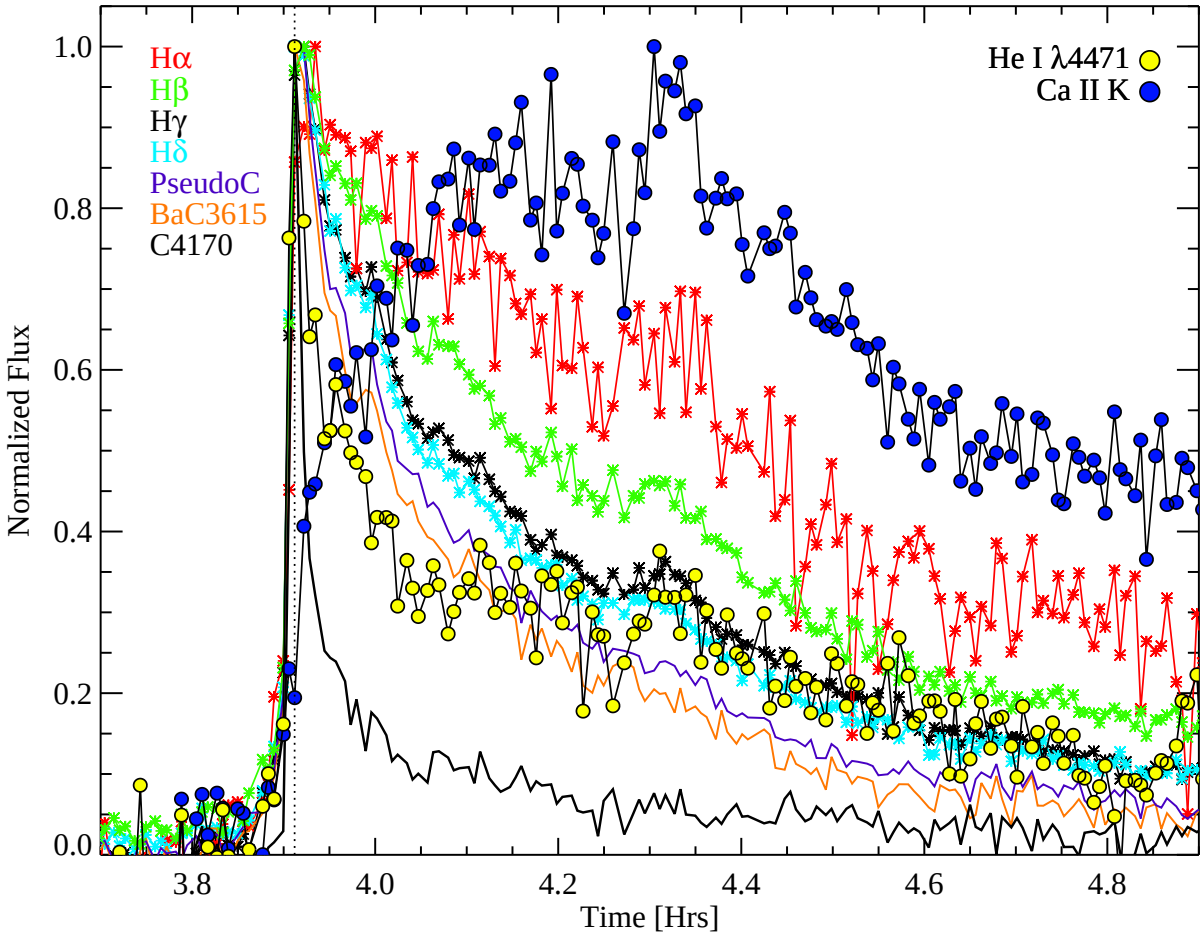

Figure 4.9 Line and continuum evolution for IF9. Symbols same as in Figure 4.8.

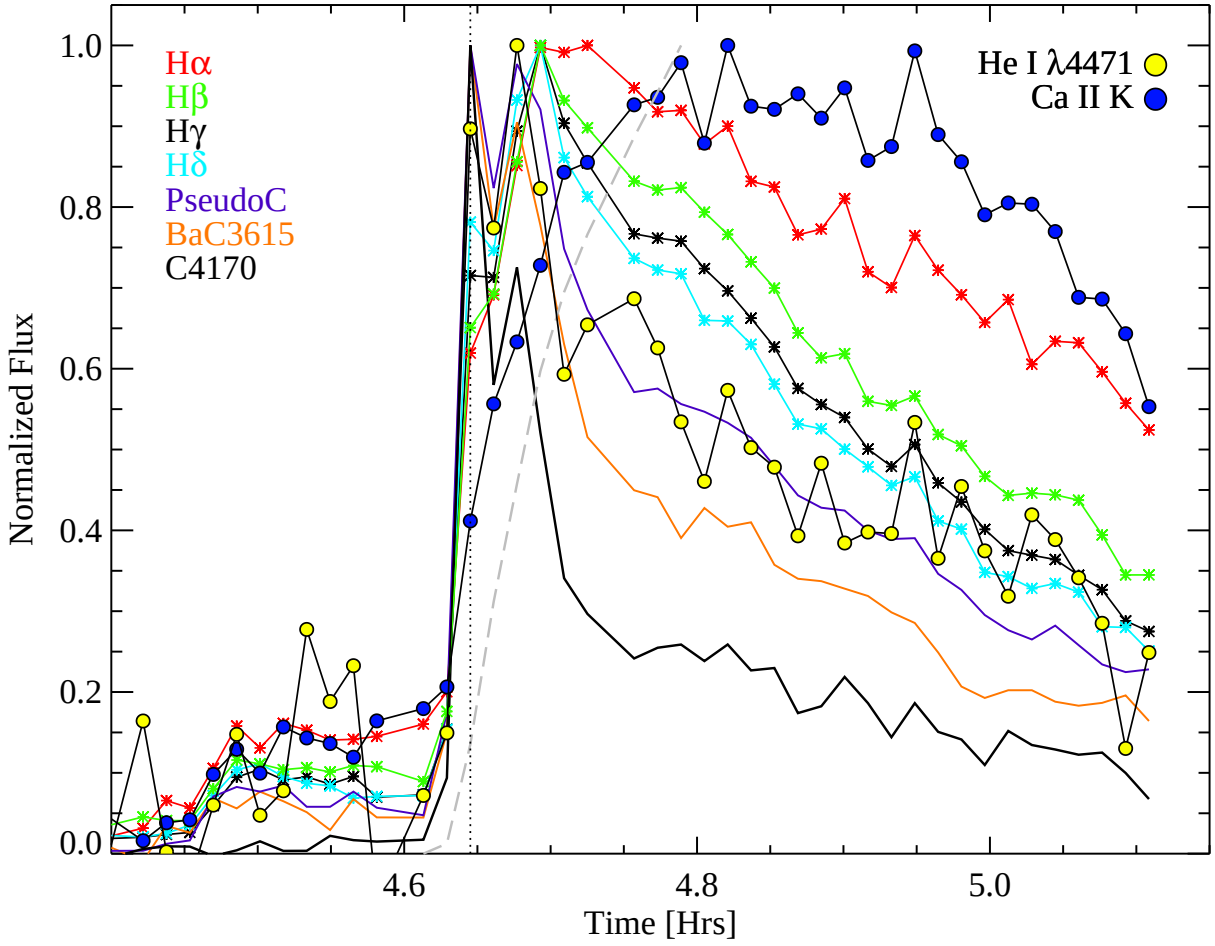

Figure 4.10 Line and continuum evolution for HF2. Symbols same as in Figure 4.8. The dashed line is the cumulative integral of the C4170 from the flare start to the beginning of the extended gradual phase.

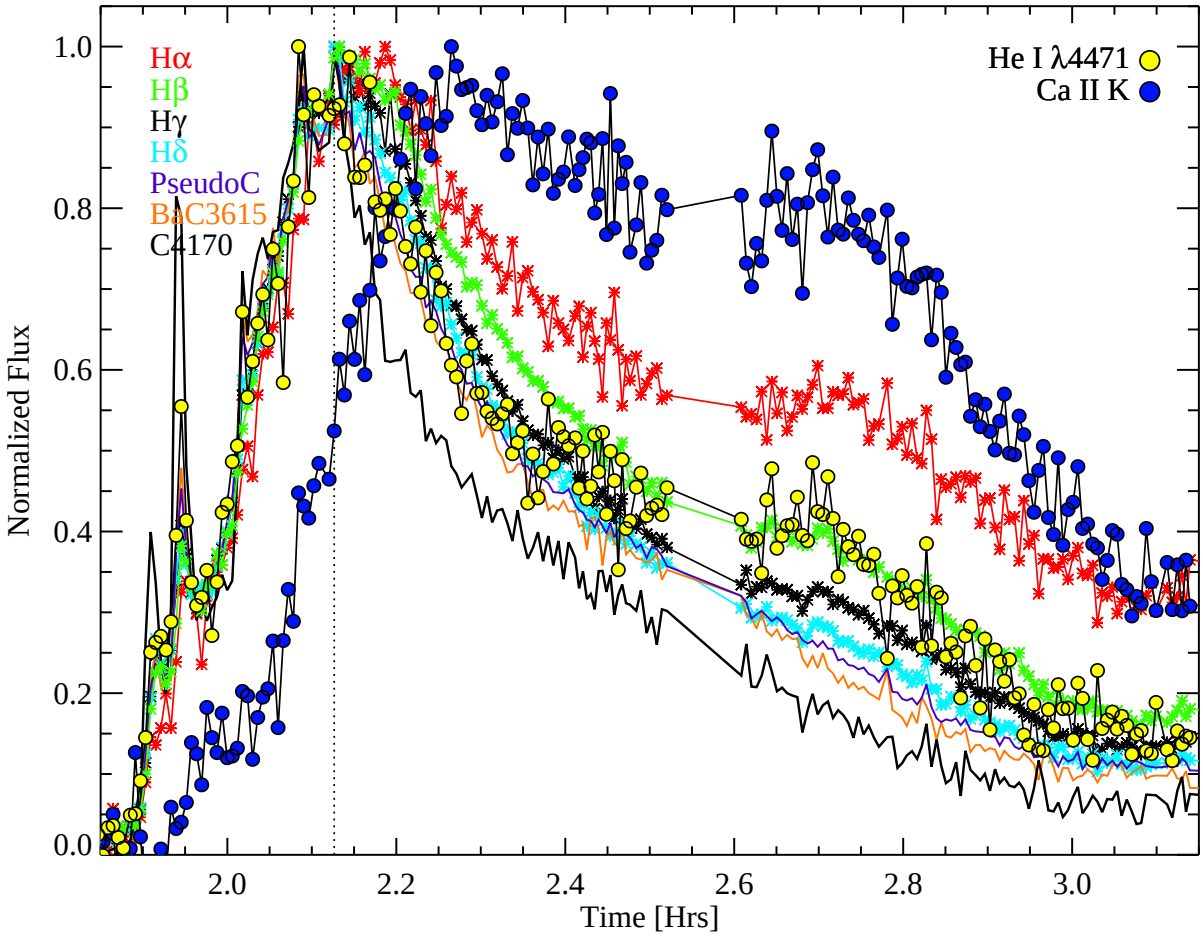

Figure 4.11 Line and continuum evolution for GF1. Symbols same as in Figure 4.8.

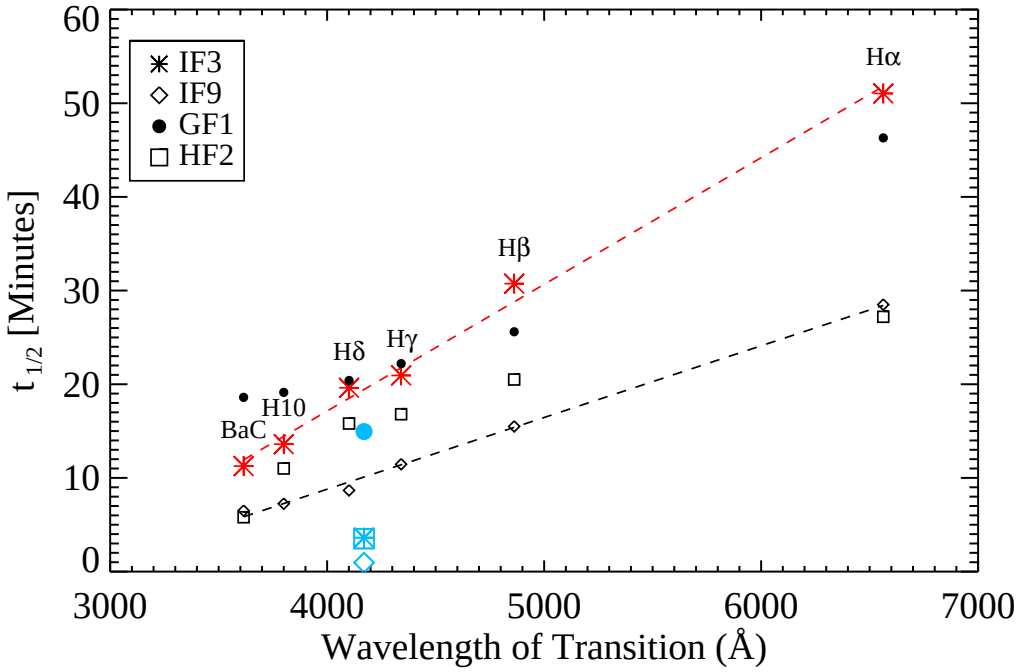

Figure 4.12 We show the values of $t_{1/2}$ of the Balmer emission features for IF3, IF9, and GF1 and HF2. The $t_{1/2}$ value for H10 is shown as a representative member of the PseudoC. The higher order lines evolve faster, and the evolution timescale is inversely proportional to the energy of the transition. A linear fit to the Hydrogen Balmer features for IF3 is shown as a red dashed line. The $t_{1/2,\mathrm{C4170}}$ values are shown as large, light blue symbols and are not included in the fit.

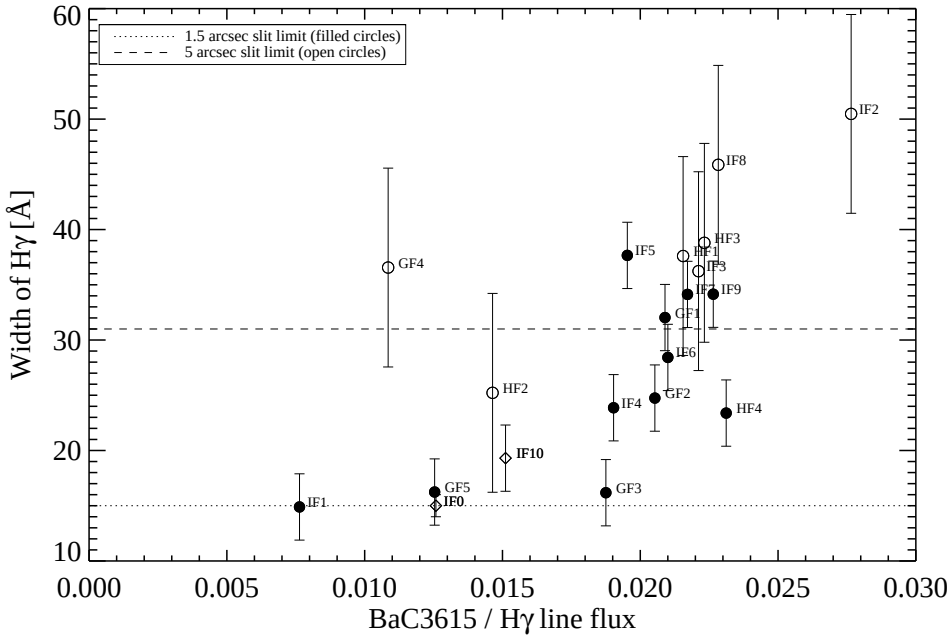

Figure 4.13 In this plot, the symbols represent 0.1 widths of Hγ at the maximum Hγ emission; filled circles are for 1.5" slit data and open circles for 5" slit data. The horizontal lines are the formal limits for measuring 0.1 widths with these low-resolution DIS data. The diamonds represent IF0 and IF10, which were measured with different instruments. Note, HF2 is below the 5" slit limit; these limits were determined from the arc lines, which were broader than the emission lines from target spectra (See Table 2.5). Therefore, the limiting resolution indicated on this figure is a conservative estimate.

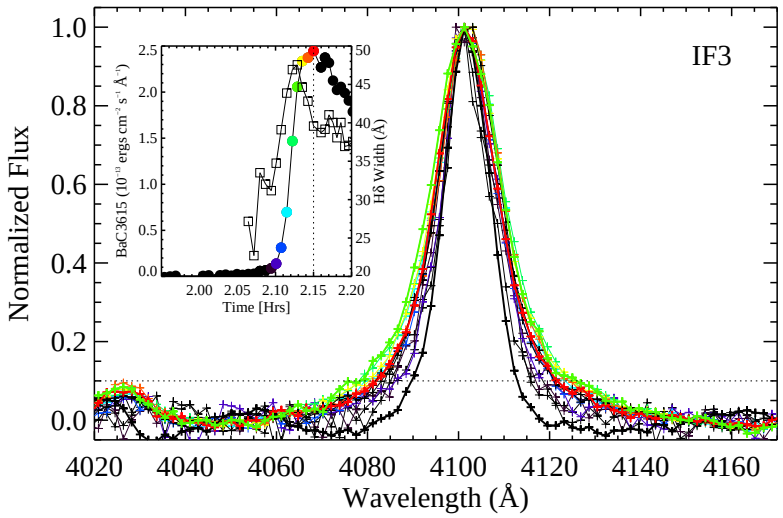

Figure 4.14 A time-resolved look at the line broadening of Hδ during the rise phase of IF3. The quiescent line profile is shown in dark black (0.1 width is $\sim$24Å). The line profiles are color-coded to the inset, which shows the BaC3615 light curve (left axis, circles). The line width evolution is also shown (right axis, squares). The vertical dotted line indicates the time of maximum continuum emission.

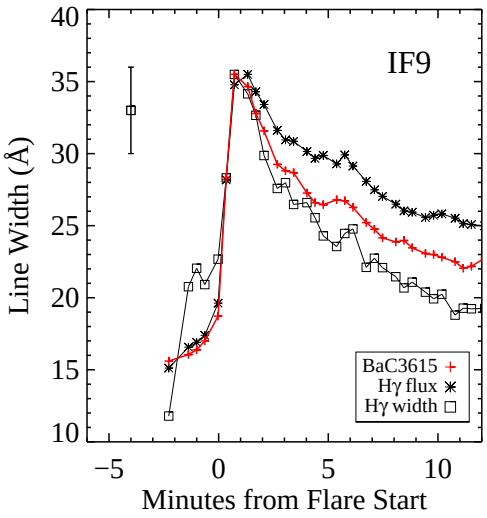

Figure 4.15 The Hγ line widths for IF9. The BaC3615 (red, crosses) and Hγ line flux (asterisks) have been plotted, with the 0 flux level corresponding to 15Å on the left axis; the maximum line flux corresponds to 35Å on the left axis. Displaying this way allows us to compare the timescales. The line width evolution is faster than the evolution in flux, similar to but even faster than the evolution of BaC3615.

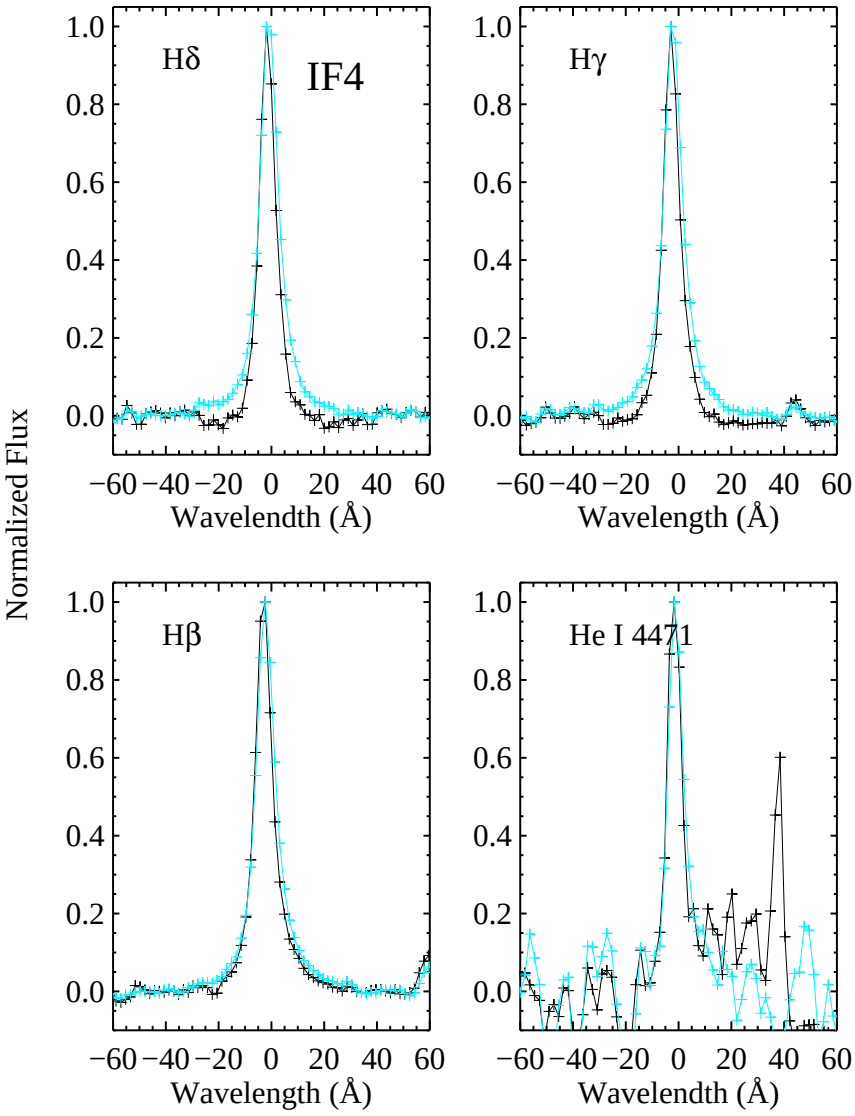

Figure 4.16 The Hδ, Hγ, Hβ and He I λ4471 profiles of IF4 at peak continuum emission (S#665, black) and peak Hβ emission (S#672, torquoise/grey), normalized to the maxima of the line profiles. For Hδ, Hγ, and Hβ respectively, the widths are (15.5Å, 16.7Å, 21.4Å; i.e., the Hδ and Hγ lines are nearly unresolved) at maximum continuum and (21.8Å, 22.6Å, 23.7Å) at maximum line emission. The maximum line emission occurs at the same time for the three lines, $\sim$4.5 minutes after the maximum continuum emission. The feature at +40Å in the He I panel is possibly a cosmic ray.

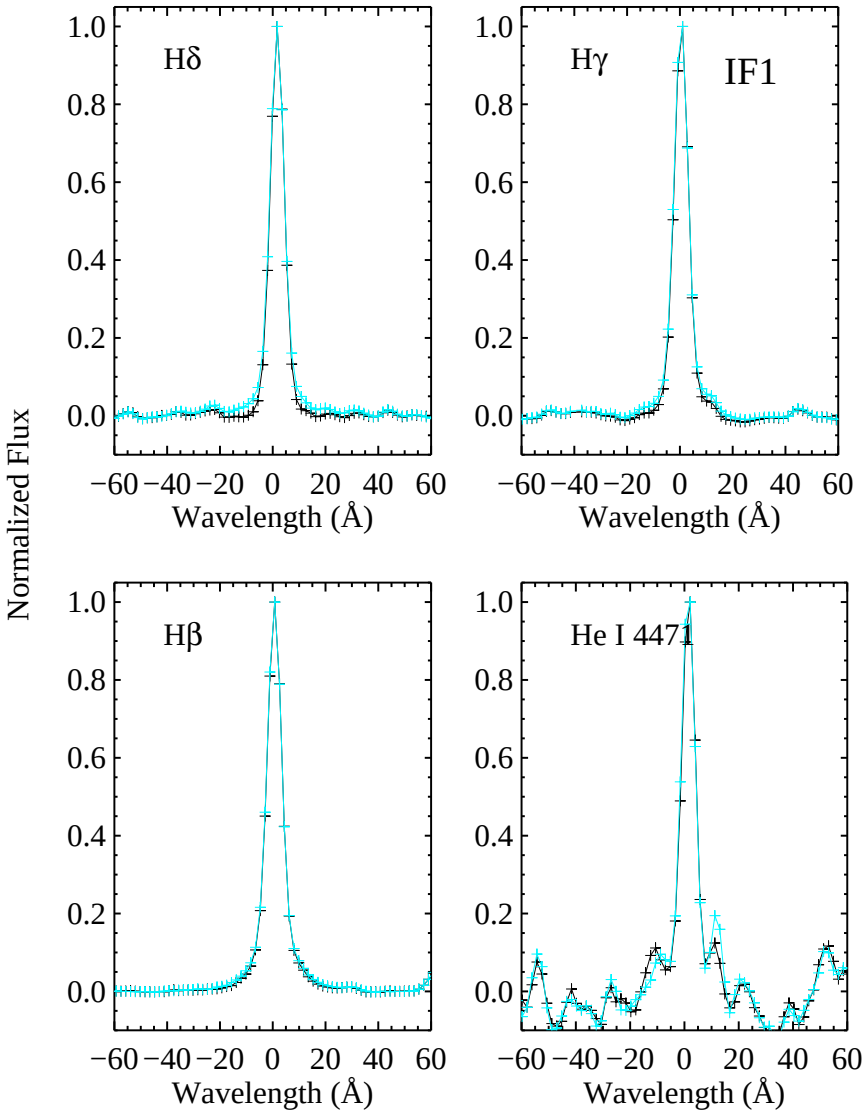

Figure 4.17 The Hδ, Hγ, Hβ and He I λ4471 profiles of IF1 for the pre-secondary flare spectrum (S#102, torquoise/grey) and at the peak of secondary flare (MDSF2, S#113, black), normalized to the maxima of the line profiles. Similar to IF4, the line emission is less at maximum continuum emission (black), and the wings are depressed, which is most apparent for the higher order lines. The widths of Hδ, Hγ, and Hβ, respectively, are 12.2Å, 12.6Å, and 15.2Å at maximum continuum and 13.5Å, 13.5Å, and 15.8Å before the secondary flare. The feature at +10Å from Helium is likely Mg II λ4481.

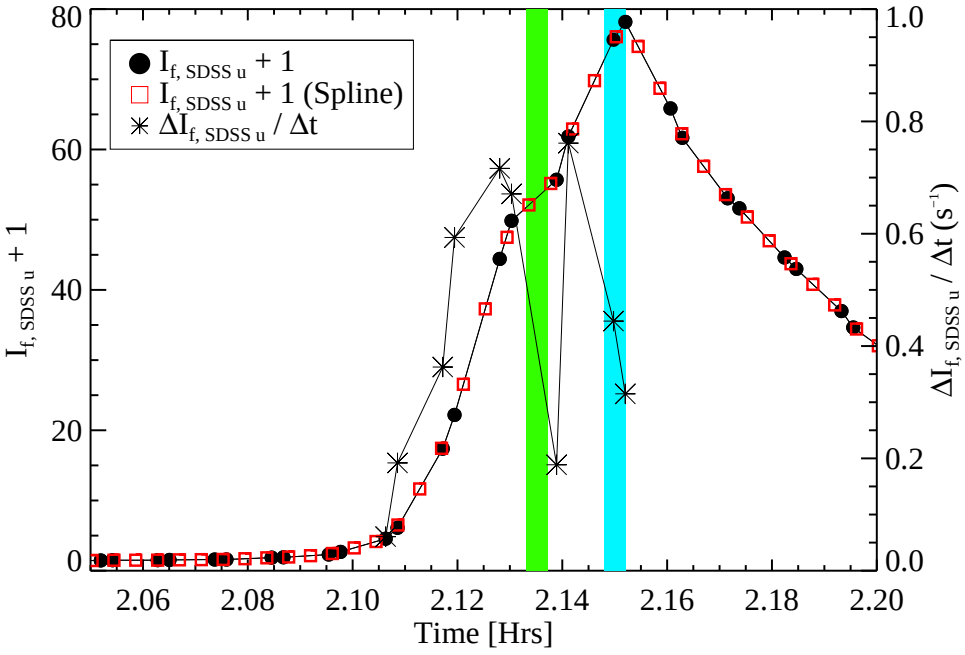

Figure 4.18 The SDSS *u*-band light curve of the rise phase of IF3 (left axis, black circles) and the first derivative of the light curve (right axis, asterisks). The vertical shaded bars correspond to the line profiles in Figure 4.19. The *u*-band light curve is interpolated using a spline function and binned to 15 seconds (red squares, left axis) to show the smoothed evolution.

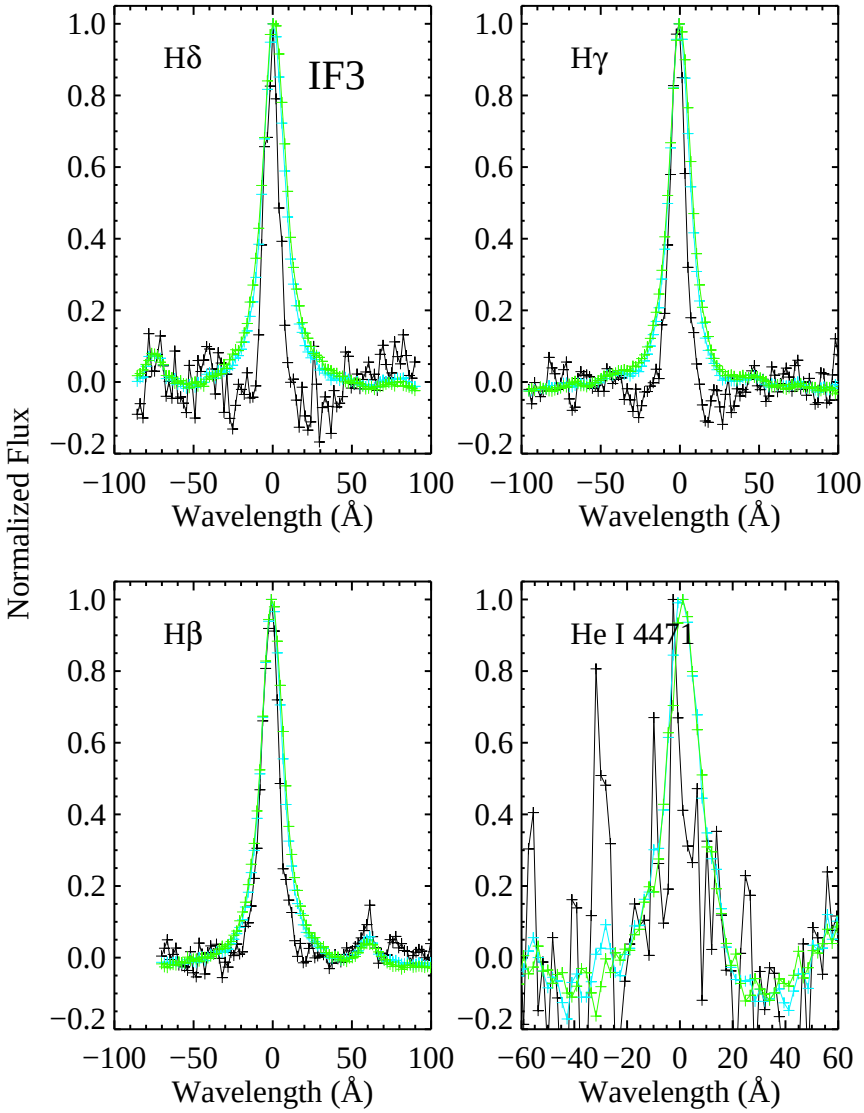

Figure 4.19 The Hδ, Hγ, Hβ, and He I λ4471 of IF3 for the total emission at $\sim$75% of the maximum continuum emission during the rise phase (S#29 normalized, green), at maximum continuum emission (S#31 normalized, turquoise) and the newly formed line emission at peak continuum (S#29 subtracted from S#31 then normalized; black). Before the normalization of these three spectra, the local continuum trend is subtracted with a linear fit. The times from which these spectra are taken are shown in Figure 4.18

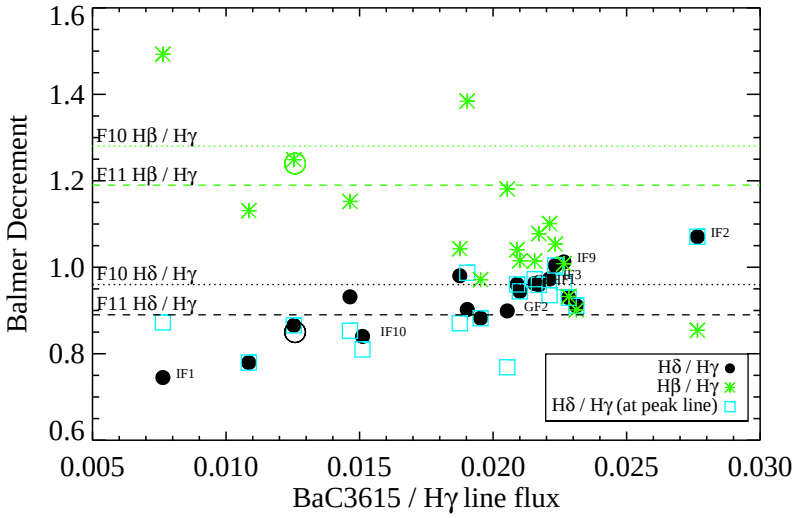

Figure 4.20 The Balmer decrements at peak continuum emission plotted against BaC3615 / Hγ line flux. The horizontal lines are the RHD model predictions from Allred et al. (2006): The dashed lines for F11 and dotted lines for F10, green lines for Hβ decrement, black lines for Hδ decrement. The values for IF0 are shown as large open green and black circles.

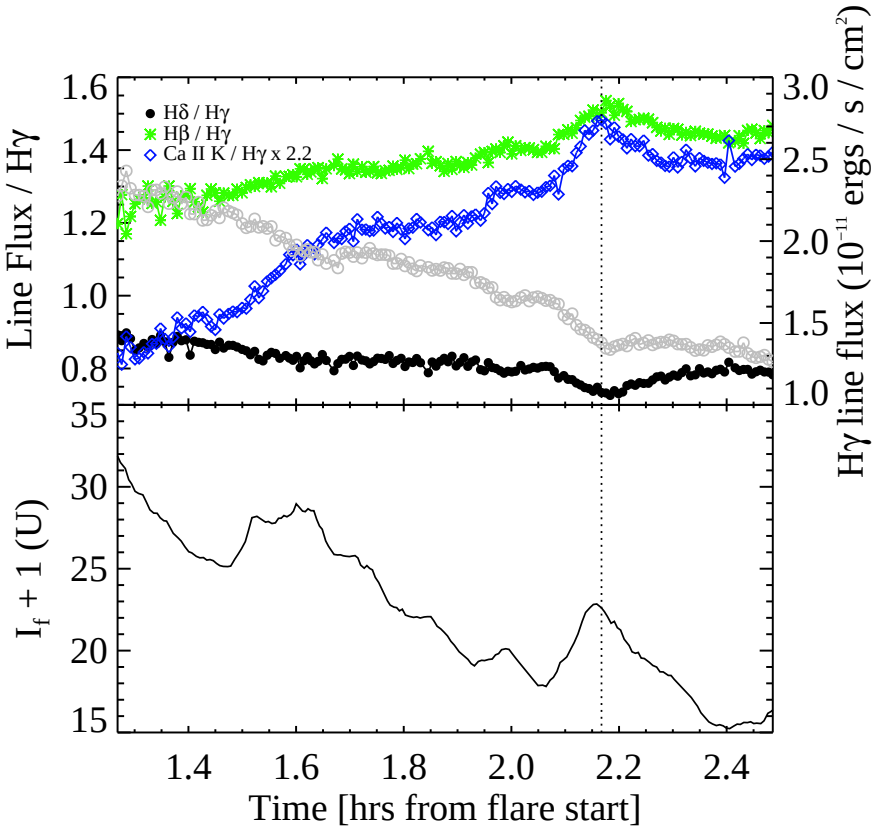

Figure 4.21 (Top Panel) The Hβ (green) and Hδ decrements (black) and Ca II K decrement (blue, multiplied by 2.2 to be visible on the plot) for the IF1 decay phase. The grey open circles (right axis) are the Hγ line fluxes. (Bottom panel) The U-band light curve. The vertical dotted line is shown for S#116, after the peak of MDSF2, but before the maximum and minimum Hβ and Hδ decrements respectively.

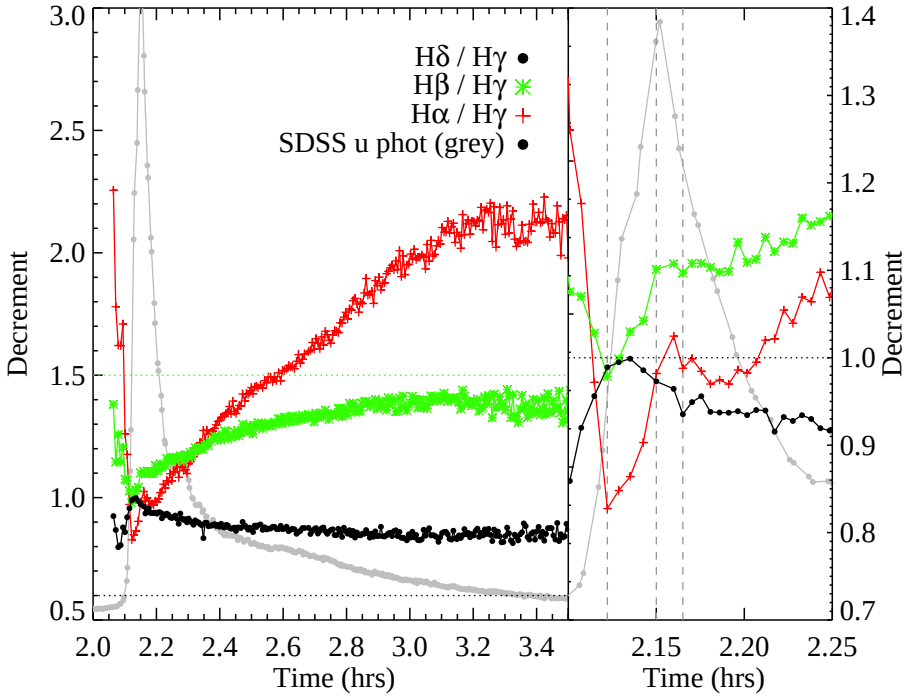

Figure 4.22 The time-resolved Balmer decrements for IF3. The figure to the right focuses on the impulsive phase. The horizontal lines in the left panel indicate the approximate quiescent decrements for Hδ (0.6) and Hβ (1.5). The quiescent decrement of Hα is 5.6 (Table 2.8). The vertical dashed lines in the right panel indicate the times of minimum Hα decrement (S#27), maximum continuum emission (S#31), and maximum line emission (S#33). The horizontal dashed line in the right panel indicates a decrement of 1.0. The Hδ and Hβ decrements are 1 in the mid-to early rise and have complex behavior throughout the rest of the impulsive phase. The Hα decrement is 0.82 in the mid early rise and increases near the peak before decreasing again in the middle of the fast decay.

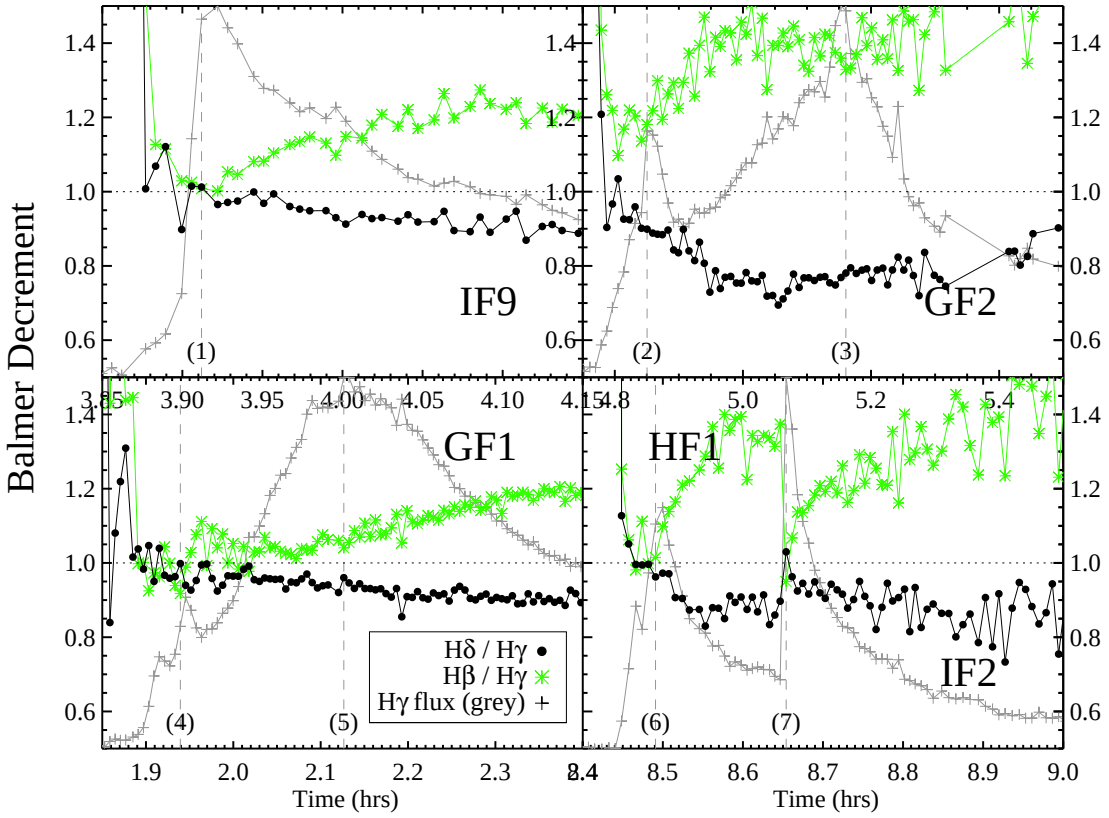

Figure 4.23 The time resolved Balmer decrements for select flares (right axes, same scale for all), and Hγ line flux (grey). Important times are indicated with vertical grey lines: (1) maximum C3615 emission of IF9, (2) maximum C3615 emission in the first flare peak of GF2, (3) maximum C3615 emission in the second peak of GF2, (4) maximum C3615 emission during the spike flare in GF1, (5) maximum C3615 emission of GF1, (6) maximum C3615 emission of HF1, (7) and maximum C3615 emission in IF2.

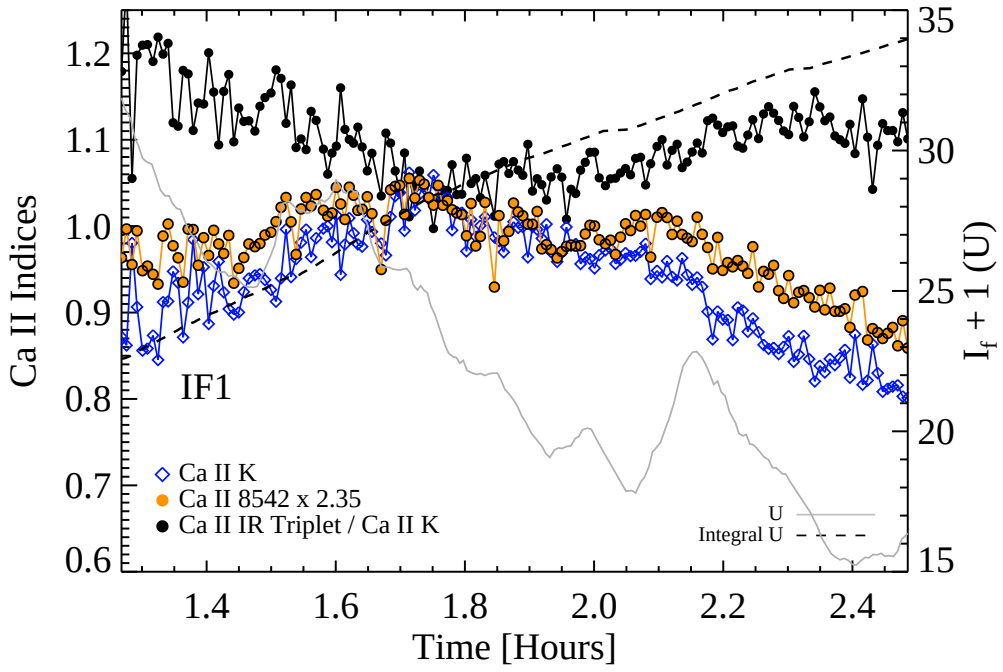

Figure 4.24 The evolution of the Ca II features in IF1, which peak near 1.7 hours. The IR 8542 line is scaled to the maximum of Ca II K for comparison. The black dashed line is the integral of the *U*-band (scaled to the plot range), showing an approximate Neupert like relation between the optical continuum and Ca II features until ∼1.75 hours.

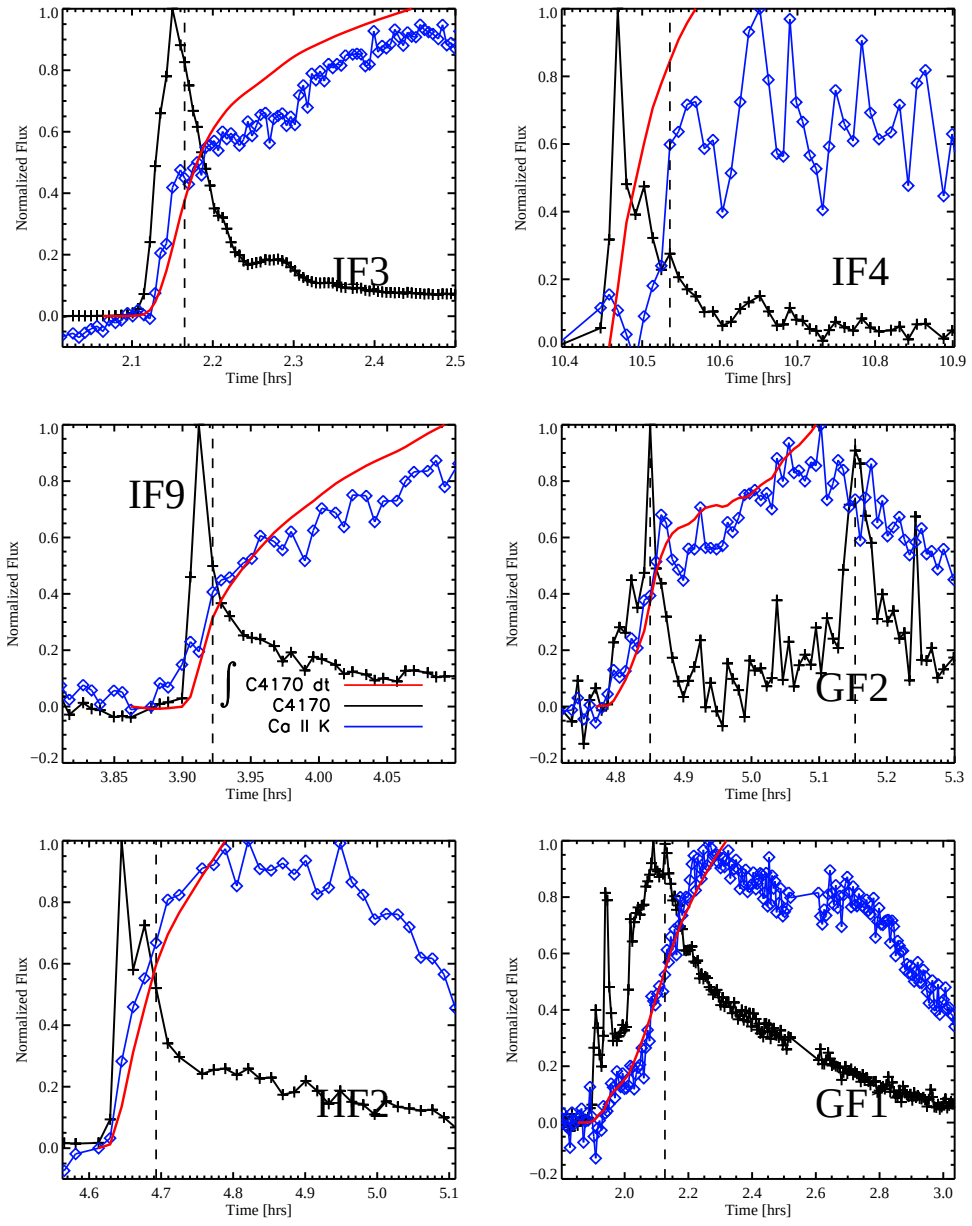

Figure 4.25 Ca II K fluxes compared to the flux of C4170 and the cumulative integral of C4170 (dotted). The times of maximum Hγ line emission are indicated by vertical dashed lines. All are normalized to 1. The preflare value in Ca II K was elevated for HF2 and IF3 and was subtracted from the Ca II K line fluxes. The Ca II K max occurs at the end of C4170 impulsive phase for most flares; for IF3, IF4, IF9, and GF2, the maximum Ca II K line flux occurs later in the gradual phase. Panels continued in Figures 4.26 and 4.27.

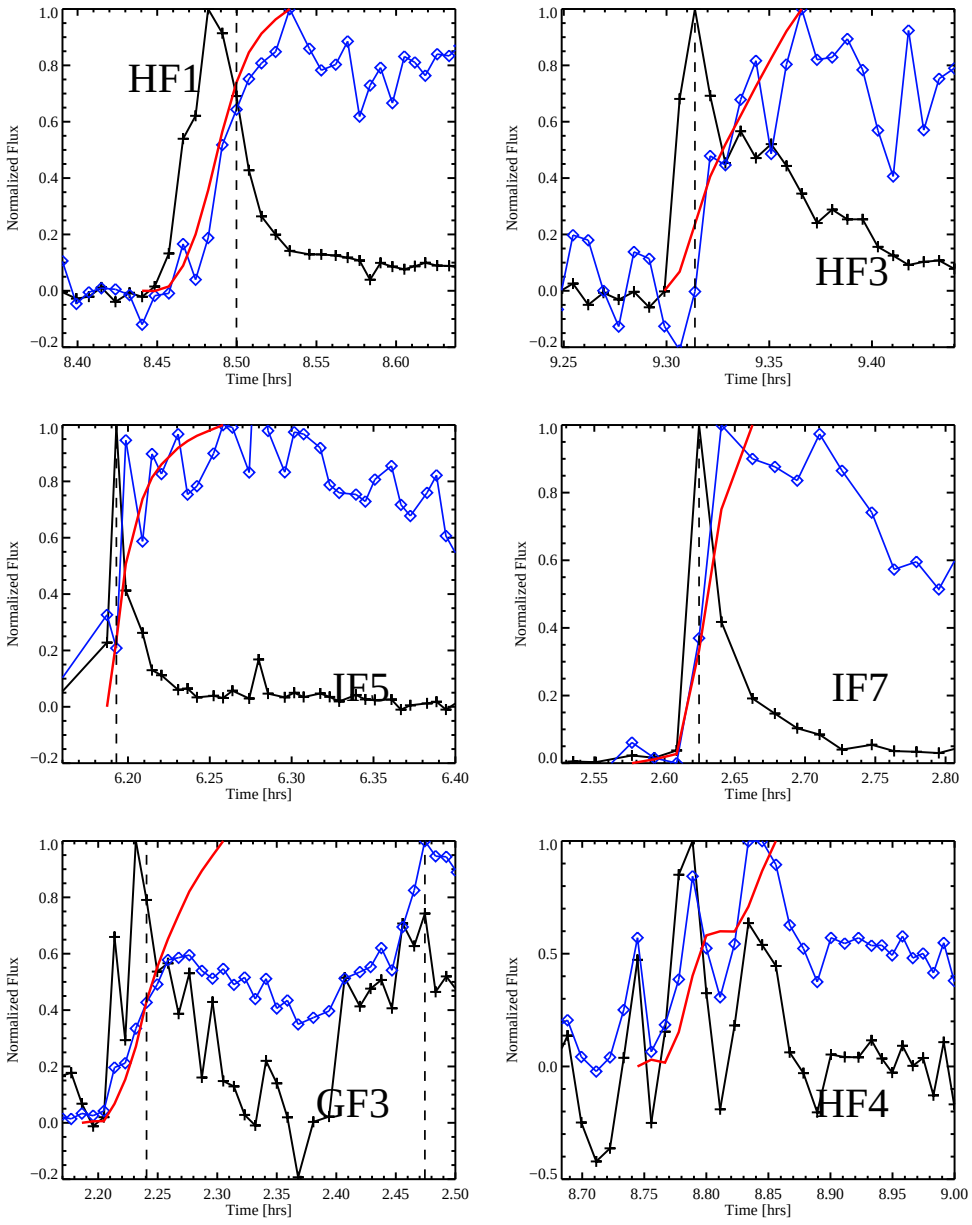

Figure 4.26 Same as for Figure 4.25.

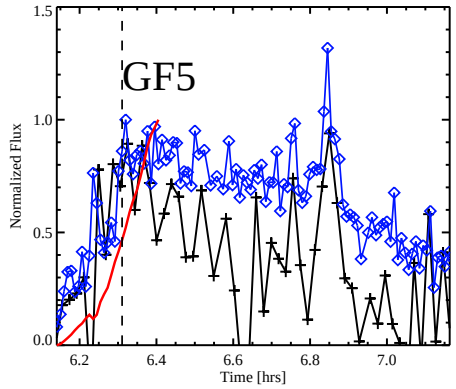

Figure 4.27 Same as for Figure 4.25 but for GF3. The C4170 data were binned.

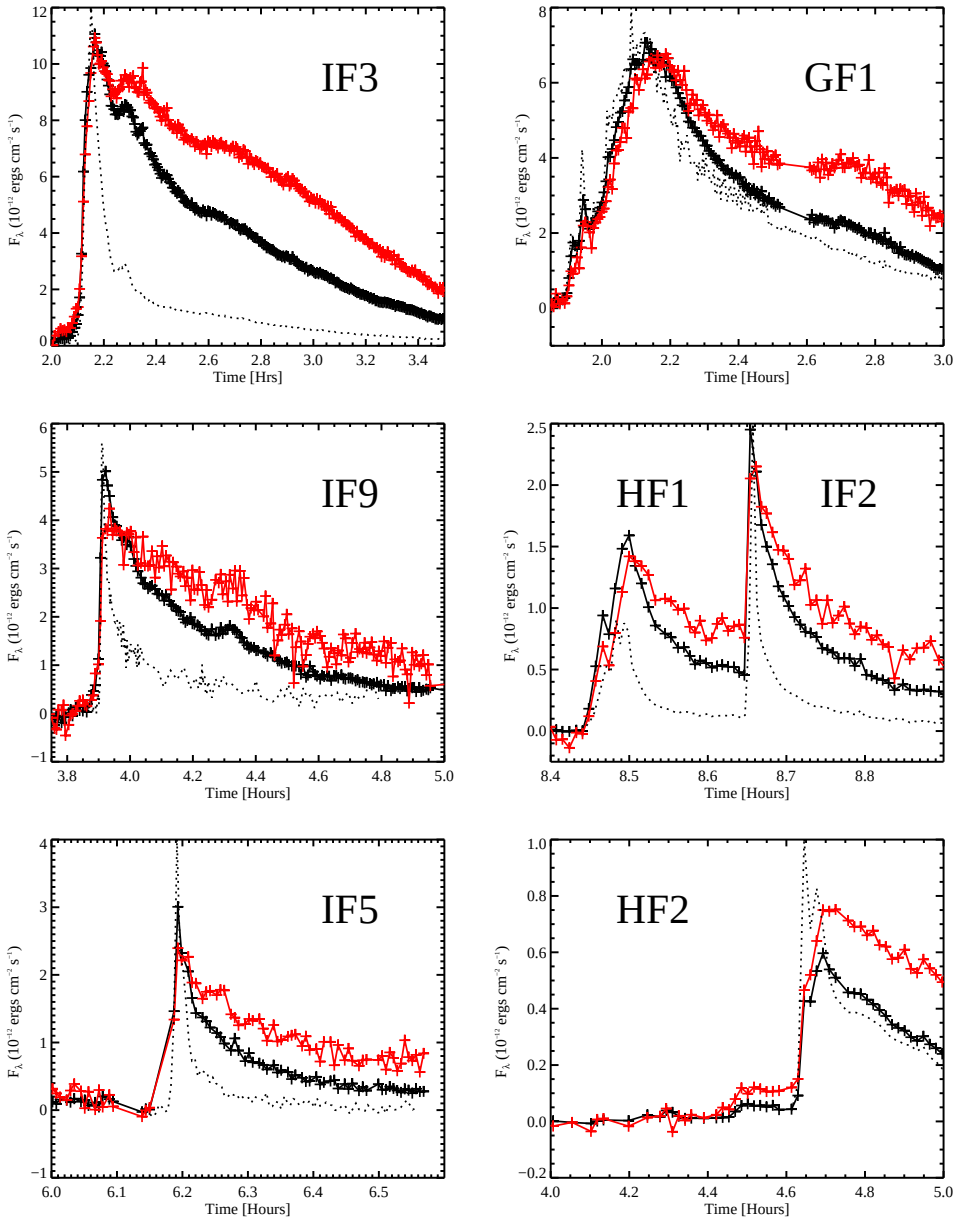

Figure 4.28 Hα (red crosses) and Hγ line fluxes (black crosses). The photometry is shown as a dotted line with an arbitrary flux scaling to display in the figures (all photometric data are SDSS u or Johnson U except for IF9, which is SDSS g and binned to 10 seconds). HF2 and GF5 "photometry" are synthetic U-band measurements.

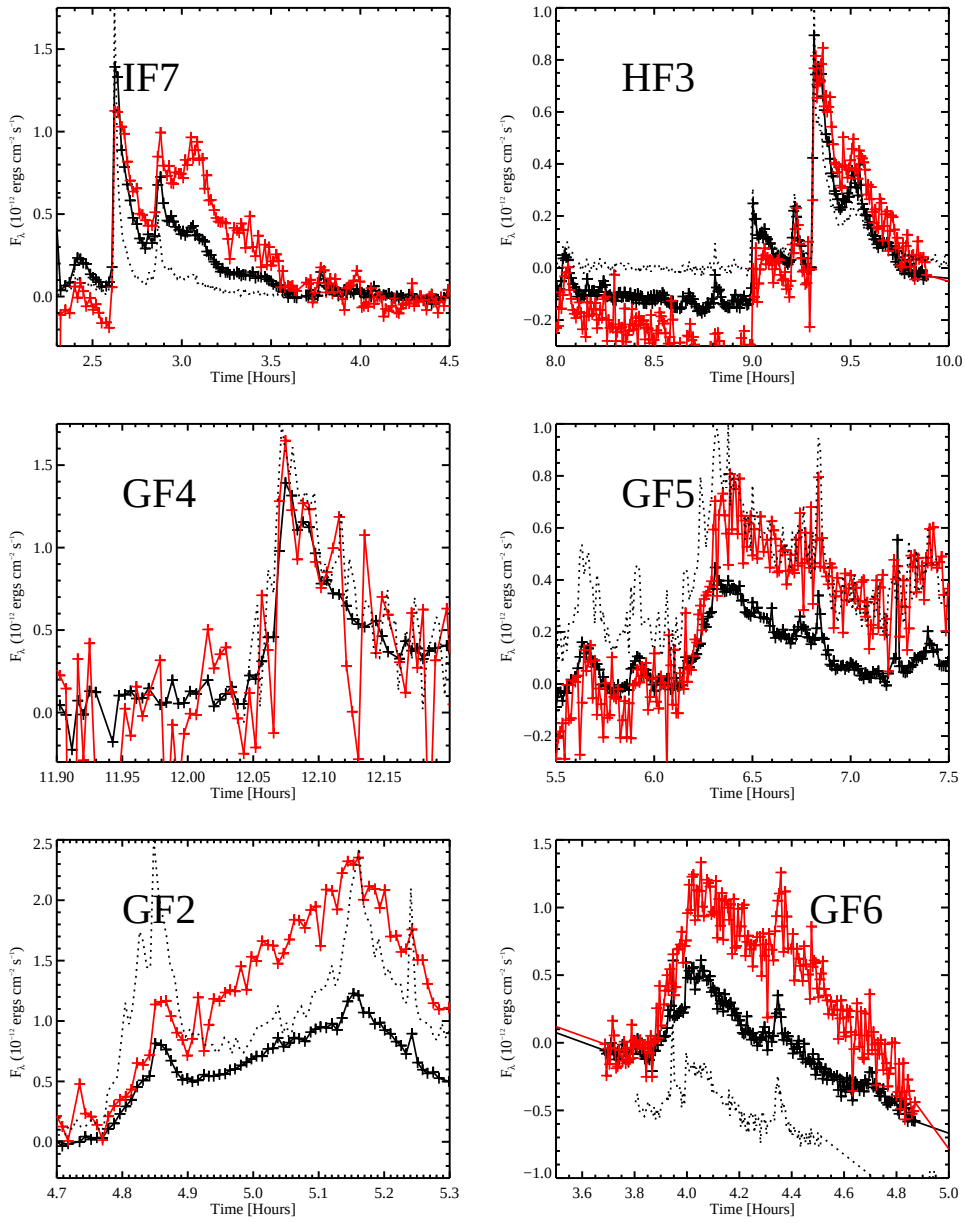

Figure 4.29 Hα (red crosses) and Hγ line fluxes (black crosses), and the photometry is shown as a dotted line; see Figure caption for Figure 4.28. Note that GF6 is not included in the rest of the analysis (see Flare Atlas description).

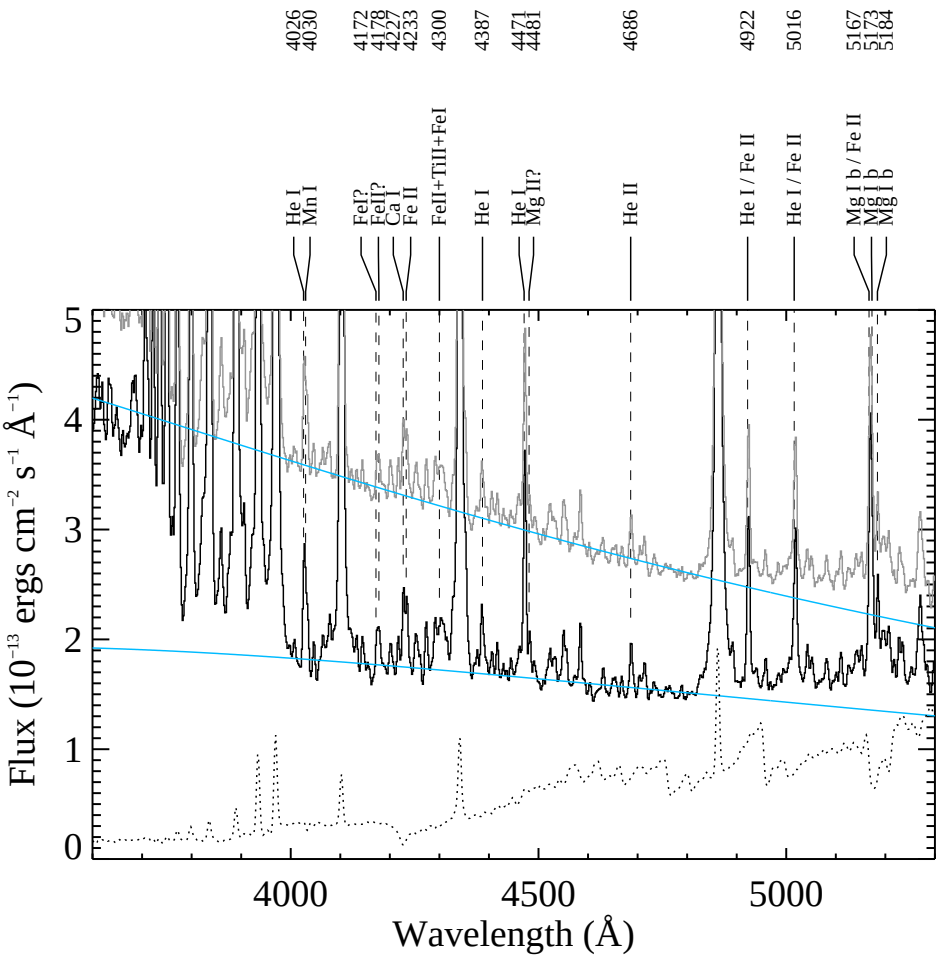

Figure 4.30 We show two flare spectra from the decay phase of IF1 – black line is S#102 (the pre-secondary flare), the medium shade grey is the peak of the secondary flare (MDSF2, S#113) and dotted is the quiescent. The flare spectra are "flare-only" emission. The light blue lines are best fit blackbody curves to the blue-optical (see Chapter 6). The statistical signal-to-noise at $\lambda \sim 4170$Å in S#102 is approximately 70, implying that the low-level variations are minor emission lines. Several tentative identifications are provided at top using high spectral resolution data of other flares as a guide.

Table 4.1. Line Energy Budgets

Flare ID	Hot : Warm : Cool : Hα	Warm : Total	HB : Total	Total Energy (3420-5200Å; 10^{32} ergs)
IF1	0.041 : 1.00 : 0.26 : –	0.084	0.26	128.5
IF2	0.053 : 1.00 : 0.06 : 0.26	0.056	0.24	0.6
IF2+HF1*	0.036:1.0:0.15:0.43	0.10	0.35	1.87
IF3	0.031 : 1.00 : 0.19 : 0.47	0.085	0.29	33.8
IF4	0.038 : 1.00 : 0.16 : –	0.052	0.19	10.9
IF5	0.028 : 1.00 : 0.15 : 0.49	0.15	0.42	0.68
IF6	0.040 : 1.00 : 0.15 : 0.38	0.091	0.28	0.15
IF7	0.037 : 1.00 : 0.14 : 0.33?	0.082	0.26	0.82
IF8	0.047 : 1.00 : 0.15 : –	0.052	0.15	0.09
IF9	0.040 : 1.00 : 0.16 : 0.42	0.10	0.36	4.9
HF1	0.033 : 1.00 : 0.12 : 0.37	0.10	0.35	0.72
HF2	0.023 : 1.00 : 0.14 : 0.52	0.17	0.44	1.93
HF3	0.032 : 1.00 : 0.10 : 0.36	0.12	0.39	0.29
HF4	0.060 : 1.00 : 0.25 : –	0.2	0.71	0.89
GF1	0.031 : 1.00 : 0.11 : 0.41	0.11	0.41	11.1
GF2**	0.034 : 1.00 : 0.17 : 0.67	0.26	0.68	1.2
GF3**	0.028 : 1.00 : 0.16 : 0.35	0.11	0.33	1.8
GF4	0.041 : 1.00 : 0.22 : 0.29	0.37	0.94	0.13
GF5	0.036: 1.00 : 0.28 : 0.71	0.17	0.48	0.58

Note. — *IF2+HF1 calculated without subtracting the preflare (decay of HF1); results in signifcant change in Hα and cool lines because they are slower.**For the entire event. Note, flux ratios and energy ratios are inherently the same because all energies are computed with the same factor of $4\pi d^2$.

Table 4.2. Peak and Extended Decay Times

Flare ID	Peak Time (S#)	Decay Time (S#)
IF0	1038 (36, 40)	1497 (45)
IF1	2.1441 (113)	1.4576 (24)
IF2	8.6540 (542)	8.6747 (545)
IF3	2.1500 (31)	2.4512 (87)
IF4	10.4686 (665)	10.5690 (674)
IF5	6.1929 (516)	6.2205 (520)
IF6	4.7934 (261)	4.8300 (264)
IF7	2.6245 (19)	2.6785 (22)
IF8	11.6274 (390)	11.6506 (392)
IF9	3.9120 (121)	3.9508 (126)
IF10	4.9070 (31)	5 (32), 5.1431 (34)
HF1	8.4909 (521)	8.5455 (527)
HF2	4.6452 (106)	4.7891 (114)
HF3	9.3138 (234)	9.3658 (241)
HF4	8.7889 (550)	8.8672 (557)
GF1	2.1265 (69)	2.3194 (101)
GF2	4.8504 (119)	4.9158 (127)
GF3	2.2317 (34)	2.3140 (43)
GF4	12.0746 (316)	12.1062 (323)
GF5	6.3106 (332-335)	6.3769 (336-345)

Note. — The time and spectrum number for the "peak" and "extended decay". The times are given in hours (MJD). Note that three spectra around the extended decay time listed above are averaged when we refer to "extended decay". The times for IF0 are given in seconds as presented in HP91.

Table 4.3. Evolution of Hydrogen Balmer Radiation

Flare ID	H Balmer / Total (Peak)	H Balmer / Total (Decay)
IF0	0.12	0.44
IF1	0.15	0.34
IF2	0.13	0.32
IF3**	0.11	0.37
IF4	0.03	0.29
IF5	0.24	0.52
IF6	0.22	0.42
IF7	0.15	0.32
IF8	0.12	–***
IF9	0.17	0.34
IF10	0.15	0.43
HF1	0.24*	0.44
HF2	0.31	0.48
HF3	0.35	0.42
HF4	0.35	0.56
GF1**	0.38	0.43
GF2	0.48	0.64
GF3	0.35	0.50
GF4	0.51	0.64
GF5	0.51	0.51

Note. — *Peak in C4170 one spectrum earlier, so averaged S#520-521. **Including an estimate for Hϵ, the percentages change to 12% (peak) and 39% (decay) for IF3 and 40% (peak) and 45% (decay) for GF1. ***There is no extended gradul phase for IF8 (or it is very low). ****Note that the flares IF0 and IF10 have a narrower wavelength coverage because the data were obtained with different instruments. The IF0 data do not include continuum flux at $\lambda > 4440$Å and Hβ, and the IF10 data do not include continuum flux at $\lambda > 4700$Å and Hβ.

Chapter 5

A WHITE-LIGHT MEGAFLARE ON THE DM4.5E STAR YZ CMI

In this Chapter, we present the Astrophysical Journal Letter reporting on the spectral observations during the decay phase of IF1. The two-component continuum analysis provides the basis for Chapter 6.

Sections 5.1 through 5.3 of this chapter were originally published in collaboration with Suzanne L. Hawley, Jon A. Holtzman, John P. Wisniewski, and Eric J. Hilton in the May 2010 edition of the Astrophysical Journal Letters (Kowalski et al., 2010, ApJL Vol. 714, pp. 98 – 102;) and is reproduced below with permission of the author and the American Astronomical Society.

5.1 Abstract

On UT 2009 January 16, we observed a white light megaflare on the dM4.5e star YZ CMi as part of a long-term spectroscopic flare-monitoring campaign to constrain the spectral shape of optical flare continuum emission. Simultaneous U-band photometric and 3350 – 9260Å spectroscopic observations were obtained during 1.3 hours of the flare decay. The event persisted for more than 7 hours and at flare peak, the U-band flux was almost 6 magnitudes brighter than in the quiescent state. The properties of this flare mark it as one of the most energetic and longest-lasting white light flares ever to be observed on an isolated low-mass star. We present the U-band flare energetics and a flare continuum analysis. For the first time, we show convincingly with spectra that the shape of the blue continuum from 3350Å to 4800Å can be represented as a sum of two components: a Balmer continuum as predicted by the Allred et al radiative hydrodynamic flare models (Allred et al., 2006) and a T ∼10,000K blackbody emission component as suggested by many previous studies of the broadband colors and spectral distributions of flares. The areal coverage of the Balmer continuum and blackbody emission regions vary during the flare decay, with the Balmer

continuum emitting region always being significantly ($\sim$3 – 16 times) larger. These data will provide critical constraints for understanding the physics underlying the mysterious blue continuum radiation in stellar flares.

5.2 Analysis

5.2.1 U-Band Flare Energetics

This flare event is remarkable in its total energy, peak luminosity, total duration, and emission morphology. A small precursor, sometimes seen prior to large flares (Moffett, 1974), began at 04:14:54UTC which increased the U-band flux by a factor of $\sim$2, and represents the onset of the flare event. At 04:32:00UTC, there was a $\sim$10 min impulsive rise to flare peak, where the U-band flux was a factor of $\sim$200 times the quiescent value. The decay phase included many smaller events, and the U-band flux was still elevated by over a magnitude above quiescence at the end of the night. In Section 5.3, we discuss the extremely long duration of this event.

The total U-band flare energy is used to quantify the energy release in continuum radiation during stellar flares (Moffett, 1974). We integrate under the light curve to obtain an equivalent duration (Gershberg, 1972) of 4.25×10^5s, which is the amount of time that the star would spend emitting at the pre-flare level to produce the same total amount of energy as the flare. Multiplying the equivalent duration by the non-flaring U-band luminosity of 4.00 $\times 10^{28}$ ergs s^{-1} (Moffett, 1974) gives $E_{U,flare} > 1.7 \times 10^{34}$ ergs (this is a lower limit since flare emission is still seen at the time the light curve ends). At peak, the flare was emitting with a U-band luminosity of 8.3×10^{30} ergs s^{-1}, or $\sim$37% the stellar bolometric luminosity (M_{Bol}= 10.25, Reid & Hawley, 2005). This flare was $\sim$100 times more energetic and persisted for more than 10 times as long as the largest U-band flare event observed on this star during 55 hours of monitoring from the large statistical flare study of Moffett (1974) and Lacy et al. (1976). Although it is unknown if the power law fit to the flare-frequency distribution of Lacy et al. (1976) holds at high flare energies, an extrapolation predicts that flares with U-band energies $> 1.7 \times 10^{34}$ ergs occur at a rate of $\sim$once per month.

5.2.2 The Flare Continuum

The spectral data were obtained while the U-band emission was still elevated 15-37 times (3-4 mag) over quiescence. Complex morphology is seen in the U-band light curve during this time period (see Figure 5.1a), allowing us to study the flare continuum variations during several smaller impulsive events. Figure 5.1b shows a spectrum ($t = 76.6$min after the flare start) from 3350Å$-$5500Å near the beginning of our spectroscopic observations during the U-band decay from a large secondary emission peak. A quiescent spectrum of YZ CMi (see Section 2) is also shown in Figure 5.1b and has been subtracted from the flare spectrum to give a "flare-only" spectrum. Our spectra have the highest time resolution with high signal to noise in the blue/NUV (S/N > 50 at 3600Å) ever obtained during a large stellar flare. They are also unique in having simultaneous high quality photometric information so that we may relate the spectral evolution to the light curve morphology.

We have for the first time convincingly identified two distinct continuum components that simultaneously contribute to the optical/NUV flux in flare spectra. The first component dominates the spectrum from 4000 – 4800Å and exhibits the rising trend of a $T \sim$10,000K blackbody, which is plotted on the spectrum in Figure 5.1b using a filling factor, X_{BB}, of 0.22% of the projected stellar disk area. We follow Hawley et al. (2003) to constrain the filling factor of blackbody emission as a function of time using the equation:

$$F_{fl,\lambda}(t) = X_{BB}(t)\frac{R_\star^2}{d^2}\pi B_\lambda(T_{fl}) \tag{5.1}$$

where $F_{fl,\lambda}$ is the flare flux observed at Earth in the continuum windows from 3995 – 4020Å, 4140 – 4210Å, 4425 – 4450Å, and 4600 – 4800Å; $R_\star = 0.3\times R_{Sun}$, $d = 5.97$ pc (Reid & Hawley, 2005) and $T_{fl} = 10,000$K.

From Figure 5.1b, it is clear that the blackbody fit does not explain all of the continuum emission at wavelengths shorter than ∼3800Å. Starting near H10 (3799Å), there is a rise to H15+H16, the last two apparent Balmer lines in emission. Blueward of ∼3700Å, the flare spectrum becomes flat into the NUV, and there is excess flux visible above the 10,000K blackbody at these wavelengths.

A06 presented RHD flare simulations for a medium (10^{10} ergs cm^{-2} s^{-1}, F10) and a

strong (10^{11} ergs cm^{-2} s^{-1}, F11) impulsive flux of nonthermal electrons into an M dwarf atmosphere. The A06 models predict strong Balmer continuum radiation with a noticeable Balmer jump at 3646Å, together with a photosphere that is warmed by ∼1200K to a temperature of 4600K. We isolated the Balmer continuum component of the A06 F11 model spectrum taken at the last time-step of their simulation (t = 15.9s), and fit it to the observed flare spectra. Figure 5.1c shows the flare spectrum from Figure 5.1b with the 10,000K blackbody component subtracted and the model Balmer continuum component scaled to the excess emission in the 3600Å $< \lambda <$ 3646Å region. The shape of the observed excess emission is well-described by the F11 flare model prediction (shown in red). Although there is no abrupt discontinuity indicative of a Balmer jump in our observed spectrum, we posit that blending (possibly due to Stark broadening; Donati-Falchi et al., 1985) of the higher order Balmer lines in the 3646Å $< \lambda <$ 3800Å region effectively hides the sharp discontinuity that is seen in the model spectrum.

5.2.3 Relative Filling Factors

The filling factor for the F11 model spectrum is calculated by scaling the model flux in the 3600 – 3646Å region ($F_{\lambda,Model} = 1.14 \times 10^7$ ergs cm^{-2} s^{-1} Å^{-1}) to the flux excess observed at Earth after subtracting the 10,000K blackbody. The contribution function for the Balmer continuum in the F11 model shows that the emission arises from a relatively thin layer in the atmosphere (J. Allred, private communication); it is therefore reasonable to approximate changes in the filling factor to changes in the emitting area of the Balmer continuum.

In the upper panel of Figure 5.1d (black points), we show the ratio of the filling factors for a 10,000K blackbody and the model Balmer continuum component. The error bars are obtained by using 9000 and 11,000K temperatures for the blackbody. The ratio for the sample spectrum in Figure 5.1b is $X_{BB}/X_{Model} = 0.10\pm^{0.04}_{0.02}$. The filling factor ratio indicates that the two emission components exhibit significantly different time evolution, with the blackbody source emitting from a region ∼3-16 times smaller than the source of the Balmer continuum.

The inferred area filling factor (X_{BB}) of the blackbody component is shown separately

(red points) and exhibits very similar morphology to the U-band light curve (reproduced in the lower panel). Although we expect the *total* continuum flux to follow the U-band since we scaled the spectra to achieve absolute flux calibration (§3.2), it is surprising that *only* the blackbody component follows the U band.[1] It appears that the deviations from the general flare decay seen in the U band primarily arise from the changing area of the blackbody emission region. When the deviations are strongest near the peaks at $t \sim 95$ min and $t \sim 130$ min, the spectra are increasingly dominated by the blackbody component. This is consistent with the flare-peak spectra from Kahler et al. (1982), Hawley & Pettersen (1991), and Fuhrmeister et al. (2008) and the photometry of Zhilyaev et al. (2007). We also note preliminary evidence of an apparent increase in the best-fit blackbody temperature to $T \sim 13,000$K at the peak near $t \sim 130$ min.

The derived filling factor ratios should be regarded as illustrative since our Balmer continuum spectrum from the F11 model of A06 assumes that the nonthermal electron flux is constant at 10^{11} ergs cm^{-2} s^{-1}. Also, we use the model flare spectrum from only one time-step in the RHD simulation. It is likely that the nonthermal electron flux varied both with time and over the geometry of the flaring region. Any further assessment is beyond the scope of this Letter, but we note that the less energetic A06 F10 flare spectrum at $t = 230.0$s gives nearly 10 times larger filling factors for the Balmer continuum.

5.2.4 Balmer Line and Continuum Radiation

The time-evolution of the Balmer continuum closely follows the hydrogen Balmer lines. We show the variation in the Balmer continuum (using the integrated flux in a 30Å window centered at 3615Å) compared to the Hγ line flux and the U band in the lower panel of Figure 5.1d. The fluxes are normalized to the last spectral observation we obtained. The Balmer continuum shows a slow decay throughout our observations, as is typical of the Balmer line radiation (Hawley & Pettersen, 1991). This overall decay is probably extended emission from the previous, much more luminous, impulsive events seen in the U-band light curve. The larger variations in the Balmer continuum compared to the Hγ emission

[1] These trends are also visible in the data before the flux calibration scaling was applied.

may be partially due to small errors in isolating the Balmer continuum by subtracting the underlying blackbody continuum (the Hγ flux is well measured as it has a local continuum). As noted above in the filling factor discussion and evident by comparing the upper and lower panels of Figure 5.1d, the Balmer line and continuum radiation exhibit quite different time evolution compared to the blackbody emission component. We propose two possible explanations:

(a) The hydrogen-emitting regions exhibit a delayed and more gradual response to each successive impulsive (blackbody) event. In this scenario, the gradual increase in hydrogen Balmer emission around $t = 122$ and $t = 137$ min are associated with the impulsive events in blackbody emission (upper panel) at $t = 117$ min and $t = 127$ min, respectively. Also, Balmer emission around $t = 80$ min and $t = 105$ min is elevated yet only slowly decreasing, and could be gradually declining emission from the large U-band peaks at $t \sim 60$ min and $t \sim 95$ min, respectively.

(b) The time evolution of the blackbody emission and the Balmer emission may be anti-correlated. If true, this may provide an important constraint on the origin of the blackbody emission. The possible anti-correlation is most apparent during the U-band rise starting at $t = 124$ min. In ~ 5 min the Balmer continuum decreases by $\sim$40% while the blackbody filling factor almost doubles. Hydrogen continuum dimming is predicted by flare models (Abbett & Hawley, 1999; Allred et al., 2005), but only for very short durations (0.1s) at the onset of a flare.

More detailed models will be required to understand these complex variations, and in particular, the seemingly anti-correlated trends between the blackbody and Balmer continuum and lines during the time intervals when the blackbody filling factor is increasing in Figure 5.1d.

5.3 Summary and Speculation

We observed a white light megaflare on the dM4.5e star YZ CMi in the U band and with simultaneous optical/NUV spectroscopy. The U-band energetics and light curve morphology

qualify this flare as an extraordinary and rare event, similar to the $\sim 6.6 \times 10^{34}$ erg flare on YZ CMi seen by Andrews et al. (1969), Lovell (1969), and Kunkel (1969). Following a solar analogy, we speculate that the flaring region on YZ CMi was a complex arcade of sequentially reconnecting magnetic loops. Each reconnecting loop accelerated a beam of nonthermal electrons that impacted the lower atmosphere, producing the observed blue/NUV line and continuum emission. The sum of a large number of individual emitting regions may have enabled this flare to persist for such an unusually long time.

Using high time resolution, high signal-to-noise spectra, we have shown that the blue/NUV flare continuum radiation can be explained as a sum of a T ∼10,000K blackbody component and a Balmer continuum component, with only the blackbody emission present from 4000-4800Å. The relative filling factors of the two components indicate that the Balmer continuum comes from a larger region, plausibly originating from the flaring loops at chromospheric heights, where the Balmer lines originate. This is consistent with the height of the Balmer continuum emission derived from solar flare data (Hudson et al., 2010), and also with the height of formation predicted by the RHD model of A06.

We found that the blackbody emission arises from a region ∼3-16 times smaller in area than the Balmer continuum emission region. This blackbody emission may possibly originate in concentrated magnetic footpoint regions in the lower atmosphere, similar to the localized areas that emit in white light during solar flares (Metcalf et al., 2003; Fletcher et al., 2007; Isobe et al., 2007; Jess et al., 2008), which are often spatially and temporally coincident with impulsive heating by nonthermal electrons inferred from hard X-ray observations (e.g., Rust & Hegwer, 1975; Hudson et al., 1992; Neidig et al., 1993; Fletcher et al., 2007). In accordance with this scenario, a large complex of photospheric hot spots may have been created during the first impulsive events in the YZ CMi U-band light curve. As the nonthermal electron beams weakened (in energy and/or in spatial extent) so did the areal coverage of these hot spots. This gradual decay extends into the time covered by our spectral observations and is seen in the overall decline of the blackbody areal coverage in the upper panel of Figure 5.1d. During our spectral observations, a few new hot spots may have been created at the footpoints of newly reconnected loops, causing the transient increases seen in the U-band and in the effective area of the blackbody emitting region.

We see strong evidence through all of our observations for a blackbody continuum emission component with an approximate temperature of $10,000$K. The persistence of the hot blackbody emission indicates that a continual source of particle acceleration and plasma heating likely still exists during the decay phase of the flare. Yet, the A06 models, which employ a nonthermal electron beam as is seen on the Sun, predict the photosphere of an M dwarf to be heated by at most $\sim$1200K during a large flare. The physical mechanism which generates the strong blackbody emission (presumably from a more strongly heated photosphere) therefore remains unknown. The possible anti-correlation between the Balmer continuum and blackbody emission components may provide an important clue to the nature of the heating mechanism that is responsible for the blackbody emission.

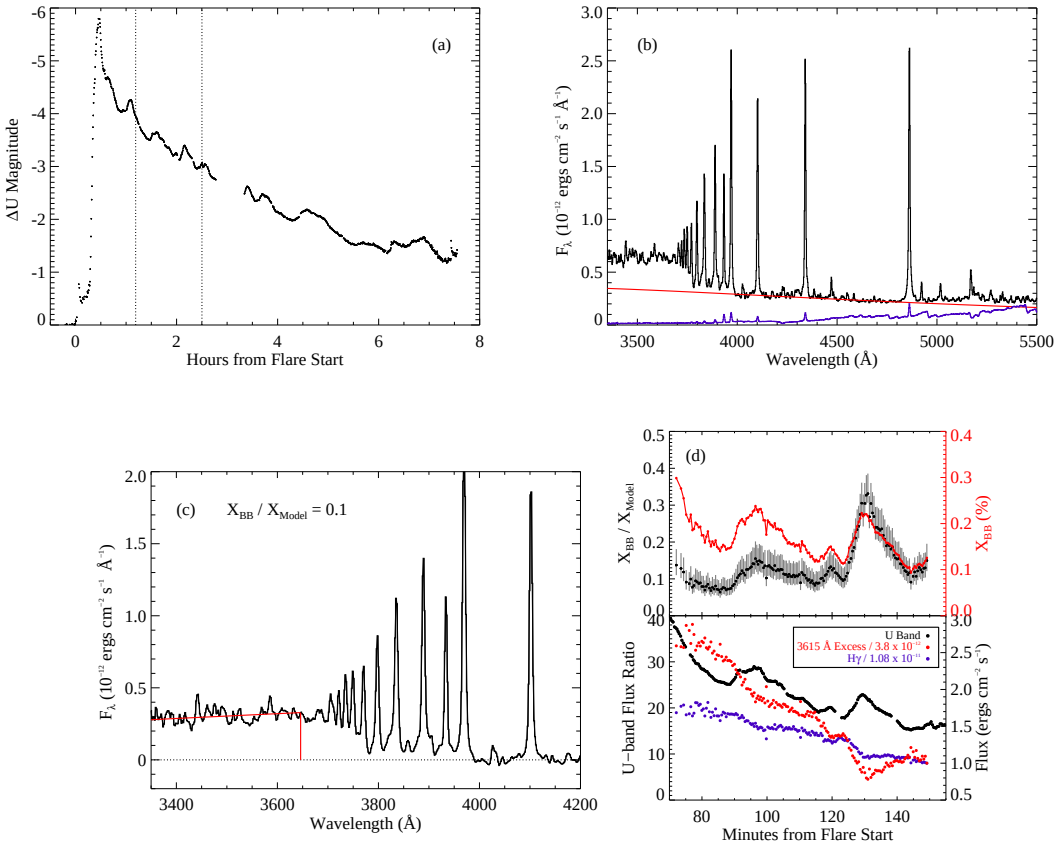

Figure 5.1 (a) The flare U-band light curve with vertical lines indicating the period of spectroscopic observations. (b) A flare spectrum at $t = 76.6$min after flare start. The quiescent spectrum is shown in purple for comparison. The continuum from 4000 - 4800Å was fit with a $T = 10,000$K blackbody and a filling factor of 0.22%. There is excess emission above the blackbody blueward of 3800Å. (c) The 10,000K blackbody component has been subtracted from the spectrum in panel (b) and the F11 flare spectrum from A06 fits the excess (Balmer) continuum at wavelengths shorter than 3646Å. (d) (upper panel) The filling factor ratio (X_{BB}/X_{Model}, black points) and the inferred area coverage of the blackbody component (red points). (lower panel) The time-evolution of the U-band (left axis), and the Balmer continuum and Hγ fluxes (right axis).

Chapter 6

BLUE CONTINUUM ANALYSIS

6.1 Two-Component Analysis of the Flare Atlas

We find convincing evidence that the two continuum components in Kowalski et al. (2010) (Chapter 5) account for nearly all of the NUV/blue continuum in both gradual and impulsive phases of all flares in our sample. The relative amount of each component is important for understanding the distribution of flare heating in the stellar atmosphere. In this section, we present a new interpretation of the blackbody component and apply it to the flares in our sample. Under this interpretation, we assume that the blackbody component is produced deep in the atmosphere, and therefore results in significant flux redistribution throughout the spectrum; this has been motivated by our finding in Kowalski et al. (2011a) (Chapter 6.6.1 of this dissertation) of a "hot-star" spectrum during a flare with absorption features present.

6.1.1 The Impulsive Phase Blackbody Emission

We find that typically only 10 – 18% of the flux in the peak spectra of the IF events is accounted for by Hydrogen Balmer emission (Figure 4.7). We attribute the unaccounted flux to blackbody emission that pervades the entire NUV, blue-optical, and red-optical zones. We calculate a color temperature, T_{BB} of the blue-optical continuum by fitting the flux using the windows from $\lambda = 4000 - 4800$Å (BW1 – BW6, similar to those used in Chapter 5) given in Table 3.1. We do not include the flux at shorter wavelengths due to the difficulty in determining bona-fide continuum from PseudoC and due to the contribution from the Balmer continuum. We do not include flux from redder wavelengths, because we find evidence for complicated behavior in the red-optical (Section 6.9). We fit the flux with a Planck function characterized by temperature ($T_{\rm BB}$) and filling factor ($X_{\rm BB} = R_{\rm fl}^2/R_{\rm star}^2$; as in Hawley et al. (2003) and Chapter 5) using the IDL routine *mpcurvefit*, where X is

the fraction of the visible hemisphere covered by the projected area of the flare[1]. The two parameters are fit simultaneously, an important distinction to the analysis from Chapter 5, which fixed $T_{\rm BB}$= 10 000 K. The fits for IF1 are redone here using the new flux scaling (Section 2.2.3), and some quantities change compared to those in Chapter 5. Good quality fits are obtained for the IF flares except IF6[2], the HF flares, GF1, GF3 (but see note about calibration in Section 3) and GF5.

In Section 3.2, we showed the flare spectra at peak times for all flares: Figures 3.8 – 3.11. The peak spectra exhibit a ubiquitous steeply rising continuum, which continues into the NUV beyond our spectral range. We find that this component is represented by a Planck function with $T_{\rm BB} = 10\,000 - 14\,000$ K for the IF flares (Figure 3.8). By comparing to the dotted (pre-flare) spectra we see that the hot, blackbody component is present for a variety of flare amplitudes, appearing in flares with peak U-band enhancements greater than $I_{f,U}+1 \sim$3, and as large as $I_{f,U}+1 \sim$80. The high signal-to-noise ratio of our spectra makes the characterization of this component possible even with relatively small contrast in the blue-optical at $\lambda > 4500$Å. The BB component contributes $\sim 74-96\%$, and on average 84%, of the $\lambda = 3420-5200$Å flux during the peak times for the IF flares. The peak spectra of the HF flares (Figure 3.10) also show the hot, blackbody component, with temperatures between $T_{\rm BB}\sim 9500-12\,000$ K. The lower amplitudes of these flares are noticeable, e.g., by comparing to the pre-flare spectra. The HF flares also have a conspicuous amount of excess emission above the extrapolated light blue curve at $\lambda < 3800$Å. Of the GF flares in Figure 3.11 only the large-amplitude, high energy gradual flare GF1 shows convincing evidence of a hot blackbody, with $T_{\rm BB}\sim$ 9000 K. A significant NUV excess is also present during this flare. GF3 shows evidence of a high temperature, but these data have an uncertain calibration (Chapter 3) so we do not include them in our analysis. We have averaged four spectra at the peak of GF5, which results in a relatively good fit, but with a lower temperature of $T_{\rm BB}\sim$6700 K. In GF2 and GF4, we cannot accurately ascertain the characteristics of the slope of the continuum; nonetheless, the very low-amplitude flares ($I_f + 1 \sim 1.3-2.2$,

[1]In Chapter 8, we study the difference between continuum intensity and flux.

[2]See note on calibration in Chapter 3

$|\Delta U| < 1$ mag; GF2 – GF5) do show excess C4170 emission.

The formation of a blackbody with $T_{\rm BB}\sim$10 000 − 12 000 K is independent of flare amplitude over a large range of peak U-band specific luminosities, total energies, and light curve morphologies. In Figure 6.1 (top), we show the distribution of T_{BB} at maximum continuum emission for the sixteen flares with well-determined temperatures. GF1 has a small-amplitude impulsive phase with a strong response in C4170 that occurs before the main peak that has $T_{\rm BB}\sim$9000 K (see Figure 4.11); the newly formed flare emission in this peak has $T_{\rm BB}\sim$14 500 and is included as GF1*ι*.

The ∼5% blue-continuum shape uncertainty coupled with the uncertainty in the scale factor, R (see Chapter 2 and Appendix A), and also the selection of continuum windows lead to systematic uncertainties in the blackbody temperatures of about 500 − 1000 K. In Chapter 5, we found a ±1000 K range in temperatures that represented the blue continuum shape. The statistical uncertainties for our data are ∼200 K. In Appendix F, we examine the detailed systematic errors involved with temperature fitting. The important result is that for IF2, the extreme amount of line broadening causes the BW1 and BW2 fitting windows to be possibly contaminated with Balmer wing emission; the acceptable range of $T_{\rm BB}$ for this flare is therefore 11 700 − 14 100 K (indicated on Figure 6.1), however, the temperature of 14 000 K better accounts for the shape of the total emission in the BaC. NUV data at the peak of the continuum would allow for more precise determinations of the blackbody temperatures.

A note about fitting a Planck function with $T_{\rm BB}$= 10 000 − 12 000 K in this wavelength region: this temperature range implies a peak at ($\lambda_{\rm peak} = 2400-2900$Å), which is consistent from NUV and FUV photometry of flares that indicate a turnover in the spectrum (Hawley & Pettersen, 1991; Hawley & Fisher, 1992; Hawley et al., 2003). However, the blue-optical zone in the current study is not quite red enough to be in the Rayleigh-Jeans tail approximation ($h\nu \sim 3 - 4 \times kT$ not $<< kT$ at the blue-optical wavelengths). Therefore, the spectrum would not be expected to strictly follow a λ^{-4} slope according to the Rayleigh-Jeans law. Instead, a linearly decreasing fit to the blue gives a reasonably good fit and looks very similar to the Planck function at these wavelengths ($\lambda = 4000 - 5000$Å). That is, in the $\lambda^{-5} \times (e^{hc/(\lambda kT)} - 1)^{-1}$ part of the Planck function, the steeply decreasing λ^{-5} multiplies

the increasing exponential part, giving a linear decrease. The similarity in the fits between a linear and Planck function is illustrated for the peak spectrum of IF9 in Figure 3.2.

6.1.2 Impulsive Phase Balmer Continuum Emission

There is always excess flux in the NUV zone, above an extrapolation of the Planck function at these wavelengths. As explained in Section 3.1.2, we use the BaC3615 quantity as a measure of this excess flux. In the first column of Table 6.1, we give the ratio of BaC3615 to C3615. The IF, HF, GF events are generally ordered according to this quantity with larger ratios of $\sim 0.5-0.8$ occuring at the peaks of the HF and GF events. The IF events have typical values of $0.2-0.33$, but some (IF5, IF6) also have large excesses of ~ 0.4 or greater. The IF4 event has an anomalously low ratio of 0.05.

The slope of the total NUV spectral zone emission at peak generally follows the same slope as the underlying Planck function. In Figures 3.8 - 3.11, we scale the Planck function to the flux at C3615, and show this in yellow matching the flux at $\lambda < 3646$Å, illustrating that the overall shape of the continuum at $\lambda < 3646$Å for the IF, HF, GF1, GF2, and GF5 events can be represented by about the same temperature fit as for the blue-optical. We measure the slope of the NUV flare emission at $3420 \leq \lambda \leq 3630$Å by fitting a line to three wavelength bins in this region. These values are given in Table 6.2 (columns 2 and 3), and indicate that the emission is blue for the IF and HF events, as we found by scaling the blackbody functions (yellow curves). The flux calibration errors in the NUV are larger ($\sim 5-10\%$), and the statistical uncertainties in the fits can also become comparatively large, and higher signal to noise measurements should be obtained in the NUV. Nevertheless, the spectral slope of the total flux at $\lambda < 3646$ matches the blackbody slope, which is an important aspect for modeling the NUV as a combination of blackbody *absorption* and Balmer continuum emission, because the Balmer continuum emission component has a much flatter slope than the blackbody (see Section 7.5.3) at these wavelengths.

Although the *total* flux at $\lambda < 3646$Å follows the same general slope as the underlying blackbody, we attribute the *excess* flux in the NUV to chromospheric Balmer continuum (BaC) radiation from Hydrogen recombination. To model the flare Balmer continuum, we

use the impulsive-phase RHD model spectrum at $t = 15.9$ sec from the F11 simulation of Allred et al. (2006), as in Chapter 5. We have subtracted a linear extrapolation of the blue-optical zone to estimate the amount of flux originating from only the Balmer continuum. We refer to this model Balmer continuum as BaCF11, whereas we refer to the total Allred et al. (2006) ($t = 15.9$ sec) RHD F11 model spectrum as RHDF11[3]. As with the blackbody component, we calculate a filling factor for the Balmer continuum by scaling the BaCF11 to the BaC3615 flux observed at Earth; the filling factor is denoted by $X_{\rm BaCF11}$. We note that at peak in some flares (IF2, IF3, IF9), the slope of the excess flux is still blue (columns 4 and 5 of Table 6.2) and is not consistent with the red slope of the BaCF11 ($\sim$5, bottom of Table 6.2). This finding implies that our understanding of the impulsive phase Balmer continuum is *not* complete, although we assume here (for lack of a better model) that it is represented by BaCF11.

In Chapter 8, we discuss in detail the plasma conditions that give rise to the model BaC. We find that the BaC originates from a range of column masses where the electron density and chromospheric temperature structure are strongly coupled. Thus a simple isothermal slab (e.g., Kunkel, 1970) does not provide an accurate estimate of the plasma conditions describing or the Balmer continuum originating from a real atmosphere. RHD models are required to give physically self-consistent values.

6.1.3 Filling Factors

Larger U-band emission at peak is due to a combination of both increasing blackbody and BaC areal coverage. In Figure 6.1 (bottom) we show the distribution of $X_{\rm BB}$ and $X_{\rm BaCF11}$ at flare maximum. The blackbody component shows an areal coverage ranging from 0.005% (HF3, $I_{f,U} + 1 \sim 3$) to 0.27% (IF3 $I_{f,U} + 1 \sim 78$) of the visible stellar hemisphere, a range of $\sim$50x in area coverage. The Balmer continuum emitting region is also compact, though larger than the blackbody component, originating from $\sim$0.05% to 1.7% of the visible stellar hemisphere.

A strong trend exists between the projected areal coverage of the blackbody component

[3]RHDF11 is the total RHD model prediction including BaC, PaC, and backwarming whereas BaCF11 is only the Balmer continuum prediction

at peak, $X_{\rm BB}$, and the U-band peak specific luminosity[4] over $\sim$2 orders of magnitude in peak specific luminosity. Due to a steep dependence of the Planck function on temperature, small variations in temperature may also lead to a larger U-band peak; we consider that slightly increasing temperature also contributes to increased amounts of U-band emission in Section 6.7.3.

The ratio of the inferred surface area coverages, given in Figure 6.2 (black), is $1-26$, with the apparent amount of BaC originating from a larger area than the blackbody. The range of $3 \leq X_{\rm BaCF11}/X_{\rm BB} \leq 15$ is found to represent most flares at peak emission; this range was also found during the decay phase of IF1 in Chapter 5, as the flare went through successive impulsive and gradual phases of secondary flares. The largest luminosity flares have areal ratios of $\sim 1-10$. Ultimately, the areal ratios in Figure 6.2 are rather unconstrained by the data, due in large part to the uncertainty in the area of the Balmer continuum. We discuss the reasons for the uncertainty in the Balmer continuum in detail in Section 6.1.6. A major source of uncertainty is rooted in the amount of possible *absorption* from the blackbody component. Due to flux redistribution in the atmosphere, the areal coverages of the blackbody component are larger than for a Planck function. We find that the inferred ratios would decrease as a result due to flux redistribution and wavelength-dependent opacities, and we now investigate this further.

6.1.4 Filling Factors of the Blackbody Emission Component using Model Hot Star Atmospheres

An important concern is that real stellar atmospheres do not produce featureless blackbodies. This affects the inferred areas from fitting a Planck function to the flare emission; in this section, we investigate the corrections obtained from models of hot star atmospheres, and we find that the areal coverages in Section 6.1.3 increase by a factor of $1.4-3.1$ for the peak temperatures of the flares in our sample.

The fits to the blue-continuum zone were done with isothermal, optically thick, thermal radiation (i.e., blackbody radiation). An important distinction must be made between

[4]obtained from the nearest photometric data point

the color temperature T_{BB}, the effective temperature of the flare atmosphere, T_{eff}, and the temperature at a given column mass of the atmosphere that is emitting the observed radiation. The $T_{\rm BB}$ used in the fitting is simply an observational diagnostic of the continuum slope. From modeling hot stars with this $T_{\rm eff}$ range, we know that the observed wavelength-dependent radiation is generated over a range of temperature and column mass as demonstrated by the contribution function (Carlsson & Stein, 1997, see discussion for flare atmospheres in Cram & Woods (1982)). Vega, for example, has a well-known effective temperature of 9500 K, but the slope of the blue-optical matches a blackbody slope with $T_{BB} \sim 16\,800$ K. For Vega, the flux re-distribution results from the wavelength-dependent Hydrogen Balmer and Paschen opacities (Mihalas, 1970), such that the flux at C4170 originates from a deeper, hotter layer than the flux at C3615, hence, giving the appearance of the Balmer jump in "absorption". The gravity of an M dwarf is at least an order of magnitude higher than for hot stars, and so we do not expect the optical flux distribution to originate from such a large range of column mass.

In Figure 6.4 (top), we show the relation between the measured color temperature and the implied effective temperature that would generate the same amount of bolometric flare energy taking into account flux redistribution in the flare atmosphere. We show curves for different values of the gravity; log $g = 5$ for M dwarfs is shown as the red curve. We have obtained these values from the Castelli & Kurucz (2004) model stellar atmospheres (thereby, temporarily assuming a chromosphere-less, corona-less M dwarf), and we measured the slopes in similar continuum regions as for the measurements of the flare spectra (Table 3.1). The color temperatures of $9000-14\,000$ K for log g = 5.0 imply effective temperatures of $7700-9400$ K, a relatively narrow range of temperature. This effective temperature range also implies a factor of $\sim$1.8 in the range of bolometric surface flux at peak time among the flares. The values on the top axis indicate the bolometric surface flux ($\sigma T_{\rm eff}^4$), which will provide important constraints for new flare models (Chapter 8).

In Figure 6.4 (bottom), we show the ratio of the surface flux at $\lambda = 4500$Å for a blackbody and Castelli & Kurucz (2004) (log $g = 5$) model for a given $T_{\rm BB}$. This ratio gives the adjustment to the $X_{\rm BB}$ that must be applied to give a surface coverage using a Castelli & Kurucz (2004) hot-star model, $X_{\rm CK}$. Thus, if a color temperature of 12 000 K is found

by fitting a Planck function to a flare spectrum, and a scale-factor, $X_{\rm BB}$, from that Planck function is used for the surface area coverage of the flare region, the surface area coverage of the flare area is likely underestimated by a factor of $1.5-2$, *if* the flare region has the same flux redistribution properties as a high-gravity hot star atmosphere. For the range of temperatures of $9000-14\,000$ K at peak emission in our sample, the resulting corrections are between $1.4-2.3$. We show the corrected $X_{\rm BB}$ in the bottom of Figure 6.1 (red circles) and the corrected ratio with $X_{\rm BaCF11}$ in red asterisks in Figure 6.2. The ratio of areal coverages after applying the area corrections (denoted by "CK") ranges between $2-8$ for twelve out of the sixteen flares with well-determined blue-optical temperatures. Hereafter, we continue to refer to the primary white-light continuum component as "blackbody", for simplicity, although we mean "a continuum with Hydrogen Balmer absorption features that matches the slope of a blackbody function from $\lambda = 4000-4800$Å".

6.1.5 Filling Factors with Model "Hot Spot" Atmospheres

One striking implication for the CK models is that under this interpretation the measured amount of Balmer continuum flux (i.e., BaC3615) could be as much as three times smaller than the intrinsic amount of Balmer continuum emission originating from the flare chromosphere. In other words, a line extrapolation from the blue optical may vastly underpredict the true amount of Balmer continuum. In Chapter 7 (Kowalski et al. (2012)) we will model the MDSF2 total flare emission as a sum of the RHDF11 model and a phenomenological "hot-spot" model. The phenomenological hot spot models are rather similar to the CK hot star models analyzed here: they show the Balmer features in absorption and have a blue-optical color temperature of $11\,500-18\,000$ K due to flux redistribution from wavelength-dependent opacities. These models are discussed in detail in Chapter 7, but we note here that they also predict that we do not account for all of the Balmer continuum chromospheric emission using a linear extrapolation from the blue-optical zone. A hot star model and a hot spot model with the same blue-optical shape have $\chi_{\rm flare}\sim$0.45 and 0.8 respectively; therefore, the hot star model predicts more "missing" Balmer continuum emission than a hot spot model.

The CK models may not be the only source of the total blue-optical (e.g., C4170) flare continuum emission at $\lambda > 3646$Å at peak times during flares. The RHDF11 model predicts continuum flux at $\lambda > 3646$Å. Therefore, the observed total amount of C4170 flux at a given time during the rise of MDSF2 is not due only to a hot-spot model, but instead is a sum of the RHDF11 continuum *and* the hot-spot model; the hot-spot model alone will account for the flux of the newly formed flare emission only, but this too represents an average temperature over the entire flare region. As a result the filling factor of the hot-spot model would be less than if the hot-spot emission was the only source of continuum emission at wavelengths longer than $\lambda = 3646$Å.[5]

Therefore, the blackbody areal coverages are upper limits in Figure 6.1. If the hot-star models *are* the only source of blue-optical continuum, we estimate that the intrinsic areas of the BaCF11 are three times larger than what we calculate from BaC3615, due to filled-in absorption. In Figure 6.3, we show the modeling of the continuum for the IF2 peak spectrum (S#542) using a Planck function (light blue), a hot star model (green), and a hot spot model (dashed purple). The detailed shape of the Balmer continuum absorption needs to be modeled properly (e.g., Chapter 7) in order to understand how much chromospheric Balmer continuum is "missing" using an extrapolation from the blue optical to calculate BaC3615. We suspect that if the blackbody was the only source of blue-optical continuum, the absorption signatures would be more prominent in flare spectra; even in giant flares, such as IF3 and IF4, the absorption phenomena only become measurable at peak emission when the blackbody has reached an areal coverage of $\sim$0.2% of the visible stellar hemisphere (corresponding to a physical area of $\sim 3 \times 10^{18}$ cm^2).

We model the flare spectra with hot-spot atmospheres in Chapter 7.

---

[5]Even during MDSF2, the temperature of the newly-formed flare emission (ie., Vega) is an average temperature; if the flare is increasing in area and temperature, the blackbody fit is an average over all the flare area emitting at that time, including area that may be decaying from the previous spectrum. It is not apparent how to deal with this degeneracy involving 2D spatial variation in temperature during a rise phase. In the other flares in the sample, this is more of a concern because only in MDSF2 could we isolate the blackbody component. The "Conundruum" (see Section 6.8) is an indication during the impulsive phases of other flares that additional continuum components are present at a low level in the blue optical, as in the *total* flare emission during MDSF2. We discuss this in the Chapter 7.

6.1.6 Summary of Uncertainties in the Filling Factors of Each Component

In this section we summarize the uncertainties in determining filling factors in Figure 6.1 and Figure 6.2. The areal coverages of the blackbody emitting region is now better constrained due to the CK corrections, but the values in Figure 6.1 may be upper limits due to other unaccounted continuum emission at blue-optical wavelengths (Chapter 7). The systematic and statistical uncertainties in fitting temperatures are a concern, but the systematic uncertainties dominate and these are no larger than ∼30% (Appendix F).

The dominant uncertainty in Figure 6.2 is the area of the Balmer continuum emitting region. First, $X_{\rm BaCF11}$ depends on our selection of the F11 model to represent the Balmer continuum. The filling factor ratio ($X_{\rm BaCF11}$/ $X_{\rm BB}$) increases for lower assumed beam fluxes and decreases for higher beam fluxes. Using the Balmer continuum from the F10 RHD model of Allred et al. (2006), the inferred areal coverages of the BaC-emitting region would then by 8 times larger than the F11 model. The model BaC shape is *not* constrained from the observations due to the very small differences: $< 2\%$ in the shape of the BaCF11 and BaCF10[6] between $\lambda = 3300-3646$Å. We are seeking to determine a method for constraining the appropriate model of the BaC in a given flare (Chapter 8). In Chapter 8, we discuss the shape and inferred areas using a F12 Balmer continuum.

Second, the filling factor of the BaC is uncertain due to the amount of hot-star absorption that would cause the measured BaC3615 to be less than the actual amount of BaC3615. This uncertainty is likely largest at peak when the blackbody component is hottest and has the largest area. Recall that $X_{\rm BaCF11}$ is calculated directly from BaC3615; accounting for BaC3615 that has filled in ("veiled") the blackbody absorption would increase the ratio. IF4 may be an instance of complete veiling, with very little apparent BaC3615[7].

Third, a more accurate modeling of the energy deposition by nonthermal electrons would take into account the pitch-angle distribution of electrons via the a Fokker-Planck beam formulae. Because the energy deposition is not as localized in the chromosphere, employing

---

[6]Like BaCF11, BaCF10 refers to the Balmer continuum from the RHD model that has the extrapolation from the blue-optical subtracted.

[7]However, recall these observations were taken at high airmass; nonetheless, it is curious that later in the flare, at higher airmass still, there is obvious Balmer continuum in emission

these formulae for a given beam flux would likely require the areas of the RHD Balmer continuum to be larger to account for the observed emission (Mauas & Gomez, 1997; Allred et al., 2006).

Therefore, the values of $X_{\rm BaCF11}$ (and $X_{\rm BaCF11}/X_{\rm BB}$) are only given as a rough guide to the actual flare areas, indicating that both sources have a compact geometry, or that the emission observed is dominated by radiation from a compact geometry. Detailed modeling using Fokker-Planck formulation and using an observational diagnostic to constrain the beam flux (F10 vs F11 vs F12) are necessary for accurately determining how the geometries are different for the Balmer continuum and blackbody emitting regions. However, we predict that accounting for all the aforementioned effects would ultimately *increase* the ratio of Balmer continuum emitting area to blackbody emitting area, given that the CK (or hot spot model) model corrections are applied.

6.2 The "Local" and "Global" Energy Budget of the Blackbody

The blackbody component is an energetically important contribution to the white-light continuum. Therefore, knowing its bolometric energy provides a useful guide for total heating amounts in RHD models, which predict the entire XEUV through far-IR spectrum (see Chapter 8). Hawley et al. (1995) considered two flares on AD Leo with $E \sim 3-5\times10^{33}$ ergs and calculated total energies in the blackbody component to be $> 2-10$ times the (coronal) thermal energy during the flare impulsive phases. A possible concern however, is that the flux redistribution in the blackbody component could cause one to miscalculate the bolometric flux when using a smooth Planck function to fit the entire blue-optical spectral zone. However, the flux redistribution may only be very significant near the peak of the flare when the blackbody component is hottest and has the largest areal coverage (e.g., Kowalski et al., 2012).

In Figure 6.5, we show a tight relationship for the flares in our sample between the time-integrated specific energy in C4170 ($\mathcal{E}_{\rm C4170}$) and the $\lambda = 3420-5200$Å energy of the blackbody function used to fit the $\lambda = 4000-4800$Å region ($E_{\rm BB}$). The relation is

$$E_{BB} = 1230 \times \mathcal{E}_{C4170}^{1.00} \tag{6.1}$$

where $E_{\rm BB}$ is the flux of the blackbody fit integrated from $\lambda = 3420$Å to 5200Å, integrated over the duration of the flare, and multiplied by $4\pi d^2$. This implies that if the flux is measured locally in the blue-optical for a given flare, the energy of the continuum throughout the entire $3420 - 5200$Å region can be estimated fairly well. Only the IF flares from DIS were used for this fit; however, the HF flares also fall near the relation. Note, the GF2 flare doesn't match well, but when its two main events are considered separately (red squares), the match is much better. This relation can be used to calculate total energies of the blackbody component for single-filter ULTRACAM data of stellar flares (Kowalski et al., 2011b) and ROSA data of solar flares (Christian et al. 2012, in prep).

Although numerous Fe I and Fe II lines are likely present in C4170 (Paulson et al., 2006; Fuhrmeister et al., 2011), we calculate that they contribute at most 10% of the C4170 flux in the decay phase and $< 2\%$ during the peak phase. Section 4.9 describes this contribution in more detail. The Fe I and Fe II line features in the C4170 region cause the error bars in $\chi_{\rm flare}$ to be larger than the standard error in the mean.

6.3 Explaining $\chi_{\rm flare,peak}$ using the Blue/NUV Continuum Components

In this section, we analyze the observed $\chi_{\rm flare}$ values in terms of single continuum component and two-continuum component emission models. In Figure 3.12, we showed that the evolution of the impulsive phase (characterized by $\mathcal{I}$) is connected to the steepness of the NUV/blue continuum at maximum emission (characterized by $\chi_{\rm flare,peak}$=C3615/C4170). We also showed that $\chi_{\rm flare,peak}$ is *strongly* related to the ratio of the Hγ line flux to C4170 (Figure 3.13). In the flare sample, $\chi_{\rm flare}$ and the Hydrogen Balmer (HB) contribution were found to increase from peak to decay phases (Figure 4.7). The detailed time-evolution of IF1 (Figure 4.6) showed that both the HB component and $\chi_{\rm flare}$ are anti-correlated with the total emission. The two component continuum model explains the trends in $\chi_{\rm flare}$ and Hydrogen Balmer emission.

Single component continuum models are consistent with the lowest values of observed $\chi_{\rm flare,peak}$ ($\sim$1.6) only for very hot ($> 10^5$ K) temperatures. In Figure G.1 of Appendix G, we show the $\chi_{\rm flare}$ values for single component models. In single component, isothermal optically thick blackbody models, larger values of $\chi_{\rm flare}$ imply hotter temperatures and

smaller values cooler temperatures, and at arbitrarily large temperatures, $\chi_{\rm flare}$ approaches 1.77. The values of $\chi_{\rm flare}$ for $T < 14\,000$ K are less than 1.4. However, isothermal blackbody functions do not give good fits to the entire blue/NUV continuum for even the flares with $\chi_{\rm flare,peak}$<1.8. Even without the spectral information, we know that blackbodies cannot account for the continua in any gradual phase, since $\chi_{\rm flare,decay}$>2.2. Balmer continuum is needed to explain the observed $\chi_{\rm flare}$ values. In single component, isothermal optically thin Hydrogen (bf+ff) models, larger values imply cooler temperatures (Kunkel, 1970) (reproduced in Figure G.1). The observed values of $\chi_{\rm flare}\sim 1.5-4$ argue against these single component models for a reasonable range of chromospheric temperatures and densities. Kunkel (1970) reached the same conclusion: a single component Hydrogen bf+ff model could not explain the redder colors of flares in $U-B$, $B-V$ color-color diagrams.

As we have shown, $\chi_{\rm flare}$ can be modeled with a two-component continuum model with a reasonable BaC model (BaCF11) and a blackbody temperature that is consistent with many past continuum measurements. $\chi_{\rm flare,peak}$ is a simple measure of the continuum steepness that traces the relative evolution of the blackbody and Balmer continua. The $\chi_{\rm flare}$ evolution is consistent with a two-component white-light continuum with $\chi_{\rm flare,peak}$=(BaC3615 + BB3615) / BB4170, where BB3615 and BB4170 are the blackbody fluxes at $\lambda = 3615$ and 4170Å, respectively. Flares that have larger $\chi_{\rm flare,peak}$ also have larger relative contributions from the Balmer continuum component. At peak, IF events have smaller $\chi_{\rm flare,peak}$ and are more dominated by the blackbody component. Because the BaC is relatively small at peak, the $\chi_{\rm flare,peak}$ is closer to the value for the single component isothermal blackbody of that temperature: any BaC present leads to an increase of the $\chi_{\rm flare}$ value from the value for that blackbody temperature. The evolution we see in $\chi_{\rm flare}$ is explained by the variation in the relative contribution from Balmer emission. $\chi_{\rm flare}$ is a straightforward measurement to compare models and observations. Our results indicate that RHD models seeking to explain the blackbody component at the peak phase must produce $\chi_{\rm flare}= 1.5-2$ with the total Hydrogen Balmer (line and continuum) contribution $\sim$15% of the wavelength integrated ($\lambda = 3420-5200$Å) energy.

Since the "blackbody" component in flares is not a featureless Planck function, the $\chi_{\rm flare}$ is affected by the amount of blackbody absorption at C3615: as demonstrated by

IF1, the $\chi_{\rm flare}$ for a pure blackbody with $T_{\rm BB}$∼16 000 K and a BaCF11 is larger than for a hot-star spectrum (also $T_{\rm BB}$) plus a BaCF11 model. A current aim of this chapter and future studies is to answer the following question: *what is the threshold of* $\chi_{\rm flare}$ *that signifies hot star absorption forming during the flare?* The lowest $\chi_{\rm flare,peak}$ values are 1.5 – 1.6, and these flares show the evidence of Balmer absorption. At values higher, >1.8, the Balmer continuum and Balmer line wings with a chromospheric origin may veil any possible absorption. According to our hot-star modeling, the absorption should still be present in relatively large amounts (see Figure 6.3).

6.4 Global Continuum Trends: C4170 vs. BaC3615

Here, global trends between peak emission in the C4170 and BaC3615 specific luminosities are established for the IF, HF, and GF events. By reproducing the peak properties of all three groups, models can be used to determine the important physical mechanisms that vary from one type of flare to another. The time evolution of the continuum components can also be directly compared to RHD models with a gradual phase. Also in this section, we will show that the U-band properties jointly depend on the BaC3615 (primarily via total energy) and the C4170 (primarily via peak luminosity).

The peak specific luminosities of C4170 and BaC3615 are shown in Figure 6.6. A 1:1 relation is shown as the dotted line. In general, the IF events are more luminous in C4170, the GF events are more luminous in BaC3615 and the HF events are slightly more luminous in BaC3615. The points are color-coded by the $\chi_{\rm flare,peak}$, and the red numbers indicate the ratio of Hγ flux to C4170. This diagram sorts the flares also by $\chi_{\rm flare,peak}$, indicating that flares with larger $\chi_{\rm flare,peak}$ have larger amounts of Balmer continuum emission and larger relative amounts of Hγ line emission. The flares that are equally luminous in C4170 and BaC3615 (IF5, IF6) also have large $\chi_{\rm flare,peak}$ values.

These trends could be related to the amount of absorption produced at peak. The relationship between $\chi_{\rm flare,peak}$ and the two continuum components was established previously in Section 6.3. A smaller $\chi_{\rm flare,peak}$ results from a more dominant blackbody component; if this blackbody component has absorption at $\lambda < 3646$Å, then the amount of BaC3615 that we measure is less than if there isn't any absorption; absorption at peak – therefore

low BaC3615 – is a consistent scenario with the IF flares that have low $\chi_{\rm flare,peak}$ (the blue points) on this plot. The green and red points either produce intrinsically more BaC3615 than the blue points, or they produce less BaC3615 absorption. We cannot discern these two scenarios without detailed modeling.

In Figure 6.7, we show the specific luminosities during the extended gradual phases in asterisks, with lines connecting the values at peak continuum. The gradual phase has greater BaC3615 emission compared to C4170; all flares cross the 1:1 line. In other words, all flares have prominent Balmer continua during the decay phase, whether or not they have prominent Balmer continua during the peak phase. This has profound implications for understanding the flare mechanism: *all flares produce Balmer continuum in emission, but some flares produce only a small relative amount during the peak phase.*

The slopes in log-log space and the slopes in linear-linear space uniquely tell us about flare evolution. To the eye, all slopes in log-log space are flatter than the 1:1 line, indicating that there is a larger percentage drop in the C4170 than in the BaC3615. The C4170 rapidly decreases, but does not disappear entirely, after the peak phase, whereas the BaC 3615 experiences a smaller percentage (slower) decrease. These properties can be seen qualitatively in the light curves of C4170 and BaC3615 in Figures 3.15 - Figure 3.18 and in Figures 4.8 - Figures 4.10.

The slopes of the lines connecting the peak and gradual phases are sorted and displayed in the lower right of the figure. In linear space, the slopes sort the flares according to the general IF/HF/GF classification. The values indicate a larger decrease in C4170 relative to the decrease in BaC3615 for the IF flares. HF1 and HF2 have approximately equal amounts of decrease in BaC3615 and C4170 and the GF flares have a larger amount of decrease.

The light blue star indicates the values for the newly-formed (Vega-like) spectrum just before the peak of MDSF2 (S#113). Interestingly, it falls along the general sequence extrapolated from lower energy flares. The dark blue circle for IF1 represents the values derived from the *total* S#113 flare spectrum just before the peak of MDSF2.

6.5 Connecting the Components to the U-band

A large range of flare properties are observed in the U-band. We now seek to connect these properties – in particular, the morphology, the peak specific luminosity and total energy of the U-band – to the individual properties of C4170 and the BaC3615. In the future, with self-consistent models that can explain both components, we should be able to tweak the flare parameters to be able to reproduce the gamut of flare morphologies.

- **U-band Morphology** In Chapter 5, we showed that the blackbody component contributed to C4170 and that $X_{\rm BB}$ traced the evolution of the U-band; thus, C4170 also traced the evolution in the U-band. The U band encompasses the NUV and intermediate spectral zones. The blackbody is measured in the blue-optical zone but it extends into the NUV zone. The BaC is also observed in the NUV zone. Thus, the U-band evolution must be related to the evolution of both C4170 (the blackbody flux in the blue-optical zone) and BaC3615.

  In Table 6.1, we give the ratio of BaC3615 to C3615 at peak continuum emission; these values relate how much the BaC3615 contributes toward the total continuum emission at this wavelength near the center of the U-band. In Figure 6.8, we plot BaC3615/C3615 and find a sharp separation between the IF, HF, and GF flares. There is a general decreasing trend with peak specific U-band luminosity, but there is a range of values within each class, especially for the IF events. The IF events are least dominated by BaC3615 ($0.2-0.35$) and are most dominated by the blackbody emission component which also contributes to the flux at C3615. Again, the IF5 and IF6 events stand out as having larger values ($\sim$0.4). The HF events have about equal contributions ($\sim 0.5-0.6$ of the C3615 flux is contained in BaC3615), and the GF events have the majority of their peak U-band emission ($0.55-0.8$) in Balmer continuum emission. Thus, the general morphology in the U-band is related to how much the Balmer continuum contributes at the peak of the flare. Of the ten large-amplitude events ($\log \mathcal{L}_U > 26.5$ ergs s^{-1} Å^{-1}, nine are IF events and eight have BaC3615/C3615 $<$0.35. The distribution in this plot is similar to the distribution of

$L_U/L_{\mathrm{H}\gamma}$ at peak emission (Figure 4.3, top panel), implying that the ratio of BaC3615 to C3615 indicates a similar emission process (from a similar emitting region) as the ratio of Hγ to U-band. Although not shown, we also note that the ratio of BaC3615/C3615 correlates well with the ratio of Hγ to C4170.

We therefore conclude that the slower evolution of the GF events is due to a larger influence from the BaC, which is slower than the blackbody component (as characterized by $t_{1/2}$, Figure 4.12); conversely, the faster evolution of the IF events is due to the dominance of the blackbody, which evolves the quickest as diagnosed by C4170. The HF events are intermediate because of the approximately equal contributions to the U-band at peak. Due to the largely different timescales among the spectral components, the relative amounts present at peak are related to the overall light curve morphology. This helps us understand to what degree one flare is a "scaled up" version with larger area compared to another flare. That is, one must independently consider the degree to which the Balmer continuum emitting region and blackbody emitting regions are scaled between two flares of similar and different morphologies. Referring to solar flare structures, there may be a different scaling between compact, transient blackbody-emitting kernels and extended, long lasting Balmer emitting ribbons.

- **Peak U-band Luminosity**

In Figure 6.9, we show the peak flare specific luminosities of C4170 and BaC3615 (the same quantities plotted in Figure 6.7; from the spectra) against the U-band specific peak luminosity (from photometry) over 2.5 orders of magnitude. The 1:1 line (dashed line) is shown to give the reader an idea of the BaC3615 contribution to the U-band at the peak. The differences between the line and the BaC3615 data points are the approximate amounts of blackbody at $\lambda = 3615$Å. The best-fit to each distribution (for the DIS sample only) is shown as black and light blue lines, indicating different slopes for the distributions: 1.10±0.05 for C4170 (light blue) and 0.69±0.06 for BaC3615 (black). The slope indicates that the U-band flux is almost completely dominated by BaC at U-band specific luminosity of $\log \mathcal{L}_U \sim 25.7$ ergs s^{-1} Å^{-1} (which corresponds to

a U flux enhancement of $I_f + 1 = 2$ for YZ CMi's quiescent luminosity). Furthermore, as the flare peak becomes larger in U, the amount of C4170 becomes increasingly larger, supported by the slope differences. A slope of 1.1 for the C4170 indicates nearly equal percentage scalings between the U-band and C4170 between flares. For example, if the U-band is 5 times larger between flare A and flare B, then C4170 is 5.5 times larger whereas BaC3615 is only 3.5 times larger. The scatter in Figure 6.9 about the best fit lines is also somewhat smaller for C4170 (0.13 dex) compared to the scatter around the BaC3615 relation (0.18 dex). Thus, the peak C4170 is better correlated with the U-band peak luminosity, whereas in Section 4.1.2 (Figure 4.3), we found that the peak luminosity of the BaC3615 component of the U-band is better correlated with Hγ.

It is characteristic, though not always true, that the IF flare C4170 values lie above the light blue line, but the highest energy flares lie slightly below the blue line, suggesting that some flares like IF3 produce more U-band than would be expected based on the C4170 properties.

Finally, the steeper C4170 relation compared to the BaC3615 may indicate the presence of increasing amounts of absorption at $\lambda < 3646$Å, causing both the C4170 to increase faster than the U band and also causing us to underestimate the amount of BaC3615. The best-fit lines cross at log $\mathcal{L}_U \sim 26.4$ ergs s^{-1} Å^{-1} (at the point where most flare have BaC3615 / C3615 ≥ 0.5, Figure 6.8); for a given U-band luminosity greater than this, the trends predict more C4170 than BaC3615. At this point, the peak U-amplitude starts to become more influenced by C4170. Spectroscopic data between log $\mathcal{L}_U = 27 - 28$ ergs s^{-1} Å^{-1} ($|\Delta U| > 3 - 4$ mags) would be useful for understanding if indeed absorption effects become important at this threshold, leading to the shallower trend with the BaC3615.

- **Total U-band Energy**

In Figure 6.10, we show the trends for the time-integrated specific energy ($\mathcal{E}$) of each measure. The 1:1 line is again shown, and the use of specific energies lets one directly

compare the absolute levels. The distributions are much tighter here. In contrast to Figure 6.9, the BaC3615 shows a tighter correlation with the U-band energy. The slopes of the best fit lines are 0.97±0.05 and 0.88±0.15 for the Bac3615 energy and C4170 energy, respectively – in other words, both ∼1 within the errors.

In summary, the time integrated values of the U-band are well-correlated with both BaC3615 and C4170, whereas the peak luminosity of the U-band is more strongly influenced by C4170. In log-log space, the scatter is apparently less for both components in their total energies, compared to the peak luminosities. This suggests that overall the total energy scales between flares, but that the energy is released at different rates and at different times in the two components – C4170 mostly during the impulsive phase and BaC3615 moderately during the impulsive phase but more significantly over the gradual phase evolution. These effects can be seen qualitatively in Figures 3.14 - 3.18 where the normalized evolution of the C4170 and U band are very similar in the impulsive phase but they start to diverge in the gradual phase, when the U-band becomes more strongly influenced by the presence of the Balmer continuum, which takes longer to decay.

- In both figures, we consider the relation among the DIS classical flares with $\chi_{\rm flare,peak}$ of $1.6 - 1.8$ – IF2, IF3, IF7, IF8, and IF9 (red stars are used to indicate them in Figure 6.9 and 6.10). They do show a stronger trend with the U-band with a slope of 0.98 ± 0.03 ($\mathcal{L}_{C4170}$ vs $\mathcal{L}_U$) and 0.92 ± 0.01 ($\mathcal{E}_{C4170}$ vs $\mathcal{E}_U$). In other words, classical flares show nearly equal percentage increases in peak specific luminosity and total specific energy in C4170 (blackbody) and the U-band over 2.5 orders of magnitude in U-band energy. There is evidence for the relation with peak luminosity being stronger among these flares, with a slope closer to 1 than for total energy. The peak U-band is therefore largely determined by the blackbody presence in these cases, and we conclude there must be a stronger influence from the Balmer continuum in the other flares. Note that IF5 is a classical flare that does not fall on the relation with these five IF flares due to a larger amount of BaC (and larger $\chi_{\rm flare}$) at peak.

6.6 Case Studies: Impulsive Phase Parameters

We now use the high-cadence aspect of our data to examine the evolution of $\chi_{\rm flare}$, $T_{\rm BB}$, $X_{\rm BB}$, $C4170$, BaC3615, and the U band during the high-energy flares IF1, IF3, and GF1. We will find differences between the amount of BaC in emission and BaC in absorption among these flares. We also find a difference in BaC behavior between $\chi_{\rm flare,peak}\sim 1.5-1.6$ IF events, $\chi_{\rm flare,peak}\sim$1.8 IF events and $\chi_{\rm flare,peak}> 2$ IF events. Therefore, in addition to dividing the sample between GF and IF, we will also show spectral differences that differentiate between IF and HF events, and between IF events with low $\chi_{\rm flare,peak}$ and high $\chi_{\rm flare,peak}$. First we start by showing evidence of hot-star absorption during MDSF2 of the decay phase of IF1.

6.6.1 An "A star" on an "M star": The continuum evolution of MDSF2 during IF1

We first re-examine the decay phase of IF1. The results have been presented in Chapter 5; here, we summarize several of the results and explore other aspects in more detail, to facilitate connection with the properties of other flares. The detailed energy budget of the blue-continuum, the evolution of the percentage of Hydrogen emission in the blue/near-UV continuum, and line decrements were presented in Chapter 4, along with evidence of absorption in the wings of the Hydrogen lines. In this section, we focus on additional characteristics of the blue continuum indicating the formation of absorption features during this flare. The types of flares, and the times during flares, that exhibit absorption are important to understand because they constrain the origin of the continuum to significantly high densities.

The indication for the presence of absorption in (spatially unresolved) flare data is an anti-correlation between the apparent amount of BaC3615 and the overall level of the blue/near-UV continuum, as diagnosed by the U-band or C4170. This is what was observed during the secondary flares in the decay phase of IF1 in Chapter 5 (Figure 1d) and presented graphically through a sequence of rise-phase spectra in Figure 1 of Kowalski et al. (2012) (reproduced here in Figure 6.11, illustrating that as the U-band increased during the secondary flare (MDSF2), the entire blue/near-UV continuum became dominated by the blackbody component.

At the times of an anti-correlation, the plasma properties giving rise to the continuum emission must change dramatically. We found that although the total flare emission did not show absorption features, the *newly formed* emission exhibited $T_{\rm BB}{\sim}16\,000$ K and absorption in the BaC, very similar to a hot star spectrum such as Vega.

We now propose that another way to diagnose the presence of absorption during flares is the time evolution of the *purely observational* quantity, $\chi_{\rm flare}$– i.e., no need for a BB fit to the continuum. We showed this behavior in Figure 4.6 (top), which was presented in Figure 2 of Kowalski et al. (2011b) (where the nearby synthetic filters, NBF3500 and NBF4170 were used instead of C3615 and C4170, respectively). The anti-correlated time-evolution of $\chi_{\rm flare}$ and the U-band is conspicuous, and is reminiscent of the anti-correlation between the percentage of Hydrogen Balmer emission contributing to the blue SED (Figure 4.6, bottom). In fact, $\chi_{\rm flare}$ reaches its minimum value after the peak of the U band during the MDSF2, which is curiously also the time when the Hδ decrement reaches a minimum.

Determining a threshold value of $\chi_{\rm flare}$ that signifies hot-star absorption would be a valuable tool to diagnosing absorption during other flares, as we have discussed in Chapter 4. However, this is difficult because of the large amount of veiling (or filling-in) that can occur due to chromospheric Balmer continuum *emission*. Consider the following *gedanken* experiment:

1. Suppose that a flare produces a rapidly increasing amount of blackbody emission with no absorption.

2. Suppose also that this flare reaches an equilibrium state early on in the BaC production from the chromosphere, such that $d{\rm BaC}/dt = 0$.

3. Then, as the blackbody flux rises, $\chi_{\rm flare}$ would decrease generating an anti-correlation. However, we did not assume absorption in this *gedanken* experiment.

To determine a threshold $\chi_{\rm flare}$ at which absorption is formed, we require a relation between maximum $\mathcal{L}_{\rm BaC3615}$ and maximum $\mathcal{L}_{\rm U}$ (e.g., Figure 6.9); unfortunately, we cannot use the relation shown in Figure 6.9 to determine if there is a scaling in the *absolute* amount

of BaC3615, because we concluded that the relation in this figure may actually be *due* to the formation of different amounts of absorption on the star. Therefore, the BaC3615 in Figure 6.9 (and in all other figures), we emphasize, is the *apparent* amount of Balmer continuum flux at 3615Å.

We now return to the present analysis of IF1. During MDSF2, we found direct evidence for a hot-star spectrum that formed during the secondary flare. Figure 6.12 shows the subtracted flare spectra during the rise (black; same spectrum as presented in Kowalski et al. (2011a)) and just prior to the sub-peak (grey) from $\lambda = 3350 - 6500$Å. In both cases, the blue-optical shapes are well-matched by hot star spectra, such as Vega (scaled and plotted in red to show the remarkable similarities). Also, note the similarities in the widths of the Balmer absorption lines between the hot star and the flare spectrum; this is the source of the "depressions" in the line wings of the total flare emission that was discussed (Figure 4.17). The difference between the BaC flux ($\lambda < 3600$Å) in the new flare sub-peak (grey) and the BaC flux in Vega could be due to either increased chromospheric BaC forming during the event or due to the difference in gravity between the hot star and an M dwarf (log g= 4 vs log g= 5).

Temperature evolution over the course of the rise of the MDSF2 is evident in Figure 6.12 by comparing the blue-optical spectral shape to Vega from rise to peak. In Figure 6.13, we show the temperature evolution of the new flare emission (obtained from subtracting the decay of the previous flare, S#102). In Chapter 7, we show that $T_{\rm BB}$ increased during the secondary flare to nearly 13 000 K, but that this was only an apparent effect resulting from the newly formed emission adding on to the previously decaying emission: the temperature of the new emission is larger, ∼16 000 K. The temperature evolution of the total flare emission (measured without subtracting the decay spectrum of the previous flare) is shown in Figure 6.13 in turquoise. Here, the temperatures are systematically about 1000 K cooler than quoted from previously published work in Chapter 7 (because of the new spectral scaling; Appendix B); but the general trend of increasing $T_{\rm BB}$ by about 2500 K as the secondary flare occurs is still apparent. Also on this figure we show the $T_{\rm BB}$ (blue asterisks) and $X_{\rm BB}$ (blue circles) evolution of the newly formed emission during this secondary flare. There is a factor of ∼2 increase in $X_{\rm BB}$ and perhaps a slight overall increase in temperature

as well (from $T_{\rm BB}$= 14 000 K to $T_{\rm BB}\sim 18\,000 - 21\,000$ K). The $X_{\rm BB}$ values directly derived from fitting a Planck function to the spectra are shown as blue circles; if we apply the CK corrections (see Section 6.1.4) to the $X_{\rm BB}$ values, we get the evolution shown in the open black circles - the same time evolution, but at about $2.3 - 3.1$ times the inferred surface area coverage for this range of temperatures. The red star indicates the surface area coverage obtained from fitting a RH hot spot model, as presented in Chapter 7 (called $X_{\rm HS2}$ in Figure 7.4). The CK corrections give approximately the same answer as the hot spot model. Finally, note that the vertical dotted line indicates the minimum value of $\chi_{\rm flare}$ and the HB flux decrement (see Section 4.6), which occurs *after* the peak of the secondary flare in the U band (shown as grey line). The $\chi_{\rm flare}$, the HB flux decrement, and the HB flux percentages are all tracers of absorption, which can persist after the peak in the total continuum emission.

In Appendix F.1.3, we estimate the amount by which the flux of the previously decaying emission has decreased and apply it in order to better isolate the newly formed flare emission. We find that the color temperatures are $\sim$1800 – 2500 K cooler than in Figure 6.13.

6.6.2 Principal Component Analysis of Flare Spectra

Principal component analysis (PCA) provides a useful technique for analyzing flare spectra. A complete investigation of the principal components for all flares in the sample is beyond the scope of this dissertation, but we provide a preliminary illustration of the results for the decay phase spectra of IF1.

Following the method of Connolly et al. (1995), we compute the eigenspectra of IF1; the first three ($i = 1, i = 2$, and $i = 3$) are shown in Figure 6.14. The average flare-only flux is subtracted prior to computing the eigenspectra and is shown in this Figure (top, left). The eigenspectra are computed from the ensemble of all flare spectra from the night. The first principle component ($i = 1$) resembles the average IF1 spectrum and the decay phase emission in Figure 5.1(b). Note the larger Balmer jump and smaller Ca II K in the $i = 1$ spectrum compared to the average. The second component ($i = 2$) has no power at continuum wavelengths and shows asymmetric profiles in the emission lines; this reflects

instrumental shifts of wavelength on the detector over the course of the observations, which is a known effect with the DIS spectrograph. The lines in the red spectra show the *opposite* asymmetry, further suggesting that $i = 2$ is instrumental. The third eigenspectrum ($i = 3$) reflects the component of the secondary flares and the anti-correlation between the Balmer line emission and the hot-star continuum emission: the spectra are negative in the lines and positive in the continuum ($\lambda > 4000$Å).

In a future study, it may be possible to search for signatures of continuum anti-correlation and hot-star absorption spectra using eigenspectra during flares.

6.6.3 The Anti-Correlation between $\chi_{\rm flare}$ and U-band in IF3 and GF1

As mentioned in the previous section, the anti-correlation between $\chi_{\rm flare}$ and the U-band indicate possible times when hot-star like spectra (with Balmer absorption) are forming during the flare. We examine ∼0.5 hours of the evolution of $\chi_{\rm flare}$ for IF3 and GF1 in Figure 6.15. C3615 represents the NUV continuum light curve (note, it includes both BaC and BB contributions). We show that $\chi_{\rm flare}$ is anti-correlated with the C3615 during impulsive phases of both flares and that the decay phase of gradual and impulsive (high-energy) flares have different $\chi_{\rm flare}$ and therefore different relative amounts of BaC and blackbody components.

The grey shaded region in the IF3 figure illustrates the time period when $\chi_{\rm flare} < 2$, the value that *most* other IF flares, of various sizes attain at their peaks (see Figure 4.7, right panel). During the rise phase of IF3, $\chi_{\rm flare}$ decreases rapidly from 3.5 to 1.6, which coincides with the maximum in the C3615 light curve. The crossover from $\chi_{\rm flare,peak} > 2$ to $\chi_{\rm flare} < 2$ occurs at S#28, about halfway up the rise phase. Although C3615 decreases immediately after the peak, the $\chi_{\rm flare,peak}$ stays low at 1.6 for one more spectrum; this is reminiscent of the delay between $\chi_{\rm flare}$ and the U-band (and also the decrements and the U-band) following the subpeak of MDSF2 in IF1 (see Figure 4.6, top and Figure 4.21). Perhaps this is indicative of the slower decay of a hot star spectrum that appears at the peak. In Section 6.7.2, we will show that the area of the blackbody component also does not decrease immediately following the peak. The $\chi_{\rm flare}$ decreases during the secondary peak at

$t = 2.25$ hours and reaches a nearly constant value of 2.7 during the extended decay phase. The large error bars in the decay phase are not representative of the scatter from point-to-point: they are the result of low-level emission features (e.g., Fe I, Fe II) that appear in the decay phase, which generate larger flux standard deviations in the flux windows of C3615 and C4170, and hence larger errors.

GF1 has very complex evolution in both its light curve and in $\chi_{\rm flare}$. $\chi_{\rm flare}$ is anti-correlated with the C3615 flux when there are fast changes in the C3615 at $t = 1.95$ hours and $t = 2.2$ hours, reaching values of $\chi_{\rm flare}$ as low as ~ 2.3 during the first event. Recall also that the first event marks a drop in the percentage of Hydrogen Balmer contribution from 40% to 25% (Section 4.3). During the third fast rise period ($t = 2.2$ hours), the $\chi_{\rm flare}$ does not drop as low ($\chi_{\rm flare}\sim3$) as in the previous event. During the times of slow rise in C3615, there is a constant or slightly increasing (correlated) trend in $\chi_{\rm flare}$.

In the extended decay of GF1, $\chi_{\rm flare}$ is about 3.5 whereas in the extended decay of IF3, $\chi_{\rm flare}$ is about 2.7. Apparently, not all large energy flares have the same decay phase spectral shape, which could imply a difference in the persistent heating mechanism responsible for the sustained gradual phase emission.

In summary, there are periods of strongly anti-correlated behavior in $\chi_{\rm flare}$ and C3615 in these rather dissimilar flares. A similar anti-correlation pattern to IF3 was observed in the lower-amplitude impulsive flare presented in Kowalski et al. (2011b) (their Figure 3; note, that flare also has a small hump after the fast decline phase but before the spectral observations began). Next, we discuss how the anti-correlation relates to $T_{\rm BB}$ and $X_{\rm BB}$ during IF3.

6.6.4 Connecting the $\chi_{\rm flare}$ with $T_{\rm BB}$ and $X_{\rm BB}$ of IF3

In this section, a detailed evolution of $T_{\rm BB}$ and $X_{\rm BB}$ is presented for IF3, whose (2.7 minute) rise and (5 minute) fast decay allow for a unique time-resolved study of a large-amplitude flare. We will use the properties of this flare to explain the fast rise and fast decay light curve morphology and relate the morphology to the speed at which new flare regions are heated. Ultimately, we will show that the anti-correlation of $\chi_{\rm flare}$ and the photometry is

not the result of obvious absorption formed during the flare.

The light curves of SDSS u, C4170, and BaC3615 are given in the left panel of Figure 6.16. The light curves are displayed normalized to peak to illustrate that BaC3615 is significantly different than u, but the C4170 is generally similar to u (except for a slight difference in the peak to decay flux ratio). The absolute flux levels for C4170 and BaC3615 are shown in the right panel; one can see that at peak, C4170 is approximately three times BaC3615, while in the decay the ratio becomes 0.66 (see Figure 6.7 for this evolution). The data points in the right panel are labeled by their $T_{\rm BB}$ value, in units of kK (10^3 K).

During the rise phase, C4170 experiences a relatively constant rise rate, whereas BaC3615 has a larger variance in the rate of emission, experiencing two large jumps (S#26-27 and S#27-28) but tapering off to a nearly constant emission level around the peak of BaC3615 starting at S#29 – when C4170 is only at ∼65% of its peak emission. A similar rise structure was seen in the Hydrogen Balmer lines (see Figure 4.8). The temperature evolution is as follows: almost immediately in the rise, a blackbody with temperature of 10 kK appears (S#25 − 26). The $\chi_{\rm flare}$ is very large when this happens, ∼3.3 (S#25) and ∼2.7 (S#26). The rise occurs as this temperature increases to ∼ 11.5 kK (at 25% of peak emission in C4170) and stays at this temperature until 80% of peak emission; at peak, the maximum temperature of ∼ 12 kK is attained. The fast decay phase features an immediate drop in temperature (note, exposure times were reduced from 15 to 7 sec following the peak) to 11 kK, followed by a monotonic decrease (and nearly constant ΔT ∼ few hundred K / spectrum) to $T_{\rm BB}$= 8300 K by the end of the fast decay phase. For equal flux levels during the fast rise and fast decay, the fast decay is > 1 kK cooler. This implies that the area ($X_{\rm BB}$) must be greater during the decay: in other words, the fast rise is hotter and smaller than the fast decay.

We next show the areal ($X_{\rm BB}$) time evolution in Figure 6.17 (top), color-coded according to the $T_{\rm BB}$ (temperatures also shown on right axis, and with grey asterisks). The rise phase results in a fast appearance of a hot, $T_{\rm BB}$∼10 000 K component, which then undergoes a monotonic increase in surface area coverage. At peak, $X_{\rm BB}$ has increased by about a factor of 20 relative to when it first appears (S#25, at 7% of peak flux) over a time window of ∼150 seconds. The temperature of the blackbody also undergoes an apparent ∼2000 K increase in

the rise phase. We note that this temperature increase is similar to the temperature increase measured from the total flare emission during the rise phase of MDSF2. The increase in temperature also contributes to increased luminosity in the flare, but largely the luminosity increase is due to increasing area. Therefore, we have an explanation for the evolution of $\chi_{\rm flare}$ during the impulsive phase of this flare: $\chi_{\rm flare}$ changes relatively little from 1.8 to 1.6 over the time period (S#28-31) during which the hot blackbody component has reached 11 500 K, the BaC3615 has reached its peak level, and the blackbody component continues to increase in area while maintaining approximately constant spectral slope. This is consistent with the *gedanken* experiment developed in Section 6.6.1, whereby an anti-correlation does not result from immediately obvious absorption forming in the flare continuum (although, see Figure 4.19 for evidence of absorption at the peak). Instead, the anti-correlation results from different rates of increase in the BaC3615 and C4170 (recall, the amount of BaC3615 present in the spectrum also contributes to the C3615 flux, and therefore also to the $\chi_{\rm flare}$ value), and a nearly zero rate of increase in the BaC3615 while a large increase in the blackbody emission (with approximately isothermal temperature) causes $\chi_{\rm flare}$ to change very little around the peak.

During the initial decay, the $\chi_{\rm flare}$ stays at a low value because, although the temperature of the blackbody decreases, its area *continues* to increase. The BaC3615 also contributes to the post-peak $\chi_{\rm flare}$ evolution as it stays elevated for longer.

In Figure 6.17 (bottom), we show the same figure but with $T_{\rm eff}$ and $X_{\rm CK}$, which are the temperatures and areas adjusted using the Castelli-Kurucz models of hot star atmospheres (Section 6.1.4) which account for hot-star absorption. $X_{\rm CK}$ is approximately 1.8 times larger than $X_{\rm BB}$at flare peak; at $t = 0.2$ hours the $X_{\rm CK}$ and $X_{\rm BB}$ are about equal. Similar trends are apparent with $T_{\rm BB}$ and $X_{\rm BB}$, but the $X_{\rm CK}$ stays about the same from peak through the initial fast decay phase before decreasing. The change in $T_{\rm eff}$ is only about 700 K during the rise phase to a maximum of $T_{\rm eff}\sim$8900 K. The Ca II K line flux evolution is also shown to illustrate that the Ca II K flux decreases when the $T_{\rm eff}$ drops from 7200 K to 6500 K.

6.7 The Speed of an Expanding Flare Area

We now use the rate of areal ($X_{\rm BB}$) increase during the rise phase of IF3 to estimate the quantitative rate at which the flare area is changing. The speed of the flare area increase must be related to the heating mechanism of this blackbody component.

We use a simple flare area model, whereby the white-light emitting region is circular with radius r, and the filling factor, X, is changing at a rate dX/dt (where $X = X_{\rm BB}$). Then, the speed of the leading edge of the expanding circular flare area is given by

$$v(t)_{\rm flare} = 1/2 \times dX(t)/dt \times (1/r(t)_{\rm flare}) \times R^2_{\rm Star} \tag{6.2}$$

and $r(t)_{\rm flare} = (R^2_{\rm Star} * X(t))^{1/2}$ and $dX/dt = (X_i - X_{i-1})/(t_i - t_{i-1})$ where i is the spectrum number with midtime t. If instead we assume a more complex geometry having two expanding flare areas to represent the two footpoint structures observed during solar white-light flares (Hudson et al., 2006; Maurya & Ambastha, 2009), the inferred speeds decrease by a factor of two. When we describe the speeds below, the first number is derived using $X_{\rm BB}$, the second number is derived from using $X_{\rm CK}$ which result in typically larger speeds (the two numbers are separated by a dash). When we show just one speed, we refer to the $X_{\rm CK}$. We show the results for the $X_{\rm CK}$ in Figure 6.18. The uncertainties in the speed calculations are estimated to be $\sim$40%, using the systematic uncertainties in the temperatures (see Appendix F). According to this simple flare model, the leading edge of the flare is moving at larger speeds ($\sim 50 - 100$ km s^{-1}) during the beginning and middle of the flare and decreasing to small speeds (< 10 km s^{-1}) after the peak. The average speed during the flare rise is $40 - 50$ km s^{-1}, and the maximum speed ($80 - 110$ km s^{-1}) is attained in the mid rise phase. The rise-phase speeds are supersonic for the photosphere of an M dwarf ($c_s \sim 5 - 10$ km s^{-1}) and we suggest several mechanisms below that could be responsible for the expansion rates observed. van den Oord et al. (1996) also considered the expansion speed[8] of an erupting filament during a white-light flare on YZ CMi, and found speeds $\sim 100 - 500$ km s^{-1} but did not have spectra to determine the speed of the blackbody continuum component.

[8] van den Oord et al. (1996) used the area derived from U-band data at peak emission and the larger area implied from radio observations in the gradual phase.

IF9 is the only other (IF) event in our sample where the blackbody has a rise *and* peak phase detection. Applying the same analysis, we find velocities of 100 – 130 km s^{-1}, 70 – 90 km s^{-1}, and 20 – 0 km s^{-1} in the rise, peak, and fast decay respectively. Although the uncertainties in the calculation of speeds are again ∼40%, a suggestive trend is that IF9 and IF3 show the same pattern: fast speeds in the mid rise and decreasing speeds at peak (and continuing just after peak in IF3). Note, $X_{\rm BB}$ increases after the continuum peak, but $X_{\rm CK}$ just after peak continuum is equal to the $X_{\rm CK}$ at peak continuum (Figure 6.17, bottom). More precise measurements and modeling of flare emission just after the time of peak continuum would help clarify if area increases or remains constant during the fast decay phase.

We repeat these calculations for the rise phase of MDSF2 because it is the only other flare with a simple, time-resolved rise phase. Here, we use just the CK corrected areas (see Section 6.1.4) because they were shown to better represent the areas derived from the RH hot spot models for this flare (and there are large corrections needed to the areas because the $T_{\rm BB}$ is high, see Figure 6.4). Only the average velocity is calculated because the areal evolution is noisy (see Figure 6.13). We find that during the rise phase, the area is expanding with an average velocity of ∼8(±40%) km s^{-1}, much smaller than during IF3 and IF4, and which, coincidentally, is consistent with the speed (5 – 10 km s^{-1}) of the expanding disturbance from the initial $|\Delta U|$ ∼6 mag event that we assumed triggered MDSF2 in Kowalski et al. (2012) (Chapter 7). Under the scenario envisioned in Chapter 7, this would signify a physical connection between the speed of a wave disturbance in the lower M dwarf atmosphere and the rate at which flare heating occurs at a new site. Also in this scenario, the wave disturbance is the source, not the site, of flare heating, for example due to triggering a lower atmospheric reconnection event in a nearby, unstable magnetic field region. In Section 6.7.3, we compare the flare speeds for HF1 and IF2.

6.7.1 The Meaning of Flare Speeds

There are several possible scenarios which could drive the expansion of a flare area, and we discuss the two most extreme here.

- **Scenario 1:** $v_{\rm flare} \sim c_s$**,** $dA_{\rm beam}/dt = 0$ For this scenario, we assume that the beam bombardment occurs at a fixed location and over a constant area ($dA_{\rm beam}/dt = 0$). The sound speed is an important parameter for the expansion of a flare area occuring on the dynamical timescale in response to persistent nonthermal particle bombardment from above (e.g., from the particles driven into the lower atmosphere during reconnection). As pressure equilibrium is achieved with the ambient atmosphere at the speed of sound, radiative and conductive heating could lead to a temperature increase in the surrounding region as it responds to the distant particle heating. The rate at which the flare area expands is therefore related to the sound speed, and the rate at which the temperature increases is a combination of the rates from these heating processes which depend on the detailed physics and chemistry (e.g., specific heat) of the heated atmosphere. As the flare area expands, the average temperature may eventually drop because the particle heating can no longer sustain the temperatures against cooling due to expansion. This may be the phenomenon that we observe at flare maximum and during the initial fast decay. It is known from 1D RHD models that constant heating of a given region increases the column mass in the corona so as to inhibit further beam penetration (Allred et al., 2006); future studies of this effect with (3D) RHD models would illustrate how relevant Scenario 1 may be during flares.

- **Scenario 1b:** $v_{\rm flare} \sim c_s$**,** $dA_{\rm beam}/dt > 0$ The flare speed would also equal the sound speed if, for example, a sound wave triggers the reconnection from above. This is what we envisioned as the connection between the initial $|\Delta U| \sim 6$ mag peak of IF1 and the MDSF2 (Chapter 7). Therefore, a degeneracy with a second scenario exists whereby the areal increase is related to the speed at which flare-accelerated particles heat new regions. We now discuss this second extreme scenario.

- **Scenario 2:** $v_{\rm flare} \sim v_{\rm reconnection}$**,** $dA_{\rm beam}/dt > 0$

  A second scenario, which may be important during the rise phase of impulsive flares, is transient heating of many small regions over a relatively large area of the active region. In this scenario, the nonthermal heating "beam" area increases. This could

happen at a speed which is driven by the speed of reconnection at a heights above where the heating occurs (Fletcher et al., 2004): significantly larger than the speed of sound in the lower atmosphere. Each area that is heated by a "burst" of nonthermal particles expands according to the physics described above, and the emission we see at any given time is a superposition of all flare areas. The increase of flare area during the rise phase is then related to the increasing *number* of these individually heated regions, and not to the expansion of an individual region (although persistent heating and expansion could still be taking place in each region). Alternatively, supersonic expansion may imply heating contributions from an expanding shock wave.

Of the many important physical parameters that would inform this picture, we consider the depth of continuum formation and the decay timescale of the continuum. Given the depth of continuum formation, we then know the sound speeds that are most important and can test the relative roles of shock heating, conduction, and radiative heating during the dynamical expansion. The timescales of continuum decay give insight into how long the nonthermal particle heating (or other heating mechanism) needs to persist in individual flare areas on the surface in order to explain the observed amounts of emission.

From the parameters of the phenomenological modeling in Chapter 7, we find that the continuum forms at a column mass of $\sim$3 g cm^{-2} and peak temperatures at this column mass of $\sim 12\,000 - 20\,000$ K. The sound speed at this column mass and temperature is $\sim$ 15 km s^{-1}, giving a dynamical time of $\sim$20 seconds for the atmosphere to adjust to the pressure gradient if the heat source is persistent (H. Lamers, priv. communication, 2012). A simple energy argument ($3/2kT_{\rm max}m_{\rm c}/(\mu m_{\rm H}) \sim t_{\rm rad}\sigma T_{\rm max}^4$) gives radiative cooling timescales ($t_{\rm rad}$) on the order of $1-6$ seconds for these hot spots if the heat source disappears. In future work, we will study the evolution of these hot spots with 1D (and eventually 3D) dynamical models. The short cooling timescales have obvious implications for the persistence of a heating mechanism to maintain the levels of blackbody radiation on the observed timescales (minutes to hours).

The different speeds for IF3 and MDSF2 signify a physical connection between the speed and the type of blackbody spectrum (and therefore type of flare heating) observed. The speed during MDSF2 is a factor of > 5 times slower than the average rise phase flare velocity during IF3. IF3 produced large amounts of chromospheric (e.g., Hγ, BaC3615) radiation, especially during the first half of the rise phase when the velocities were higher. We speculate that the slower flare velocity in MDSF2 led to more prolonged heating in a given area, hence the higher temperatures and more easily detectable absorption signatures (Scenario 1). In order to be consistent with the lack of Balmer line emission produced in MDSF2, it is also possible that the heating source was deep in the atmosphere (similar to the heights at which reconnection is thought to occur in order to produce solar Ellerman bombs, as speculated by Kowalski et al. (2012) in Chapter 7). If IF3 is described by Scenario 1, then the flare heating would be higher in the atmosphere to be consistent with larger sound speeds. However, the rise phase of IF3 could also be Scenario 2, implying that the areal increase would be related to the rate of individual areas being heated. Understanding the depth of formation of the IF3 continuum would allow us to place constraints on the heating of individual bursts so that they superpose correctly to form the observed light curve. As IF3 reached its peak, the speeds decrease to a range of $3 - 50$ km s^{-1}, which is when we see the largest temperatures in the flare and the absorption signatures (see Figure 4.19). This implies Scenario 1 at peak emission and therefore a possible connection between the speed of an expanding flare region and the (average) temperature of that region, such that lower speeds result in more prolonged (and possibly deeper) heating of the atmosphere.

We speculate that the expanding white-light areas during IF3 and MDSF2 are similar to the motions of white-light, hard X-ray, Hα and CIV kernels observed on the Sun during the formation of two-ribbon flares (Kosovichev & Zharkova, 2001; Wang, 2009; Nishizuka et al., 2009; Krucker et al., 2011; Inglis & Dennis, 2012). These have been observed to propagate at similar speeds of between $50 - 120$ km s^{-1} during the development of two-ribbon structures parallel to the magnetic polarity inversion line (PIL) (Fletcher & Hudson, 2001; Schrijver et al., 2006). There is also slower motion perpendicular to the flare ribbons at the locations of kernels, outward from the PIL with velocities of $\sim$15 km s^{-1} (Fletcher et al., 2004; Keys et al., 2011) or as small as a few km s^{-1} (Qiu et al., 2010), presumably

the result of reconnection at progressively higher heights. Perhaps, the higher speeds in the rise phase are analogous to the formation of flare ribbons, and the decreasing speeds at flare maximum (and just after flare maximum) represent the perpendicular motions (e.g., "spreading moss" Berger et al., 1999). This scenario has been deduced by UV/HXR observations of solar flares to explain flare light curve morphology in the rise and peak times (Qiu et al., 2010). The heating of new flare footpoints, resulting from increasing flare area, was a conclusion from the models of Hawley & Fisher (1992, 1994). During solar flares, it is an open question what triggers particle acceleration (a possible source of flare heating) in neighboring flare regions (Inglis & Dennis, 2012). Possible scenarios are an unstable flux rope that erupts sequentially along a flare arcade (the "tether-cutting scenario" Moore et al., 2001) and magnetoacoustic slow waves that propagate away from the initial flare site (Nakariakov & Zimovets, 2011). Three-dimensional models of reconnection predict motions of the reconnection site, which undergo changes in velocity to slower speeds due to mass loading (Linton & Longcope, 2006).

Additional higher time resolution data during the rise phase of other types of (smaller) flares would help us understand these phenomena and also provide invaluable constraints on future 3D models that attempt to reproduce the formation of the hot blackbody continuum during the impulsive phase of solar and stellar flares.

6.7.2 Explaining the Fast Decay Phase

The fast decay phase occurs in the impulsive phase of flares and follows immediately after the time of peak continuum emission. We found in Section 6.6.4 that the fast decay phase emission of IF3 is described by a cooler and larger blackbody emission component compared to the fast rise phase. Here we continue to employ the high time-cadence data for IF3 to provide a phenomenological explanation for the fast decay phase of classical flares. This explanation will be tested with the other IF flares in the sample. C4170 has a characteristic rapid time evolution during all flares; understanding how the spectral properties (such as the continuum slope) change during the fast decline would provide clues to the mechanism by which it is produced. Moreover, it will provide important constraints on time-evolution

of impulsive energy input in flares. We seek to explain why the fast decay is fast and why the fast decay time is almost always longer than the fast rise time. In this section, we use the areas directly obtained from fitting a Planck function (i.e., the CK-corrections are not applied to the areas) since this section is just illustrative.

Figure 6.17 shows that $X_{\rm BB}$ continues to rise for three spectra after the peak, in a time that the continuum declines to 80% of its peak value. By the end of the fast decay phase, the continuum is ∼20% the peak value and $T_{\rm BB}$ has dropped to ∼8300 K. We search for this trend in the rest of our sample. We ask, do all flares exhibit this pattern that the initial moments of the fast decay exhibit a decrease in temperature and increase in $X_{\rm BB}$? For the flares with a robust blackbody temperature determination at peak, we compare the $X_{\rm BB}$ and $T_{\rm BB}$ in the spectrum immediately following the peak. The results are shown in Table 6.3, with + indicating an increase and − indicating a decrease. We find that most of the flares indeed exhibit this behavior. Noticeable exceptions are IF5, IF7, and HF2. In the next section on the gradual phase evolution (Section 6.8), we will find that most flares also reach $T_{\rm BB}$∼8000 K in the extended decay phase, which was first shown for a flare in Mochnacki & Zirin (1980).

We now illustrate how the combined effects from increasing area and decreasing temperature produce a fast decay. The decreasing temperature results in a very rapid decay in flux, via the Planck function's steep dependence on temperature. Therefore, even if the area increases by the same percentage as the decrease in the blackbody component's temperature, a fast decay still results. In Figure 6.19, we show the evolution of a flare spectrum that has increased in area by 33% and decreased in temperature by 33% ($T_{\rm BB}$= 12 000 K to 8000 K, as observed). At some point the area also begins to decrease, further accelerating the fast decay. Then, the blackbody temperature is very important in regulating the observed flux, and precise measurements of $T_{\rm BB}$ and $X_{\rm BB}$ are important and provide meaningful constraints during flares.

Two interesting results come from this simple simulation (shown in Figure 6.19). First, a monotonic increase in area and a monotonic decrease in temperature (by the same percentage) generate a decay to nearly 20% of the peak value in 2 – 3 minutes, which is typically the level of the IF flares at the end of the fast decay. Second, the resultant light curve is

well-fit by an exponential decay function with a time constant that is 2.5x the total fast decay time. In the observed light curves, an exponential (nearly linear) function matches the fast decay of several flares (see Appendix E for fits to IF1, IF3, and a flare from Kowalski et al. (2011b)); however, the exponential time constant is much shorter than implied by our simulation. The faster decay time constant in the observations would result from the area beginning to decrease at some point during the flare decay. This is demonstrated by IF3 (Figure 6.17, right panel); we also find that the mid-to-late fast decay has contributions from a lower temperature *and* lower area in HF1.

In summary, the onset of the fast decay is caused by decreasing $T_{\rm BB}$, whereas the mid-to-late fast decay is accelerated because the decreasing $X_{\rm BB}$ also contributes to an overall reduction in flux. This phenomenon was first shown for a flare on YZ CMi in Mochnacki & Zirin (1980). However, we have demonstrated it phenomenologically and established the pattern for a variety of flares. If the fast decay phase is related to slow motions of flare kernels away from the PIL (see Section 6.7), then perhaps less energy flux is delivered to the lower atmosphere after the peak phase thereby allowing the kernels formed in the rise phase to begin cooling while the area increases. The flares IF7 and IF5 are interesting exceptions where both the area and temperature decrease immediately following the peak. NUV observations are important for accurately measuring the blackbody temperature during the decay phase, when it becomes faint and the errors increase.

Although this interpretation can also be applied to the fast decay of the U-band (and C3615) in flares, the U-band evolution is actually more complex due to the slower decay of the Balmer continuum. The differences in the fast decay between the C4170 and u-band are apparent in Figure 6.16. Precise fast decay rates can be measured with high-cadence data obtained from ULTRACAM (Kowalski et al., 2011b). Because of the additional contribution from the BaC and its slower decay rate, we predict that the fast decline in the NBF3500 (similar to C3615) would be slightly slower than the decay in the NBF4170 filter (similar to C4170).

6.7.3 "Stacking Peaks": Temperature differences in HF1 vs IF2

The flares HF1 and IF2 have respectively a higher (2.33 ± 0.11) and lower (1.74 ± 0.04) $\chi_{\rm flare,peak}$. They also occurred on the same star (YZ CMi), consecutively and at similar airmass, under similar conditions; thereby offering robust comparison of two flares with extremely different flare morphologies (multiple peak vs. single peak). During the impulsive phase of HF1, there were a series of peaks, and we ask the question whether adding the peaks together would produce the same spectrum as the main peak in IF2. If they match, then it would be reasonable to think that the fast and large peak of IF2 is a result of smaller peaks (like those seen in HF1) that "stack" together very quickly.

After adding HF1 S#518−S#521, the total flare-only emission in C3615 is 2×10^{-13} ergs s^{-1} cm^{-2} Å^{-1}, the same level as in the peak of IF2. We show the spectra in Figure 6.20 (top) and the lightcurves in the bottom panel (where grey vertical bars indicate the temporal regions considered). The spectra show noticeable differences in the blue-optical shape such that the stacked HF2 spectrum (black) has $T_{\rm BB} \sim 10\,700$ K and the peak IF2 spectrum (purple) has a steeper slope with $T_{\rm BB} \sim 14\,000$ K. There is also a difference in the relative amounts of Hγ to C4170 formed (ratios of 39 for HF1 and 17 for IF2) and the percentage of Hydrogen Balmer emission (∼25% for HF1 and ∼15% for IF2). The evolution of the percentage of HB emission is shown in red asterisks in Figure 6.20 (bottom); in the gradual phase, a similar percentage is achieved (∼40-45%), but the gradual phase value is attained relatively quickly in HF1 and slowly in IF2.

This exercise has important implications for flare heating mechanisms. Larger peaks are not necessarily a straightforward "areal" sum of smaller peaks; instead, larger peaks can result from an increased temperature of the blackbody component produced from the flare. The flare heating during the very impulsive events could be more concentrated, temporally and spatially, in the atmosphere whereas the smaller peaks that are spread out in time (and space) could result from a diffuse heating of several individual kernels over a larger area thereby producing a cooler blackbody in each kernel and relatively more Hydrogen Balmer emission. We estimate the speed of areal increase to be ∼100 – 200 km s^{-1} for IF2 and ∼5 km s^{-1} for HF1, and we find that the flare temperature is correlated with the speed for these

two flares. In contrast, we found that the speed is inversely correlated with temperature by comparing MDSF2 and IF3. Perhaps shock heating is an important contribution to the larger temperature of IF2 (due to supersonic speeds), or the calculation of speed in HF1 is affected by there being several distinct areas on the surface at a given time during the impulsive phase. There may be a difference in the flare mechanism or heating rates between slow speeds with lower temperatures and slow speeds with higher temperatures.

Individually the area of each peak in HF1 is $< 40 - 60\%$ the area of the blackbody of IF2, but the decay phase value of the percentage of HB emission is attained slowly in IF2; we speculate that this is reflecting the larger area of IF2 (hence, longer time to decrease in size assuming the heating beam turns off gradually) or larger column mass heating of IF2 (hence, longer time to cool).

6.8 The Gradual Phase Continuum

The gradual phase begins when the emission has begun an exponential decay after the fast decay phase. The U-band has typically reached $\sim$50% of the peak flux in the gradual flares and $10 - 20\%$ of the peak flux in the impulsive flares by the start of the gradual phase. To study the gradual phase, we average three spectra at the times given in Table 4.2 in order to increase the signal to noise in the blue-optical zone for determining a blackbody temperature fit.

Understanding the flare mechanism means determining if the gradual decaying continuum is due to the long cooling time scales of material that was heated impulsively in the beginning of the flare, or if it is due to continued, low-level impulsive heating (at cooler temperatures than in the beginning of the flare) during the gradual phase. If there is continued heating, then we must determine if particle heating or backwarming is the source. Due to its long duration, a large amount of energy is emitted in the gradual phase, with 29% of the U band energy emitted during the IF0 event (Hawley & Pettersen, 1991). In the other flares, we sometimes find much higher percentages. For example, 73% of the U-band energy in IF1 and 60% of the u-band energy in IF3 were emitted in the gradual phases. In Figure 4.7, we found that only $30 - 65\%$ of the wavelength-integrated flux at the beginning of the

gradual phase can be attributed to Hydrogen Balmer[9] radiation. Given that Ca II, Mg I, and the Helium I lines only account for a few additional percent ($\sim 5\%$) of the emission, this leaves $30-65\%$ of the gradual phase emission unaccounted for by Balmer radiation. According to Table 6.1, $> 60\%$ of the flux in C3615 is due to the BaC3615 contribution, leaving <40% of the specific flux in the NUV unaccounted for by Balmer continuum.

The "extended" gradual phase is marked by either a sharp break (e.g., IF4 or the *g*-band light curve of IF5) or a smooth transition into slowly decaying emission (e.g., IF2 and IF7). The gradual phase has often been fit with an exponential decay, and we do find a good fit using an exponential decay constant (for example, in IF3 $\tau_{\rm SDSSu}$ ~40 minutes); though, sometimes the decay constant appears to evolve (HF1, IF1, IF2) particularly during these events that have multiple impulsive events (though IF10 shows a good match to a single exponential and it has three peaks but one clearly dominant one). A detailed characterization of the decay constants and gradual phase properties from the photometry alone (or with Kepler photometry) would provide useful constraints for future models (see Chapter 8).

A study of the gradual phase continuum during IF1 was presented in Chapter 5. We used a two-component model consisting of a $T_{\rm BB}= 10\,000$ K blackbody and a RHD model Balmer continuum to derive a filling factor ratio of $\sim 3-16$. The IF1 gradual phase showed direct evidence for a Balmer continuum. We found that $X_{\rm BB}$ was primarily responsible for driving changes in the continuum level. In this dissertation, we have fit the continuum by allowing both $T_{\rm BB}$ and $X_{\rm BB}$ to vary in order to search for possible temperature evolution in addition to areal evolution. In Chapter 7, we model the total gradual phase continuum (near-UV zone to blue-optical zone) with a hot spot model having $T_{\rm BB}\sim 11\,000$ K plus the RHD backwarming model consisting of cool blackbody and Paschen continuum.

6.8.1 Gradual Phase Spectra

Figures 6.21 – 6.25 show spectra from the beginning of the gradual phase (Table 4.2 and indicated by vertical red lines in Figures C.1 – C.19) for fifteen of the eighteen flares with

[9]Recall that the HB component includes the Balmer continuum, the PseudoC, and Hδ, Hγ, Hβ.

two-component fits, allowing $T_{\rm BB}$, $X_{\rm BB}$, and $X_{\rm BaCF11}$ to vary. The spectra are averaged over three consecutive observations in order to increase the signal-to-noise when the emission was changing slowly (except for IF4, IF5, and HF4 which are only shown for a single spectrum because the data quality was highly variable during such low levels of emission). The gradual phase spectrum for IF10 is given as S#32 even though it contains contributions from secondary flares and gradual phase emission. The quiescent spectra are shown in grey. In parentheses, we have listed $\chi_{\rm flare,decay}$, $T_{\rm BB}$, and $X_{\rm BaCF11}/\ X_{\rm BB}$. The blackbody fits and $\chi_{\rm flare,decay}$ values are excluded when they are not well-determined (i.e., very little or no emission in the blue-optical zone).

A striking similarity among the gradual phase spectra is the value of $T_{\rm BB}$, $\sim$7300 – 8500 K in the flares IF1, IF2, IF3, IF7, IF9, IF5, GF1, and HF2 (typically around 8000 K). Some flares have unusual characteristics. The gradual phase of IF4 was taken near the peak of the line emission (so as not to sample too far into too high of an airmass), and this flare has a hotter temperature of 9500 K. The gradual phases of HF1 and HF3 are even hotter with temperatures exceeding 10 000 K). We have averaged the spectra just following the peak (synthetic U-band) emission of GF5[10] to show the remarkable detection of white-light continuum (and all the typical flare emission lines) in an event with only $I_f + 1 < 1.5$ and $I_{C4170} + 1 \sim 1.03$. This flare has $T_{\rm BB}\sim$4900 K, the lowest detected temperature, and is about 2000 K cooler than at peak. We remind the reader that $T_{\rm BB}$ is a parametrization of the continuum slope and may not have physical significance. Note that the gradual phase spectrum of IF1 (Figure 6.21) is that shown in Figure 5.1(b) in Chapter 5, where we modeled this spectrum with a $T = 9\,000 - 11\,000$ K blackbody. When allowed to vary, $T_{\rm BB}$ is $\sim$8250 K and results in a larger inferred areal coverage, $X_{\rm BB}\sim$0.4% of the visible hemisphere ($\sim$2 times that given in Chapter 5). Among the three spectra averaged to form the decay spectrum of IF1 in Figure 6.21, the inferred temperature range is between 8000 – 8500 K. The difference between 8250 K and 10 000 K is may be significant as our estimate of the systematic uncertainty in the temperature determinations is $\sim$1000 K (Appendix F).

To model the Balmer continuum in the gradual phase spectra, we add the BaCF11

[10]This spectrum is averaged over five spectra just after the peak time.

model spectrum to the blackbody fit at $\lambda < 3646$Å and display this in red in Figures 6.21 – 6.25. We quantitatively compare the slopes of the observed Balmer continuum emission (after subtraction of the blackbody) to the slope of the BaCF11. These slopes are given in column 5 of Table 6.2. The slope of the BaCF11 is $\sim 5 \times 10^{-4}$Å^{-1} of the flux at $\lambda = 3615$Å (bottom of Table 6.2). In all of the decay spectra, there is a relatively good match to the positive slope (increasing towards redder wavelengths) of BaCF11, as we found for IF1 (Figure 6.21, see also Chapter 5). The statistical fitting errors on the slopes (given in parentheses) are quite large, likely due to the difficulty in modeling the "true-continuum" underlying the forest of low-excitation metallic lines that are likely present in the NUV during the decay phase. There are also systematic errors due to flux calibration of $\sim$5 – 10% at these wavelengths (Appendix A); this uncertainty corresponds to about 2 – 4 in the units given in the table. The best matches to the BaCF11 model are obtained during IF9 and GF1, which have BaC slopes of 4.9±2.4 and 5.9±1.3, respectively. We conclude that the observed BaC are representing flare chromospheric conditions (Chapter 8), which are predicted relatively well in the gradual phase using (impulsive phase) RHD beam models having a non-thermal electron flux of 10^{11} ergs cm^{-2} s^{-1}. However, more accurately flux calibrated spectra at higher spectral resolution in the NUV would provide better constraints for the models. The persistence of the BaC at these late stages and the relatively good match to the shape of impulsive phase RHD model Balmer continuum, implies continued heating from accelerated particles during the gradual phase of these flares. We do not exclude other sources of heating that could produce late phase Balmer emission as discussed in Canfield et al. (1993) for solar flares, but energization of the atmosphere appears to be driven by an external source such as nonthermal particles. Gyrosynchrotron microwave radiation has been detected far into the gradual phase of white-light flares on M dwarfs, suggesting that nonthermal particles are accelerated after the impulsive phase (van den Oord et al., 1996; Osten et al., 2005), but the heating from these particles in particular is not completely understood. More simultaneous optical (spectra) and radio data would help understand the timing of gyrosynchrotron emitting particles and the white-light radiation.

The spectra become weak and noisy later in the gradual phase. For a few flares, the signal-to-noise remains high and we investigate beyond the beginning of the gradual phase.

In IF3, the g-band was elevated at relatively high levels during the first hour of the decay ($I_f + 1 \sim 1.9$ to 1.3). From Figure 6.17, we find that a blackbody with $T_{\rm BB}\sim 7000 - 8000$ K persists even 1 hour after the flare. The plateau of the temperature at these values, especially considering its rapid evolution during the impulsive phase, could be due to sustained heating, which either might be from direct (unaccounted for in the RHD models) particles or from the relatively large amount of chromospheric (and coronal) Hydrogen backwarming. The values of $\mathcal{L}_{\rm BaC3615}$ and $\mathcal{L}_{\rm C4170}$ during the gradual phase spectra are indicated by large purple circles in Figure 6.7. We find a strong trend among them, and the IF events showing $T_{\rm BB}\sim$8000 K emission – IF1, IF2, IF3, IF5, IF7, and IF9 – are described by the relation,

$$\mathcal{L}_{\rm BaC3615} = 2.5 \pm 2.2 + 0.91(\pm 0.08) \times \mathcal{L}_{\rm C4170} \tag{6.3}$$

Fitting only the blue points ($\chi_{\rm flare,peak} < 2$) also gives a relation that is consistent with a slope of 1. A slope of 1 in this log-log space predicts that the BaC3615 and C4170 increase in equal proportions during the gradual phase according to the size of the flare. The flares with $\chi_{\rm flare,peak} > 2$ and which form a $T_{\rm BB}\sim$8000 K component – IF5, HF2, and IF5 – in the decay may form a second distribution which is offset from the $\chi_{\rm flare,peak} < 2$ distribution. However, it is not clear whether the distribution is offset horizontally (signifying that they are deficient in C4170) or vertically (signifying that they have excess BaC3615). In any case, the figures suggest that the formation of C4170 with $T_{\rm BB}\sim$8000 K formation is related to the formation of BaC3615 in the gradual phase.

We now connect the IF3 gradual phase $\chi_{\rm flare}$ evolution, the time-evolution of the fraction of HB flux, the blackbody flux, C4170, and *excess* emission unaccounted for by all of these components, which we will come to call the "Conundruum". The $\chi_{\rm flare}$ value is approximately constant in the decay phase of IF3 and GF1 (Figure 6.15), further indicating that the Hydrogen BaC and the C4170 (and also consequently the $T_{\rm BB}\sim$8000 K blackbody component) are linked during the extended decay phase. However, the interpretation of $\chi_{\rm flare}$ is complicated because the blackbody and Balmer continuum contribute toward the emission. Figure 6.27 disentangles the contributions in $\chi_{\rm flare}$, showing that the ratio of BaC3615 to C4170 is similar to the evolution of $\chi_{\rm flare}$, each relatively constant over $\sim$0.6 hours of the decay. We conclude that the local flux in the BaC at $\lambda = 3615$Å follows the local flux in

the blackbody at $\lambda = 4170$Å during the gradual phase.

Furthermore, we find that the fraction of HB to total $\lambda = 3420 - 5200$Å flux follows a similar trend as in Figure 6.27. The fraction of total HB flux (recall that it does not include Hϵ and Hα) to the total blue flux is shown in Figure 6.27 (bottom panel), and changes from 0.12 at peak to 0.37 in the gradual phase. The fraction of HB and $\chi_{\rm flare}$ were also found to vary quite similarly in the decay phase of IF1 (Figure 4.6). Therefore, the $\chi_{\rm flare}$, fraction of HB flux, and ratio of BaC flux (at 3615Å) to blackbody flux (at 4170Å) vary similarly in the decay. This means that these three measures similarly trace the changing relative contributions from Balmer emission and blackbody emission.

There are complications with the flux budget from $\lambda = 3420 - 5200$Å of IF3 beyond what is presented here. First, the ratio of Hγ flux to C4170 flux was found to have a steeper increase in the gradual phase. Second, if we consider not just the ratio of HB to total flux, but instead the ratio of HB to blackbody flux, the ratio decreases steeply in the gradual phase, like Hγ flux / C4170. Therefore, there must be an extra amount of flux in addition to the blackbody that contributes to the gradual phase emission to make the HB / total flux approximately constant. From the excess flux (non-HB, non-blackbody) we also subtract Ca II K, Ca II H, the Helium I lines, Fe II / Mg Ib. The excess is shown in Figure 6.27 (bottom) as green. We refer to this excess emission as the "Conundruum", which has a relative contribution that steadily rises into the decay phase contributing a maximum of $\sim$9% of the total $\lambda = 3420-5200$Å flare flux. The decreasing $T_{\rm BB}$ in Figure 6.17 after $t = 0.6$ hours probably is due to the increasing contribution from the conundruum at the redder end of the blackbody fit ($\lambda \sim 4800$Å). It is interesting then that the BaC / C4170 is relatively constant, implying that the Balmer continuum and $T \sim 8000$K blackbody vary similarly in the decay phase. In contrast, the total HB to wavelength-integrated ($\lambda = 3420 - 5200$Å) blackbody flux decreases steeply in the decay phase: the HB component has larger and larger contributions from the lower order lines which stay elevated longer whereas the blackbody continues to decrease relatively quickly. The increasing Conundruum contribution over time then explains why the HB to total flux ratio is nearly constant in the gradual phase (i.e., total flux = HB + blackbody + Conundruum + Ca II + Hϵ + and minor emission lines). In future work with RADYN (Chapter 8), we will explore the formation depths of Paschen

continuum at λ =4170Å (mostly blackbody) and at λ =5200Å (much more Conundruum than at λ = 4170Å) to see if there is a connection with the BaC for the former continuum wavelength and the lower order Balmer lines for the latter continuum wavelength.

In summary, we find evidence for a $T_{\rm BB}$∼8000 K component at the beginning of the extended gradual phase during eight flares, mostly the IF events. It is not known if the emission is formed in the same areal region as the impulsive phase emission (with $T_{\rm BB}$∼9000−14 000). Interestingly, the gradual phase blackbody emission has a nearly constant temperature in the flares that we can measure (IF1, see Chapter 5; IF3, see Figure 6.16). Also, the time variation of the fractional flux in HB follows $\chi_{\rm flare}$ in IF1 and IF3 during the decay phases. We find a strong correlation between the C4170 ($T_{\rm BB}$∼8000 K) specific luminosity and BaC3615 specific luminosity during the extended gradual phase, suggesting that the persistence of C4170 and BaC3615 are driven by the same process. The gradual phase C4170 may also be a combination of Paschen continuum and increased (H^-) photospheric emission from Balmer continuum backwarming – i.e., – as predicted by the RHD models of Allred et al. (2006); however, color temperatures as high as 8000 K have not yet been produced in these models.

6.8.2 A Comparison of Gradual Phase Spectra over Three YZ CMi Flares

Three flares – IF1, IF7, and GF5 – are particularly interesting to compare because their spectra were obtained with the same resolution (1.83Å per pixel, using the 1.5" slit). The decay phase spectra of these three flares on YZ CMi are presented in Figure 6.28 (from the times in Table 4.2). We show the smallest amplitude flare (GF5, purple), a medium-amplitude flare (IF7) and the largest amplitude flare (IF1) in the sample. At the times of these spectra, the U-band was emitting at 1.4, 2 and 25 times the quiescent level, respectively, illustrating that the gradual emission is almost identical in flares of all amplitudes and energies. The best-fit $T_{\rm BB}$ values for IF7 and IF1 at these times are 7600 K and 8300 K, respectively. GF5 has very low amounts of emission, but is fit nonetheless with $T_{\rm BB}$∼4600 K.

Despite these differences, there are striking similarities across the NUV and blue-optical

zones, including the small-scale features at the base of the Hydrogen lines, the appearance of all the prominent Helium I lines (and He II λ4686), the Ca I λ4227 (+Fe II λ4233) lines, the two plateaus in the underlying level of the pseudo-continuum (one from $\lambda = 3780 - 3950$Å and one from $\lambda = 3650 - 3760$Å) and the Hydrogen lines which are resolved through H14 λ3722Å (H15 λ3712Å, H16λ3704Å, and He I λ3704Åare blended). In the NUV spectral zone, there are even similar small-scale features, which may be blended Fe and Ti lines in emission in addition to the Balmer continuum emission at these wavelengths.

6.8.3 The Conundruum

Finally, we bring attention to the continuum rise at $\lambda > 4900$Å in Figure 6.28, representing excess "Conundruum" flux above the best-fit blackbody that is present during the decay of some flares (IF1, IF2, IF3, IF7, HF1, HF2, GF3, and GF5). The feature is also apparent in some peak spectra (IF1, IF2, IF3, IF4, IF7, HF1, GF2; Figures 3.8-3.11). In the time resolved rise phase of IF3, it is detected starting at S#25 - the first spectrum with a hot ($T_{\rm BB} \sim 10\,000$ K) blackbody component and also copious BaC. The relative flux budget of this excess "Conundruum" flux (hereafter, Conundruum) has been presented in Section 6.8.1 for IF3.

Possible sources of the Conundruum are the following:

- We first considered whether it was a calibration issue, as the DIS dichroic affects the flux calibration in the Johnson V-band range. The largest effect is near 5500Å (e.g., in flat-field lamp exposures). We took a conservative range and did not consider the flux between $\lambda = 5200 - 5800$Å due to this issue.

- It is well-known that spectra of QSO's and Seyfert 1 galaxies have a forest of Fe II lines between $\lambda = 5000 - 5500$Å (Osterbrock, 1977; Puetter et al., 1981). There have been detections of strong Fe II lines in stellar flares (Abdul-Aziz et al., 1995) and Fe I and Fe II lines solar flares (Severnyi et al., 1960; Johns-Krull et al., 1997) at these wavelengths. Other authors have concluded the presence of Fe lines in this range (Eason et al., 1992); many small scale features are visible in the high signal-to-noise spectra of IF1 (see Figure 4.30), and the Conundruum may be a blend of these lines.

- Due to the appearance of the iron forest at these wavelengths, line blanketing (Rutten, 2003) could cause the nearby continuum to increase, like what has been attributed to flux redistribution generating a higher-than-expected effective temperature for the Sun (Böhm-Vitense, 1989). Higher spectral resolution data of flares from 4500 – 6000Å would help characterize bona-fide continuum regions. Line blanketing-induced continuum enhancements should also be understood throughout the entire blue optical and NUV zones.

- By including the bluemost windows in the blackbody fitting (BW1, BW2), it could be a concern that we misfit the continua at longer wavelengths. These continuum windows have low-lying features within their narrow range. In extreme cases, the wings of Hδ and Hϵ could contaminate the continuum windows. When fitting the Castelli-Kurucz continua, we found that the absorption wings of hot stars could affect the fit and lead to larger amounts of apparent conundruum in hot stars[11]. In Appendix F, we tested whether erroneous fitting can lead to the Conundruum. In three of the four cases tested, some various amounts of Conundruum remained after excluding the bluemost continuum windows.

- In Figure 2 of Kowalski et al. (2012), we accounted for the Conundruum through a superposition of model spectra using the hot spot models and the RHDF11 model[12]. This model ascribes the flux at redder wavelengths as due to a combination of Hydrogen Paschen continuum and increased photospheric continuum that results from chromospheric backwarming. Combined, these continua produce a color temperature in the blue-optical of $T_{\rm BB}\sim$5000 K in the model.

- Finally, we note that there is a Helium II continuum edge (n =infinity to $n = 5$) at λ =5694 Å. Helium II continuum has been detected in solar flares in the EUV (Linsky et al., 1976; Milligan et al., 2012).

---

[11] Except, in hot stars, the Conundruum is an *underprediction* of the blackbody extrapolation to those wavelengths.

[12] Note, BaCF11 is different than RHDF11, as specified in Kowalski et al. (2012) and described in Chapter 7.

6.9 The Red Continuum

A reddening continuum shape during the gradual phase of IF0 in the V and R-bands was noted in HP91, who speculated about the presence of a Paschen continuum at these wavelengths. The best-fit blackbody temperature in the gradual phase to the $UV, UBVR$ photometry was $8400 - 8800$ K, similar to the lower temperatures we find in the decay phase of the DIS sample using only the blue-optical continuum fitting. The mismatch to the blackbody continuum implied by these temperatures in Figure 11 of Hawley & Fisher (1992) (bottom two panels) is due to the addition of this red component. Excess flux in the R-band is also apparent in several flares on AD Leo described in Hawley et al. (2003).

We speculate that the Conundruum rises into the red and accounts for the excess R-band flux observed in these studies. Therefore, the flare flux in the red-optical is due to both hot, blackbody emission ($T_{\rm BB}$$\sim$$10\,000 - 14\,000$ K in the impulsive phase, $\sim$8000 K in the gradual phase) and the Conundruum.

In Figure 6.29 (top), we show for the first time a complete flare SED from λ=3350 − 9200Å. This is S#24 from the IF1 decay phase[13]. The $T_{\rm BB}$ fit to the blue-optical zone is shown in blue and clearly does not account for all of the red continuum emission. The color temperature of the red optical zone for this flare ranges between $T_{\rm BB}$ $4500 - 5500$ K. In Figure 6.29 (bottom), we show the complete SED during the decay phase of IF3 (time listed in Table 4.2). This flare also exhibits a red color, with a best fit blackbody temperature of $\sim$3700 K (at peak, the best fit blackbody temperature in the red part of the spectrum is 7700 K, see next section).

The RHDF11 model coincidentally accounts for the shape of the red optical extremely well (for IF1), with a best-fit blackbody temperature in the red of $T_{\rm red} \sim 4600$ K (RHDF10 shows about the same color in the red). None of the RHD models (F10 or F11) show a slope of < 4000 K in the red part of the spectrum, as is needed to explain the red emission in the IF3 gradual phase. The RHDF11 spectrum predicts increased photospheric radiation from chromospheric UV backwarming and Paschen continuum from Hydrogen recombination

[13]Independent confirmation of the very red color at late times comes from The MEarth survey (Irwin et al., 2011). They observed this flare in their i+z filter and the light curve shows about $\sim$0.2 magnitude enhancement near the time of the S#24 spectrum (Irwin, private communication).

from the flare chromosphere. The opacity description in the RADYN model is missing molecular features that are important in M dwarfs (e.g., TiO) and which would likely have a strong influence on the energy balance in the photosphere, and hence the backwarming physics. Modeling the backwarming is further complicated due to the large area over which it may originate (Fisher et al., 2012; Isobe et al., 2007). Obtaining separate models for the Paschen continuum and backwarming radiation is not currently possible with RADYN.

Models of Paschen continua with typical temperatures of the flare chromosphere (6000 – 8000 K) typically have a red color (Hawley & Fisher, 1992), and we consider the possibility that the red continuum emission (and hence Conundruum) is primarily due to Paschen continuum. From the RHDF11 spectrum, we estimate the height of the Paschen jump at $\lambda\sim$ 8204Å as 1/16.5 times the height of the Balmer jump. We show predicted flux of the Paschen jump in Figure 6.29 as a red circle symbol with error bars indicating the height of the Paschen jump (1/16.5 times the flux of BaC3615). We do not find evidence of a Paschen jump to indicate the presence of Paschen continuum emission, but the spectral region around the Paschen jump is contaminated by features from the Earth's atmosphere and instrumental fringing which make the quiescent subtraction uncertain and therefore the characterization of flare-only continuum extremely difficult at these wavelengths. The Paschen jump has been (tentatively) detected in a solar flare (Neidig & Wiborg, 1984).

In Appendix G, we explore the shapes of Paschen continua with simple, isothermal, isodensity, optically thin, Hydrogen bf+ff slabs. If one fits only to the red continuum, $\lambda = 6000 - 6800$Å, one needs $T_e = 12\,500 - 25\,000$ K (where T_e is the electron temperature) to achieve a blackbody temperature of $T_{\rm BB}\sim$4500 – 5500 K (which correspond to the color of the RHDF11 impulsive phase spectrum and IF1 gradual phase red spectrum). In Chapter 8, we will find that the Paschen continuum forms at temperatures that are lower than this value and more importantly, over a relatively large *range* of temperatures and electron densities. If we consider the red gradual spectrum of IF3, which has a redder $T_{\rm BB}$ compared to IF1 ($T_{\rm BB}\sim$3500 – 4000 K), this shape is reproduced by an isothermal model with $T_e = 7000 - 9500$ K. Coincidentally, this *is* the approximate range of temperatures that give rise to Paschen continuum from the flare chromosphere (Chapter 8). However, a large range of electron temperatures can give rise to a relatively small range of red con-

tinuum colors. Targeted observations of the red continuum with spectra or (simultaneous VRI) broadband photometry complemented with detailed, multithermal, self-consistent atmospheric modeling are needed to make further progress in understanding this enigmatic continuum component.

6.9.1 Impulsive Phase Red Continuum

There is direct evidence of the presence of this third, red continuum component (the Conundruum) in the IF3 flare in Figure 6.30. Several continuum fluxes measured relative to C4170 are: C6010 in the red, C4500 in the blue optical, and C3615 at the Balmer jump (the latter ratio is the usual $\chi_{\rm flare}$). In addition, we show the Hγ equivalent width (using the C4170 as the continuum). The figure illustrates that C6010/C4170 has a similar time-evolution to $\chi_{\rm flare}$. The C4500/C4170 ratio, on the other hand, is relatively flat showing small variations that reflect the change in $T_{\rm BB}$ through the impulsive phase and into the gradual phase. We have already explored the anti-correlated behavior of $\chi_{\rm flare}$(t) with the total continuum (shown as the C3615 flux in Figure 6.30), and concluded that it arises due to the different time-evolution of the BaC and blackbody. Therefore, the similar behavior seen in the relative evolution of C6010 and C4170 suggests a time evolution of red-optical emission that more closely resembles the blue Hydrogen Balmer emission. It's interesting in the decay phase that the C6010/C4170 actually resembles the Hγ equivalent width evolution more closely than the $\chi_{\rm flare}$. We conclude that the Conundruum has a time-evolution that is closer to the lower order Balmer lines than to the BaC, consistent with the Conundruum flux becoming relatively more prominent in the far decay phase (Figure 6.27, bottom), like the lower order lines, which stay elevated longer. We speculate that Conundruum has a large contribution from Paschen and possibly Brackett continua (recombination to $n = 3$ and $n = 4$ respectively); a subsequent transition to $n = 2$ from either of these two levels would result in emission of an Hα or Hβ photon, respectively. This scenario would nicely lead to the observed relation between the Conundruum and the lower order lines.

In Figure 6.31, we show the extrapolation of a blackbody curve fit to the blue-optical at the peak emission during IF3 (S#31) in order to illustrate the excess flux at C6010

unaccounted for by a simple isothermal Planck function. There is not as much excess at C6010 during the IF3 peak as there is during the IF1 decay (Figure 6.29). In Chapter 7, we explore various ways of fitting the entire SED in Figure 6.31, including with hot-spot models and a superhot free-free emission model. During the impulsive phase of most moderate-size flares, an extrapolation of the blackbody fit to the blue optical accounts for most of the flux at C6010; the flare emission during the impulsive phase of four moderate/large flares (IF2, IF7, IF9, HF2) are shown in Figure 6.32. The spectral trend implies that the flare-flux continues to rise blueward of our spectral range; observations in the NUV would provide a more complete understanding of the white-light flare continuum.

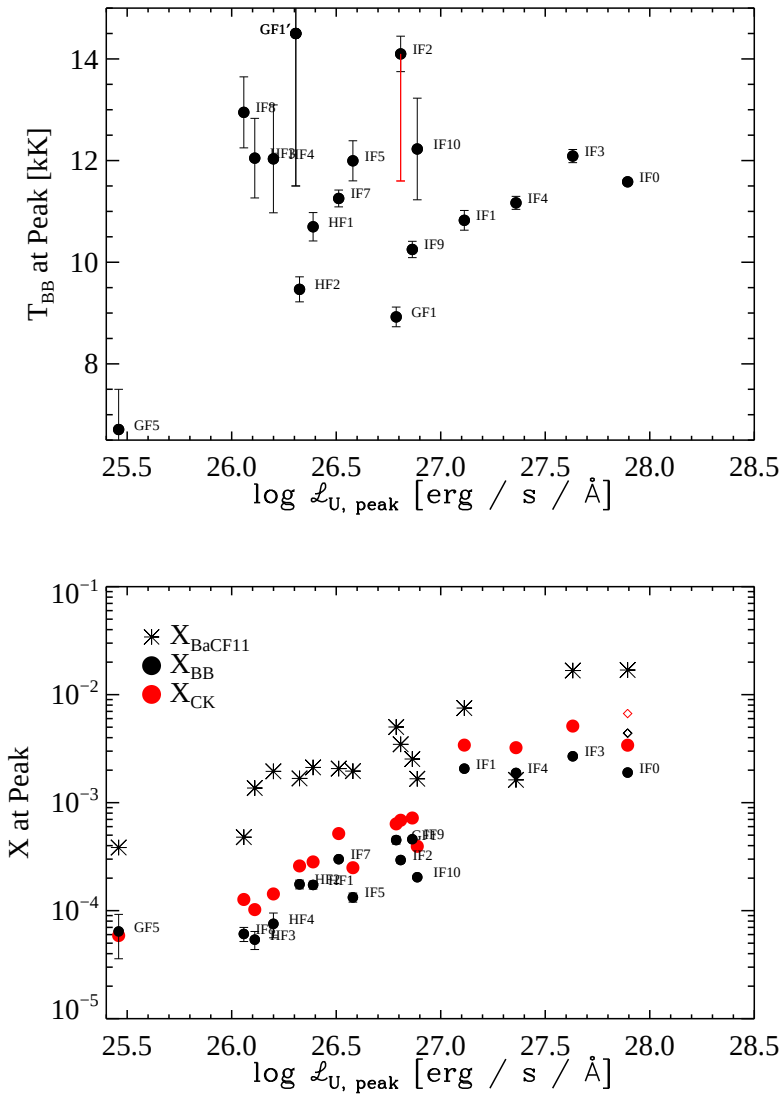

Figure 6.1 (Top) The formation of a 9 000 − 14 000 K component is present for large and small amplitude flares, on a variety of stars. The GF1' flare is the measured temperature from the initial spike event in GF1, assuming that it originates from a newly heated flare region. The red error bar on IF2 is a lower limit obtained from excluding the bluemost continuum windows in the fitting (see Appendix F) (Bottom) We plot the peak $X_{\rm BB}$ (color temperature from blackbody slope) and $X_{\rm BaCF11}$ for the fifteen flares with well-measured peak temperatures as a function of the specific luminosity in the U band. The $X_{\rm CK}$ is the filling factor ($X_{\rm BB}$) corrected using the Castelli-Kurucz models of hot star atmospheres (Section 6.1.4).

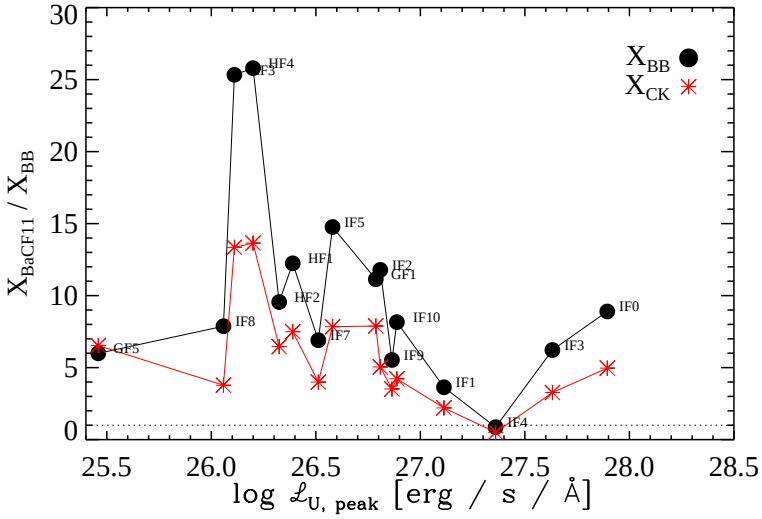

Figure 6.2 The ratio, $X_{\rm BaCF11}/\ X_{\rm BB}$ for the fifteen flares with well-determined temperatures (black circles). Red asterisks are the ratios after applying the CK corrections to the blackbody areas (Section 6.1.4). The horizontal line is a ratio of 1. The two flares with large values of $X_{\rm BaCF11}/\ X_{\rm BB}$ are HF3 and HF4.

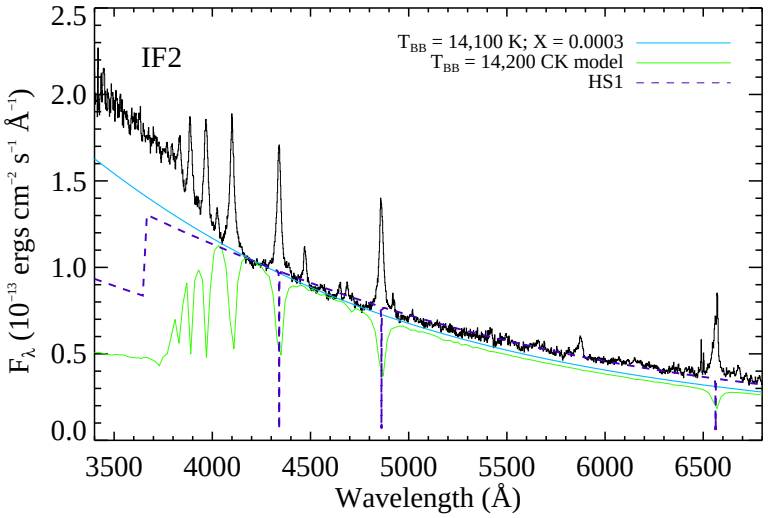

Figure 6.3 The peak flare-only emission from IF2. The best-fit Planck function ($T_{\rm BB}$= 14 000 K) is shown in light blue. The hot star log $g = 5$ model atmosphere is shown in green with a best-fit blue-optical shape of 14 200 K (Section 6.1.4). The hot star modeling predicts a large amount of Balmer continuum absorption. A "hot-spot" model (HS1, $T_{\rm BB}\sim$11 000 K) is also shown in the purple dashed line (see Chapter 7).

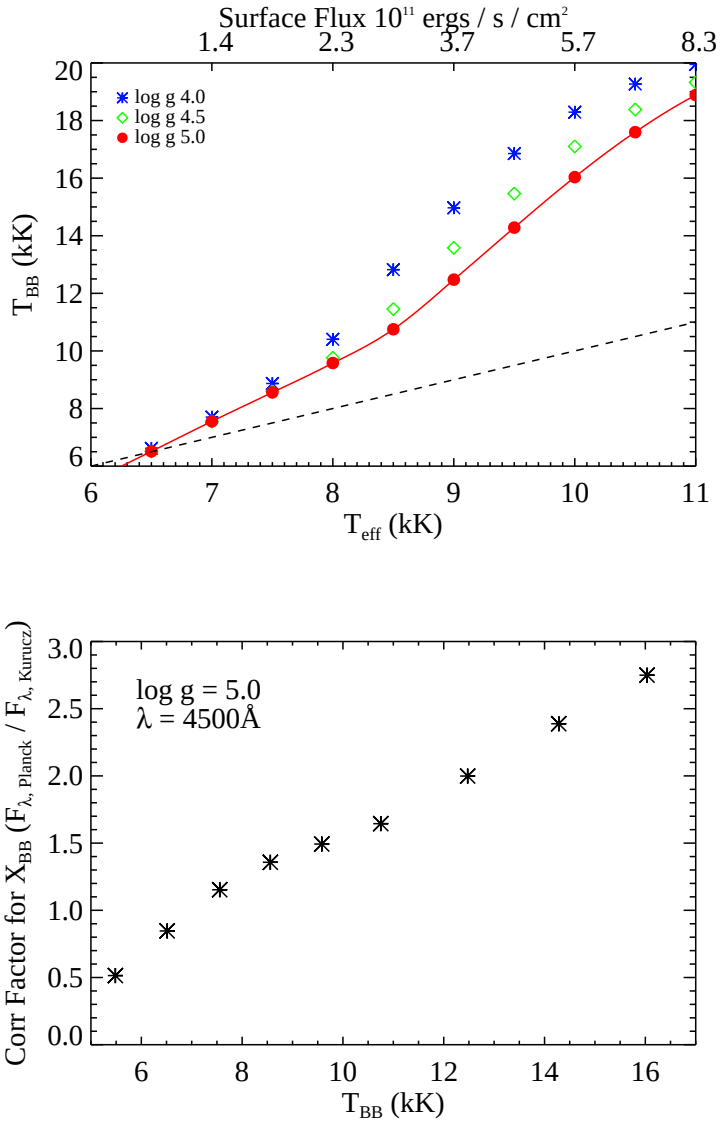

Figure 6.4 (Top) The relation between the color temperature (y-axis) and the effective temperature (x-axis) for a suite of hot-star models from Castelli & Kurucz (2004). The dashed line is 1:1 line. The top axis is discussed in the modelling section, Chapter 8. (Bottom) The correction factor to apply to a surface area derived from fitting a Planck function with a given color temperature ($T_{\rm BB}$) if the flare atmosphere is identical to a *log* g = 5.0 hot star atmosphere.

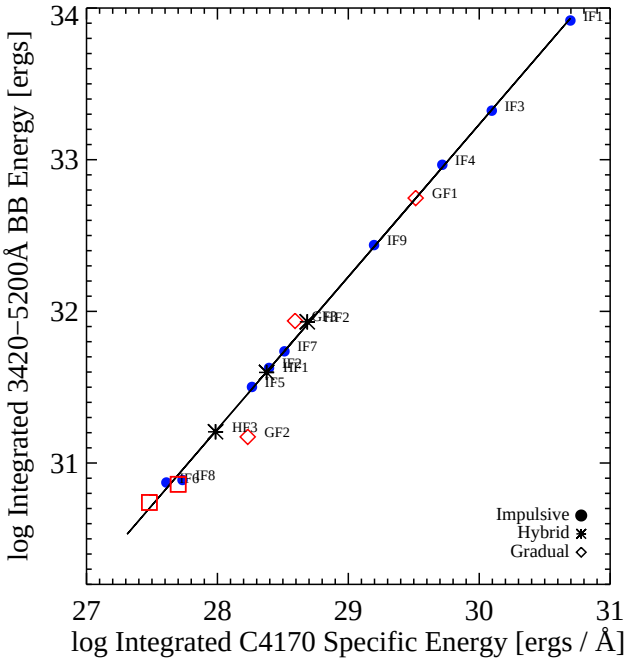

Figure 6.5 The time-integrated energies of the blue-optical blackbody and C4170. The two peaks of GF2 are considered individually as the square symbols.

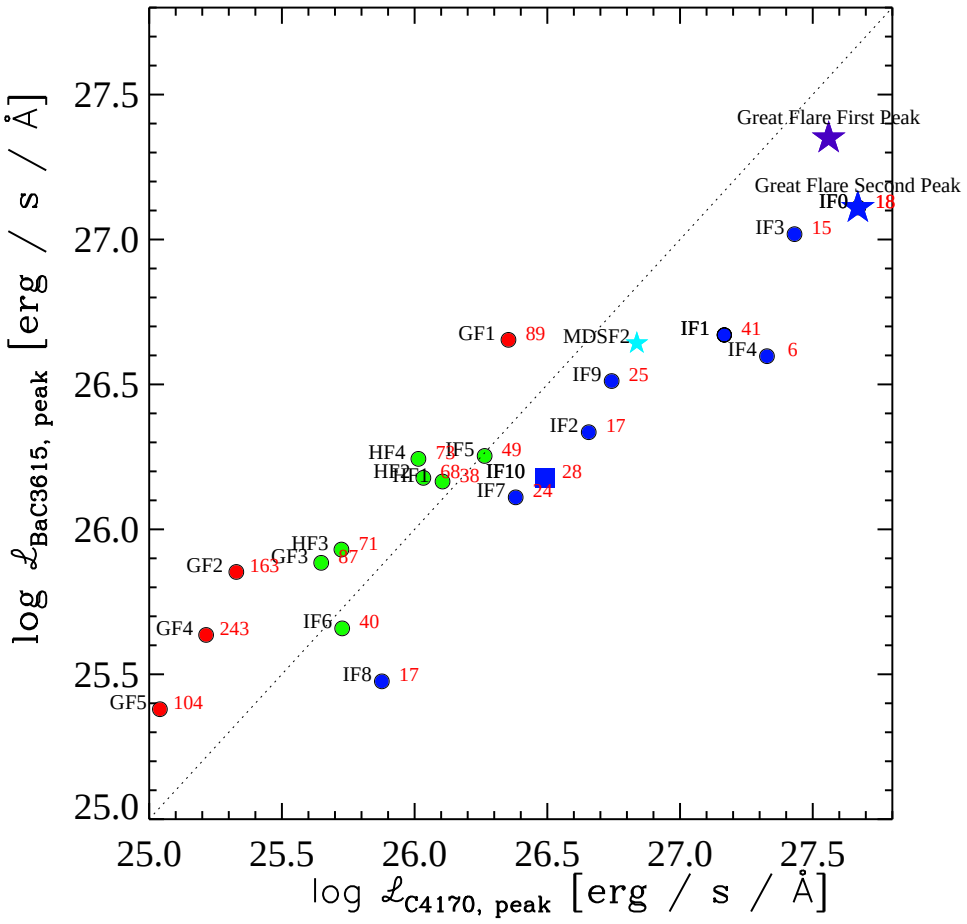

Figure 6.6 The peak specific luminosity in the two primary continuum components for the DIS sample (filled circles), IF0 (dark blue and purple stars), and IF10 (filled square). The light blue filled star is the newly formed flare emission from MDSF2 of IF1: the amount of BaC3615 (absorption) is not that different from the amount of BaC3615 in emission in the other flares. $\mathcal{L}_{\mathrm{C4170}}$ is a diagnostic of the blackbody component. The dashed line is the 1:1 relation, and the points are color-coded by $\chi_{\mathrm{flare,peak}}$: blue ($\chi_{\mathrm{flare,peak}} < 2$), green ($2 \leq \chi_{\mathrm{flare,peak}} < 3.0$), and red ($\chi_{\mathrm{flare,peak}} > 3.0$). The red numbers indicate the Hγ / C4170 ratio.

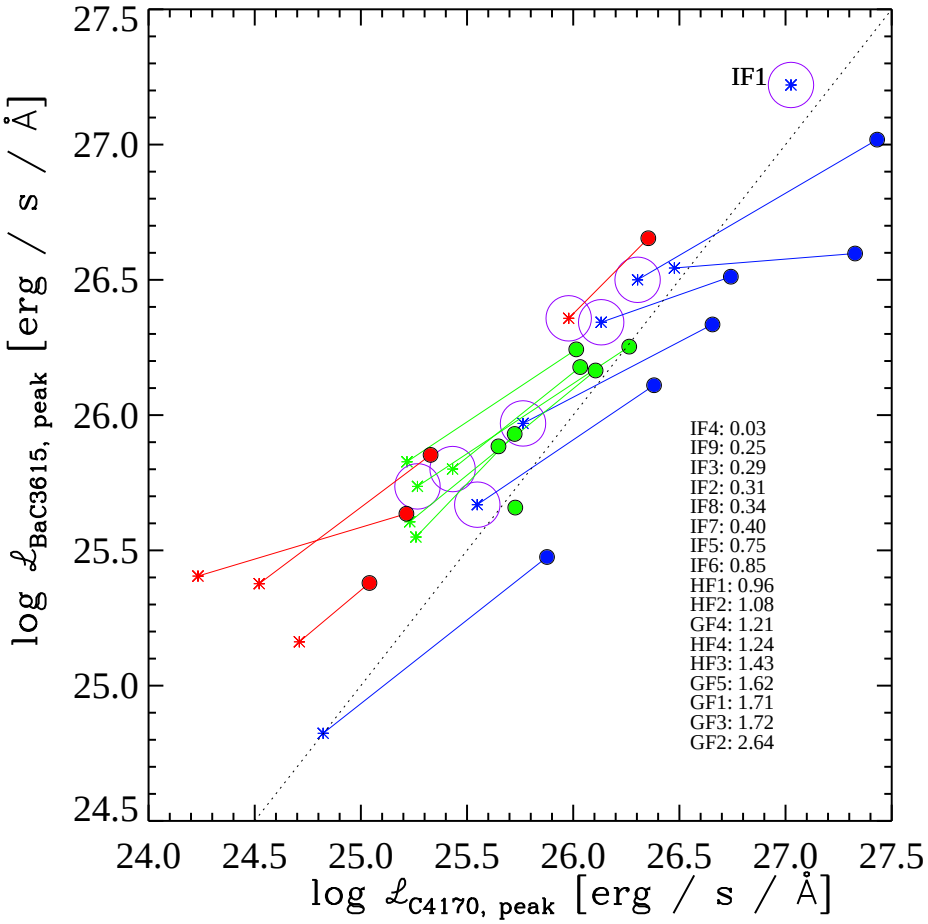

Figure 6.7 The specific luminosities during the extended gradual phases of the DIS flares in asterisks, with lines connecting to the values at peak (filled circles) from the previous figure. The dashed line is 1:1, and the circles, lines, and asterisks are color-coded by the $\chi_{\rm flare,peak}$: blue ($\chi_{\rm flare,peak} < 2$), green ($2 \leq \chi_{\rm flare,peak} < 3.0$), and red ($\chi_{\rm flare,peak} > 3.0$) as in the previous figure. In the bottom right, the slopes of the lines are given in increasing order (see text). Note that all flares evolve to the left of the line (toward BaC3615 > C4170) in the gradual phase and the slopes increase generally according to the IF/HF/GF grouping with IF5 and IF6 having large slopes for their IF designation. IF1 is unusual because the observations were obtained during a highly elevated decay phase. Note, the large purple circles refer to Section 6.8 and indicate the flares with a $T_{\rm BB}$~8000 K component in the gradual phase spectrum.

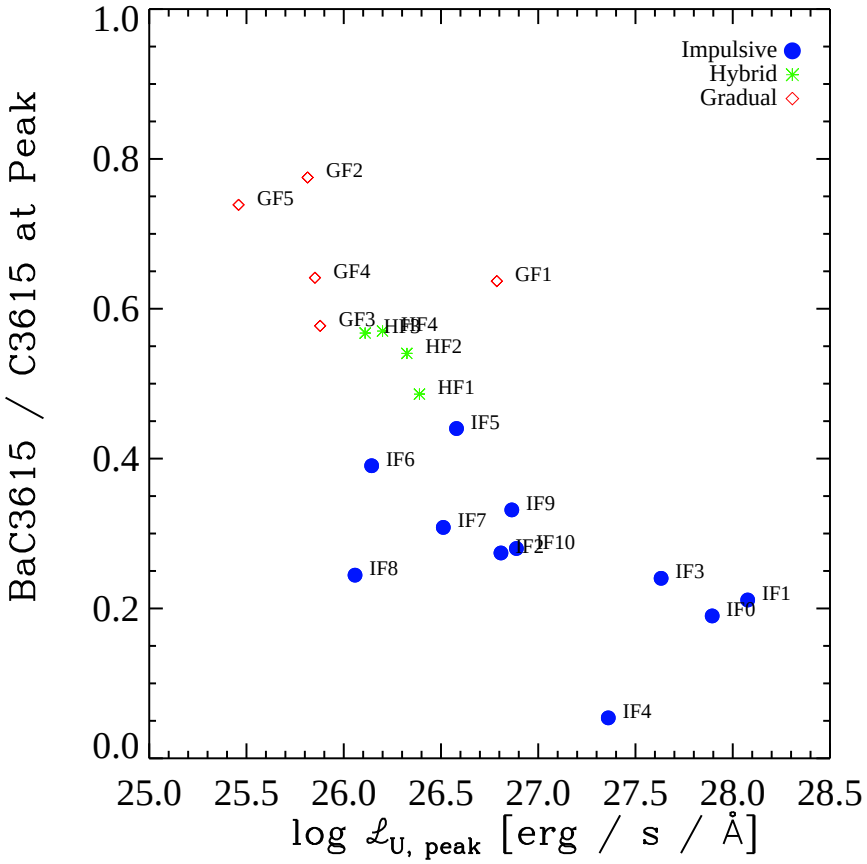

Figure 6.8 The fraction of the C3615 flux that originates from BaC3615. We color code the points according to their light curve morphology: IF events as blue circles, HF events as green asterisks, and GF events as red diamonds. Note the decreasing contribution from the BaC3615 as flares become larger amplitude and also more impulsive.

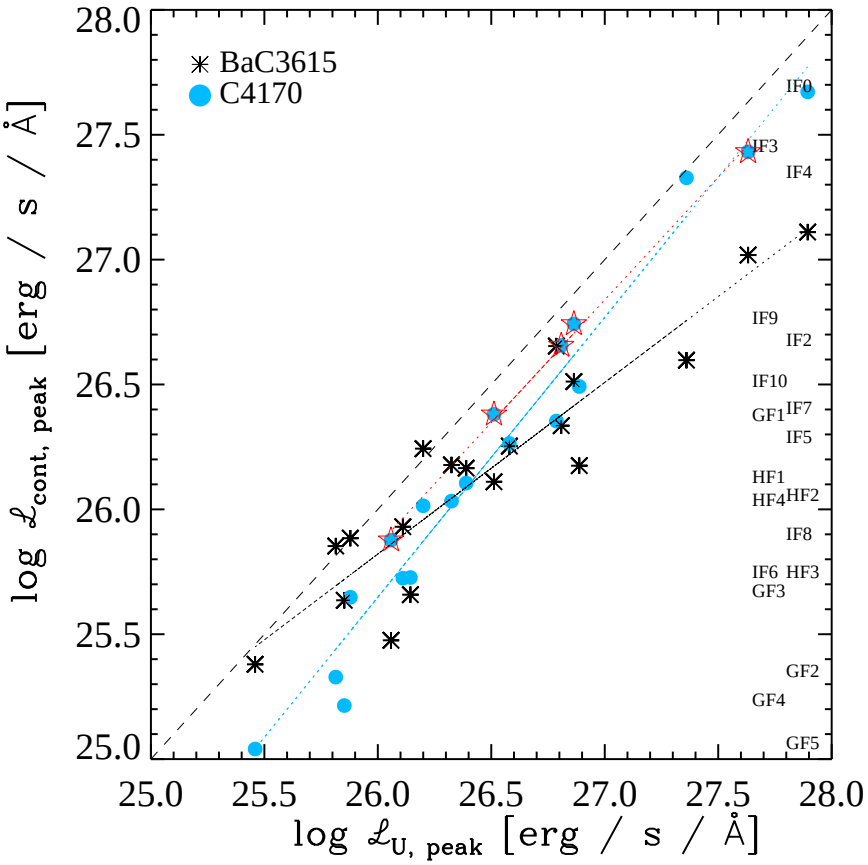

Figure 6.9 The peak specific luminosities of BaC3615 and C4170 vs the peak specific luminosity of the U band. IF0 is taken from the secondary peak (the U band specific luminosity is adjusted according to the photometry at that time). IF10 taken from first spectrum (both quantities) and U band adjusted by a factor of 5 because the long exposures integrated over the entire U-band peak. Labels shown at right opposite C4170 value for each flare. The red stars are the classical flares IF2, IF3, IF7, IF8, IF9 and the red line is a fit to them. Dashed line shows the 1:1 relation.

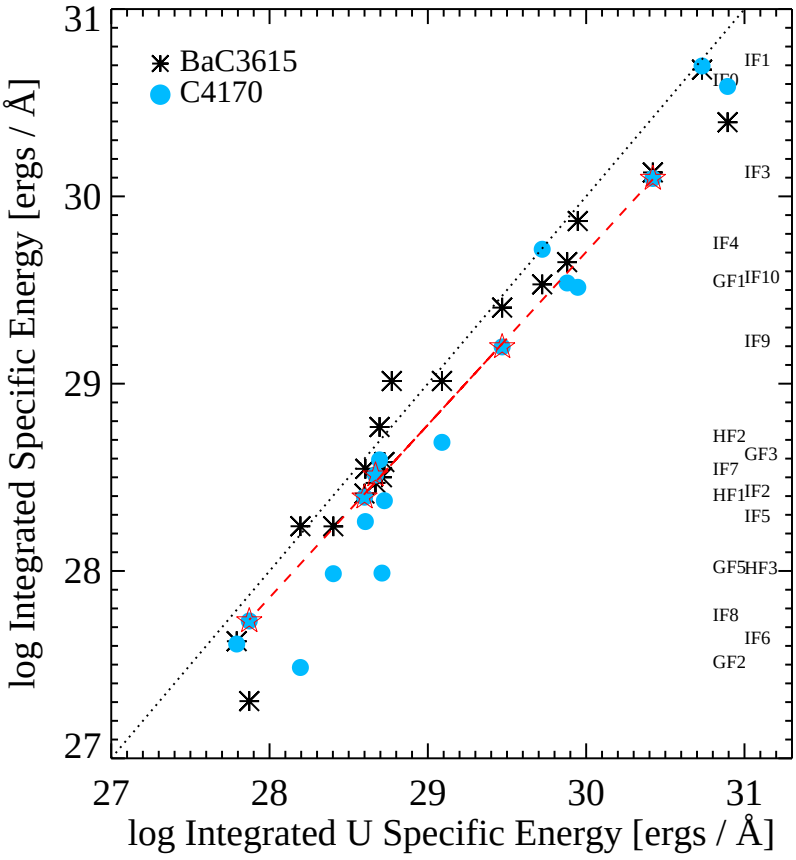

Figure 6.10 The time-integrated specific energies of BaC3615 and C4170 vs the time-integrated specific energy ($\mathcal{E}$) of the U-band. The GF2 point is shown only for the first peak, and GF4 is not included because C4170 is only detected very close to peak emission. The red stars are the classical flares IF2, IF3, IF7, IF8, IF9 and the red line is a fit to them.

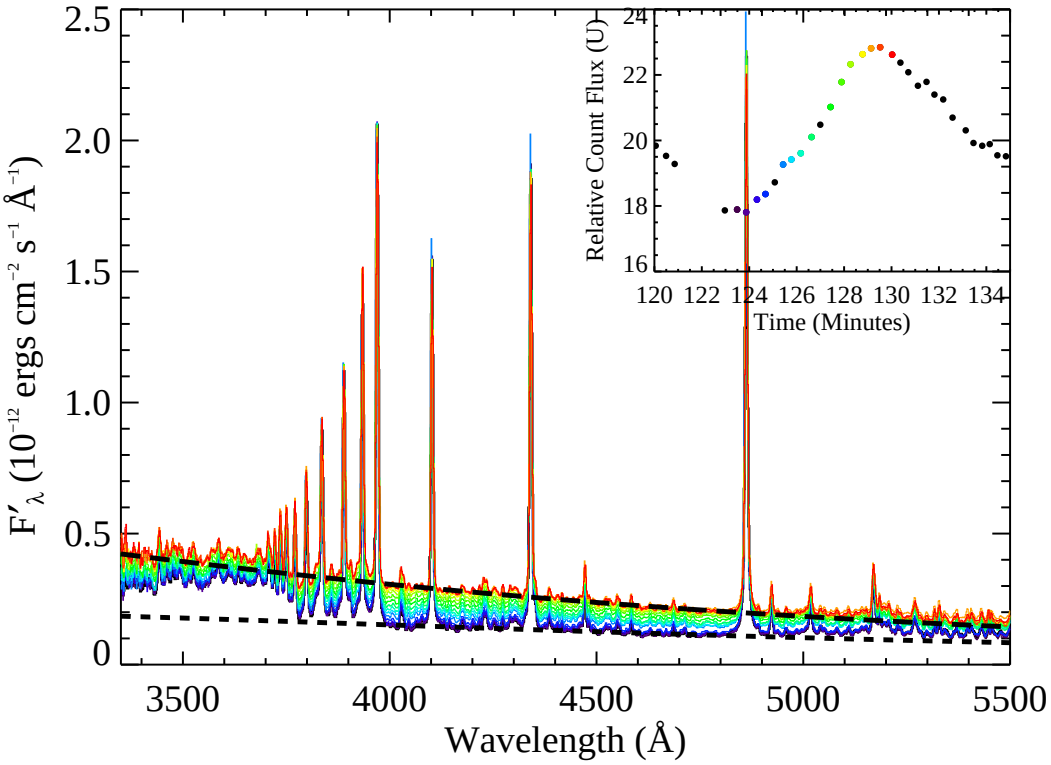

Figure 6.11 A series of 16 flare spectra obtained prior to the onset and through the peak of the secondary flare MDSF2 during the IF1 decay. The quiescent level has been subtracted. The *U*-band light curve (inset) is color-coded to the spectrum obtained closest in time. The best-fit blackbody curves to the black- and red-colored spectra are shown as the short-dashed and long-dashed lines respectively. This figure was originally published in Kowalski et al., 2012, SoPh Vol. 277, Issue 1, pp. 21 – 29; ©2012 by Springer. Springer and *Solar Physics*, Volume 277, 2012, pp. 21 – 29, "The Multiple Continuum Components in the White-Light Flare of 16 January 2009 on the dM4.5e Star YZ CMi", Adam F. Kowalski, Suzanne L. Hawley, Jon A. Holtzman, John P. Wisniewski, and Eric J. Hilton, Figures 1 – 3 is given to the publication in which the material was originally published, by adding; with kind permission from Springer Science and Business Media.

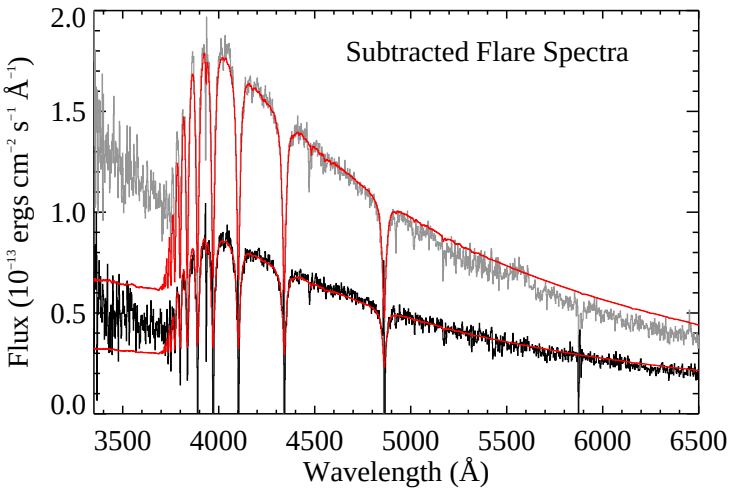

Figure 6.12 The black is the newly formed flare emission half way up the rise of the secondary flare MDSF2 (S#108-109) and the grey is the newly formed flare emission just prior to the peak (S#113). The red is the spectrum of Vega scaled to each flare spectrum.

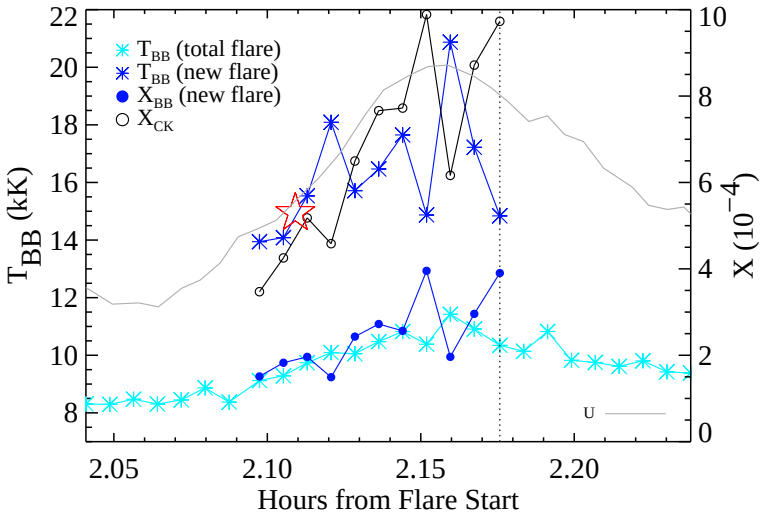

Figure 6.13 The grey line is the U-band light curve during the secondary flare (MDSF2) of IF1. The circles are $X_{\rm BB}$ derived from fitting a Planck function with $T_{\rm BB}$ (dark blue asterisks) to the newly formed emission during the rise. The red star represents the $X_{\rm HS2}$ from Kowalski et al. (2012) (see Chapter 7). The black open circles are $X_{\rm BB}$ adjusted using the Castelli-Kurucz hot star models.

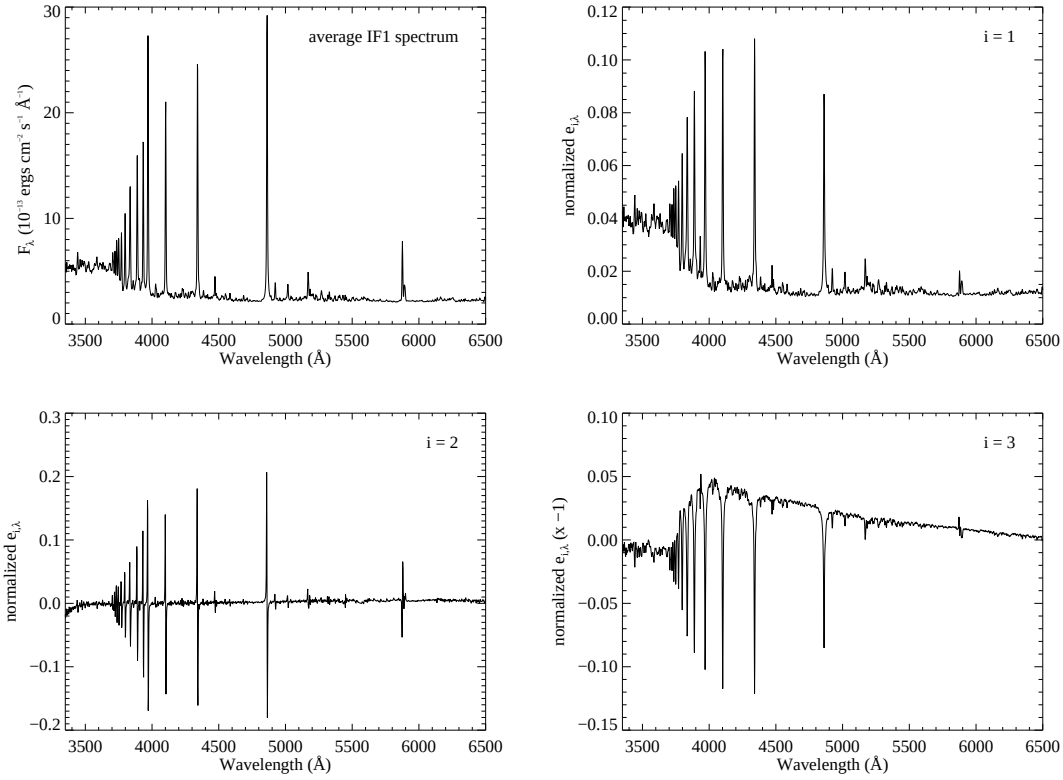

Figure 6.14 The average spectrum and the first three normalized eigenspectra for the decay phase of IF1. The $i = 2$ eigenspectrum is instrumental.

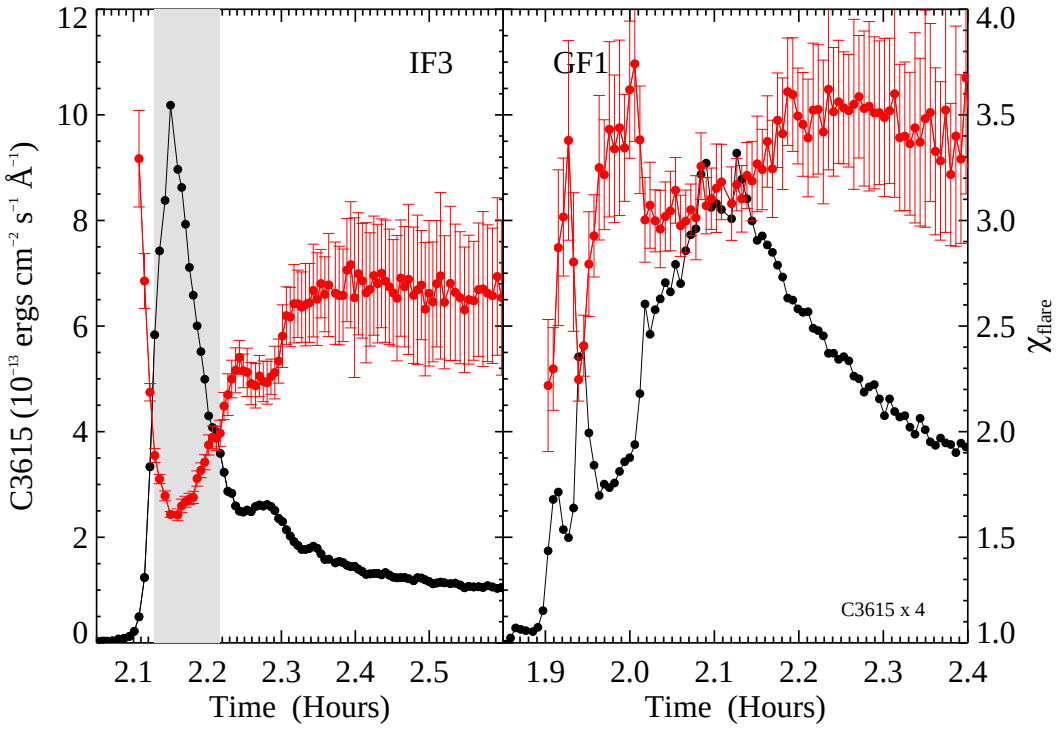

Figure 6.15 The evolution of $\chi_{\rm flare}$(right axis, red/grey points) compared to the C3615 (left axis, black circles) for the two high-energy flares, IF3 (left panel) and GF1 (right panel). The time axis covers ∼0.5 hours in both plots.

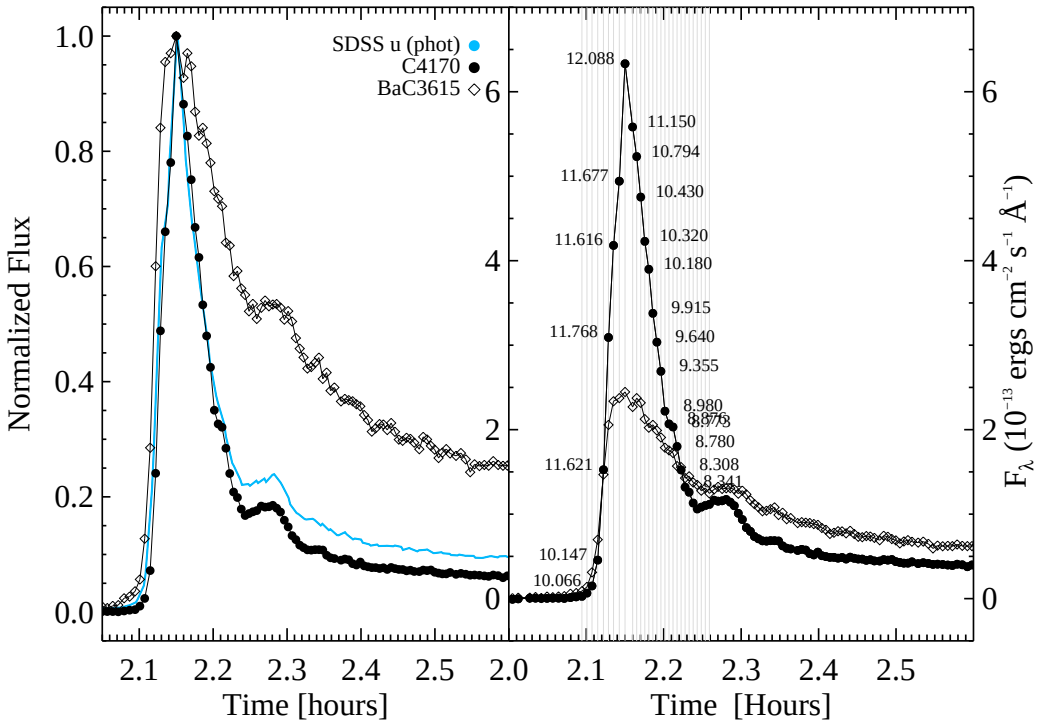

Figure 6.16 The temperature evolution of IF3 during the rise phase for C4170, BaC3615. In the right panel, vertical lines indicate midtimes of the spectra. Points are labeled by $T_{\rm BB}$ in kK. Note, the largest C4170 flux corresponds to S#31.

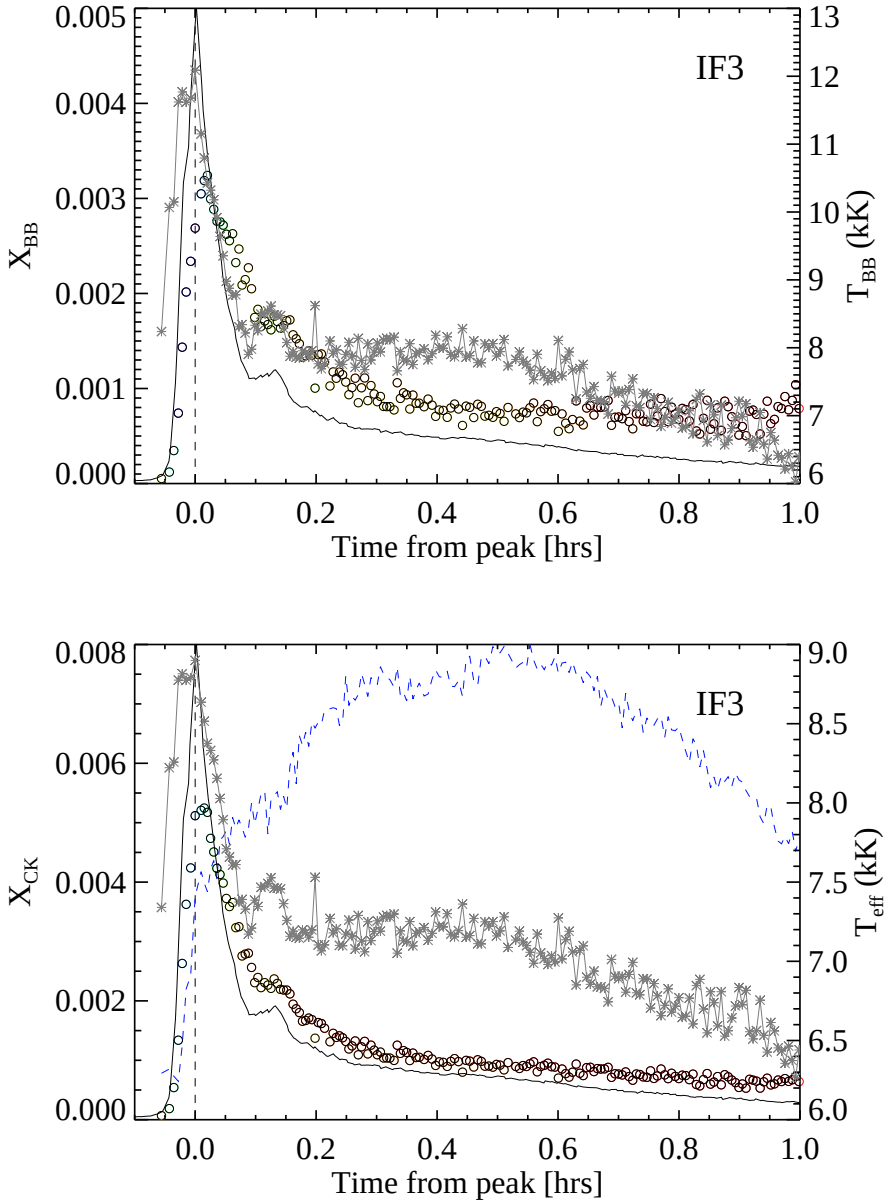

Figure 6.17 (Top) Areal evolution ($X_{\rm BB}$) of IF3 (open circles, left axis). The circles are color-coded by $T_{\rm BB}$ (grey asterisks, right axis). The SDSS u-band evolution is shown as the solid black line. The vertical dashed line indicates the maximum continuum emission. (Bottom) The same as the top panel but the circles are $X_{\rm CK}$ and are color-coded by $T_{\rm eff}$ (right axis, grey asterisks) derived from the CK corrections. The Ca II K line flux is shown as the blue dashed line (see text).

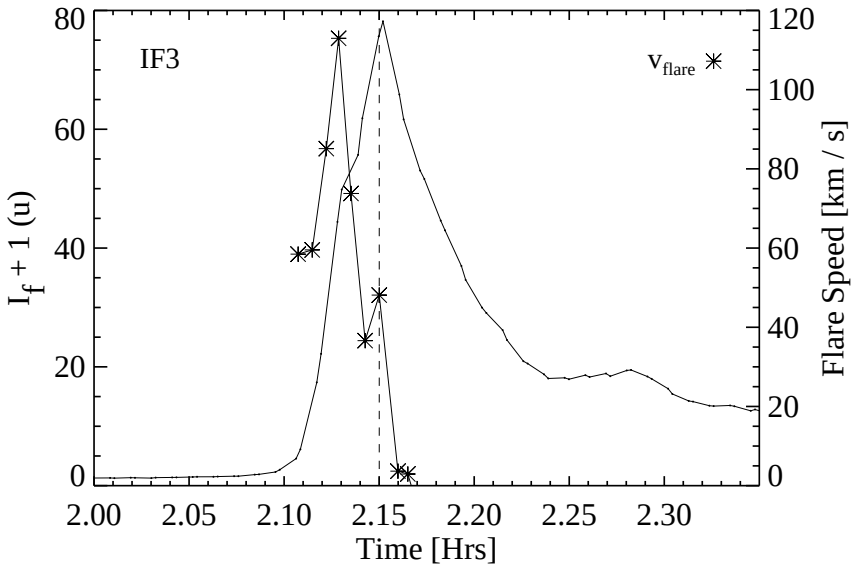

Figure 6.18 SDSS u band and derived speed of the expanding flare area during the rise phase. These speeds were inferred using the CK-corrected areas. See Appendix F.1.4 for a figure showing the speeds derived from the uncorrected areas.

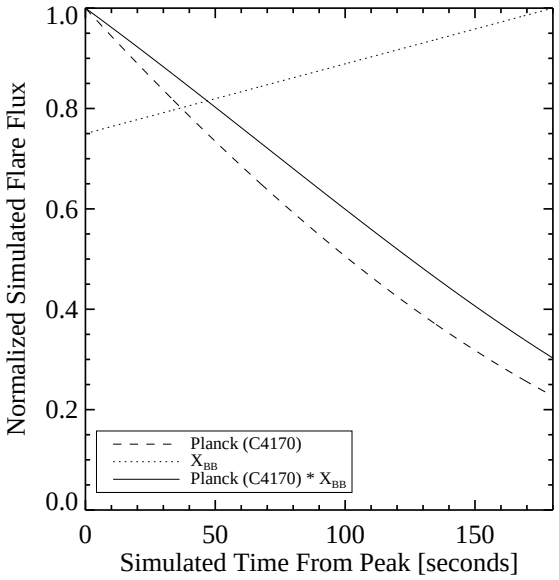

Figure 6.19 The evolution in flare flux at C4170 during the fast decay of a flare that has a 33% decrease in temperature and 33% increase in $X_{\rm BB}$ over 3 minutes. The temperature evolution causes a fast decline in Planck function intensity (dashed line), while the increasing $X_{\rm BB}$ (dotted line) slows the decline slightly (solid line).

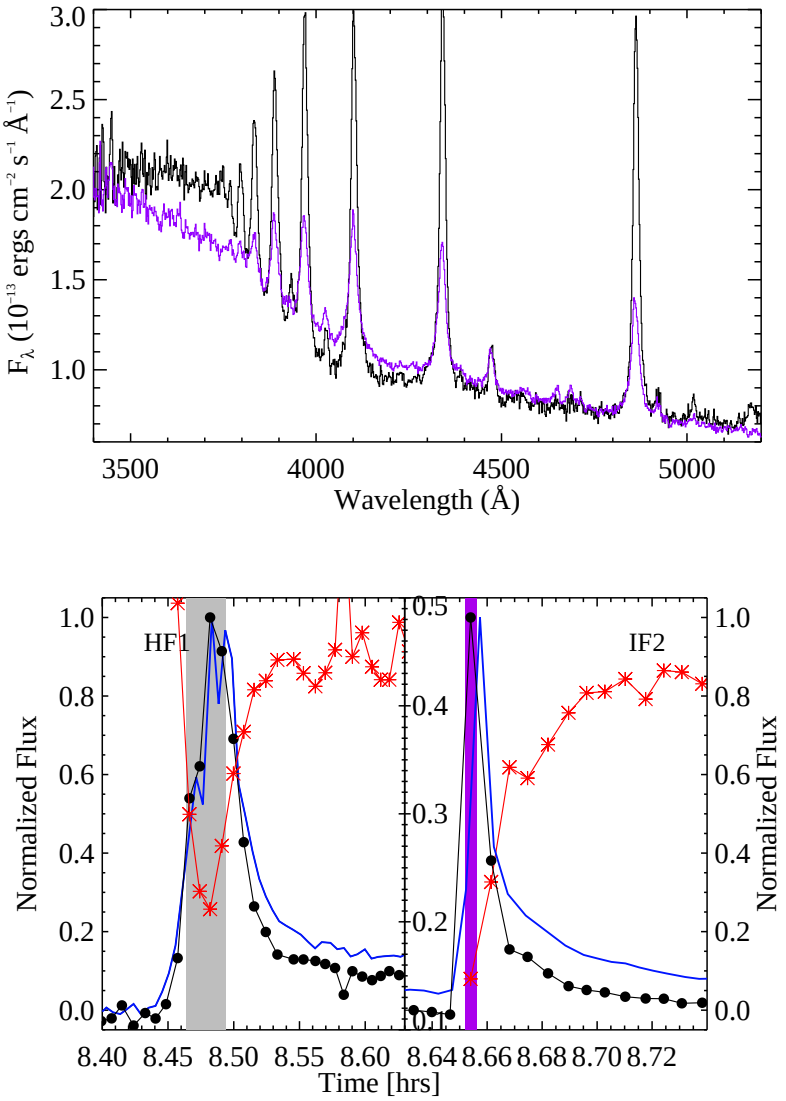

Figure 6.20 (Top) Comparison of stacked spectrum from the impulsive phase of HF1 (black) to the peak spectrum of IF2 (purple). (Bottom) The times considered are indicated in the bottom panel (shaded grey area and shaded purple area). The bottom panel also shows the light curves for C4170 (black circles) and the U-band (blue line). The leftmost and rightmost axes are these quantities normalized to peak. The middle axis (red asterisks) is the Hydrogen Balmer fraction (Hydrogen Balmer flux / total 3420 – 5200Å flux; see Section 4.3) as a function of time.

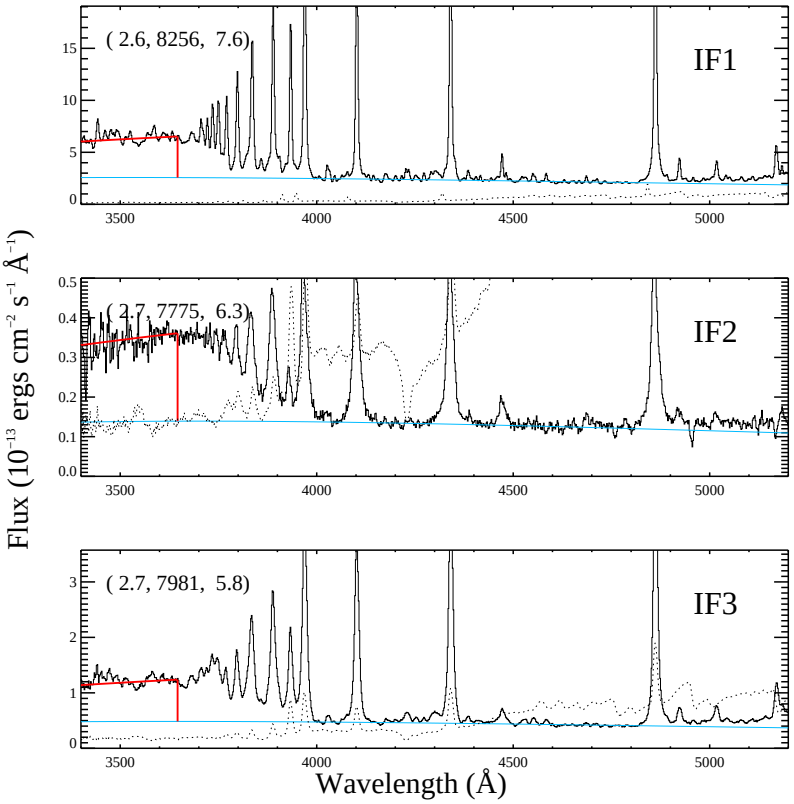

Figure 6.21 The flare-only gradual phase emission (black) compared to the quiescent emission (dotted line). The two-component model is shown: the BaCF11 model in red, the best-fit blackbody in light blue. In parentheses, the $\chi_{\rm flare,decay}$, $T_{\rm BB}$, and $X_{\rm BaCF11}/X_{\rm BB}$ are listed.

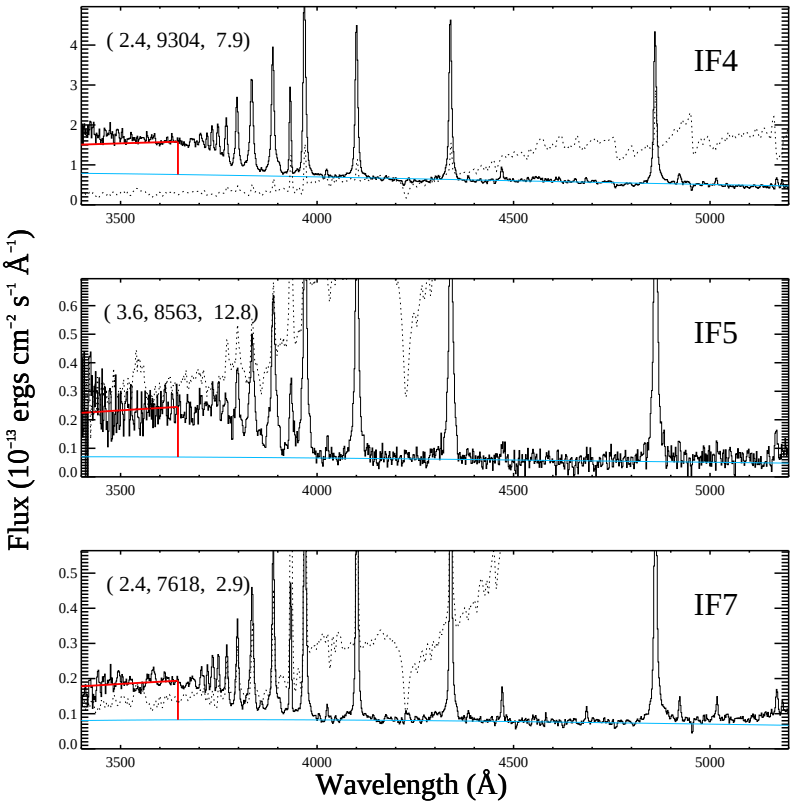

Figure 6.22 Same as for Figure 6.21.

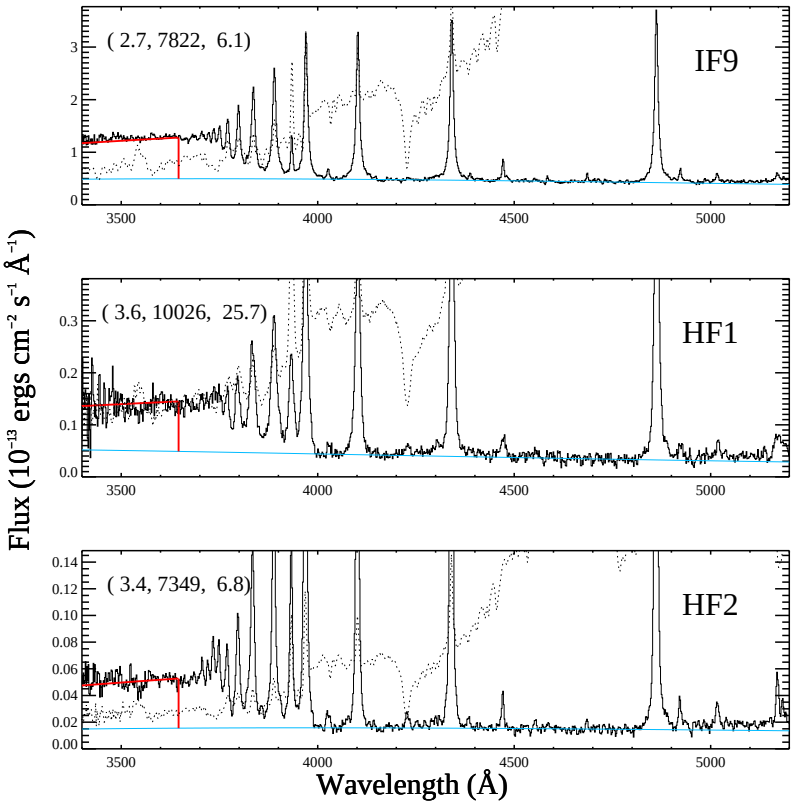

Figure 6.23 Same as for Figure 6.21.

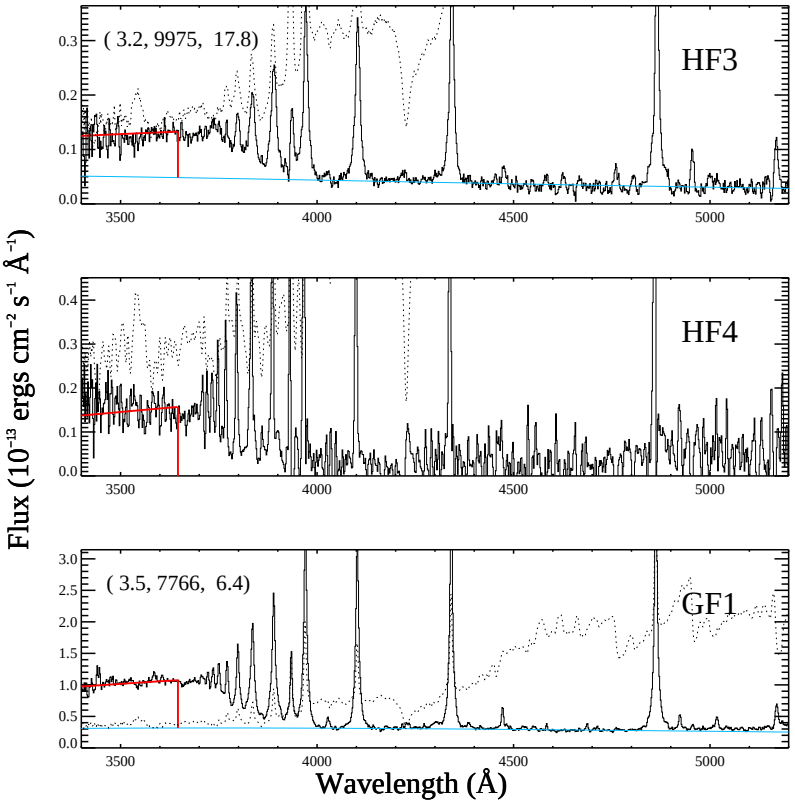

Figure 6.24 Same as for Figure 6.21. HF4 does not have well-determined values of $\chi_{\rm flare,decay}$ and $T_{\rm BB}$; only the BaCF11 model is plotted for this flare.

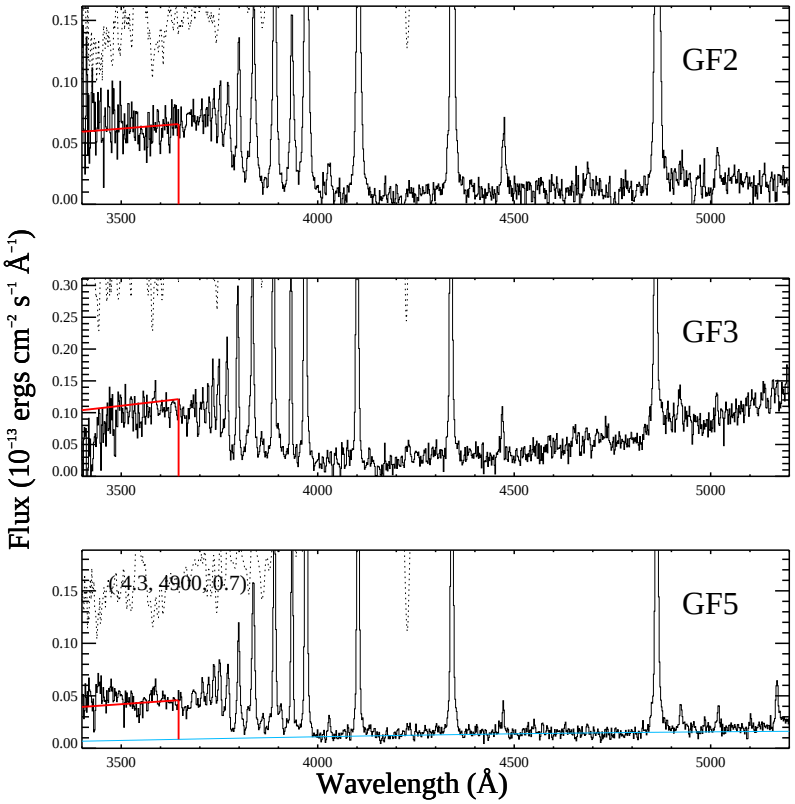

Figure 6.25 Same as for Figure 6.21. GF2 and GF3 do not have well-determined values of $\chi_{\rm flare,decay}$ and $T_{\rm BB}$; only the BaCF11 model is plotted for these flares.

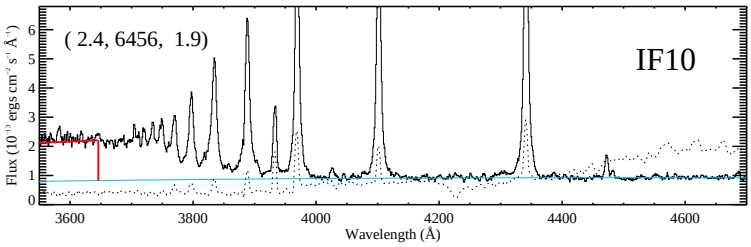

Figure 6.26 Same as for Figure 6.21. Note the different wavelength range. Although the extended gradual phase is listed as S#34 in Table 4.2, we show spectrum S#32 which encompasses a secondary flare and the beginning of the extended gradual phase.

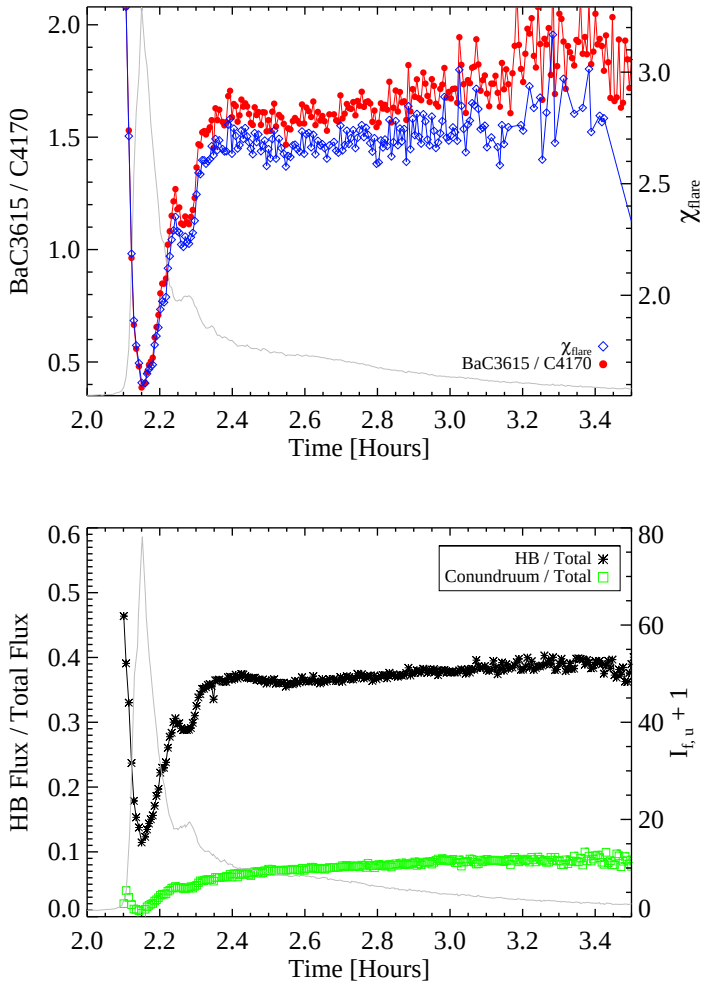

Figure 6.27 (Top) The BaC3615 / C4170 ratio (left axis, red circles) and the $\chi_{\rm flare}$ value (right axis, blue diamonds), showing similar time-evolution in the extended decay phase. (Bottom) Time evolution of the fraction of Hydrogen Balmer (HB) flux in the spectrum from $\lambda = 3420 - 5200$Å compared to the time evolution of Conundruum flux (green). The Conundruum flux contribution increases into the decay phase.

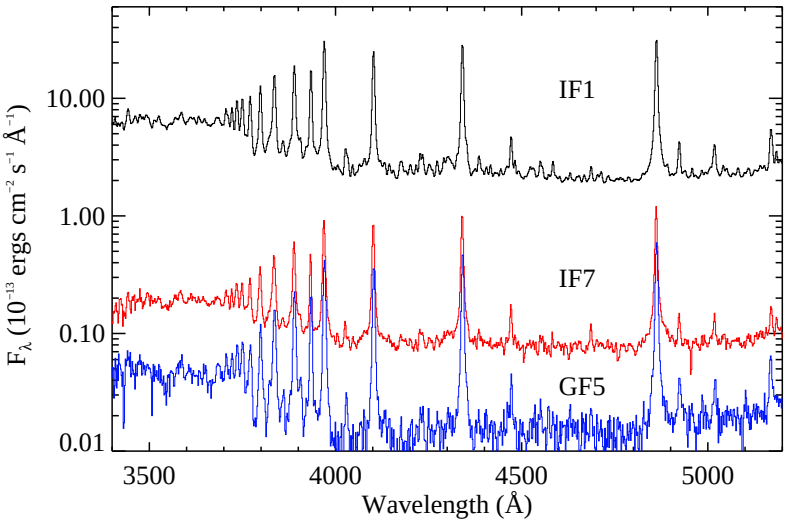

Figure 6.28 Flare-only decay phase spectra from IF1 (black), IF7 (red), and GF5 (blue). These data have the same spectral resolution, and many features are common between the smallest and largest flares in the sample.

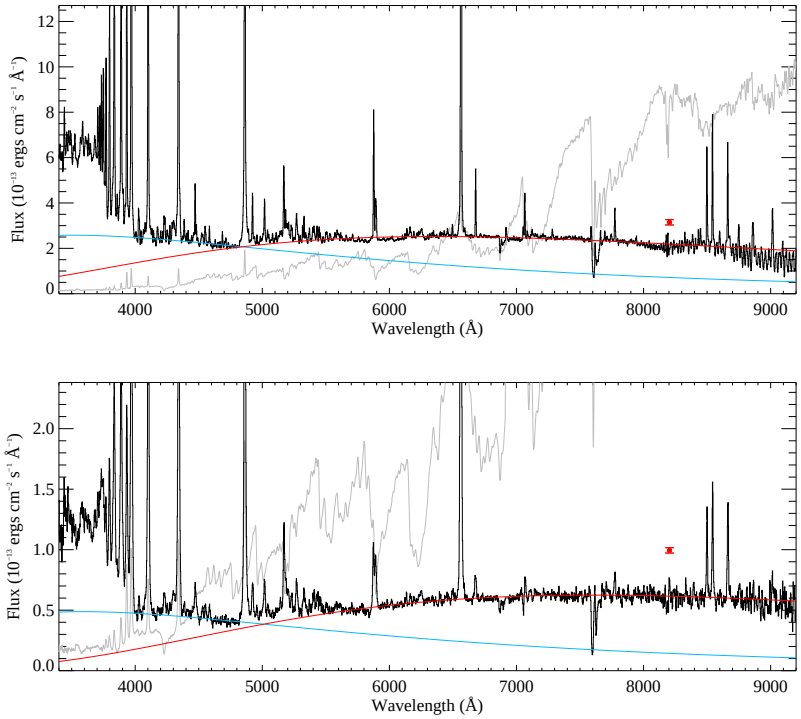

Figure 6.29 (Top) The $\lambda = 3350 - 9200$Å flare-only spectrum, average of S#23-25 of the decay phase of IF1. The quiescent spectrum is shown in light grey. The blackbody fit to the blue optical is shown as light blue, the blackbody fit to the red shown as a red line. The red point with error bars is the height of the Paschen jump predicted from the RHDF11 spectrum. (Bottom) The $\lambda = 3350 - 9200$Å flare-only spectrum during the decay phase of IF3. In both figures, the Conundruum is the break in the spectrum where the blue and red lines cross at $\lambda \sim 5000$Å.

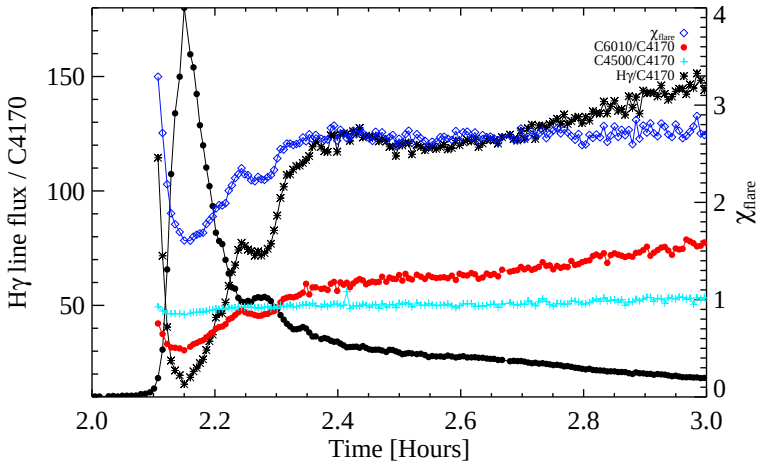

Figure 6.30 The evolution of the continuum flux ratios, C6010/C4170 (red), C4500/C4170 (turqouise), and C3615/C4170 ($\chi_{\rm flare}$, blue) for IF3. The line flux of Hγ (relative to C4170, asterisks) and the C3615 light curve (black filled circles) show much stronger reaction to the impulsive phase near flare peak.

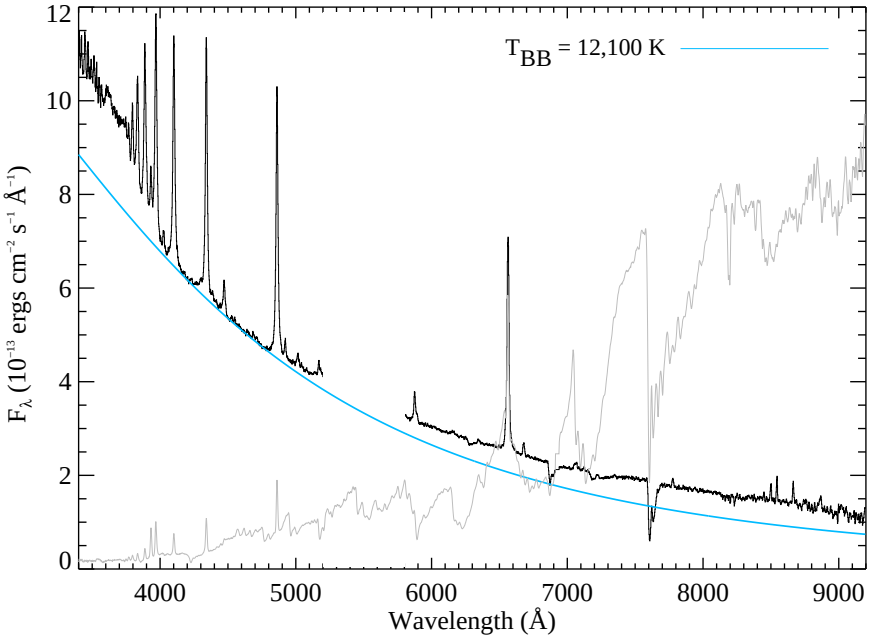

Figure 6.31 The peak flare-only spectrum of IF3 (S#31). The blackbody fit to the blue-optical zone is shown in light blue. The quiescent is shown in grey.

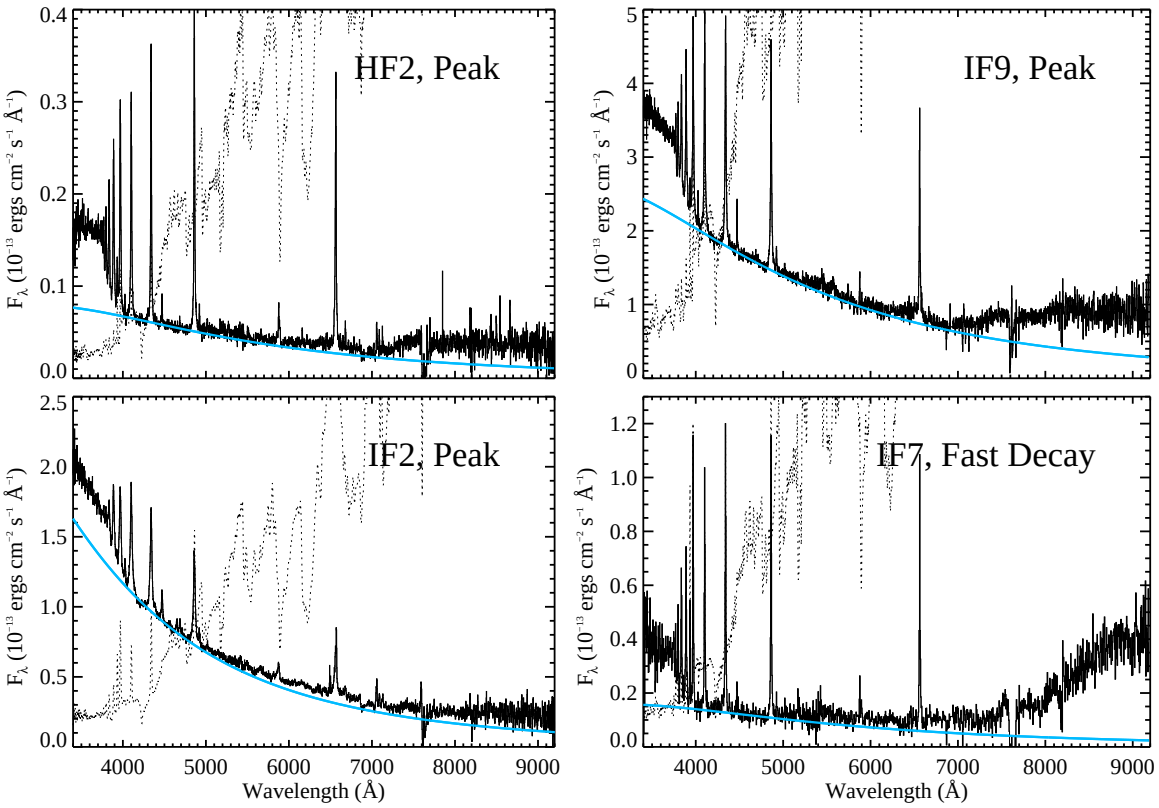

Figure 6.32 The full flare spectral energy distributions for four select flares. The blackbody fit to the blue optical zone is shown light blue. Note, the flux calibration is suspect at 5500Å and at wavelengths longer than 7500Å; the flux at these wavelengths cannot be trusted. The quiescent spectra are shown as dotted lines.

Table 6.1. Relative Amounts of BaC3615

Flare ID	BaC3615 / C3615 at Peak	BaC3615 / C3615 at Extended Decay
IF0	0.19	0.66
IF1	0.21	0.59
IF2	0.27	0.58
IF3	0.24	0.59
IF4	0.05	0.51
IF5	0.44	0.71
IF6	0.39	0.83
IF7	0.31	0.57
IF8	0.24	–
IF9	0.33	0.59
IF10	0.28	0.61
HF1	0.49	0.67
HF2	0.54	0.66
HF3	0.57	0.62
HF4	0.57	0.89
GF1	0.64	0.69
GF2	0.78	1.0
GF3	0.58	1.0
GF4	0.64	0.90
GF5	0.74	0.80

Note. — Peak value for IF0 given for second maximum in flare. Decay value for IF10 given for spectrum immediately following the peak spectrum (S#32); the value for S#34 is 0.69.

Table 6.2. NUV Spectral Slopes

Flare ID	Peak	Decay	Peak − BB	Decay − BB
IF0	0.0 (0.0)	0.0 (0.0)	0.0 (0.0)	0.0 (0.0)
IF1	0.1 (3.5)	1.5 (4.6)	14.9 (18.4)	4.1 (10.6)
IF2	-5.9 (0.0)	4.8 (1.2)	-6.4 (0.3)	8.3 (2.1)
IF3	-4.1 (0.1)	3.0 (8.1)	-4.2 (0.5)	4.7 (13.4)
IF4	-2.5 (0.1)	-6.9 (1.0)	34.5 (2.7)	-10.8 (1.3)
IF5	-0.5 (0.3)	-0.3 (7.7)	5.0 (0.8)	6.8 (8.7)
IF6	-4.1 (1.4)	13.4 (9.1)	1.3 (4.5)	20.2 (15.2)
IF7	-1.9 (0.3)	6.3 (2.0)	2.8 (1.1)	9.1 (3.3)
IF8	-3.3 (0.8)	40.7 (4.4)	3.9 (4.3)	44.3 (11.4)
IF9	-4.1 (0.0)	3.0 (1.4)	-7.0 (0.0)	4.9 (2.4)
IF10	0.0 (0.0)	0.0 (0.0)	0.0 (0.0)	0.0 (0.0)
HF1	-0.8 (0.1)	1.2 (8.9)	1.9 (0.2)	-4.7 (18.0)
HF2	-1.5 (1.7)	4.1 (3.7)	-1.2 (3.1)	7.3 (3.9)
HF3	-0.3 (0.2)	9.3 (3.7)	3.1 (0.5)	15.8 (3.5)
HF4	-8.1 (0.3)	-8.3 (1.8)	-11.2 (0.6)	-9.2 (4.0)
GF1	2.1 (1.9)	4.6 (0.9)	3.9 (3.0)	5.9 (1.3)
GF2	1.9 (1.7)	13.8 (1.5)	1.4 (2.1)	8.1 (13.5)
GF3	1.1 (2.6)	18.1 (12.4)	5.9 (4.8)	22.6 (9.5)
GF4	5.1 (6.3)	19.0 (9.0)	11.1 (10.1)	17.2 (5.7)
GF5	11.0 (8.8)	-6.1 (4.0)	12.7 (10.3)	-29.9 (10.6)
F10 (230s)	7.3	···	5.5	···
F11 (15.9s)	5.4	···	5.1	···
F12 (4.8s, 5.6s)	3.3	–	3.0	6.2

Note. — NUV slopes from $\lambda = 3420 - 3630$Å. The spectra are normalized by C3615 before calcuating slopes. The fractional change in flux at λ in the Balmer continuum relative to the flux in C3615 is approximated by $(\lambda - 3615) \times m \times 10^{-4}$, where m is the slope give above. Positive values of m indicate red slopes, negative values of m indicate blue slopes.

Table 6.3. Fast Decay Phase Evolution

Flare ID	$T_{\rm BB}$	$X_{\rm BB}$
IF0	−	+
IF1	−	+
IF2	−	+
IF3	−	+
IF4	−	+
IF5	−	−
IF6	n/a	n/a
IF7	−	−
IF8	+	−
IF9	−	+
IF10	−	+
HF1	−	+
HF2	−	−
HF3	−	+
HF4	n/a	n/a
GF1	−?	+
GF2	n/a	n/a
GF3	n/a	n/a
GF4	n/a	n/a
GF5	n/a	n/a

Note. — In this table, the − symbol indicates a decrease, + symbol indicates an increase.

Chapter 7

PHENOMENOLOGICAL MODELING

In this section, I will draw from my published papers Kowalski et al. (2011a) and Kowalski et al. (2012), which have been reproduced with the consent of the author, and have minimal changes to the text (with consent from the author) in order to improve the continuity with the rest of the thesis. Section 7.1 (Figures 7.1 – 7.3) summarizes the results in Kowalski et al., 2011a in Choudhary, D.P., Strassmeier, K.G. (eds.) Physics of Sun and Star Spots, 6, 261. Sections 7.2 through 7.4 (Figures 7.4, 7.5, of this chapter and Figure 6.11 of Chapter 6 were originally published in Kowalski et al., 2012, SoPh Vol. 277, Issue 1, pp. 21 – 29; ©2012 by Springer. Springer and *Solar Physics*, Volume 277, 2012, pp. 21 – 29, "The Multiple Continuum Components in the White-Light Flare of 16 January 2009 on the dM4.5e Star YZ CMi", Adam F. Kowalski, Suzanne L. Hawley, Jon A. Holtzman, John P. Wisniewski, and Eric J. Hilton, Figures 1 – 3 is given to the publication in which the material was originally published, by adding; with kind permission from Springer Science and Business Media.

First, I will explain the static, phenomenological models in Section 7.1. Then I will summarize the observations that we will attempt to model. I will show how we try to empirically determine atmospheres that will match these observations in Section 7.2 – Section 7.5. In the next chapter, Chapter 8, I will discuss dynamic models that try to reproduce those atmospheres using self-consistent heating. These models, unfortunately, do not reproduce the observed blue continuum properties, but they give us insight into how to move forward.

7.1 Summary of Basic Phenomenological Hot Spot Models

In Kowalski et al. (2011a), the newly formed flare emission during the rise phase of MDSF2 (Figure 6.12) was modelled phenomenologically with the static NLTE, 1D radiative transfer code, RH (Uitenbroek, 2001), as a Gaussian temperature bump ("hot spot") with a peak

temperature $T = 20\,000$ K (HS2). The hot spot is placed below the temperature minimum region at high column mass, log $m_c/(1g\ cm^{-2})= 0.5$, in the quiescent M dwarf atmosphere. We also produced a cooler hot spot (HS1), with peak temperature of 12 000 K, placed at the same column mass. The temperature profiles for these hot spots are shown in Figure 7.1. The emergent radiation is calculated with the static NLTE code RH with a 5 level (plus continuum) Hydrogen atom. We consider some relevant molecular species that include Hydrogen (e.g., H_2) in the chemical equilibrium calculation of the atmosphere. The emergent hot spot spectra are shown in Figure 7.2. The model spectra have color temperatures of $T_{BB}\sim$11 000 K (HS1) and 18 000 K (HS2). The Balmer continuum and lines are in absorption, similar to the subtracted flare spectra in Figure 6.12. In Figure 7.3, we show the match of HS2 to the subtracted flare spectrum, S#113, just prior to the peak of MDSF2. In future work, we will include Helium and metallic transitions, additional levels in the Hydrogen atom, and refined electron densities using a new version of RH provided by H. Uitenbroek that recalculates electron density from NLTE ionization[1]. We will also further constrain the column mass of the hot spot and place the hot spot in an atmospheric model with a flaring chromosphere. Note that the speed of sound in the quiescent atmosphere is given in Figure 7.1 by the dashed line (assuming $\gamma = 5/3$), to which we will refer later.

7.2 Anti-Correlated Continuum Components and Continuum Veiling during IF1

The effect that we will model is the anti-correlation during IF1 between the time evolution of the apparent amount of Balmer continuum flux, BaC3615, and the flux of the blackbody emission component, C4170. The anti-correlation between the blackbody and BaC components was first presented in Chapter 5, Figure 5.1d for IF1. An anti-correlation is also evident between χ_{flare} and the U-band and between the fraction of HB flux and the U-band (Figure 4.6). The anti-correlation can be understood qualitatively using Figure 6.11, where we showed the spectral evolution of the total "flare-only" flux (denoted throughout this Chapter as F'_λ) during the rise phase of the secondary flare (MDSF2) at $t \approx 130$ minutes.

[1] A known problem with these models is that the electron density has not been recalculated to be consistent with the modified temperature structure.

The spectra are color-coded to the nearest (in time) U-band measurement in the inset panel. At times prior to and near the beginning of the secondary flare (black, purple, and dark blue spectra), two distinct continuum components are clearly present in the spectra. The best-fit blackbody (short-dashed line) accounts for most continuum emission at $\lambda > 4000$Å, whereas the BaC emission above the blackbody is conspicuous at $\lambda < 3750$Å. During the rise and at the peak of the secondary flare (green, yellow, and red spectra), the BaC component seemingly disappears and the best-fit blackbody (long-dashed line) can fit the continuum shape throughout the entire wavelength range. Chapter 5 showed that the Hγ line flux exhibits an anti-correlated relation with the blackbody component. This effect is also present in Figure 6.11: In the red (secondary flare peak) spectrum, the continuum at $\lambda \approx 4200$Å is highest, yet the peaks of the hydrogen Balmer lines are lowest.

The secondary flares at $t \approx 95$ minutes and $t \approx 130$ minutes are events during which the blackbody flux becomes stronger while the BaC flux becomes weaker. In Chapter 5, we quantified this as an increasing filling factor (areal coverage; percent of stellar disk) of the blackbody (with constant temperature, $T = 10\,000$ K) during the rise phase of each secondary flare. In Figure 6.11, we present an alternative interpretation. The blackbody curves (dashed lines) were fit to the spectra by allowing both the temperature and filling factor to vary. The best-fit blackbody temperatures and filling factors are $T \approx 10\,400$ K and $X_{\rm BB} \approx 0.1\%$ (at $t = 122.9$ minutes; short-dashed line) and $T \approx 13\,000$ K and $X_{\rm BB} \approx 0.1\%$ (at $t = 130$ minutes; long-dashed line). Strikingly, if both parameters are allowed to vary when fitting a blackbody function to these *total* (sum of previously decaying and recently begun rise phase) flare spectra, the temperature increases by ≈ 2500 K while the filling factor remains approximately constant. Fitting a blackbody to the flare spectrum (either by holding T constant, or by allowing X and T to vary) gives only the *average* properties of the entire flaring region at that time. We next show that these interpretations can be improved by isolating the newly-formed flare emission.

In Section 6.6.1, we found that the newly-formed flare emission (denoted throughout this chapter as F''_λ, obtained from subtracting the preflare decaying emission) during the rise phase of MDSF2 resembles the spectrum of a hot star, with the defining features being the hydrogen Balmer continuum and lines in *absorption* and a steeply rising continuum

towards the blue at $\lambda > 4000$Å (Figure 6.12 shows that the new flare emission, obtained by subtracting the pre-secondary flare spectrum (average of three black and purple spectra around $t = 123.4$ minutes) from the average of two green-colored spectra around $t = 126.5$ minutes in Figure 6.11, is very similar to the spectrum of the A0 star Vega). The observed anti-correlation between the continuum components in Figure 6.11 is a result of a 'hot star spectrum' forming during the secondary flare. The hot star ("blackbody-like") spectrum causes an increase in the continuum at $\lambda \approx 4200$Å by an amount, F''_{4200}, whereas an increase in the continuum at $\lambda \approx 3500$Å occurs by only $\approx 0.6 \times F''_{4200}$. In other words, the flux in the continuum on both sides of the Balmer jump increases, but the continuum at $\lambda \approx 4200$Å increases by a larger amount. Thus, the apparent decrease in the total amount of BaC in emission from $t = 123$ minutes to 130 minutes occurs as a result of 'continuum veiling' (similar to the continuum veiling observed for accreting T Tauri stars – see, *e.g.*, Hartigan et al. (1989); Hessman & Guenther (1997); Herczeg & Hillenbrand (2008)).

7.3 Combining Continuum Components using Phenomenological Hot Spot Models

Now, we use a sum of individual hot spots and the RHD model spectrum (RHDF11) of Allred et al. (2006) to model the total flare emission (F'_λ) at two times during IF1. Figure 7.4 shows flare spectra from Figure 6.11 averaged around $t = 123.4$ minutes ($F0'$; grey) and at $t = 126.5$ minutes ($F1'$; black). These are the flare-only spectra corresponding to times immediately before and nearly half-way up the rise phase of the secondary flare (MDSF2), respectively.

To model $F0'$, we add the RHDF11 spectrum and HS1 with a ratio of filling factors of $10 : 1$ and $X_{\rm RHDF11} = 1.2\%$, as found in Section 5.2.3. The total model spectrum is shown as the light blue (short dashes) curve in Figure 7.4. As we observed a temperature increase of 2500 K in the total flare emission (Figure 6.11 and Figure 6.13), we model the secondary flare (MDSF2, F''_λ) as HS2, a hot spot with a higher peak temperature than the previously decaying hot spot. To reproduce the total flare emission, we add HS2 to RHDF11 and HS1, giving the red (long dashes) spectrum in Figure 7.4. In order to match the amount of newly formed emission ($F''_{\lambda=4170}$), the areal coverage of HS2 needs to be 0.46

as large as the areal coverage of HS1. These combined model spectra match the observed continuum levels in the total flare emission at all wavelengths in the figure. Moreover, the continuum veiling / anti-correlation effect is readily apparent: the height of the Balmer jump at $\lambda = 3646$Å decreases from black (no hot spots) to blue (one hot spot) to red (two hot spots). The model fluxes are slightly lower than the observed fluxes at $\lambda < 3750$Å. At these wavelengths, there is a forest of metallic lines (*e.g.*, Fe I, Fe II) that are blended in our low-resolution spectra; our model is satisfactory in matching the *underlying* level which is likely closer to the actual level of the BaC. Note that in Chapter 5, we intentionally used only the BaC from the RHDF11 spectrum to model the continuum, whereas the RHDF11 predictions for the Paschen continuum, photospheric-backwarming continuum, and also the pre-flare continuum components are included in the total fluxes in this work.[2]

The origin of the hot spots is unknown, as they are not predicted by self-consistent radiative hydrodynamic models that employ a solar-type non-thermal electron heating function (Allred et al., 2006). We explore the amount of heating at log $m_c/(1\text{g cm}^{-2})\sim0.5$ in the new RHD models in Chapter 8. In the proposed phenomenological hot spot model, we use the fewest number of components necessary to fit the overall shape and reproduce the anti-correlation. However, HS1 may represent a sum of individual decaying hot spots from previously heated flare regions, and HS2 may also represent an average of several unresolved, individually heated and cooling regions. Because the speed at which the area of HS2 increases is near the sound speed of the lower atmosphere (Section 6.7), we argued that HS2 is probably a single hot spot that is persistantly heated rather than a sum of individually heated spots.

7.3.1 Future Work with Hot Spot Models

We are working to produce a grid of phenomenological models which will be used to constrain the column mass of the hot spots, the detailed temperature evolution, and the uniqueness

[2]In future work, we must address whether the quiescent RADYN model should be subtracted from the total model flare spectrum. If the blue-optical flare primarily comes from PaC, and the blue-optical quiescent from the photosphere, it seems correct to subtract the quiescent photospheric contribution from the flux at $\lambda > 3646$Å. However, I am not entirely sure, since the model photosphere is not representative of an M dwarf to begin with due to the lack of important molecular transitions.

of the continuum fit. We will use the new functionality employed in RH (courtesy of H. Uitenbroek) to recalculate charge balance from NLTE ionization in the modified temperature structures. Radiative hydrodynamic models (with RADYN) of the gradual phase are also forthcoming (Chapter 8) and will provide a more accurate representation of the BaC and photospheric backwarming in the decay phase. We also plan to run a RADYN simulation by placing a phenomenological heating function at high column mass, log $m_c/(1g\ cm^{-2})\sim0.5$.

7.4 The Solar Analogy

Figure 7.5 shows how a spatially resolved observation of IF1 might have appeared. We use the continuum components and filling factors to make analogies to several flare structures and phenomena observed in large solar flare arcades. The complex morphology of the U-band light curve leads us to speculate that IF1 involved a large arcade, or several large arcades of flare loops. The main features of Figure 7.5 are the following:

- **BaC (yellow ribbons)**: Throughout the spectral observations (72 minutes $< t <$ 149 minutes), the hydrogen BaC and lines were highly elevated and decreasing (likely from the initial flare peaks seen in the U-band light curve), implying that this emission had originated from the footpoints of a previously heated magnetic arcade in the flaring chromosphere. These may manifest as a complex of flare ribbons, as is commonly observed in Hα during solar flares (*e.g.*, Rust & Hegwer, 1975; Berlicki et al., 2004; Balasubramaniam et al., 2010). In some solar flares (*e.g.*, Neidig, 1983), the BaC appears to have a spatial morphology that is more compact than an extended Hα ribbon. Spectroscopic observations are needed to compare the plasma properties and conditions of BaC and Balmer line emitting ribbons and kernels.

- **HS1 (purple spots)**: Immediately prior to the secondary flare beginning at $t \approx 123$ minutes, a series of phenomenological hot spots (HS1) are present near the photosphere. These hot spots were formed during the previous secondary flares (*i.e.*, at $t \approx 65$ minutes, ≈ 95 minutes; see Chapter 5), and they are emitting from a total source size that is $\approx 1/10$ as large as the area of the chromospheric flare region (*e.g.*,

Hα ribbons). The spectra of these hot spots have the hydrogen BaC and lines in absorption. They might be similar to the compact white-light kernels during solar flares, as in Wang et al. (2007), Fletcher et al. (2007), Jess et al. (2008), or they may be similar to Ellerman-bomb phenomena (see Section 7.4.1). Also emitting from the photosphere is a larger region heated from chromospheric (BaC) backwarming; we assume the size of this backwarmed region is the same size as the flaring chromosphere.

- **HS2 (white spot)**: The secondary flare at $t \approx 130$ minutes is the result of the formation of a new hot spot (HS2), hotter and smaller than HS1 but at the same column mass. At this time, we see a sudden decline in the BaC flux. When all of these components are spatially unresolved, as in our stellar spectra, continuum veiling gives rise to the observed anti-correlation. We have placed HS2 assuming it was triggered by a disturbance induced by the huge initial flare peak at $t \approx 28$ minutes (Figure 3.3). The time-evolution of the Hγ and BaC fluxes in Figure 1d of Chapter 5 indicates an apparent lack of new hydrogen Balmer line emitting-regions during the secondary U-band peaks (we cannot definitively determine whether there is a newly-formed hydrogen Balmer-emitting (chromospheric ribbon) component cospatial with the hotspot because the observations are unresolved). Therefore, the disturbance likely propagated through the lower atmosphere, below the height of hydrogen Balmer line formation (upper chromosphere; J. Allred, private communication 2010). Using a range of sound speeds in the lower atmosphere for the speed of the disturbance ($\approx 5 - 10$ km s^{-1}; Figure 7.1, dashed line, right axis), we find that HS2 is located at a distance that is approximately $30 - 60$ Mm ($R_{\mathrm{YZ\ CMi}} \approx 200$ Mm) from the site of the initial flare event.[3]

[3]The white-light and hard X-ray footpoints have been observed to propagate along the polarity inversion line during large solar flares such as the famous 14 July 2000 flare (Fletcher & Hudson (2001); Kosovichev & Zharkova (2001); Qiu et al. (2010), but the spatial location of these kernels appears to change much faster, $\approx 170 - 200$ km s^{-1}.

7.4.1 Are the Secondary Flares Stellar Ellerman Bombs?

Ellerman bombs are transient, compact phenomena observed near evolving or emerging magnetic fields in solar active regions (Ellerman, 1917; Severny, 1968; Georgoulis et al., 2002, and references therein). A typical signature of Ellerman bombs is emission in the wings and absorption in the core of Hα relative to the nearby plage intensity (*e.g.*, Koval & Severny, 1970; Bruzek, 1972; Fang et al., 2006). The time-evolution properties include mean lifetimes of $\approx 10 - 20$ minutes and fine-structure variations (Kurokawa et al., 1982; Qiu et al., 2000). In contrast to typical white-light flares, Ellerman bombs have symmetric light curves with similar rise and decay times (Payne, 1993; Qiu et al., 2000; Jess et al., 2010a). The Ellerman-bomb mechanism is not fully understood but has been attributed to magnetic reconnection in the low chromosphere (*e.g.*, Georgoulis et al., 2002).

The secondary flares during the YZ CMi megaflare exhibit several similarities to Ellerman-bomb phenomena on the Sun. Ellerman bombs have also been modeled phenomenologically as temperature bumps at or below the solar temperature minimum region (Fang et al., 2006; Berlicki et al., 2010). The secondary YZ CMi flares have longer rise times ($\approx$ two – five minutes) and are much more symmetric about the peak compared to other white light flares with similar total energy on YZ CMi ($\Delta t_{\rm rise} \approx 0.5 - 1.8$ minutes; Moffett, 1974; van den Oord et al., 1996). The absorption features of the blackbody-like continuum component are similar to the line-center absorption observed in Hα and Ca II during Ellerman bombs; unfortunately, our observations do not have sufficient spectral resolution to separate line-center and wing profiles. The preliminary finding (Section 7.4) that the blackbody-like continuum component does not contain hydrogen-line emission may be consistent with magnetic reconnection taking place in the low atmosphere. However, in contrast to solar Ellerman bombs, which have been observed as a microflare trigger (Jess et al., 2010a), the secondary flares are possibly a *consequence* of the enormous YZ CMi flare peak event.

7.5 Modeling the Peak of IF3

The peak of IF3 produced a blackbody component with $T_{\rm BB}\sim$12 100 K and evidence of hot-star absorption in the wings. Hydrogen Balmer line and continuum emission was produced

at peak, but at a much smaller rate than during the rise (Figure 4.8, bottom). We conclude that the continuum is a sum of chromospheric Hydrogen recombination radiation (RHDF11) and the sum of the two hot spots (HS1 and HS2) that were used to explain MDSF2 (Figure 7.4), although the trend at $\lambda < 3600$Å is not explained by the limited parameter space explored by the model. In fact, there are several ways to model this continuum emission. In this section, we explore these ways. In Figure 7.6, we show the peak flare-only spectrum and the continuum fits.

7.5.1 Simple Blackbody Modeling

We modeled the blue-optical continuum emission as a Planck function with $T_{\rm BB}\sim$12 100 K in Figure 6.31 (Section 6.9.1). The blackbody accounted for most of the continuum flux and the overall shape, but there was unaccounted excess ("Conundruum"; see Section 6.8.3) emission above the blackbody at redder wavelengths. We try various combinations of fitting Planck functions to entire spectrum to account for the Conundruum. First, a single blackbody fit to both the blue and red optical zones reveals a temperature of $T_{\rm BB}\sim$10 200 K; it fits the overall shape very well, but misses the detailed shape of the blue-optical zone. If we fit a blackbody to the red optical zone only, we find a temperature of $T_{\rm BB}\sim$7700 K; this fails to account for much of the blue-optical flux.

At peak, the total emission is very likely multithermal in all three xyz spatial directions, and we try a double blackbody fit to better represent the temperatures present at flare peak. Using a *two*-component blackbody model, we find that a combination of temperatures of 6000 K and 170 000 K fit the overall flux distribution the best. Although the 170 000 K continuum would continue to rise dramatically into the NUV, $UV, UVBR$ colorimetry of other flares shows convincingly that the flare SED peaks at $\lambda \sim 3000$Å and decreases between $\lambda = 2000 - 3000$Å. FUV continuum data of M dwarf flares show larger fluxes than a blackbody prediction but still far less than the U-band flux (Hawley et al., 2003). Future NUV spectra during flares would allow us to determine the detailed properties of the NUV continuum components and locate the peak of the blackbody component. None of the blackbody fitting in this section accounts for the excess (Balmer continuum) emission and

$\chi_{\rm flare}$ (Figure G.1).

7.5.2 Simple Slab (ff+bf) Modeling

Following Kunkel (1970), we calculate the emission from an isothermal, isodensity optically thin Hydrogen slab taking into account bf+ff processes. The predictions for $\chi_{\rm flare}$ as a function of temperature are given in Figure G.1, and suggest that the $\chi_{\rm flare,peak}$ of this flare ($\chi_{\rm flare,peak}$= 1.6) is given by the model with $T_e \sim 170\,000$ K. In Figure 7.6 we show this as a red line, which coincidentally reproduces the entire continuum well. Moreover, the height of the Balmer jump ($\chi_{\rm flare,peak}$) is reproduced with this model. However, there is a discrepancy in the blue-optical, as the model does not produce a spectrum that is steep enough to match the observations. We speculate that Stark broadening could account for the necessary extra blue-optical continuum. Depending on the electron densities in the flare, the Stark broadening at the bases of higher order ($\geq$Hγ) lines could develop into a pseudo-continuum (at wavelengths longer than the PseudoC).

Most of the isothermal slab emission in Figure 7.6 is due to free-free (ff) emission. However, a Balmer jump is predicted, suggesting a contribution from Hydrogen recombination. Of course, very little Hydrogen is un-ionized at $t = 170\,000$ K. However, the recombination rates to $n = 2$ are still finite, and (apparently) non-negligible at this temperature. We use the RADYN code (see Chapter 8) to calculate the number of recombinations to $n = 2$ per second per atom per electron per volume. We find that the rate at $T = 170\,000$ K is only $\sim$15 times smaller than the rate at $T = 10\,000$ K.

Hawley & Fisher (1992) discuss that free-free emission from a 1 MK source reproduces the optical (UBVR) colors of flares well but that it cannot account for the observed turnover in the spectrum in the NUV. Eason et al. (1992) modeled the flare continuum using a lower temperature (13 000 K), optically thick free-free model. Nelson et al. (1986) discuss the possible models of the white-light continuum, including free-free emission, arguing that it better explains the lack of observed infrared continuum during flares. Tofflemire et al. (2012) recently completed an IR monitoring campaign of several moderate to large flares, resulting in upper limits to the IR continuum emission. Our thermal equilibrium, isother-

mal, isodensity free-free model is overly simplistic, as the distribution of temperatures and densities over which radiation originates varies by large amounts (see Chapter 8). In the RHD models of Chapter 8, we show that the amount of T$\sim$ 9 000 K Hydrogen emission completely outshines any Hydrogen ff+bf emission that originates from T$\sim$ 170, 000 K. As noted by Hiei (1982), the path length for free-free emission required to produce the observed amount of peak flare intensity is too large. We find that using a reasonable path length (50 km), the areas and densities for the free-free source need to be very large but not completely unreasonable.

7.5.3 Hot Spot Modeling

Finally we discuss the hot spot modeling using the same continuum components for modeling the total flare emission in the rise phase of the secondary flare in IF1 (Section 7.3). Both IF3 and the secondary flare of IF1 show an apparent increase in temperature of $\sim 2000-2500$ K from the flare start to the peak ($T_{\rm BB}$ from 10 000 to 12 000 K for IF3 and $T_{\rm BB}$ from 8500 to 11 000 K for IF1). Therefore, we try to model the total flare emission during the IF3 peak with the same components. At the peak of IF3, HS1 represents the hot spot formed during the rise phase (which may be starting to decay by the time of peak emission), HS2 represents the hot spot formed at peak emission, and the RHDF11 spectrum represents the chromospheric (primarily Balmer and Paschen continuum) radiation. We find that a combination of RHDF11 (filling factor determined from $X_{\rm BaCF11}$ 0.027), HS1 (filling factor of 1/10 RHDF11), and HS2 (filling factor 1/10 times the filling factor of RHDF11) closely matches the flux at $\lambda > 4000$Å but cannot account for the rise at $\lambda < 4000$Å. We show the total model spectrum as the purple line in Figure 7.6. Compared to HS2 in MDSF2, the HS2 in IF3 is relatively twice as large compared to the other components at peak. The hot spot spectra have a steep continuum rising into the NUV (with the color temperature at $\lambda < 3600$Å approximately the same as in the blue-optical), but their filling factors are small. Therefore the relatively large flux and flat spectral slope in the BaC dominates the shape of the total flare emission in the NUV zone. In contrast, we found that the shape of the total flare flux at $\lambda < 4000$Å is approximately the same as the shape of the blackbody

that was fit to the blue-optical spectral zone (Figures 3.8-3.11).

More accurate modeling of the hot spots is required to understand the amount of absorption and the detailed shapes in the NUV in this flare. In Section 6.7, we found that the rate of increase of the flare area in IF3 was larger than in IF1. We speculate that the speeds, depth of the hot spots, amount of total chromospheric emission, and amount of absorption from the hot spots are linked. We plan to model IF3 with hot spots at lower column mass so as to give less absorption so that the BaC has less effect on the total continuum shape at $\lambda < 3600$Å. We only consider the simple variation (above) of the filling factor combinations from the rise phase of MDSF2 and do not explore the full parameter space of filling factors. A more realistic model of the total flare emission may require accounting for the possible spatial coincidence of the hot spots and RHDF11 spectrum (e.g., the hot spot may lie directly underneath the ribbons, in contrast to the spatially distinct ribbon and kernel envisioned in Figure 7.5). A combined hot spot and RHDF11 atmospheric calculation is reserved for future work and may produce important effects on the emergent intensity, such as the NLTE effects from stimulated recombination in the chromosphere from the underlying NUV radiation originating in the hot spot.

In conclusion, we find a spectral degeneracy among several possible interpretations of the white-light continuum during the peak of IF3. The leading possibility which we have presented in detail is a blackbody component that emits from a relatively low temperature, high density optically thick region. This blackbody has a spectrum like a hot star with the Balmer continuum in absorption and Balmer continuum from the flaring chromosphere fills it in like a veiling effect. The other possibility is an extreme scenario, and possibly unphysical, but it reproduces the observed $\chi_{\rm flare}$ values. It is from an extremely high temperature region, and would require high densities to be visible. Observations in the NUV at $\lambda = 2000 - 3200$Å would help break this degeneracy. Share et al. (2004); Schrijver et al. (2006) discuss the unknown source during large solar flares of extreme broadening in the 511 keV positron annihilation line, which is thought to originate from a region with chromospheric/photospheric densities and high temperatures (several hundred thousand Kelvin). This annihilation line flux also appears to follow the hard X-ray emission in the events studied. This unsolved problem in solar flares that may provide insight into the

heating of deep layers in stellar flares.

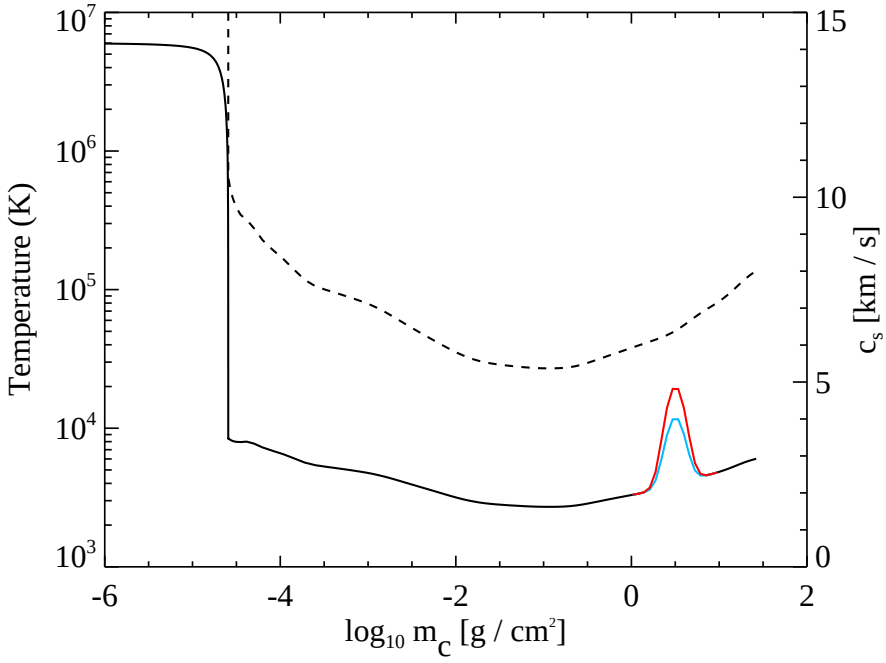

Figure 7.1 The "hot spot" temperature profiles from Kowalski et al. (2011a), placed below the temperature minimum region in the quiescent M dwarf atmosphere (black). The blue curve has a peak temperature of 12 000 K (HS1) and the red curve has a peak temperature of 20 000 K (HS2). The speed of sound in the quiescent atmosphere is indicated with the dashed line (right axis).

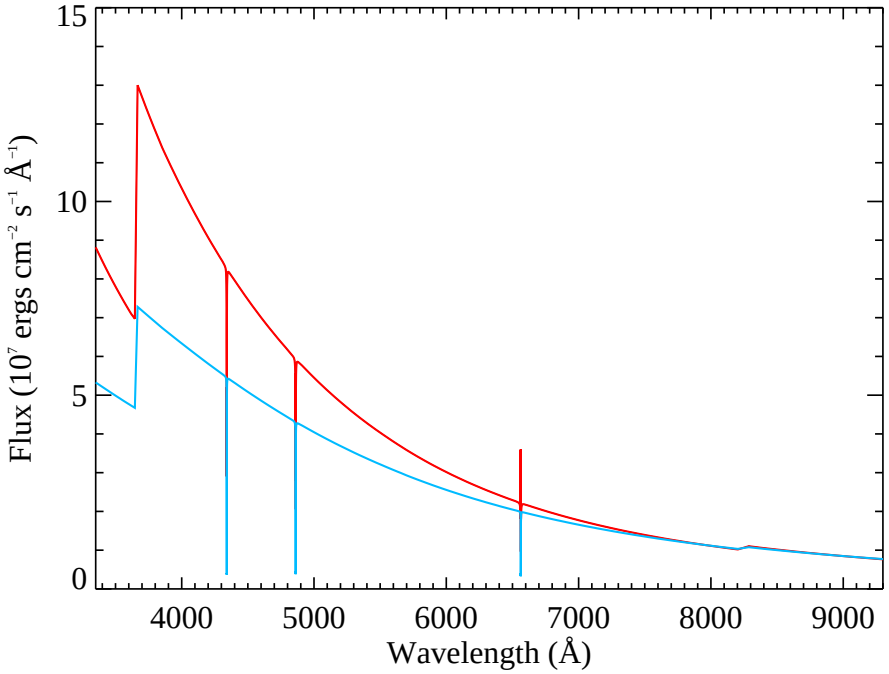

Figure 7.2 The predicted surface flux from the two hot spots in Figure 7.1.

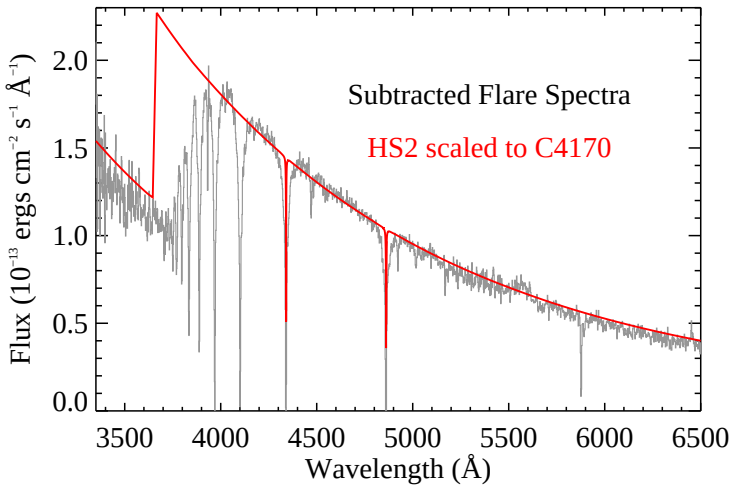

Figure 7.3 The red is the HS2 spectrum and the the grey is the newly formed flare emission just prior to the peak (S#113).

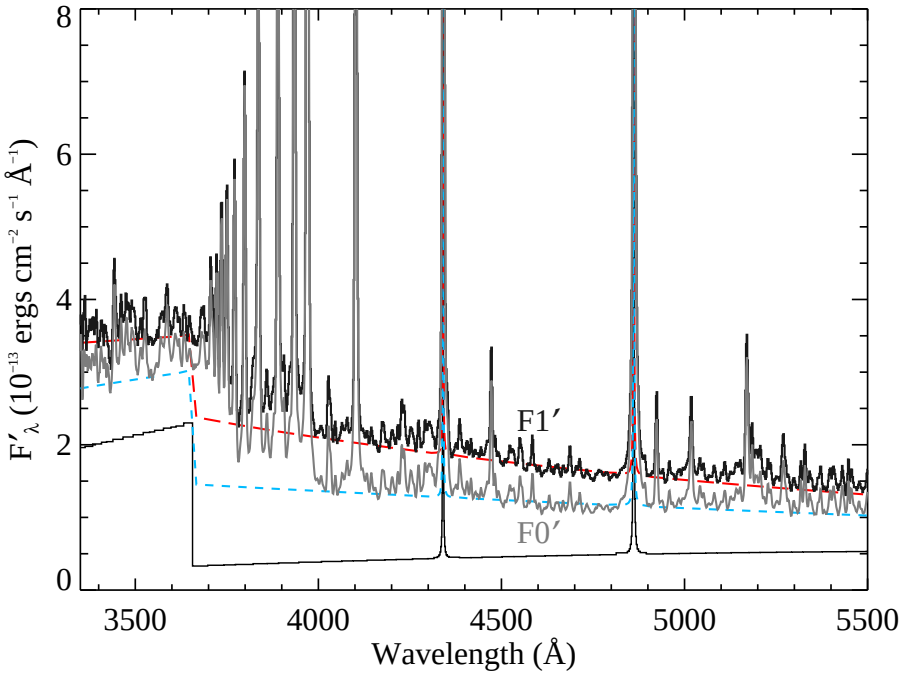

Figure 7.4 Flare spectra at $t = 123.4$ (S#102) minutes and 126.5 (S#108) minutes from Figure 6.11 are shown in grey and black, respectively. The composite model spectra are shown in blue, short dashes ($F_{\lambda,\mathrm{RHDF11}} \times X_{\mathrm{RHDF11}} + F_{\lambda,\mathrm{HS1}} \times X_{\mathrm{HS1}}$) and red, long dashes ($F_{\lambda,\mathrm{RHDF11}} \times X_{\mathrm{RHDF11}} + F_{\lambda,\mathrm{HS1}} \times X_{\mathrm{HS1}} + F_{\lambda,\mathrm{HS2}} \times X_{\mathrm{HS2}}$). The RHDF11 spectrum is shown as the thin black line. The continuum veiling effect is apparent from the different heights of the Balmer discontinuity at $\lambda = 3646$Å.

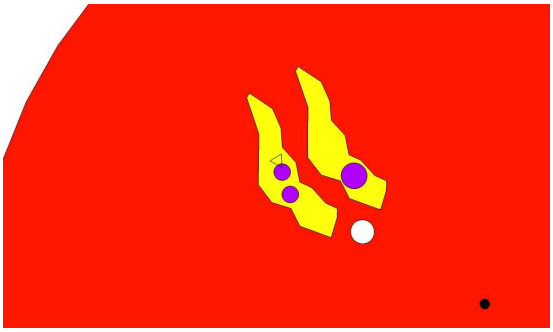

Figure 7.5 Graphic with continuum components (areas from $t \approx 126.5$ minutes to scale) as they might appear in a spatially resolved observation. The BaC emitting region (yellow) resembles a two-ribbon structure (shown here as symmetric for simplicity) in a thin layer of the heated mid-to-upper chromosphere of previously reconnected magnetic loops. HS1 is shown as a collection of previously formed hot spots (purple) and HS2 is the proposed newly-formed continuum emitting region (white). The triangle (located above the leftmost hot spot) indicates the assumed location of the inital flare peak, which generated a disturbance in the lower atmosphere that propagated into the surrounding active region and triggered the hot spots. The black circle helps orient the reader to the disk center, which has a radius $0.3R_{\odot}$. The flare region is placed at an arbitrary location on the surface. Several aspects of this cartoon were inspired by observations of solar flare arcades, such as Fletcher & Hudson (2001).

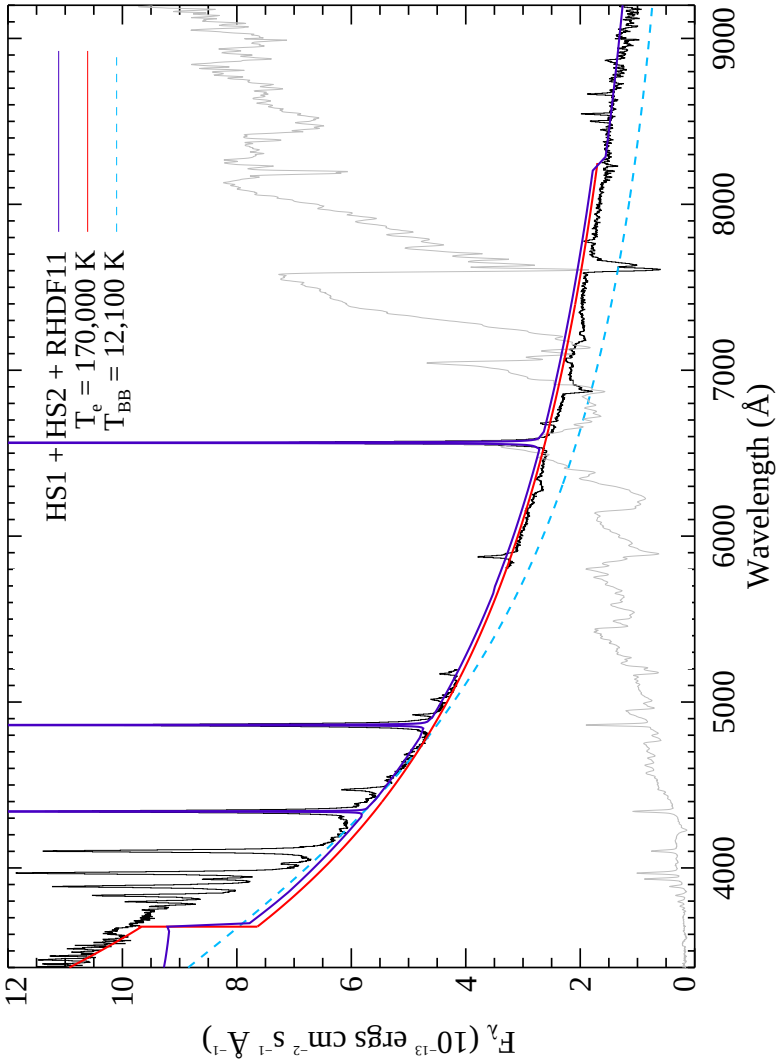

Figure 7.6 The peak spectrum of IF3 with several possible attempts to fit the entire continuum range. The isothermal blackbody is given in light blue (dashed), a simple free-free model is shown in red, and a phenomenological addition of HS1, HS2, and RHDF11 is shown in purple.

Chapter 8

RADIATIVE-HYDRODYNAMIC MODELING

8.1 Motivation

Our goal is to produce a model of a fundamental flare "burst" element that experiences transient heating for a short time and then is allowed to cool. Here, we discuss the motivation for this phenomenology from high spatial and temporal resolution images of solar flare footpoints. Compact kernels have been observed to brighten and fade sequentially across a flare region such that heating appears to occur in any given place for only a short time. These "moving footpoints" have been observed in UV and white-light emission (Kosovichev & Zharkova, 2001; Fletcher et al., 2004; Wang et al., 2007; Wang, 2009) and hard X-ray emission (Schrijver et al., 2006; Nishizuka et al., 2009; Qiu et al., 2010, see also the review by Fletcher et al. (2011) and references therein). Footpoint motion has been associated with the coronal magnetic field reconnection rate (Fletcher et al., 2004). We seek to produce a series of individually heated flare footpoints to stack together for a "1.5D" flare model, whereby the heating at any given place is transient and lasts for several seconds before it starts cooling off. The gradual phase is needed for each of these flare heating elements in order to follow their evolution. Livshits et al. (1981) discusses observational evidence of hard X-ray bursts on the Sun, which imply impulsive heating of 10 seconds or less in each burst. Recently, Wang et al. (2007) found that individual UV/white-light footpoints last for at most 30 – 60 seconds and Schrijver et al. (2006) deduced the crossing time of intense hard X-ray emitting particle precipitation sites to < 23 seconds during a solar flare, with less intense precipitation over the region in the following several minutes. Mochnacki & Zirin (1980); Hawley et al. (2003) established that increasing area is an important ingredient in understanding stellar flares using a single component blackbody model of the white-light. The same conclusion is found throughout this thesis (Chapter 6). In Section 6.7, we discussed the speeds at which solar footpoints propagate, and we connected to the rates of

areal increase in stellar flares. The observed speeds and areas will guide the development of the 1.5D models. Recent advanced 1D RHD models have begun to simulate solar flare bursts. In particular, the models of Kašparová et al. (2009) studied pulse-beam heating effects on subsecond timescales for the Balmer lines (taking into account nonthermal collision rates) with recurrent bursts having a period of one second.

In Figure 6.4, we motivate higher beam fluxes than typically employed in previous stellar flare models. The top axis of this figure shows the bolometric surface flux corresponding to a given effective temperature; the observed range of $T_{\rm eff}$ (7700 – 9400 K) implies heating fluxes $> 2 \times 10^{11}$ ergs cm^{-2} s^{-1}. Given that a fraction of the beam energy goes into mass motions and other (e.g., XEUV) line and continuum radiation, we choose to start with a total flare heating flux of 10^{12} ergs cm^{-2} s^{-1}, which is ten times larger than the largest beam flux employed in the Allred et al. (2006) models. Motivation also comes from high spatial resolution observations of hard X-rays and sub-mm radiation during X class solar flares, which can have flux levels $> 10^{12}$ ergs cm^{-2} s^{-1}(Neidig et al., 1993; Qiu et al., 2010; Krucker et al., 2011; Zhou et al., 2011).

We performed radiative hydrodynamic modeling of an F12 flare with a gradual phase. For this simulation, we used the RADYN code (Carlsson & Stein, 1994, 1995, 1997). RADYN uses an adaptive grid to resolve shocks (Dorfi & Drury, 1987) and solves for NLTE populations of H, He, and Ca II using the technique of Scharmer & Carlsson (1985). For additional description of the implementation of the RADYN code for flare studies, see Abbett & Hawley (1999); Allred et al. (2005, 2006).

8.2 The Starting Atmosphere

Obtaining a starting atmosphere was a difficult task. The starting atmosphere was converged for a high-gravity (log g = 4.75), cool ($T_{\rm eff}$ = 4260 K, $T_{\rm min}$ = 3550K, $T_{\rm BB}$= 4800K) star, corresponding to spectral type of late K or early M[1]. The basic temperature profile was obtained from Hawley & Fisher (1992) and was converged with NLTE populations for

[1]It is a known issue that the surface flux of this dwarf model is much larger than the surface flux of a dM4 star in the optical, primarily as a result of not including the molecular opacities. We have plans to modify the atmosphere to more closely represent a mid M dwarf.

a six level with continuum Hydrogen atom, a nine level with continuum Helium atom and a six level with continuum Ca II ion. Other transitions are included as background opacity in LTE. The adaptive grid was set up to be consistent with the weights established for the initial atmospheric structure. We chose the same starting conditions to be consistent with the quiescent M dwarf model in Allred et al. (2006). The upper temperature boundary was fixed at 6×10^6 K to be consistent with soft X-ray observations of active M dwarfs (e.g., Osten et al., 2006). The pressure at the top of the atmosphere was iteratively adjusted so that velocities in the atmosphere were less than 10 m s^{-1}, thereby signifying equilibrium conditions. Ultimately, we achieved velocities < 3 m s^{-1} with a pressure at the top of the atmosphere of 45.4178 dyne cm^{-2}. Constant non-radiative heating was added to the energy equation to simulate convective energy flux in the lower atmosphere at column mass greater than 3.16 g cm^{-2}. The height of the atmosphere was chosen to emulate a magnetic loop of length 10^9 cm (10 Mm). This is a short loop length compared to the previous coronal gas-dynamic simulations of Schmitt et al. (2008) (see Section 8.6.4).

The optically thin radiative cooling from free-free bremsstrahlung and coronal metal XEUV transitions is accounted for by an updated cooling function (Carlsson & Leenaarts, 2012). Hydrogen, Helium, and Calcium thin cooling terms are excluded because they are calculated in detail (e.g., like that done in Ricchiazzi & Canfield, 1983). We show the thin cooling emissivity in Figure 8.1. We are currently investigating the sources of the differences between cooling functions (e.g., compared to that employed in Allred et al. (2006)). We further discuss the thin cooling properties in Section 8.4.3.

Equilibrium was achieved while accounting for the heating from coronal XEUV backwarming radiation. In Figure 8.2 we show the temperature profile of the final converged atmosphere with and without XEUV backwarming. The XEUV heating changes the equilibrium state of the temperature minimum region and chromosphere.

8.3 Flare Heating

Following Hawley & Fisher (1994), Abbett & Hawley (1999), and Allred et al. (2005, 2006) a term is added to the energy equation to simulate nonthermal "beam" heating from mildly relativistic electrons. This term is a function of column mass and ionization fraction and

describes the energy deposition rate of a power law distribution of nonthermal electrons that lose their energy via coulomb collisions with the ambient atmosphere. The basic equations were taken from the "thick-target" (Brown, 1971) formulae from Emslie (1978) and were modified to add in the dependency on ionization fraction from Hawley & Fisher (1994). Nonthermal ionization rates from the ground level of Hydrogen are included using the formulation in Ricchiazzi & Canfield (1983). The parameters of the nonthermal electron distribution were chosen to match those in Allred et al. (2006), which were obtained from hard X-ray observations with RHESSI of the peak of the 2002 July 23 X-class solar flare (Holman et al., 2003). In particular, we use a double power law of electron energies paramaterized by $\delta_l = 3.0$ (the power law index from the cutoff energy to the break energy), $\delta_u = 4.0$ (the power law index at energies greater than the break energy), $E_c = 37$ keV (the "cutoff energy" or lowest energy for the nonthermal electrons), and $E_B = 105$ keV (the break energy). The E_c is the low-energy cutoff of nonthermal electron energy and has important ramifications on the model results due to the the power law dependency of the energy spectrum. In future work, we will employ a low-energy "rollover" as done in recent solar flare models (Liu et al., 2009; Fisher et al., 2012). The overall energy flux normalization was chosen to be ten times larger than the Allred et al. (2006) F11 model. The energy flux (integrated over all energies) of nonthermal electrons is 10^{12} ergs cm^{-2} s^{-1} (hereafter, F12). The functionality in RADYN to take a double-power law of electron energies and turn this into the flare heating function was developed by Allred et al. (2005).

We simulated a single flare "burst" by choosing a constant flare heating time profile with energy flux of 10^{12} ergs cm^{-2} s^{-1} and a duration of 5 seconds. After 5 seconds, we turned the flare heating off and let the atmosphere relax for 1000 seconds. From $0-67$ seconds, the boundary conditions were changed from the fixed upper boundary conditions of the quiescent atmosphere to a free, transmitting upper boundary. At 67 seconds, the top of the corona reached its preflare value, and we fixed the upper pressure and temperature so as to let the rest of the atmosphere relax[2].

[2]If we did not change the boundary, the atmosphere would cool below its preflare level; we found that adding a non-radiative heating term to the whole atmosphere caused problems in the transition region that resulted in periodic bursts of mass flow; therefore, we fixed the upper boundary.

8.4 Results

The analysis of the RADYN models was performed with a highly developed IDL toolkit obtained from M. Carlsson, W. Abbett, and J. Allred. In this section, we discuss the results of the models, including the optical/NUV continuum, the light curve morphological characteristics, and temperature evolution of the lower atmosphere. We find that a hot, blackbody component is not produced from the NUV backwarming or direct beam heating; extrapolating an energy budget calculation shows a larger beam flux will be necessary. We have found a striking resemblence of our simulated light curve to observed impulsive phase structure; the physics in the models therefore can be applied to understand the time-evolution of chromospheric beam heating.

8.4.1 The Simulated BaC3550 Light Curve

In Figure 8.3, we show the light curve of the $\lambda = 3550$Å continuum flux over the first 10 seconds of the simulation. The key times that we will refer to throughout this chapter are indicated with vertical lines. They correspond to $t = 0.1$ sec (rise, 35% of peak), $t = 0.5$ sec (rise, 85% of peak), $t = 1.5$ sec (end of rise, at peak), $t = 4.8$ sec (peak, just prior to the end of beam heating), $t = 5.6$ sec (during the gradual phase, 15% of peak), and $t = 16$ sec (far into the gradual phase, 2% of peak). An immediate conclusion that we draw from the simulation is that the NUV zone continuum flux closely follows the presence of beam heating, and we attribute this flux primarily to the Balmer continuum from Hydrogen recombination. Additional contributions to the continuum flux in this spectral zone are several He I continua (which are calculated in detail; see Allred et al. (2005)), Paschen continuum, and photospheric radiation. Within 1 second after the beam is turned off, the NUV continuum flux (e.g., BaC3550) decreases to ∼10% of the peak. Moreover, we find that the rise phase and initial decay phase have the same timescales, which can be approximated by two consecutive exponential functions. The fast exponential function has a time constant of ∼0.25 seconds and the slow exponential has a timescale of ∼0.5 seconds. We compare this light curve morphology to observations in Section 8.6. We refer the reader to Section 8.6.3 and Appendix H for the interpretation of these timescales. We also refer to the reader

to Abbett & Hawley (1999) for a discussion of the ionization and recombination timescales during the formation of Hydrogen continua in beam-heated atmospheres.

We show the temperature profiles at these key times in Figure 8.4. In all figures that follow, we color-code according to these times; the quiescent quantities are shown as a dotted line, and the F11 quantities from Allred et al. (2006) are shown as a dashed line. We compare to the $t = 15.9$ second F11 model spectrum because it features the maximum flux in the blue optical zone. The temperature profiles during the impulsive phase in Figure 8.4 have three conspicuous temperature "plateaus", which are common features of beam heating models (Allred et al., 2006). The first plateau is the super-heated corona, which reaches a maximum temperature of 13.7 MK in this simulation. The second plateau has a temperature range of $T \sim 40\,000 - 60\,000$ K and is the location where the beam deposits its energy and optically thin losses provide most of the energy balance. This region of the atmosphere ($\log$ m$_c$/(1g cm^{-2})~ -3.5) corresponds to where most of the nonthermal electrons at the low-energy cutoff (37 keV) deposit their energy. The third plateau is heated by the tail of the beam that contains the higher energy nonthermal electrons (these penetrate deeper, Emslie (1978)). The flare chromosphere has a temperature range of $T = 7000 - 10\,000$ K, and the temperature regulation in the third plateau is from Hydrogen recombination. The third plateau moves to higher and higher column mass as the beam tail heats up more atmosphere over time.

The Balmer continuum originates from the flare chromosphere, and the rise of the light curve in Figure 8.3 corresponds to the heating of material at higher and higher column mass, where there is more emitting material with a larger electron density at a given temperature, e.g., at 9000 K. The contribution function (Magain, 1986; Carlsson & Stein, 1997; Carlsson, 1998) is the integrand of the emergent intensity and allows one to determine where radiation is formed in the atmosphere. The contribution function for optical flare continuum emission has been studied for stellar flares in Hawley & Fisher (1992). In Figure 8.5 (top), we show the contribution function[3] to the total intensity of the $\mu = 1$ Balmer continuum ($\lambda = 3550$Å) compared to the temperature profile of the atmosphere in the rise ($t = 0.5$ sec) and peak

[3]In all figures except for Figure 8.6, the contribution function is given per frequency interval; in Figure 8.6, the contribution function is given per wavelength interval to facilitate comparison to the spectrum.

(1.5 sec). The net (volumetric) cooling over the wavelength range of the BaC is also shown and peaks at a lower column mass than the peak of the contribution function. The intensity contribution and cooling occur over a large range of column mass (∼1 dex) and temperature (ΔT ∼6000 K). Additional contribution and cooling occur at higher column mass at later times in the impulsive phase.

The intensity contribution and cooling from the Balmer continuum are also dependent on the electron density. We show the net cooling and the contribution against n_e in the bottom of Figure 8.5. The net cooling peaks with the electron density (as expected, cooling is dependent on n_e^2); but most of the contribution and cooling occur over a large range of electron densities, about a factor of ∼4 in these parameters. Compared to the cooling, the fact that the contribution peaks at a lower temperature (∼8900 K vs ∼11 000 K) and at a higher column mass (log $m_c/(1g\ cm^{-2})$∼-2.1 vs log $m_c/(1g\ cm^{-2})$∼-2.6) is interesting. The offset of the cooling from the contribution may indicate that some of the Balmer continuum photons emitted from log $m_c/(1g\ cm^{-2})$∼-2.6 and directed toward the photosphere ionize some Hydrogen in $n = 2$ at log $m_c/(1g\ cm^{-2})$∼-2.1, thereby transferring energy to the gas and causing the *net* cooling at the higher column mass to be lower.

It is of interest to compare the Balmer continuum contribution to the contribution from other continuum wavelengths. In Figure 8.6, we compare the contribution to the ($\mu = 1$ intensity) at $\lambda = 850$Å (primarily the Lyman continuum), $\lambda = 3550$Å (primarily the Balmer continuum), and $\lambda = 4300$Å (primarily the Paschen continuum). These are shown for $t = 4.8$ seconds, as this time exhibits marked differences in the contributions from these three continua. The Lyman continuum originates from lowest column mass in the atmosphere and over the narrowest range of log column mass, whereas the Paschen continuum originates at a larger column mass, and over a larger range of log column mass. The Paschen continuum contribution peaks in the mid flare chromosphere and in the flare temperature minimum region. The peak at lower column mass is presumably due to Hydrogen recombination to $n = 3$. The peak at higher column mass corresponds to the radiation emitted from the backwarmed photosphere (see next section); this radiation might be elevated levels of H^- emission in these models. There is significant Paschen continuum from the trough at log $m_c/(1g\ cm^{-2})\sim -0.5$.

8.4.2 Photospheric Heating

Does the large beam flux, either through direct heating or backwarming, cause a hot blackbody spectrum to form? We find that at peak times, $1.5{\times}10^{11}$ ergs cm^{-2} s^{-1} (15% of the beam energy) is released in the detailed Hydrogen+Helium continua; however, only $\sim$42% of *this* energy is emitted at Balmer continuum wavelengths, and 32% of the energy at wavelengths longerthan 3646Å, with the remaining $\sim$26% in the continua shortward of 1000Å (primarily from the Lyman continuum). The remaining 85% of the beam energy is contained in the thin losses (60% of the total; see Section 8.4.3), kinetic energy, and detailed line emission. Although the amount of NUV, optical and IR radiation ($\sim 1{\times}10^{11}$ ergs cm^{-2} s^{-1}) is getting close to the surface flux needed for a $T_{\rm eff}{\sim}8000-9000$ K blackbody, hot spot, or hot star spectrum that we observe ($> 2\times10^{11}$ ergs cm^{-2} s^{-1}), we find that most of the model white-light radiation is emitted from the flare chromosphere and the resulting spectrum of Balmer and Paschen continua does not match the properties (e.g., shape, Balmer jump height) in the observations. A larger fraction of the energy needs to be transported to higher column mass, and we provide a calculation for one such path at the end of this chapter.

The model F12 NUV/blue-optical ($\lambda = 3420-5200$Å) continuum at $t = 4.8$ sec is shown in Figure 8.7, compared to the F11 ($t = 15.9$ sec) model continuum (dashed). We compare these models at times near the ends of their impulsive phases, when the flux at $\lambda = 4170$Å is the maximum produced. The spectrum has a large Balmer jump and 3.9 times the surface flux of F11 at $\lambda = 3550$Å. We interpolate the continuum to $\lambda = 3615$Å and to $\lambda = 4170$Å, and we find that the model spectrum exhibits a very large $\chi_{\rm flare,peak}{\sim}6$, larger than any of the observations of $\chi_{\rm flare,peak}$. Neidig et al. (1993) calculated a solar flare spectrum using an F12 beam flux and found a very similar Balmer jump ratio of 7.

We also investigate the effect viewing angle has on the emergent continuum intensity spectrum. In Figure 8.8, we show the intensity (units of ergs s^{-1} cm^{-2} Å^{-1} s.r.$^{-1}$) for the five values of μ (0.05, 0.25, 0.5, 0.77, 0.95) calculated by RADYN. Interestingly, the spectrum emerging from the largest viewing angle ($\mu = 0.05$) has a smaller Balmer jump ($\chi_{\rm flare}{\sim}3.3$) and a steeper blue-optical slope ($T_{\rm BB}{\sim}6500$ K) than the surface flux spectrum (also shown

in this figure) and the intensity spectra with larger values of μ. The emergent flux is calculated with a five-point sum (or angle quadrature) over μ with weights of 0.118, 0.239, 0.284, 0.239, and 0.118 for $\mu = 0.047, 0.231, 0.500, 0.769, 0.953$ ($\theta = 87.3, 76.6, 60.0, 39.7, 17.6$ degrees), respectively; the $\mu = 0.047$ intensity is therefore scaled by the smallest amount in the sum. The difference in spectral shape between $\mu = 0.953$ and $\mu = 0.047$ in the blue-optical zone likely results from the $\mu = 0.047$ ray originating from higher temperatures at higher heights in the atmosphere. The continuum shapes at $\lambda < 3646$Å is also different among the viewing angle and warrants further investigation. We note that Neidig et al. (1993) have shown that the viewing angle of white-light solar flares – whether the flare occurred near disk center or near the limb – differentially affects the contrast of radiation originating photospheric and chromospheric heights.

The model flux spectrum in Figure 8.7 is shown for the peak of the flare near the time of maximum amount of heating achieved in the deep layers (see Figure 8.4). We measure the color temperature of the blue-optical continuum using the same continuum windows as for the observations, and we find that $T_{\rm BB}\sim$5500 K, still far below the observed range for flares at their peak times ($T_{\rm BB}$= 10 000 − 12 000 K; see Section 3.2 and Figures 3.8-3.11). However, the source of the blue-optical continuum in these models is not heated photosphere, but instead is largely due to the Paschen continuum from the flare chromosphere. At $t = 4.8$ sec, the maximum contribution to the total intensity ($\mu = 1$) at $\lambda = 4300$Å is at log $m_c/(1{\rm g\ cm^{-2}})\sim-1.7$, which has a temperature of ∼8100 K and an electron density of 9.5 $\times 10^{13}$ cm^{-3}. The Paschen continuum is formed at a higher column mass, and over a larger range of log column mass, compared to the Balmer continuum (Figure 8.6).

We investigate the amount and the source of heating at high column mass, log $m_c/(1{\rm g\ cm^{-2}})>$ 0. In Figure 8.9, the temperature profiles in the lower atmosphere are shown. Compared to the maximum F11 heating profile (dashed line), the F12 heating produces a flare chromosphere ($T = 6000 - 10\,000$ K) that is at a higher column mass by about 0.5 dex. The $t = 4.8$ sec temperature profile is shown as the dark line and there is about 800 K more heating than in the F11 simulation at a high column mass of log $m_c/(1{\rm g\ cm^{-2}})$= 0.

We show the main sources of the energy balance at $t = 4.8$ seconds in Figure 8.10. The temperature profile is also shown (right axis). We conclude from this figure that there is the

largest amount of net heating rates from NUV ($\lambda \sim 3000 - 4000$Å) backwarming primarily from the BaC and PaC radiation originating from the flare chromosphere. Although the beam heating and heating from the BaC are equal at log $m_c/(1g\ cm^{-2}) \sim -0.5$, the beam heating becomes very small in deeper layers. The relative amount of beam heating compared to the BaC heating at log $m_c/(1g\ cm^{-2}) = 0$ is ∼10%. The backwarming from the 10 MK coronal source is negligible in deep layers, $\sim 7 \times 10^{-6}$ relative to the BaC heating. These findings are consistent with the findings of Allred et al. (2006) for the F11 flare.

Much more heating at high column mass (log $m_c/(1g\ cm^{-2}) \sim 0 - 1$) is required in the models to match the observations. The maximum temperatures of 12 000 and 20 000 K in the phenomenological hot spot models (Chapter 7) occur at log $m_c/(1g\ cm^{-2}) = 0.5$, but in the F12 model there is only a small temperature increase of $\Delta T \sim 760$ K (from 3840 K to 4600 K) at this column mass (Figure 8.9).

We investigate the temperature evolution of the lower atmosphere and the relation to the light curve in Figure 8.3. We find that the temperatures at high column mass change relatively slowly. From the lightcurve in Figure 8.3, the continuum flux at $\lambda = 4300$ is continuing to increase, albeit rather gradually, just prior to the time when the beam is turned off; in contrast, the total flux at $\lambda = 3550$Å has declined over the duration of the peak phase. The initial rise in the light curve is due to the Paschen continuum from the flare chromosphere at lower column mass whereas we attribute the gradual increase in 4300Å at the peak to the increasing continuum radiation originating from lower layers. Therefore, the total continuum flux at $\lambda = 4300$Å is a combination of the evolution of the Paschen continuum from the chromosphere and increased temperature minimum radiation. We confirm this interpretation by measuring the height of the Paschen jump using the continuum flux values at $\lambda = 8200$Å and $\lambda = 8300$Å as a function of time. The height of the Paschen jump follows the evolution of the continuum flux at $\lambda = 3550$Å (Figure 8.3), suggesting that indeed the increase in $\lambda = 4300$Å flux at peak is from emission at higher column mass (near the photosphere). Figure 8.4 shows that the heating in the deepest layers is delayed relative to the heating of the flare chromosphere. The high densities of the lower atmosphere are able to cool the incident UV radiation (and low level beam heating) efficiently, thereby requiring a relatively larger amount of energy (and a longer time) to generate a temperature

increase. A similar principle has been invoked to explain the longer flare heating timescales on an M dwarf compared to the (overall) lower density atmosphere of the Sun (Allred et al., 2006). We speculate that as NUV backwarming continues to heat the lower atmosphere, there may be a small amount of photospheric absorption beginning to form at high column mass; therefore, we are beginning to see evidence of the "anti-correlation" effect that we modeled with hot spots in Chapter 7. Models with larger photospheric heating are required to confirm or reject this interpretation.

In the gradual phase of our simulation ($t > 5$ seconds), the temperatures at $\log \mathrm{m_c}/(1\mathrm{g\ cm^{-2}}) > -0.8$ stay elevated longer than the temperatures near the maximum beam heating, which drop precipitously by 50 000 K in 0.5 seconds (Figure 8.9 and Figure 8.4). Even after 16 seconds, the temperatures at $\log \mathrm{m_c}/(1\mathrm{g\ cm^{-2}}) > -2$ remain elevated (see Figure 8.4). We investigate the energy budget in the lower atmosphere and find that there is initially very little net cooling when the beam is turned off: the cooling from the PaC and the persistent backwarming heating from the BaC are nearly equal in the beginning of the gradual phase (whereas they both contribute to the heating in the impulsive phase). Although the Balmer continuum flux drops precipitously, the Balmer jump is visible for relatively long times; even at $t = 16$ seconds in the F12 run, the Balmer jump is still visible (Balmer jump flux is 20% of the flux just redward of $\lambda = 3646$Å), but is present at a level of 0.5% of the peak Balmer jump height. The relatively low level of incident NUV radiation is evidently enough to delay the cooling of the lower atmosphere. The contributions to the net cooling and heating in the lower atmosphere are shown over time ($t = 1.5, 4.8, 5.6$ sec) in the three panels of Figure 8.11.

8.4.3 Optically Thin Radiative Loss Function

In the current implementation of RADYN, the optically thin cooling function has been updated from that used in Allred et al. (2006), who compiled the loss rates from ATOMDB. The thin cooling function is displayed in Figure 8.1 as the dashed line. The features in this curve are qualitatively like those in Rosner et al. (1978) (their Figure 10) and Raymond et al. (1976) (but with Hydrogen, Helium, and Ca removed). Future efforts should be invested in

determining the precise contributions in the cooling function (e.g., like in Cox & Tucker, 1969) An important difference in these new F12 simulations compared to the simulations of Allred et al. (2005, 2006) is the relative importance of cooling from the optically thin radiative loss function in the total cooling and dynamics of the atmosphere. We attribute some of the important effects to the structure of the cooling function at $10^{5.2}$ K, such that a "dip" in emissivity can lead to easier runaway explosive evaporation.

In Figure 8.12, we compare the cooling rate per gram of Hydrogen at $t = 4.8$ sec between the thin losses and the detailed continuum radiative cooling components (multiplied by 20 so as to appear on this scale). Note that the cooling is integrated over wavelength and is normalized by the density. Also shown is the beam energy deposition rate, which is almost entirely compensated by thin cooling losses in the region of the peak beam energy deposition such that there is no net heating of the gas ($\log m_c/(1\text{g cm}^{-2}) \sim -3.46$); at the peak of Hydrogen cooling ($\log m_c/(1\text{g cm}^{-2}) \sim -2.7$), the thin losses contribute a comparable amount to the cooling. The F11 simulation of Allred et al. (2006) found that Helium II is a major coolant at the column mass where the beam deposits most of its energy. In the F12 simulation, about 60% of the beam energy is radiated away by the thin losses (integrated over the entire atmosphere). At the peak of the thin cooling (in the second temperature plateau, $T = 60\,000$ K), He II 304Å (purple) plays a role, but only provides $\sim$1 / 20 of the amount of cooling as the thin losses at this time. The Hydrogen Lyman continuum, the FUV continua, and to a lesser extent the He I 504Å continuum, each contribute about 1/100 of the cooling. In the Allred et al. (2006) models, only $1 - 2\%$ is radiated away by the thin losses over the entire atmosphere. The implication for future modeling efforts is therefore clear: too much of the beam energy is absorbed at low column mass, where thin losses become most important.

8.5 Comparison to Previous F12 Flare Models

Livshits et al. (1981) simulated a 10-second long burst of 10^{12} ergs cm^{-2} s^{-1} flare on a M dwarf using gas dynamic models. There are several, possibly important, differences compared to our F12 simulation. They used a phenomenological description of beam energy deposition and did not calculate the detailed radiation. The starting atmosphere also did

not include a corona. They reproduced a white-light continuum with $U - B \sim -1$, which generally matches the observations of dMe flares (Kunkel, 1970; Lacy et al., 1976). The white-light continuum originated from a hot (T$\sim$9000 K), high density ($n > 10^{15}$ cm^{-3}) condensation front that propagated at $\sim$100 km s^{-1} from the site of beam energy deposition. The properties of chromospheric condensations in our model are different than in the Livshits et al. (1981) model, as we find condensation velocities of at most $\sim$9 km s^{-1} and result primarily from the coronal overpressure that is formed after the beam heating is turned off. We note that preliminary results from an F13 simulation (below) show much higher condensation velocities; a detailed analysis of the radiation from this condensation is forthcoming.

A hydrodynamical simulation with 10 seconds of impulsive heating with 1.8×10^{12} ergs cm^{-2} s^{-1} and a gradual phase was performed by Schmitt et al. (2008) to simulate the coronal evolution during a large M dwarf flare. However, the detailed radiation and photospheric response were not reported.

8.6 Comparison to Observations

8.6.1 Balmer Continuum Spectrum

The hard X-ray signature is a well-studied phenomenon during solar flares, via RHESSI (e.g., Holman et al. 2003, Fletcher et al. 2007), but is generally too faint to observe during stellar flares, except during the most powerful events (Osten et al. 2007). Radio observations from $1 - 10$ GHz provide the only direct diagnostic of the properties of mildly relativistic nonthermal electrons during stellar flares. The interpretation of the radio emission is complicated by optical depth effects and source inhomogeneities, so in practice it is difficult to extract relevant physical parameters from the radio continuum shapes (Osten et al., 2005).

For an extremely powerful flare on EV Lac, Osten et al. (2010) combined the diagnostics of Fe Kα emission and white-light (blackbody) areas to derive a range of energy flux of nonthermal electrons between $10^{11} - 10^{14}$ ergs cm^{-2} s^{-1}. Determining the energy in nonthermal electrons from observed optical spectra would be a useful diagnostic for stellar atmospheres when the Fe Kα emission is too faint to observe and would also allow us to

characterize the total area of the Balmer continuum emitting area. The current degree of uncertainty in the area of Balmer continuum emitting region is large. The surface flux between $\lambda = 3600 - 3630$Å in the F10 is 8 times smaller than the F11, and the surface flux for the F12 is $\sim$4 times larger than the F11. Thus, there is a possible range of $\sim$32 in the areal coverage that could account for any given observed flux in BaC3615.

Therefore, we analyze the detailed NUV zone spectral shapes to determine if the color of the observed spectrum could be used to indicate which flare chromosphere model best matches the observations of the Balmer continuum shape. We refer to Table 6.2. Also, recall that there is a $\sim 5-10\%$ precision in the spectral shape of the NUV zone flux (Figure A.1 and Figure A.2 of Appendix A). In Figure 8.13, we compare the spectral slopes of the model Balmer continua for the F10, F11, and F12 models. The F10 and F11 models were taken from Allred et al. (2006) at times of $t = 230$ sec and $t = 15.9$ sec, respectively, which are the times corresponding to the maximum amount of emission at $\lambda = 4170$Å. The F12 model is taken from $t = 4.8$ sec. In all cases an estimate of the Paschen continuum (using a 3rd order fit to the blue-optical zone) was subtracted from $\lambda = 3000 - 3646$Å, and the fluxes are normalized at $\lambda = 3615$Å. An estimate of the Paschen continuum is subtracted to compare directly to the observations which have a linear fit to the blue-optical subtracted (see Section 3.1.2). The F10 and F11 impulsive phase models differ from one another by $<1\%$ in their continuum slopes, so they are indistinguishable considering representative observational uncertainties. The F12 is significantly flatter in the impulsive phase. The flux at $\lambda = 3420$Å is 94% of the flux at $\lambda = 3615$Å, indicating a $\sim$6% flux change over the DIS wavelength range for the Balmer continuum. For reference, this corresponds to a color temperature[4] of $T_{\rm BB}\sim$6650 K. For the F10 and F11, there is a 10% flux change between $\lambda = 3420$Å and $\lambda = 3615$Å. Interestingly, in the decay phase ($t = 5.6$ sec) of the F12, the Balmer continuum has steepened to that of the F10 and F11, with a $\sim$12% change in the NUV zone. These results are summarized in Table 6.2; the values in the table are given in units of fractional change of 10^{-4}Å^{-1} times the flux at $\lambda = 3615$Å. The value for the F12 is 3.0×10^{-4}. Therefore, over the wavelength range $3420-3646$Å, $\Delta\lambda = 195$Å, there is a 6%

[4]Which is *not* indicative of the actual temperature, see Section 8.4.1

change in flux.

Given that the precision in the observed continuum shapes from $\lambda = 3400 - 3600$Å is at best 5%, we cannot say reliably which beam model is constrained by the observations of the Balmer continuum. We suggest future observations with higher blue sensitivity will be able to reach the level of precision necessary for constraining Balmer continuum shapes.

Compared to the F11 and F10 model atmospheres, the difference in the Balmer continuum slope in the F12 may be due to the different chromospheric temperature and density structure from the higher flux. Another possible source of the flatter slope in the F12 model is the current updated treatment of optically thin cooling in the RADYN modeling. Since Helium cooling is now less important relative to the thin losses in regulating the beam flux, we speculate that the Helium continua throughout the entire electromagnetic spectrum are also less prominent. There are four Helium I continua calculated in detail in the NUV zone. These have edges at $\lambda = 2592$, 3110, 3408, and 3663Å. Depending on the amount of cooling in each of these continua, the spectral shape of the total continuum emission could be affected.

8.6.2 Comparison to the GF5 Peak Spectrum

The peak spectrum from the F12 model exhibits a color temperature of $T_{\rm BB}\sim$5500 K in the blue-optical zone. From our sample, the lowest temperature that we observe is $T_{\rm BB}\sim$6700($\pm$800) K during GF5 on YZ CMi, the most gradual and one of the lowest amplitude flares in the sample. In Figure 8.14, we show the $\lambda = 3400 - 6800$ K spectrum of this flare, compared to the RADYN prediction. The model spectra have been scaled to match at C4170. The best fit Planck function is also shown; both the blackbody and the RHD model can account for the (extremely) low-level continuum at $\lambda > 4000$Å. The continuum at $\lambda > 4000$Å in the RHD model is primarily Paschen continuum from the flare chromosphere at log $\rm m_c/(1g\ cm^{-2})\sim$-1.7. We speculate that this flare represents a pure "Conundruum" flare and can be modeled by Paschen continuum with similar conditions to that in the F12. Note, deep heating has not commenced at this time ($t = 1.5$ sec). The spectrum at $t = 4.8$ sec provides a closer match in the Balmer continuum level because it

contains more backwarmed photospheric radiation (and a lower $\chi_{\rm flare}\sim6$, but still not low enough to match the observations). Further modeling is required to determine if additional backwarmed temperature minimum radiation or additional Paschen continuum radiation can generate even a $T_{\rm BB}\sim6700$ K continuum.

In Figures 6.29 (top, bottom), we showed that the red continuum during the *gradual* phases of extremely large amplitude, high energy flares have red color temperatures of $T_{\rm BB}\sim3500-5500$ K, similar to the blue color temperatures of the F12 (and F11). Since we found with the models that the Balmer continuum emission rapidly decreases after nonthermal particle heating stops, we suggest that the $T_{\rm BB}\sim3500-5500$ K component in the gradual phases of the red continuum of large flares may imply persistent particle heating, similar to the type that generates the Paschen continuum during the peak of GF5. Interestingly, the $\chi_{\rm flare,peak}$ of GF5 ($\sim4.3\pm1.3$) (and the $\chi_{\rm flare,decay}\sim2.7-2.8$ in the decay phases of the IF1 and IF3 events, respectively, in Figure 6.29) are smaller than for the RHD model ($\sim6-7$) as the Balmer continuum level in Figure 8.14 is higher than the observations. The lower $\chi_{\rm flare}$ in the observations can be investigated when we understand the $T_{\rm BB}\sim8000$ K component, which, we speculate, may be the decaying emission from the peak $T_{\rm BB}\sim10\,000-12\,000$ K component, sustained by residual particle heating, and with low-levels of absorption still present in the NUV zone.

The F12 Paschen continuum model from $\lambda=4000-6800$Å should be tested with other low-amplitude ($I_{f,U}+1<1.5$), long rise ($t\sim10$ minute) flares like GF5.

8.6.3 Light Curve Morphology

We return to the light curve morphology of the $\lambda=3550$Å light curve (Figure 8.3). The continuum flux attains 93% of the peak flux in one second and declines to 7% of the peak flux one second after the beam heating is turned off: the rise and decay phase are precisely symmetric. We also mentioned that the fast rise and initial decay phases were fit with the same evolving exponential time constants that lengthened as time increased. We show these fits in Figure 8.15 (top panel). An evolving decay constant is expected for a system that is exposed to a non-equilibrium condition (e.g., turning the beam abruptly on and

abruptly off); as equilibrium is attained, the atmospheric parameters also change, resulting in evolving time constants (Carlsson & Stein, 2002, see also Appendix H). During the rise phase, equilibrium is achieved with the tail of the beam heating at log $m_c/(1g\ cm^{-2})\sim -2$ (ie., in the flare chromosphere; Figure 8.4).

A triumph of the F12 beam heating model is that the predicted NUV light curve evolution matches several important features of observed impulsive phase morphology. We introduce a new interpretation of the impulsive phase U-band emission, whereby the rise phase and fast decay phases are well-represented by exponential functions with relatively short time-constants. In Figure 8.15 (bottom), we show the impulsive phase U-band light curve of IF1 near the peak. The rise phase consists of three "bursts" of emission. We analyze the second burst, which has a duration of ∼3 minutes. The burst begins with large changes in emission and ends with small changes in emission; a third burst is observed at peak emission, similar to the peak burst in IF3 (see Chapter 4 where we isolate the newly formed flare emission during this burst). We find that the second burst in the rise of IF1 is well-represented by a function of the form $I_f \times (1 - e^{-t/\tau})$ (an "exponential rise" function), with a time constant of ∼2.5 minutes. The fast decay phase ends at ∼40% the peak emission, and we find that this phase also is well-represented by a fast exponential, with a time-constant of ∼2.1 minutes (note, the total duration of the fast decay is about 4.4 minutes). The fits are shown in red, and the residuals are displayed at the bottom of the figure. Although there are significant residuals, the overall trend is generally reproduced.

Although the impulsive phase F12 morphology matches the impulsive phase IF1 morphology qualitatively, the decay constants of the model are∼600 times shorter than the observations. Also, the rise phase and decay phase of the observations of the second burst are not precisely symmetric ($t_{\rm rise} \neq t_{\rm fastdecay}$), but the exponential time constants are closer to being equal. Also, note that the rise time and rise time constant are nearly equal, whereas the decay time is about twice as large as the decay time constant. These trends should be investigated in detail with high-cadence photometry of other smaller flares[5]. Furthermore,

[5]As IF1 is one of the largest NUV flares ever recorded with high time cadence data, 600 times must be an upper limit; In Appendix E, we show that a smaller impulsive flare from Kowalski et al. (2011b) has $\tau \sim 10$ seconds, or ∼40 times larger than the model prediction.

we found that the model spectrum is in stark disagreement with the observed properties of the white-light continuum due to the lack of the hot, blackbody component – which we speculate was extremely prominent in the impulsive phase of this flare. Nonetheless, if we apply the underlying principles of the models to the observations, we find: the observed rise phase and decay phase structure may be the result of the atmosphere attaining equilibrium with flare heating. A broader claim might also be made *that the second burst is the result of a new area on the stellar surface that experiences a sudden non-equilibrium condition; the rise phase is the equilibration of the atmosphere to the energy source and the decay phase is the response of the atmosphere as the equilibrium is suddenly lost.* Note that this interpretation differs from that presented in Section 6.7.2 whereby the fast decay phase was the result of persistent heating at an (initially) constant or larger area but lower temperature.

The rise and decay structure may not be a result of equilibrium being achieved in a single flare area. Instead, the attainment of equilibrium could apply to a larger structure, such as a flare "arcade" as observed on the Sun. In this case, an example of a sudden non-equilibrium condition could be the eruption of a filament which causes the reconnection of a large canopy of unstable magnetic field lines. Avalanche simulations (Lu & Hamilton, 1991; Charbonneau et al., 2001; Aschwanden, 2011) have provided insight into the triggering and evolution of solar flare arcades; we speculate that the light curve morphology is the result of such a mechanism. Large solar flares can comprise several individual arcades/avalanches; an example is the famous "Bastille Day" X7 flare which produced two spatially distinct arcades, with each arcade having a different speed of propagation. The areal evolution of this flare has been discussed in Fletcher & Hudson (2001); Kosovichev & Zharkova (2001); Qiu et al. (2010). Because the timescales are much longer in IF1 compared to the model timescales, we must develop a physically based methodology for stacking individual $5 - 10$ second "bursts" of FX (where X is the flare heating model that reproduces the hot, blackbody and $\chi_{\rm flare,peak}$) to simulate an arcade or avalanche of flare loops such that the exponential rise and exponential decay morphologies are maintained, but with longer timescales.

8.6.4 Ways Forward

In order to be able to apply the RHD models confidently to the observations for interpreting the physics of flare atmospheres, we must be able to produce the properties of the white-light continuum. In particular, we must be able to generate the hot, blackbody component self-consistently and identify a physical heating source. The RADYN models produce the correct spectral shape of the Balmer continuum, but there is a large range of possible beam fluxes; again, having a model that accurately reproduces the blackbody component will allow us to tune the beam flux using the combined properties of the blue, optical, and UV emission lines as well as the Balmer continuum. We have found that there can be an important interplay between the amount of observed Balmer continuum and the amount of phenomenological hot spot; therefore, until we generate enough heating at high column mass to produce absorption features in the continuum, we will always produce, simply, too much Balmer continuum from the flare chromosphere. The F12 model showed preliminary evidence for a small amount of absorption, giving rise to a low-level anti-correlation between the blue-optical and NUV flux.

There are several ways forward for RHD modeling. From the F12 model, we calculate the total NLTE radiative heating from the BaC and PaC at low atmospheric depths. This amount is 4×10^{10} ergs cm^{-2} s^{-1}. If backwarming is the source of the blackbody, then this implies that we will need five to ten times larger beam flux, assuming a linear scaling between beam flux, NUV Balmer continuum, and NUV Balmer continuum heating in deep layers. We have begun an F13 flare model using the same nonthermal electron beam parameters. The dynamics of this atmosphere are drastically different than the F12. We show a preliminary look at the temperature and ionization structure in Figure 8.16, which features a shock where the beam hits, resulting in complete Helium ionization and a $\sim$10 MK temperature bubble. At $t \sim 0.5$ sec, the color temperature of the blue-optical zone is $T_{\rm BB}\sim$6500 K, about 1000 K larger than the F12 at $t = 4.8$ sec.

If the blackbody is still not achieved by the F13, we will investigate other sources of unaccounted heating. The heating by protons is not currently calculated by the models. Protons (E$\sim$1 MeV) have been considered as a possible heating agent in solar and stellar

flares (Orrall & Zirker, 1976; Emslie, 1978; van den Oord, 1988; Doyle et al., 1988). Many gamma ray observations have revealed the presence of protons in solar flares. Hurford et al. (2006) showed convincingly that ion emission originates from magnetic footpoint structures similar in location and size to the mildly relativistic electrons. Protons have been detected once during stellar flares, when they were attributed to an increase lasting 3 seconds in the Lyα wing during a flare on the M dwarf AU Mic (Woodgate et al., 1992). These authors derived an energy flux in protons that could account for the observed transition region radiation. The role of protons during flares remains inconclusive (Robinson et al., 2001), but it has been suggested they could account for most of the impulsive flare energy (Simnett & Strong, 1984) and that they possess sufficient momentum and penetration capability to generate seismic disturbances ("sunquakes") in the solar photosphere (Zharkova & Zharkov, 2007). We will begin simulating the heating by protons by placing a phenomenological heating source with 5×10^{11} ergs cm^{-2} s^{-1} at log m$_c$/(1g cm^{-2})$\sim$0.5; RADYN has functionality to calculate the dynamics of such a simulation.

Improvements must also be made to the description of the nonthermal electron beam. First, the parameter space of the low energy cutoff should be explored and the "cutoff" should be more accurately modeled, such as with a rolling turnover (Liu et al., 2009; Fisher et al., 2012). In the future we plan to investigate the difference in the atmospheric response from using a power law index of $\delta = 3$ (or less) as has been found from radio observations of dMe flares (Osten et al., 2005). A "harder" power law index of electron number density should result in more energy deposited lower in the atmosphere, according to the thick target formulation. We will also simulate a time-variable power-law index, which is observed to change from "soft" to "hard" in the rise phase of solar flares (Holman et al., 2003).

The standard energy deposition calculations of Emslie (1978) should be modfied by the Fokker-Planck description, as has been done for recent solar flare simulations (Liu et al., 2009). Due to more accurate treatment of particle diffusion and the pitch angle distribution (currently, RADYN assumes a single downward-directed pitch angle of the electrons), the Fokker-Planck formulation is predicted to generate very different intensities for the outgoing impulsive phase (hard X-ray and white-light) radiation (Mauas & Gomez, 1997; Allred et al., 2006). Preliminary calculations indicate that the beam energy is deposited over a larger

column mass range, leading to a less concentrated peak in the beam heating function (J. Allred, priv. communication, 2011). The Fokker-Planck treatment may even allow more electrons to deposit energy in the photosphere.

Other improvements to RHD modeling are desirable, and we summarize several aspects here.

- Using a larger coronal source (100 Mm) and heating from neighboring coronal loops as soft X-ray / EUV observations (Mullan et al., 2006; Osten et al., 2010) have indicated larger loop lengths than in the simulation. A larger flare corona could increase the X-ray backwarming on both the pre-flare chromosphere and on the lower atmosphere during the flare.

- Implementing a simulated cooling term in the lower atmosphere to account for the cooling from molecular lines such as TiO as these molecules are likely important in the photospheric energy balance during flares.

- Accounting for NLTE ionization of metals in the temperature minimum region, which are currently treated in LTE. We speculate that the NLTE NUV backwarming could cause an increased electron density (from the metals) in the lower atmosphere and lead to greater H^- recombination radiation hence leading to more continuum in the blue-optical and red-optical zones and a smaller $\chi_{\rm flare}$.

- Implementing a larger gravity of $\log g \sim 5$ that be more representative of a dM3 – dM4 for which we have flare spectra. The resulting gravity would be 1.8 times larger than currently employed, and we suspect that this will increase the densities resulting in significantly different heating and cooling timescales.

- A Hydrogen atom with more levels (and more wavelength points further into the line wings) would be useful in order to compare to the blending of the lines near the Balmer jump.

- The kink instability is a known problem for the employed electron beam fluxes, and the return current must be considered for a self-consistent treatment of flare heating (E. Zweibel, priv. communication, 2011). Theoretical calculations predict the return current to affect the outgoing radiation, from X-ray emission (Holman, 2012) to the Hydrogen Balmer line emission (Štepán et al., 2007). The effects on continuum emission should be predicted in future works.

- After reconnection, Alfvén waves are thought to transport energy to the lower atmosphere where they can accelerate free electrons (Fletcher & Hudson, 2008; Brown et al., 2009). The wave energy should be included in the flare heating rates in addition to the energy deposition from electrons accelerated through wave-particle interactions.

Finally, we acknowledge that these models are limited by being 1D for both the treatment of radiative transfer (Uitenbroek & Criscuoli, 2011) and for the treatment of dynamics (Abbett & Hawley, 1999). 1D flare modeling artificially induces a magnetic field confined regime ($\beta < 1$), whereas the plasma in the lower atmosphere is dominated by the gas dynamics: in other words, the large shocks in the F13 may be unphysical because gas would (quickly) expand to neighboring regions in a three-dimensional treatment (W. Abbett, priv. communication, 2012). Many astrophysical problems remained unsolved for decades (e.g., the explosion mechanism for Type II supernovae) because of the limitations of 1D modeling; the generation of large temperatures at high column mass during M dwarf flares may be no exception.

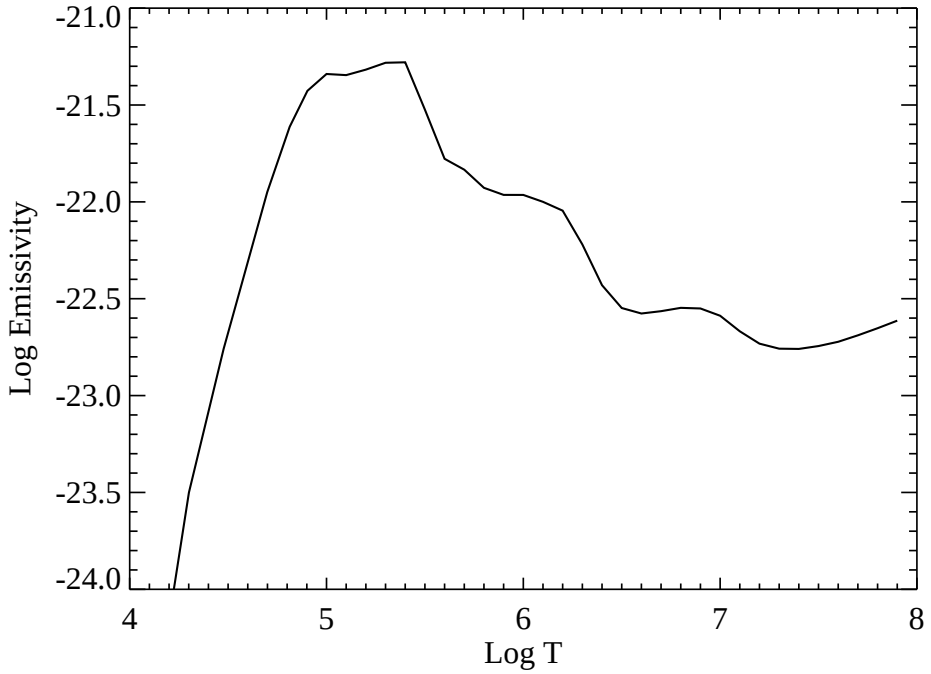

Figure 8.1 The optically thin cooling emissivity as a function of temperature.

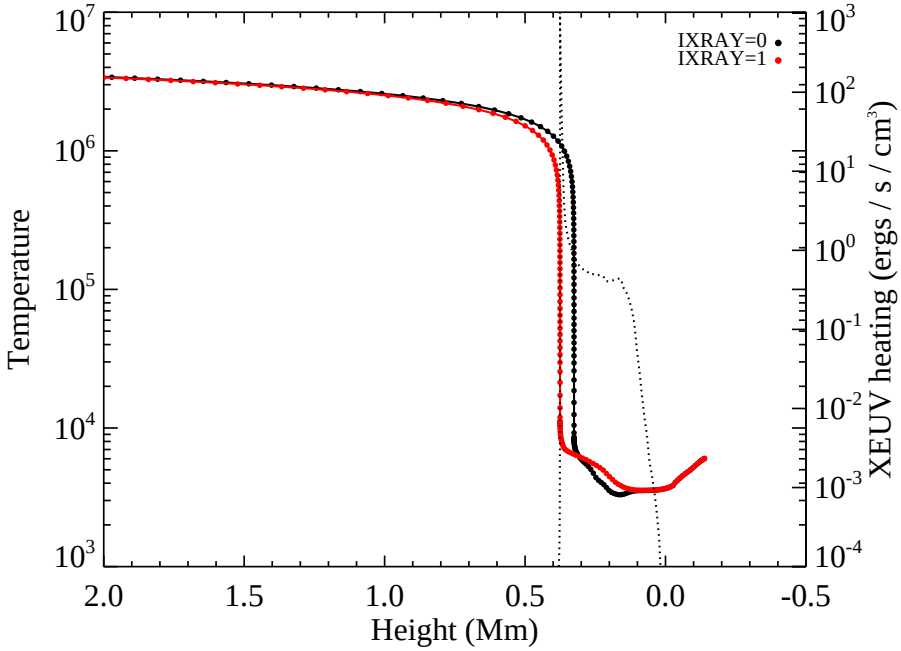

Figure 8.2 The temperature profile of the starting atmosphere, converged with XEUV backwarming (red) and without XEUV backwarming (black). The XEUV backwarming is shown on the right axis and the profile is the dotted line.

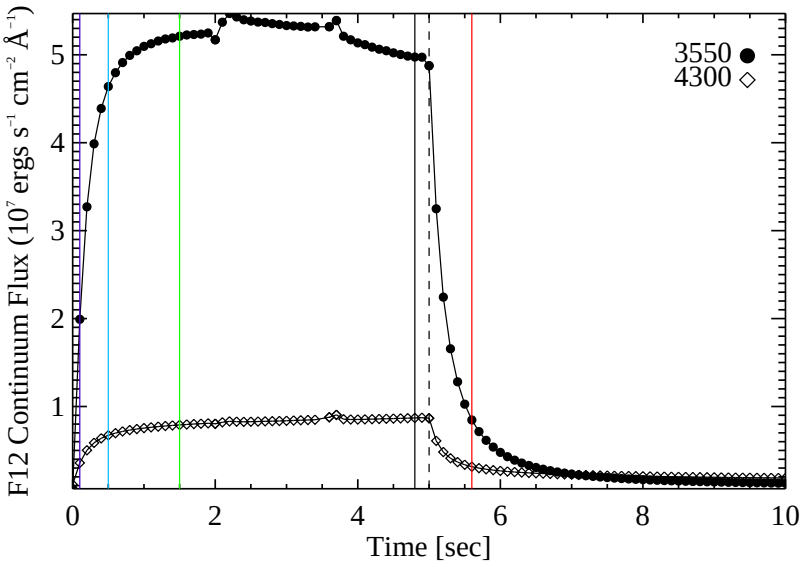

Figure 8.3 The light curve of the (Hydrogen + Helium) continuum flux at $\lambda = 3550$Å and $\lambda = 4300$Å calculated in detail. The key times discussed in the text are indicated with vertical lines ($t = 0.1, 0.5, 1.5, 4.8, 5.6$ seconds). The beam heating is turned off at $t = 5$ sec, which is indicated by a vertical dashed line.

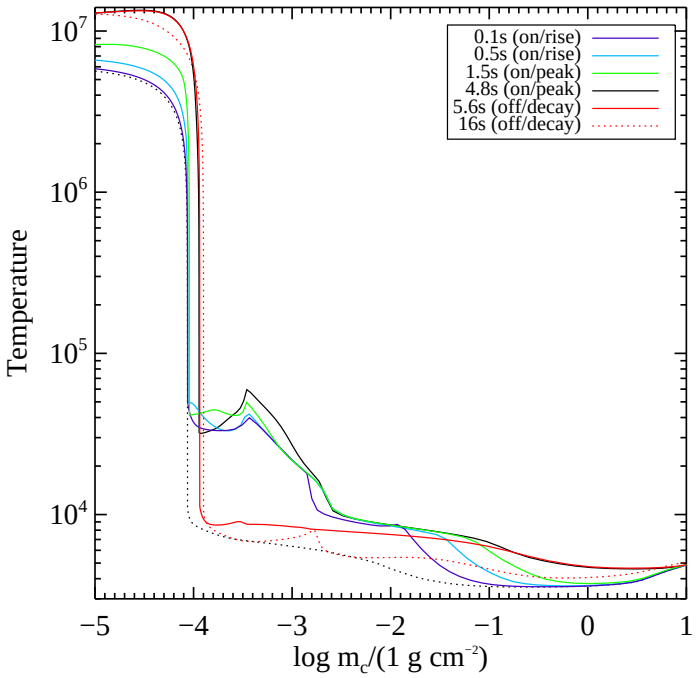

Figure 8.4 The temperature evolution of the F12 simulation at the key times indicated in Figure 8.3. We also show the far gradual phase at $t = 16$ seconds.

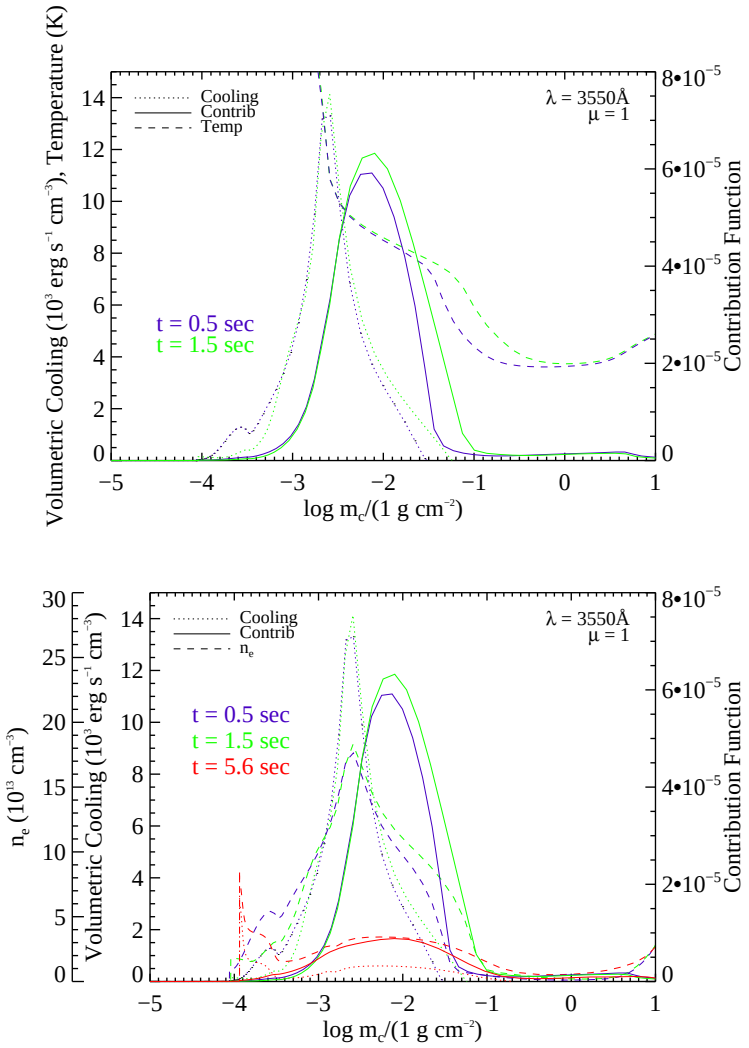

Figure 8.5 (Top) The contribution to the total $\lambda = 3550$ Balmer continuum intensity (solid) and net cooling in the Balmer continuum (dotted) are compared at two different times ($t = 0.5, 1.5$ seconds). The temperature profiles are also displayed (dashed lines) and correspond to the values on the left axis, with units of 10^3 K. The cooling and contribution have contributions at higher column mass later in the flare. (Bottom) The net cooling and contribution function are shown against the electron density (dashed) for the two times. The electron density profiles are divided by 2×10^{13} cm^{-3} and correspond to the left axis.

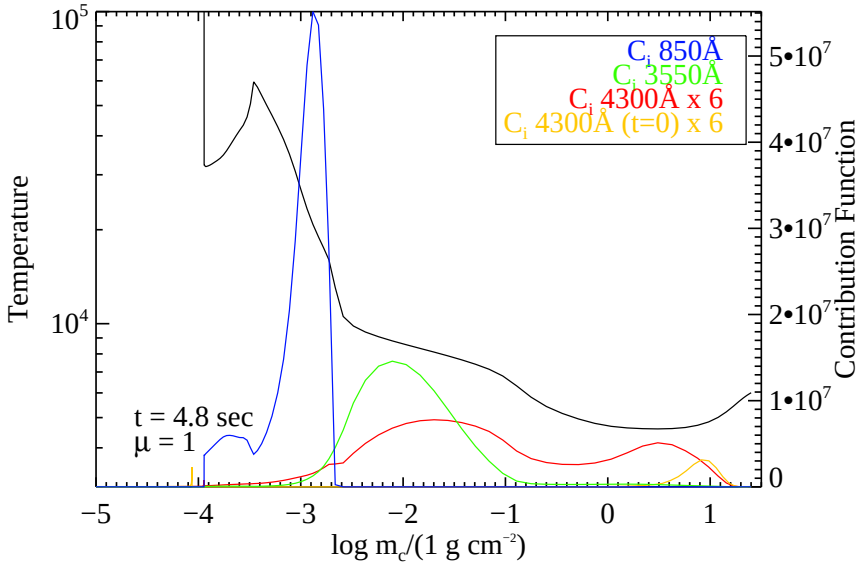

Figure 8.6 Contribution to the total intensity ($\mu = 1$, $t = 4.8$ seconds) in several continuum wavelengths. The temperature profile is also shown.

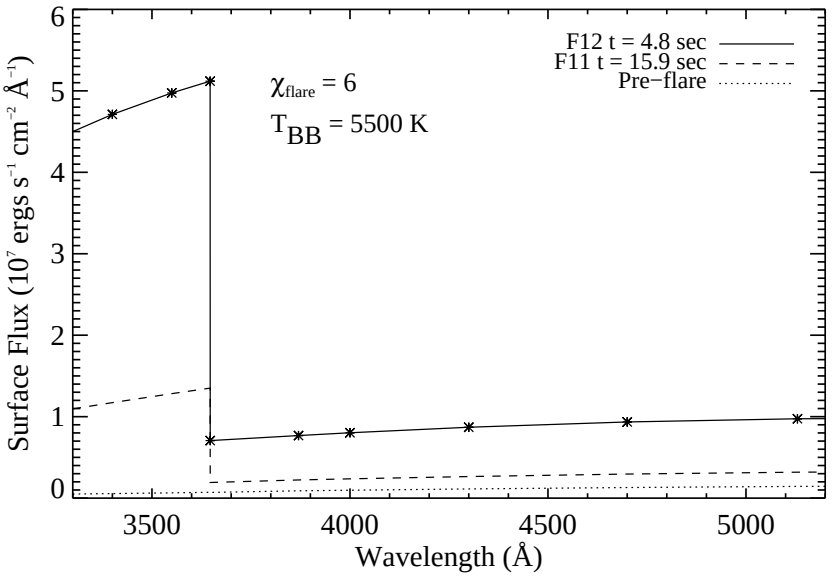

Figure 8.7 The model continuum surface flux spectrum from $\lambda = 3400 - 5200$Å, calculated in detail. The F11 continuum is shown as dashed and quiescent as dotted lines.

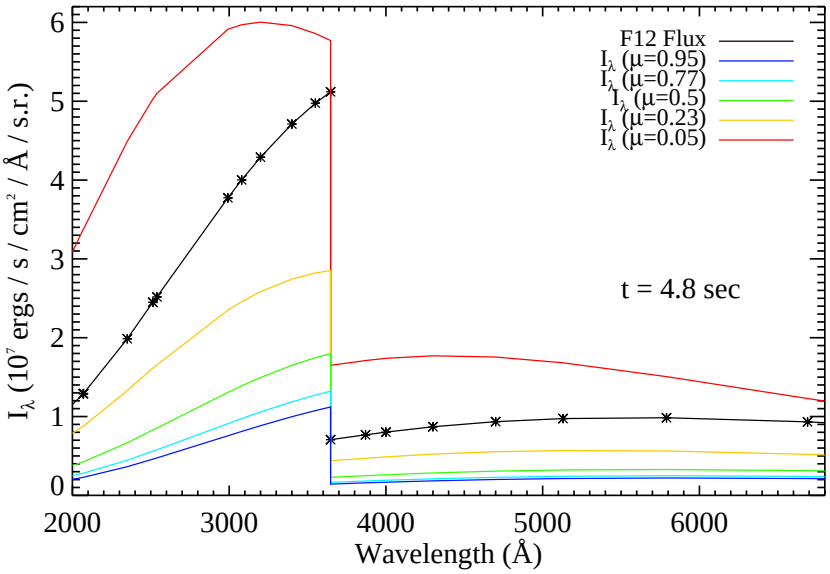

Figure 8.8 The model continuum intensity spectrum from $\lambda = 2000 - 6800$Å, calculated in detail. The five values of μ which are calculated by RADYN are shown.

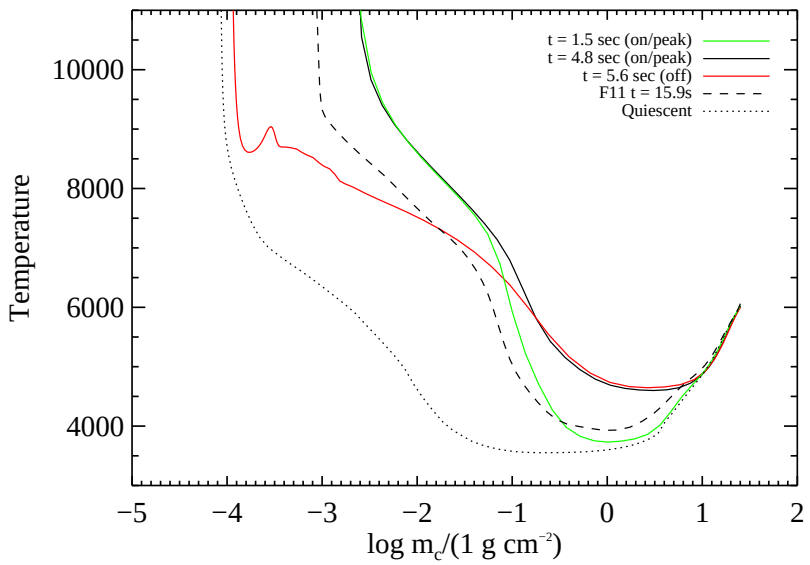

Figure 8.9 The temperature evolution of the lower atmosphere at key times in the F12 run. The F11 ($t = 15.9$ sec) is the dashed line and the quiescent temperature profile the dotted line. Compared to the F11, the flare chromosphere is at higher column mass and there are larger temperatures at log $m_c/(1g\ cm^{-2})\sim 0$. The heating at lower depths is delayed compared to the heating higher up in the F12 atmosphere.

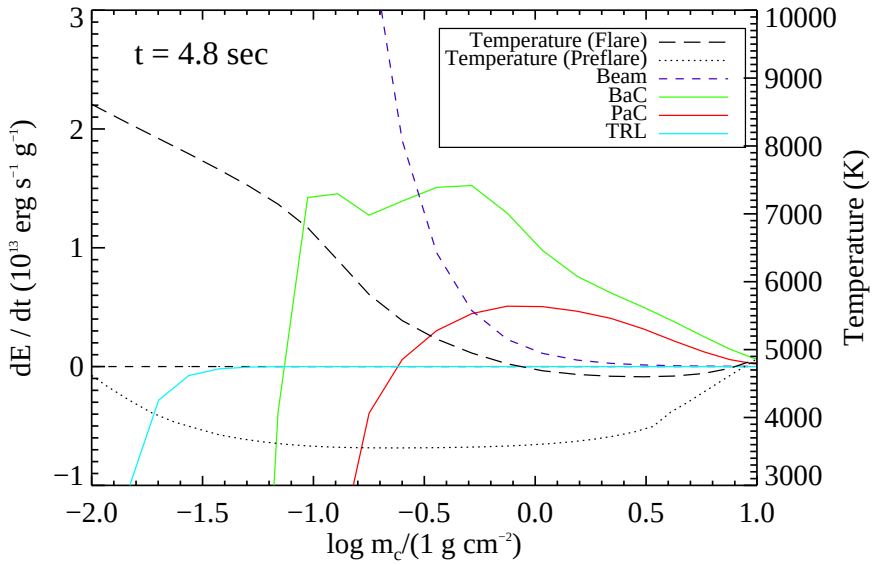

Figure 8.10 Individual contributions to the detailed radiation energy balance at $t = 4.8$ sec. The total energy balance terms at this time are given in Figure 8.11. Positive quantities represent heating and negative quantities represent cooling. The temperature profile at this time is given on the right axis (black long dashed line). The quiescent temperature profile is the dotted line.

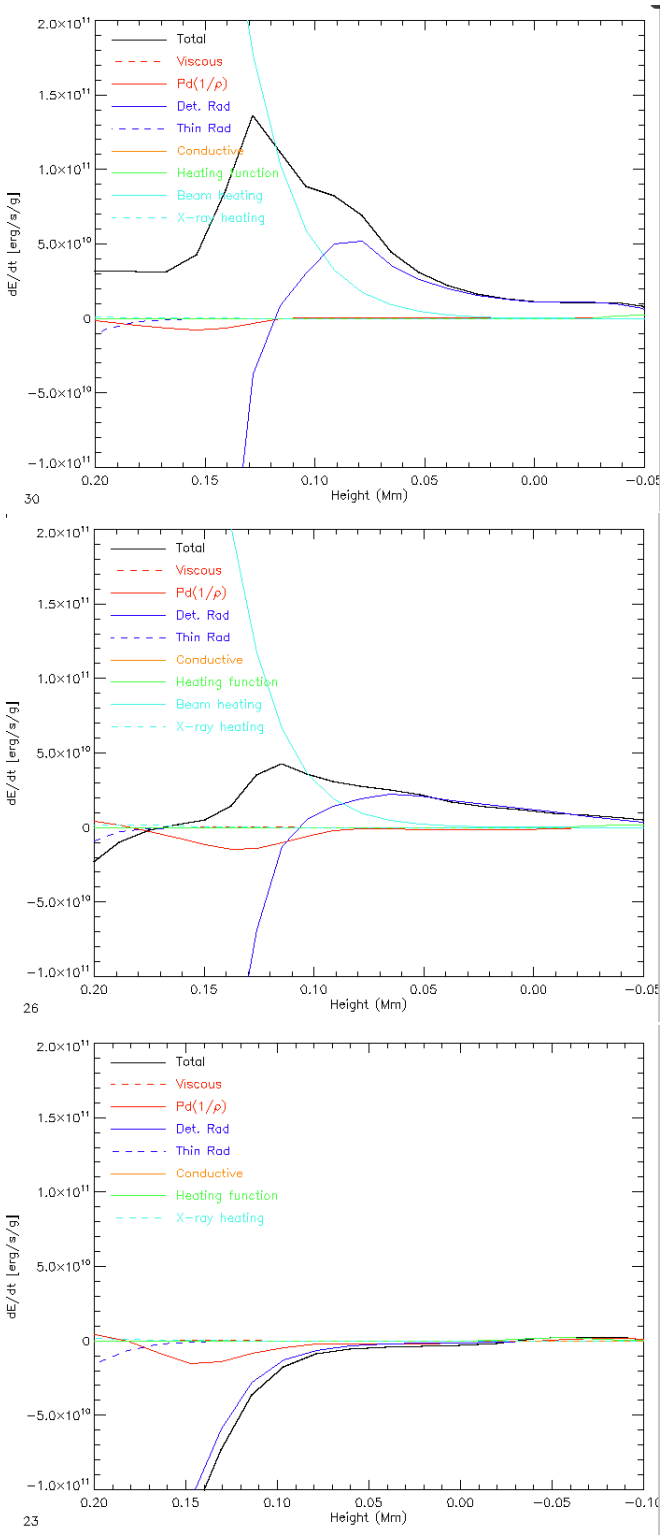

Figure 8.11 The total contributions to the energy balance in the lower atmosphere at $t = 1.5$ (top left), $t = 4.8$ (top right), and $t = 5.6$ (bottom) seconds. Negative quantities represent cooling; positive quantities represent heating. Note how there is very little net heating or cooling in the lower atmosphere after the beam is turned off. These are snapshots from the RADYN analysis tool, *emovie*, courtesy of M. Carlsson.

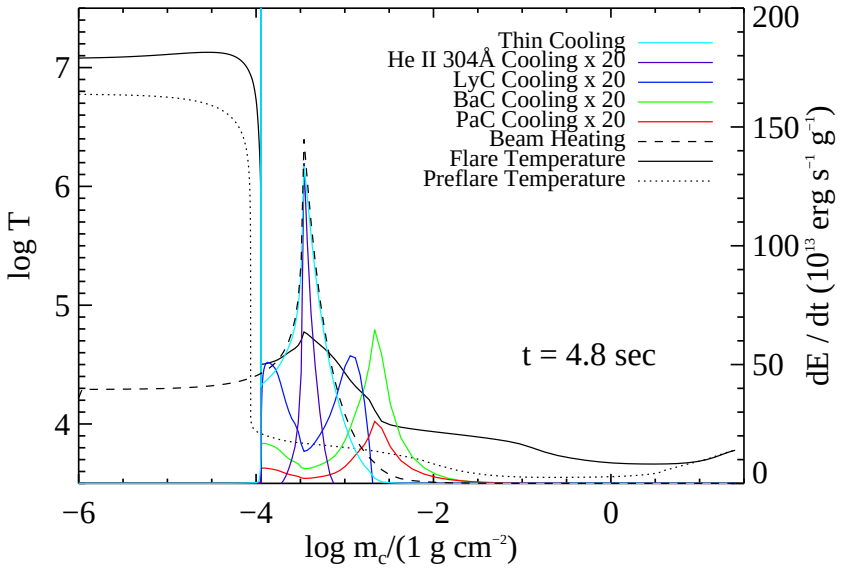

Figure 8.12 The temperature profile at = 4.8 sec is shown compared to the quiescent (dotted line). The beam heating is the dashed line and the thin cooling is the solid light blue line. The net cooling from the Lyman, Balmer, and Paschen continua, and the He II 304Å line are shown, scaled by 20. Thin cooling equalizes the beam heating and also contributes to cooling down into the flare chromosphere. Note that the beam energy deposition continues through the flare chromosphere, as apparent in the largely zoomed energy balance plot of Figure 8.11. The maximum cooling per gram from thin losses is 574×10^{13} erg / s / g, occuring in a narrow range of column mass in the flare transition region at a temperature of log T = 4.96. The thin loss rate per gram becomes very small in the corona at log T = 5.8 consistent with the thin loss curve in Figure 8.1. The rise between log T7 − 8 is due to bremsstrahlung radiation (Raymond et al., 1976).

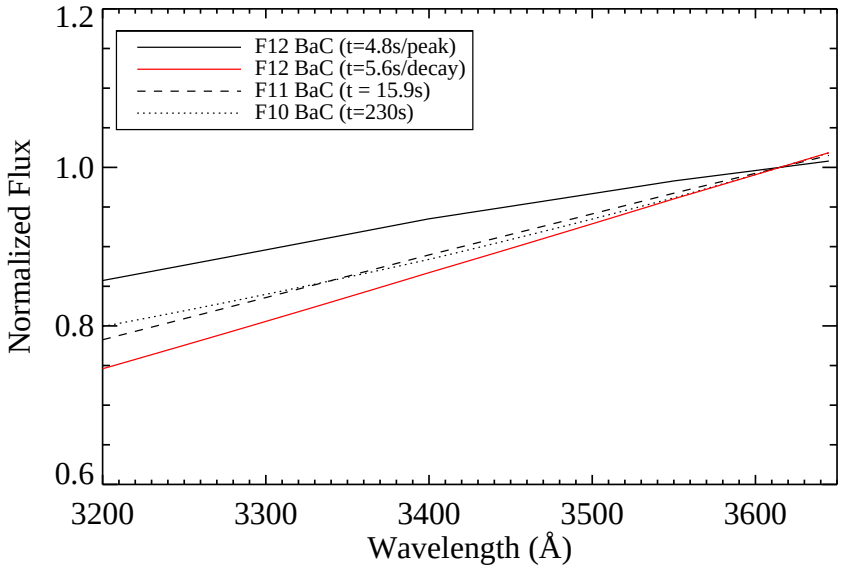

Figure 8.13 The fluxes of the BaC continua are normalized to their surface flux values at $\lambda = 3615$Å. The F10 and F11 BaC were taken from Allred et al. (2006). The F12 model spectrum is shown for the impulsive (solid black) and gradual (solid red) phases. With future observations, we hope to discriminate between the models.

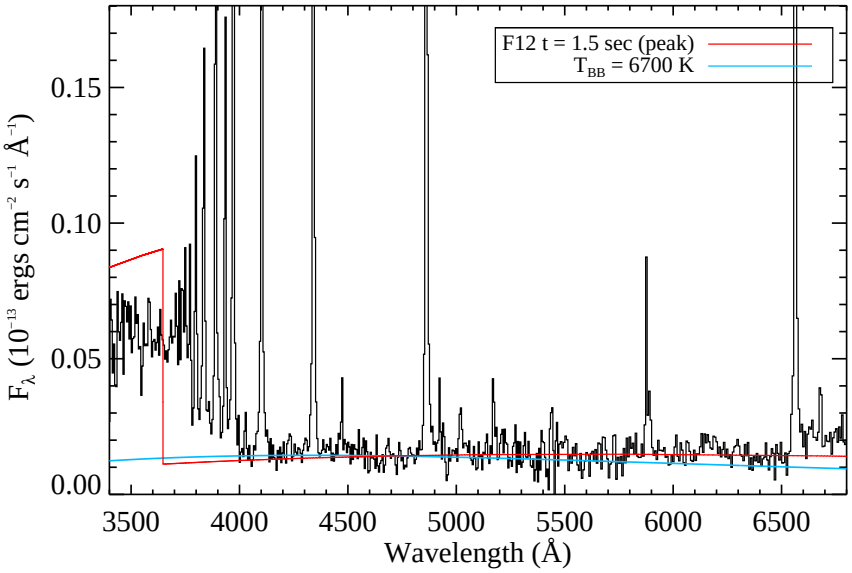

Figure 8.14 The peak emission (averaged over four spectra) for GF5 compared to the peak spectrum from the F12 model ($t = 1.5$ sec).

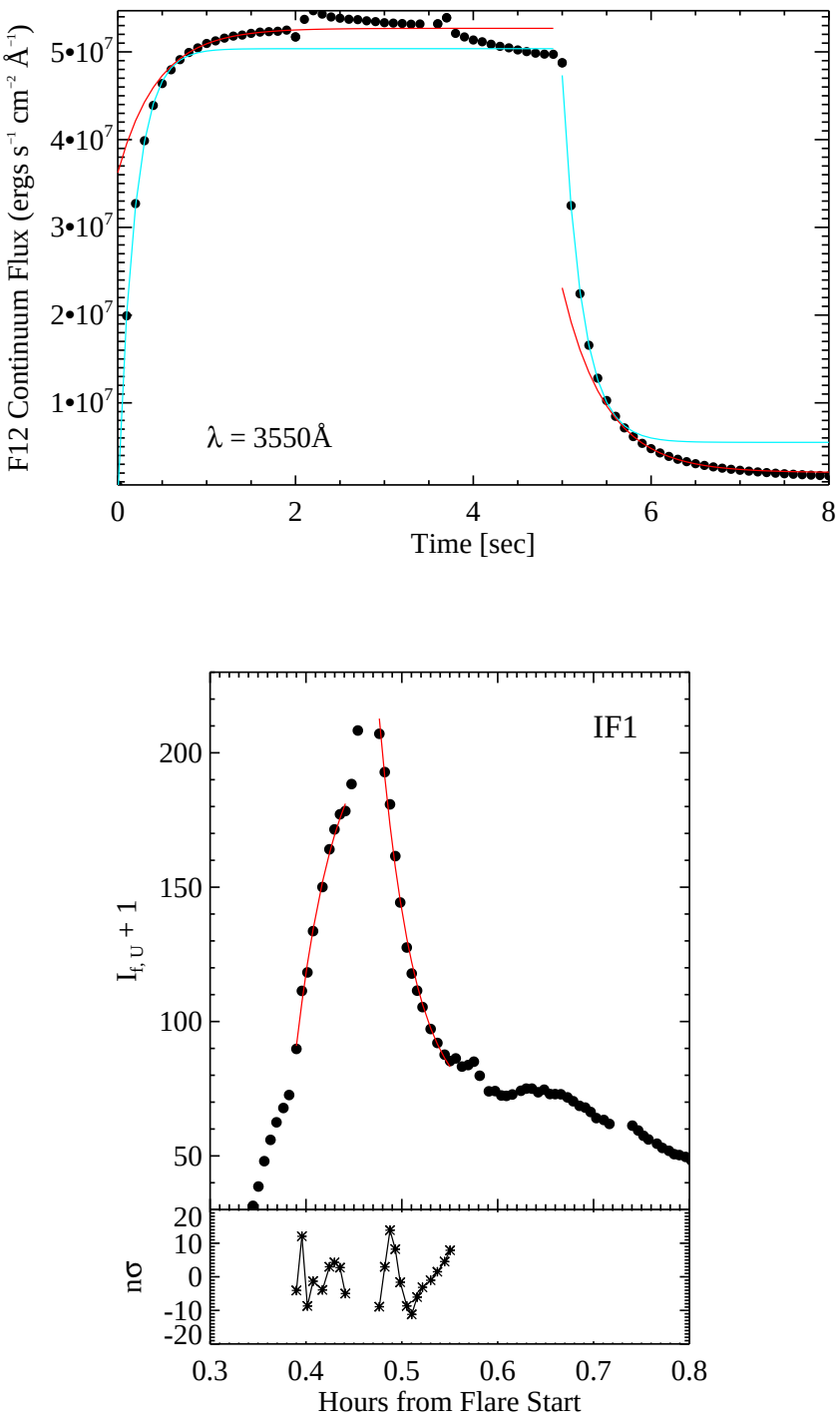

Figure 8.15 (Top) The model F12 $\lambda = 3550$Å continuum evolution; exponential fits were performed to the symmetric rise and decay phases, revealing changing time constants. (Bottom) A similar morphology is observed in IF1 impulsive phase photometry light curve, but on ∼600 times longer timescales. The best-fit exponential functions (red, 4 free parameters) are shown to the second burst in the rise phase and to the initial decay phase. The similarity either represents an equilibrium condition at a single location, or a larger-scale equilibrium condition involving many heated regions.

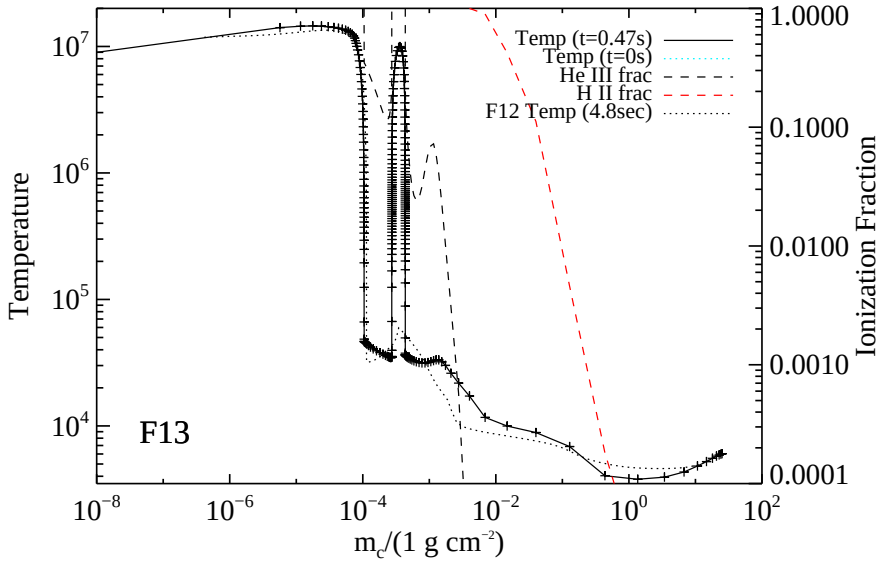

Figure 8.16 A preliminary look at the temperature structure of the F13 model at $t = 0.47$ sec. The dotted line is the quiescent profile and the black dashed line here is the F12 at 4.8 sec. The atmosphere features a superhot temperature bubble where Helium is completely ionized, a hotter flare chromosphere at log $m_c/(1g\ cm^{-2})\sim-2$ than the F12. However, the region at high column mass hasn't experienced a net heating yet. The ionization fractions are shown on the right axis and as dashed lines for the F13 model.

Chapter 9

SUMMARY AND CONCLUSIONS

In this thesis, we completed a homogeneous survey of twenty flares with simultaneous optical/NUV photometry and spectroscopy. Phenomenological models and radiative-hydrodynamic simulations were carried out in the attempt to constrain the atmospheric depth and heating mechanism that produces the white-light continuum and other lower atmospheric flare emission.

We began our study by separating the flares using their morphological characteristics and showed that the peak properties of the blue/NUV continuum are connected to the overall time-evolution of the flare light curve. We differentiate between *impulsive* and *gradual* flares according to a new value, the impulsiveness index, $\mathcal{I}$. Our designation is not to be confused with the impulsive and gradual phases of an individual flare: for example, a flare is gradual if it has a low peak amplitude and/or large $t_{1/2}$ even though it may have distinct impulsive and gradual phases. The designation is instead related to which type of emission dominates the overall evolution. The flares that had the largest value of $\mathcal{I}$ were generally the fast, classical flares (IF), and the gradual flares (GF) are typically more complex featuring a slowly changing light curve near peak but also intermittent faster continuum variations. Some flares exhibited properties of both categories and are classified as "hybrid" flares (HF); these typically had several closely spaced (in time) fast, continuum variations.

We have detected the Balmer continuum (BaC) in emission for a variety of flares, and found that it contributes significantly to the total NUV flare flux in the GF and HF events. At peak, the ratio of flux in BaC3615 to the total flare flux in C3615 is $\sim$20 – 44% (IF), 50 – 60% (HF), and 60 – 80% (GF). For the first time, we characterize the time-evolution of the BaC and find that it is generally similar to the other Balmer lines, but evolves quickly, like the higher order Balmer transitions. We established a temporal relationship – the "time-decrement" – between six of the Balmer features for several flares. The time-

decrement is a linear relationship between the wavelength (inverse relationship with energy) of the Balmer transition and the $t_{1/2}$ value of the light curve for that transition. A general explanation is found in Drake & Ulrich (1980), who connected the energy of a transition to the higher collisional excitation frequency to the lower levels of the transitions in higher electron density environments. Future efforts should connect this relation to the presence of gradual phase flare heating. The time-decrement is similar for the simple, classical flares IF3 and IF9, indicating a possible scaling relationship (same heating but larger area) between moderately large energy flares ($E_U \sim 10^{32}$ ergs) and high energy ($E_U \sim 10^{33}$ ergs) flares for the Hydrogen Balmer emitting region. We are attempting to understand the time-decrement with new RHD models.

We also found that the continuum measured just redward of the Balmer jump (C4170) is the fastest component in the blue/NUV and does not follow the time-decrement of the Hydrogen Balmer series. This "blackbody" continuum component contributes toward a large fraction of the emission throughout the NUV, blue-optical, and red-optical spectral zones. An extrapolation of this continuum beyond our spectral range suggests that it continues to rise into the NUV. The U-band amplitude – and time evolution – is largely determined by this emission component although the U band is also affected by the Balmer continuum, especially for the HF and GF events. The BaC dominance in the HF and GF events could be the reason for their smaller amplitudes and more gradual time evolution as observed in the U-band. We derive the filling factors (areal coverage) of the Balmer continuum emitting region assuming an F11 RHD model BaC, which has a spectral shape from $\lambda = 3420 - 3630$Å that generally matches the observations, especially in the gradual phase. The inferred areas indicate a compact source, but require more understanding of the precise BaC properties, especially about the beam flux level, and consequently the flare chromospheric temperature structure from which it originates. Further constraining the Balmer continuum properties during the IF events, especially at flare peak when the apparent amount of Balmer continuum does not well-match the RHD F11 model BaC, would provide important constraints and insight into the formation of the C4170 blackbody continuum, which is most prominent in the IF events.

The main parameter we use to describe the blue/NUV continuum is the $\chi_{\rm flare}$ parameter,

the ratio of flux values to the blue and red of the Balmer jump. The IF events have small $\chi_{\rm flare}$ (and hence small Balmer jumps) at peak continuum emission whereas the gradual flares have larger Balmer jumps. The Balmer jumps increase by the beginning of the exponential decay of the gradual phase, which also exhibit 20 – 30% more blue/NUV emission in the Hydrogen Balmer (continuum and line) component than at peak. We also measured the ratio of Hγ emission to nearby continuum measure, C4170. We connected the size of the Balmer jump to the Hγ line-to-continuum ratio, and found a strong linear trend such that flares with larger Hγ line to continuum ratios have larger Balmer jumps. We suggest the use of these measures in future studies of flares to understand their properties in the context of our flare sample. These trends indicate that the white-light heating/cooling mechanism in the impulsive and gradual *phases* of flares changes, as flares become more dominated by Hydrogen Balmer emission in the decay phases, which has been suggested by several works such as Moffett & Bopp (1976) and Abdul-Aziz et al. (1995). Nonetheless, the majority (50 – 90%) of the wavelength-integrated blue+NUV emission in the peak and gradual phases is emitted in other (continuum) emission aside from the Balmer radiation. We attribute this continuum emission to a "blackbody" (or blackbody-like) source.

Most of the IF events have strikingly similar peak $\chi_{\rm flare}$ values of 1.6 – 1.8 over 3.5 orders of magnitude in flare peak amplitudes. They generally also have Hγ-line-to-continuum ratios of 15 – 25 and only 10 – 18% of the emission in the Balmer component at peak. The two IF exceptions show larger $\chi_{\rm flare,peak}(\sim 2.2 \pm (0.1 - 0.2))$ and larger Hγ to continuum ratios ($\sim$40 – 50), and a larger fraction of Hydrogen Balmer flux in the blue/NUV ($\sim$40%). A narrow range of peak flare properties suggests a common impulsive heating mechanism among M dwarf flares. Moreover, the slope of the blue continuum is relatively the same among these flares. We parameterize the slope with a blackbody function and the range of peak temperatures for the IF, HF, and GF events is between $T_{\rm BB} \sim 9000 - 14\,000$ K. When the blackbody component is observed, one usually observes Balmer continuum also. Therefore, their formation must be linked together, possibly from different (but related) heating mechanisms. The four flares with the smallest amount of Balmer continuum at peak relative to the total flux are the largest amplitude events: IF0, IF1, IF3, and IF4. As illustrated by IF5 and IF6 (the flares with $\chi_{\rm flare,peak} \sim 2.2$), the relative amount of one

continuum component compared to the other is indeed variable during flares, and this relative amount at peak determines the evolution of the flare as either impulsive (lots of blackbody), gradual (lots of Balmer continuum), or hybrid (both present, but generally more BaC). Also, the Balmer continuum does not always have a slow decay but is sometimes quite impulsive like the blackbody. This occurs typically with the hybrid flares, or for the impulsive flares that have large $\chi_{\rm flare,peak}$.

In the decay phase, the blackbody component exhibits a cooler temperature of $T_{\rm BB}\sim$8000 K. We find that the evolution follows the Balmer continuum flux beginning in the extended decay phase, and it is possible that a large contribution of this is from the Paschen continuum. Another continuum component is detected redward of Hβ that rises into the red. This is detected as a rising contribution during gradual phase emission, and may be responsible for the redder colors seen in broadband photometry during the gradual phases of flares in the past (e.g., Kunkel, 1970; Hawley et al., 2003). This "conundruum" flux that rises into the red zone is present in some flares at peak also, but the hotter (blackbody) component dominates the white-light continuum shape at peak emission in the blue and to a lesser extent in the red. The origin of the Conundruum is likely the Paschen recombination continuum or H^- recombination continuum from temperatures near 6000 K. In summary, we find three continuum components that are present and are important at different stages of the flare evolution: 1) BaC (most important in mid rise and decay); 2) "Blackbody" (most important at peak, but present with cooler temperatures in the rise phase and decay phase); and 3) Conundruum or Paschen continuum (can be present in all stages, but most important in late decay).

Detailed modeling would reveal how line blanketing from the forest of low flux level, low excitation energy metallic (Fe, Ti) lines in the blue-optical affects the continua shapes that we observe. We found that the total flux in the blue-optical zone of these lines in the high signal-to-noise continuum spectra is large but accounts for at most 10% of the total continuum. Higher spectral resolution data should be obtained for line blanketing continuum flare models that seek to understand the contributions to the Balmer continuum, blackbody continuum, and conundruum that we have observed.

We began with a simple phenomenological hot, blackbody model of the white-light

continuum (component #2 above) and then extended the modeling to include the effects of flux redistribution and wavelength dependent opacities, thereby relating the continuum in the impulsive/peak phase to that of a high-gravity hot star with the Balmer features in absorption. Using this "Castelli-Kurucz" representation of the continuum, more realistic areal coverages of the white-light can be obtained, which are about a factor of 1.5 – 2 larger than if one assumes a Planck intensity. The effective temperatures corresponding to the observed $T_{\rm BB}$ (above) are $T_{\rm eff}\sim$7700 – 9400 K, with the largest being $\sim$10 500 K during the MDSF2 peak. The effective temperatures have important implications for the heating flux necessary to balance the emission.

Indeed, the impulsive phase "blackbody" continuum component is not a featureless emission spectrum. The hot star modeling was motivated by the direct detection of an A-type star spectrum during the rise and peak phases of a secondary flare that occurred during the "Megaflare" decay (Chapter 6). Absorption signatures were detected in the wings of the Balmer lines in this flare and several other flares, and we showed how the formation of "hot-star" type absorption during flares affects the Balmer flux and time decrements. These analysis techniques can be applied to other flare data to understand absorption phenomena in data that don't have broad wavelength coverage or a robust flux calibration to measure continuum slopes.

Most flares do not show obvious absorption features in the Balmer continuum or Balmer lines, likely due to the large amount of (chromospheric) Hydrogen Balmer flux in *emission* that generates an effective veiling of the absorption. The veiling can lead to an anti-correlation in the apparent amount of Balmer emission and the amount of blackbody-like continuum, such that as the absorption becomes greater - either through a larger filling factor (areal coverage) or because of larger temperatures - the measured Balmer continuum estimated using a linear extrapolation from the blue-optical zone becomes less. We observe tentative evidence of a net Balmer continuum flux of $\sim$0 (Balmer continuum absorption=Balmer continuum emission) occuring in the rise and peak of IF4, a $|\Delta U| \sim 3$ magnitude event on EQ Peg A, but more observations of this magnitude or greater are clearly important for establishing the occurrence of Balmer continuum absorption during flares. We speculate that the intrinsic amount of (chromospheric) Balmer continuum at

peak is larger than that observed due to this veiling; indeed, it may be as high as three times larger than the measured amount, assuming that the hot, blackbody-like component is the only continuum source at $\lambda > 4000$Å and the CK models are correct by reproducing blackbody continuum flux distribution.

In general, however, we do not think that the blackbody is the only continuum source. Instead the continuum in the blue-optical is a sum of Paschen continuum, and several "hot-spots" that originate from high column mass and high temperature regions, similar to those that would be found in the atmospheres of ($\log g = 5$) F/A dwarfs. We modeled IF1 and IF3 as the sum of continuum components consisting of a combination of an RHD model (which includes backwarming and Paschen continuum) that give "conundruum" flux, and a series of phenomenological hot spot models giving the rise in the NUV and the anti-correlation effect. This type of phenomonological modeling is an attempt to account for the non-isothermality within each column mass of flare atmosphere and also the inhomogeneity/non-isothermality across a spatially resolved flare region. Unfortunately, significant degeneracies will exist for this type of modeling, until a self-consistent blackbody-like component can be produced self-consistently in RHD models.

For two flares that showed an apparent increase of ∼2500 K during their rise phases – IF3 and MDSF2 of IF1 – we modeled the general properties of the blue-continuum and NUV continuum successfully only for IF1. For the peak phase of the much larger flare, IF3, this modeling only reproduced the blue-optical and red shape and did not account for the continuing rise into the NUV, though we did not explore all possible parameters. Curiously, an optically thin, superhot ($T \sim 170\,000$ K) free-free+bound-free source can account for the NUV rise in this flare. Data further into the NUV, such as with HST, are crucial for constraining the correct continuum model at peak times; by characterizing the precise properties and time-evolution of the continuum peak wavelength and turnover at shorter wavelengths, we can understand 1) the amount of Balmer absorption as hot spot models predict different peaks in the NUV compared to featureless blackbody functions, 2) the amount of possible 10^5 K free-free contribution, and 3) the peak of the $T_{\rm BB}$∼8000 K blackbody component in the gradual phase.

We measured the speeds at which the blackbody flare area grows during the rise phase

of IF3 and the MDSF2 of IF1. A realistic determination of the areas from hot-star modeling allowed us to calculate these speeds. The speeds are large in the early and mid-rise phase, with $v_{\rm flare}$ $\sim$100 km s^{-1}, and decrease to $\sim$50km s^{-1} at the peak and $<$ 10km s^{-1}in the post-maximum phase. These speeds are strikingly similar to the speeds of the development of two-ribbon flares parallel and perpendicular to the neutral line on the Sun. Therefore, $v_{\rm flare}$ is a parameter that we can use to directly tie stellar white-light observations to the high-spatial resolution observations of white-light emission on the Sun. Moreover, we found a possible relation between the average speed and the average temperature of the blackbody component during the rise phase, with slower speeds producing hotter temperatures ($T_{\rm BB}\sim$14 000 $-$ 18 000 K) and more prominent Balmer absorption features. The heating in these flares may be similar to the heating process in Ellerman bombs on the Sun, whereby reconnection is thought to occur in low chromospheric/photospheric levels. The connection to Ellerman bombs and their (possible) formation at high densities and low heights has implications for the heating properties of M dwarf flares that show Balmer absorption signatures. However, we do not exclude the possibility that the secondary flare MDSF2 (which is classified as a gradual flare event) is a "megaflare-induced phenomenon" that has different heating properties than classical flares.

Comparing the speeds between flares allows one to start to understand the possible heating scenarios. We presented two extreme scenarios: the expansion of a single hot spot (Scenario 1, $v_{\rm flare} \sim c_s$) and the formation of several hot spots (Scenario 2, $v_{\rm flare} > c_s$). Insight into the detailed physics in these scenarios requires 3D modeling, but we can gain a generally understood by comparing the speed of the flare to the speed of sound at which a hot spot / "blackbody" is formed. The higher speeds (50 – 120 km s^{-1}) apparently produced a relatively cooler (yet still very hot) blackbody, $T_{\rm BB}\sim$10 000 $-$ 12 000 K and more chromospheric Balmer continuum in emission; these speeds were found in the fast, classical, large-amplitude flares IF9, IF3, and IF2. In the impulsive phase of IF3, we find evidence of Scenario 2-type speeds during the rise and peak followed by Scenario 1-type speeds during the initial decay. A low speed and high temperature were derived from MDSF2 whereas HF1 had a low speed and a lower temperature; therefore, there is a degeneracy for low speeds ($<$ 10 km s^{-1}) whereby HF1 may be representative of Scenario 2 (having multiple continuum

spikes) and MDSF2 may be representative of Scenario 1. MDSF2 is also consistent with a variation on Scenario 1, if the reconnection (beam) was triggered by a sound wave in the lower atmosphere. More time-resolved data in the impulsive phase are needed to understand how speeds relate to rise phase morphologies.

In addition to the time-decrement and absorption signatures in the wings, we also analyzed other aspects of the emission lines. The flux decrements were measured, indicating that for most flares the decrement becomes flat before the maximum continuum emission and returns to the quiescent value very slowly. The previous RHD models are in general agreement with the observed flux decrements, but our results suggest a more closer comparison is necessary. Our data are relatively unique in having simultaneous coverage of Hα (see also Worden et al., 1984; Fuhrmeister et al., 2011) at high time resolution. Future work is required to understand the Hα light curves, especially in comparison to solar data, such as from ISOON (e.g., Balasubramaniam et al., 2010). We find that in some flares the Hα/ Hγ decrement $<$1 but that this doesn't occur in all flares; the exceptions tend to be the lower amplitude gradual events. For the flares with relatively simple light curve morphology we find a short delay, $<$ 1 minute, between the Hγ line emission peak and the continuum emission peak. Previous observations indicate that there is a relatively large time delay between the peak continuum emission and the peak line emission; we find that a large time delay occurs in flares that have a complex morphology, such as those with secondary continuum spikes or stalls that occur not long after the primary continuum enhancement. The large delay in these flares may be the result of two spatially distinct flare regions producing approximately equal amounts of Balmer line emission. Finally, we measured the line widths of Hδ, Hγ, and Hβ. The line widths in low-resolution data are difficult to interpret, but we find a suggestive relation between the width of the line at line flux maximum and the ratio of the Balmer continuum flux to the Hγ flux. For the time-resolved rise phase of IF3, the time at which the decrement becomes flat, the time at which the maximum line broadening occurs, and the time at which maximum time-derivative of the Balmer continuum flux occurs are about coincident. This relation is naively expected if the broadening, decrement, and rate of change of the Balmer continuum are connected through increased electron densities via the Stark effect; more data in the rise phase and modeling the higher

order Balmer line broadening in RHD simulations are required. The fluxes in several He I lines and the 5170Å feature (Fe II and/or Mg Ib) is calculated, should be analyzed and modeled in a future paper.

The Balmer jump has not been detected in these low-resolution spectra (although we note that several instances in different flares show suggestive features near $\lambda \sim 3646$Å). It remains an open question what causes the large amount of apparent blending (pseudo-continuum) at these wavelengths, as the Balmer jump is not even detected in high spectral resolution, $R \sim 40\,000$ spectra (Schmitt et al., 2008; Fuhrmeister et al., 2008). We raise the question, *what is the "Balmer continuum" that we observe in our low-resolution spectra?*. We suggest that the amount that we measure may be affected by the broadening of higher order Balmer line wings and the broadening of the continuum edge. More high spectral resolution, high time resolution data are needed near $\lambda = 3646$Å (while also covering some continuum regions at $\lambda \sim 4000 - 4200$Å in order to characterize the blackbody component). If supplemented by modeling the Stark broadening in the higher order lines like that done in Donati-Falchi et al. (1985) for solar flares, we may be able to understand the detailed pseudo-continuum properties from $\lambda = 3646 - 3920$Å.

The emission at flare peak cannot be explained by simply scaling up small flares to get large flares. Instead, flares show a range of blackbody temperatures and BaC contribution at peak. Because the flares show different relative amounts of BaC3615 and C4170 at peak, the flare sample as a whole are not scaled versions of one another, thereby implying a difference in heating mechanisms between IF, HF, and GF events. Within the IF sequence alone, the flares appear to be scaled versions of one another in some ways but not others (see below). For the blackbody component, we found a general relationship between the peak U-band amplitude and area of the blackbody between flares that showed narrow range of $T_{\rm BB}$ at peak. On the other hand, we found intra flare temperature variations of $2000 - 2500$ K during the impulsive phase and inter flare temperature variations ranging from 9000 K (GF1) to ∼14000 K of IF2 to ∼18000 K (MDSF2[1] of IF1). Therefore, temperature also affects the amount of radiation at peak, and NUV observations are needed to quantify

[1]But see Appendix F.1.3 where the inferred peak temperature of ∼18 000 K is corrected to a value of ∼15 000 K.

the temperature differences. As most flares show the hot blackbody emission at peak, constraining the properties and observable parameters (among a variety of flares) that are most correlated with the differences in this blackbody component can give important insight into the formation of this emission. Of the many parameters that could give rise to temperature variations that we observe, we suggest that the speed of the flare areal increase is an important parameter. However, the speed is difficult to interpret in some cases because there is a degeneracy between the areal expansion of a single heated region and the areal expansion of a larger flare structure (e.g., two ribbon) consisting of many individually heated regions.

We have found that within the IF events, there are approximate scaling relations between IF2, IF3, IF7, IF8, and IF9 – the "fast-5". We have shown several ways that IF3 and IF9 have scaled Balmer components (via the time-decrement, see also He I lines in appendix). However, the C4170 components appear to differ and do not follow a scaled up relation in their time evolution, suggesting that the C4170 is formed differently between different flares. We intend to investigate the ratio of $t_{1/2,C4170}$ vs. $I_{f,C4710}$ among a large sample of flares observed with high time cadence at C4170 with ULTRACAM (Kowalski et al. 2012, in prep). However, the IF flares at the beginning of the gradual decay phase do show more ordering in log-log relations and may indeed be scaled versions by this time in the flare due to the fast decay of the blackbody. Further evidence that gradual phase emission follows a "scaled-up" relation were deduced from a qualitative analysis of the fine spectral features and continuum shapes spanning the decay phase of IF1 (largest flare), IF7 (medium amplitude flare), and GF5 (the smallest amplitude flare).

Because the IF, HF, and GF events are not scaled up versions of one another, we question whether the BaC originates from the same atmospheric parameters in these types of flares. In other words, do the density, temperature and radiation field that give rise to the BaC in the F11 model adequately describe all flares? Using the contribution functions for the Balmer continuum we have begun to investigate the detailed formation differences in different models of flare atmospheres. In this work, we considered the hot spot atmospheres and nonthermal electron beam heated atmospheres as separate, non-interacting flare regions. In future work, we will rigorously examine if *induced* recombination from an underlying hot

spot can affect the Balmer continuum originating from the chromosphere. If the hot spot is sufficiently hot – hotter than the phenomenological models in this thesis so that the Rayleigh-Jeans criterion applies to the flux at $\lambda = 3600$Å – then lasering may contribute to the overall spectral shape observed at the peak times of flares.

We examined the scaling relationship between two flares in detail – HF1 and IF2 on YZ CMi – and concluded that indeed all peak phases do not follow a simple scaling relation, but instead show different temperatures of the blackbody in addition to different peak amplitudes. Smaller amplitudes typically result in more BaC relative to the blackbody and also a longer time evolution – but not always (see Figure 6.8). NUV observations would again be powerful for understanding the temperature differences. The light curve morphology in broad-band photometry is therefore complicated as it represents a combination of temperature and areal coverage of both the blackbody and Balmer continuum emission components. In addition, we speculate that the flare evolution (and hence light curve) is related to the speed at which the areal coverage spreads over the surface and how a flare "arcade" is sequentially ignited. Single large peaks may result from closely spaced and/or quickly ignited flare regions and multiple peaks may be the result of flare areas that are ignited slowly and/or over greater distances. At any given time assuming all other parameters being equal (e.g., heating rate), the total emitting area is smaller for the latter case, since the blackbody (C4170) decays quickly. The blackbody temperature at peak times may be related to the physics of these two scenarios, but understanding the detailed physics of these two scenarios requires 3D modeling of the radiation, dynamics, and reconnection evolution.

The blackbody component has not been reproduced self-consistently using RHD models. However, the models do show a Balmer continuum in emission that matches the gradual phase observations *after a blue-optical blackbody contribution has been subtracted*, whereas the total flare flux in the Balmer continuum in the impulsive phase generally matches the shape of the blue-optical blackbody. The surface flux ($> 2 \times 10^{11}$ ergs cm^{-2} s^{-1}) needed for the observed blackbody emission component and recent high spatial resolution observations of solar flares motivated us to explore larger heating fluxes than employed in previous RHD simulations. To this end, we simulated a F12 solar-type non-thermal electron beam heating a high-gravity cool dwarf atmosphere. The impulsive heating in the simulation was

executed for a short burst, with a gradual phase. The time-evolution of this burst will form a building block to which to sequentially add other fundamental bursts in a "1.5D" simulation. However, the F12 model white-light continuum features a strong Balmer and Paschen continuum and has $\chi_{\rm flare,peak}$ $\sim$6, larger than any of the observed $\chi_{\rm flare,peak}$ values in our survey (< 4.5). We found more heating in the photosphere than in the previous F11 model by an amount of $\Delta T \sim$800 K; as in the F11, the heating at high column mass was primarily from NUV backwarming radiation. More energy is needed in the lower atmosphere at high column mass (≥ 1 g / cm^2) in the RHD models in order to produce a hotter, denser region that could give rise to the "A-star" (blackbody-like) continuum component. We plan to run even higher beam fluxes. Preliminary results from an F13 simulation show much more drastic atmospheric dynamics and ionization evolution. We also plan to simulate the heating from protons, which are thought to be able to penetrate to higher column mass. We note that the detailed cooling processes in our F12 simulation did not produce dense, fast, and hot condensations like those in previous (less-detailed) gas-dynamic simulations of an F12 M dwarf flare (Livshits et al., 1981).

The F12 model of the gradual phase indicated that the amount of Balmer continuum responds quickly to the initiation and termination of beam heating, implying that the persistent Balmer continuum that we observe in the decay phase of flares probably requires continued particle acceleration and heating after the impulsive phase. Radio observations of gyrosynchrotron emission during the gradual phase of dMe flares suggests that particle acceleration indeed persists after the impulsive phase of the white light (van den Oord et al., 1996; Osten et al., 2005), and the radio-optical correlation should be investigated in detail. The persistence of the Balmer continuum has important implications for 3D models of reconnection and flare heating. We also used the models to inform our understanding of the fast rise and decay phases during the impulsive phase. The models show symmetric exponential rise and decay patterns with time constants of < 0.5 seconds. The observation timescales last $2-3$ orders of magnitude longer in the impulsive phase, especially in the fast decay phase. The extended decay phase timescales of continuum emission (minutes to hours) such as those observed in IF1 are certainly not produced. Therefore, in order for there to be a comparable amount of (Balmer) continuum emission in the gradual phase relative

to the amount at peak, there must be sustained heating (e.g., by nonthermal particles). Adding together individual "bursts" of beam heating models in an avalanche-type scenario, with the speeds that we derived from the areal calculations, will constitute future "1.5D" modeling efforts. The time-evolution of each burst will be modeled more accurately to include important aspects of reconnection rates, such as those studied in Martens & Kuin (1989). When we are able to reproduce the impulsive phase continuum emission, we will then proceed to modeling the gradual phase continuum properties, including the origin of the $T_{\rm BB}\sim$8000 K component and the Conundruum flux at redder wavelengths.

We speculate that the origin and transient nature of the blackbody radiation may be due to a thermal regulation process, before a temperature threshold is reached in the deep atmosphere prior to a runaway heating whereby material heats to much higher temperatures and much smaller densities. This same principle is responsible for the Balmer continuum formation: a flare chromosphere at 7000 – 10 000 K is produced at log $\rm m_c/(1g\ cm^{-2})\sim-2$, in a region where the material was previously at lower temperatures but is heated by the nonthermal electron beam during the flare. Chromospheric Balmer continuum is emitted from this region as long as the cooling it provides can balance the electron beam heating. However, once the heating excedes the BaC cooling threshold, the material heats up quickly to the next temperature plateau where LyC, He II, and primarily optically thin cooling can maintain energy balance. The observed Neupert relationship between Ca II K and C4170 (the blackbody) may be indicative of such an evaporative process taking place in the photosphere, if we can connect the formation of Ca II K emission to the evaporated plasma through, e.g., radiative backwarming, condensations (Abbett & Hawley, 1999), or heat conduction channels from the corona. An in-depth analysis of the contribution function of Ca II K remains to be understood.

Other transient astrophysical phenomena across the universe can be compared to dMe flare processes, and we plan to explore these connections in a future paper. Here, we briefly note several interesting similarities to gamma ray bursts and accretion phenomena. Gamma-ray burst (GRB) light curves have been divided into two classes based on the duration of the hard X-ray light curves: Class I GRB's with 2 to several hundred second durations and Class II GRB's with $<$ 2 second durations (Kouveliotou et al., 1993). Kouveliotou et al.

(1993) further found that the Class II GRB's exhibited harder spectral slopes in the X-rays. Similarly, we found that *impulsive* flares have different timescales and spectral slopes (given by $\chi_{\rm flare}$) compared to *gradual* flares. Hurley et al. (2005) proposed that a Class II GRB originated from magnetar flare (MF). The magnetar flare may be a subclass called soft gamma ray repeaters (SGRs) that occur relatively close to the Milky Way and account for only a few percent of the short/hard GRB's (Palmer et al., 2005); the current leading model is the merging of two compact objects, one of which is a neutron star (Blinnikov et al., 1984; Nakar, 2007). Interestingly though, the impulsive phase of a MF has been fit well with a blackbody function. In contrast to flare impulsive phase emission, the blackbody was found to have a much higher temperature by about 2×10^5. Seeing the spike or impulsive phase in the light curve during times of prominent optically thick (blackbody or blackbody-like) emission is a similarity between dMe flares and magnetar flares and implies a common cooling (and heating?) process during the most luminous events in the solar neighborhood and the most luminous events in the universe.

The second astrophysical setting in which we find similarities to dMe flares is accretion, such as during T Tauri accretion and dwarf nova accretion. The Balmer jump is a common diagnostic in T Tauri spectra (e.g., Valenti et al., 1993; Herczeg & Hillenbrand, 2008). In fact, some T Tauri spectra show small Balmer jump ratios that are rather similar to the $\chi_{\rm flare}$ values for flare spectra. Optical veiling from continua is often seen at $\lambda > 4000$Å, which can inform our understanding of the "blackbody" continuum in flare spectra. Therefore, the physics of accretion models for T Tauri spectra can be used to inform our understanding of white-light continuum. We also note that dwarf novae accretion events produce superposed Balmer line emission and Balmer line absorption features in their spectra, with most conspicuous absorption at times of maximum continuum emission that resembles an A or B type star (Hessman et al., 1984).

In summary, we need a three component white-light continuum in the RHD models of flare atmospheres. One component is a $T \sim 8\,000 - 10\,000$ K source at low column mass, $\log {\rm m_c}/(1{\rm g\ cm^{-2}}) \sim -2$, that emits a Balmer continuum in emission. These conditions are reproduced in general agreement with the observations in the current models with even a modest non-thermal electron beam flux. The relative contribution from the conundruum

flux rises in the gradual phase (like for the lower order Balmer lines), and the spectral shape is relatively consistent with the RHD model at Paschen continuum wavelengths. The "blackbody" component remains unexplained, but phenomenological hot-spot modeling indicates the required temperatures are near $T \sim 10\,000 - 20\,000$ K at higher column mass, log $m_c/(1g\ cm^{-2})\sim 0.5$. When both components can be reproduced with a self-consistent heating model, we can then begin to model the lines and continuum simultaneously in order to understand the total flare emission observed in different relative amounts between different types of flare morphologies (IF, HF, and GF events) and over the different phases of each type of flare.

We conclude with two figures, Figure 9.1 and Figure 9.2. In Figure 9.1, we show a compilation of representative model continuum spectra explored in this dissertation, including the RHD F12 spectrum from RADYN at $t = 4.8$ seconds, a Planck function with $T_{\rm BB}$= 10 000 K, the HS1 static model from RH, a model hot star ($\log g = 5$) spectrum with $T_{\rm eff}$= 9500 K, and a ff+bf spectrum from an optically thin Hydrogen slab with $T_e = 170\,000$ K. Spectral observations from $\lambda = 1500 - 3400$Å would constrain the emission mechanisms and total white-light continuum energy. We have begun a ground-based campaign (in collaboration with B. Brown, UW-Madison) using the RSS spectrograph on the South African Large Telescope to characterize the flare emission from $\lambda \sim 3100 - 3400$Å on short timescales. In January 2012, we obtained spectra from SALT and photometry with ULTRACAM/WHT (in collaboration with M. Mathioudakis, Queen's University, Belfast) with full time-coverage of a megaflare on YZ CMi (Kowalski et al. 2012, in prep).

In Figure 9.2, we show the u-band light curve of IF3 interpolated and averaged over a 1 minute cadence. This high energy flare represents a classical flare light curve with a fast rise and exponential decay. In the figure, we label each phase of the light curve with the continuum and line properties derived in this dissertation. From the spatial evolution of this flare, we relate each phase to terminology used to describe the development of two-ribbon flares on the Sun. This figure provides a framework for understanding the detailed physics of heating and cooling processes in stellar atmospheres as they relate to the total white-light brightness evolution during flares.

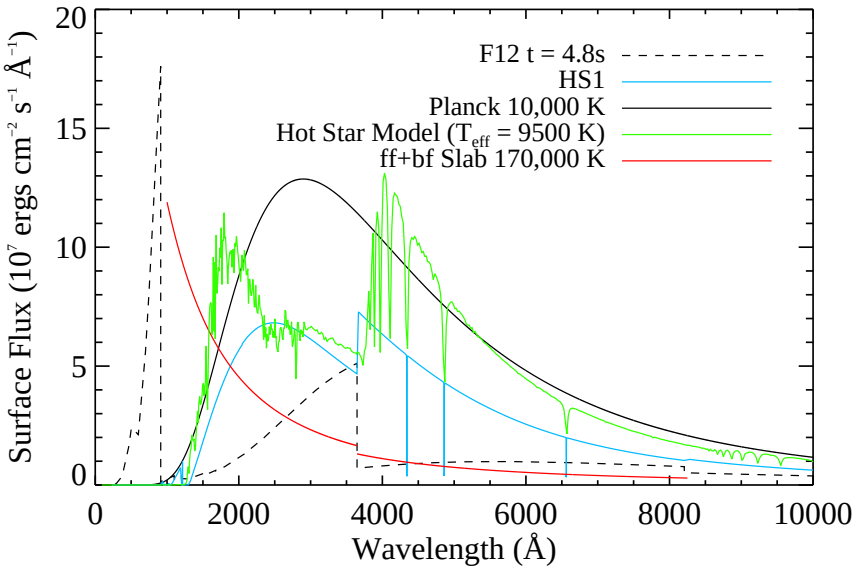

Figure 9.1 The surface fluxes of representative model spectra explored in this dissertation.

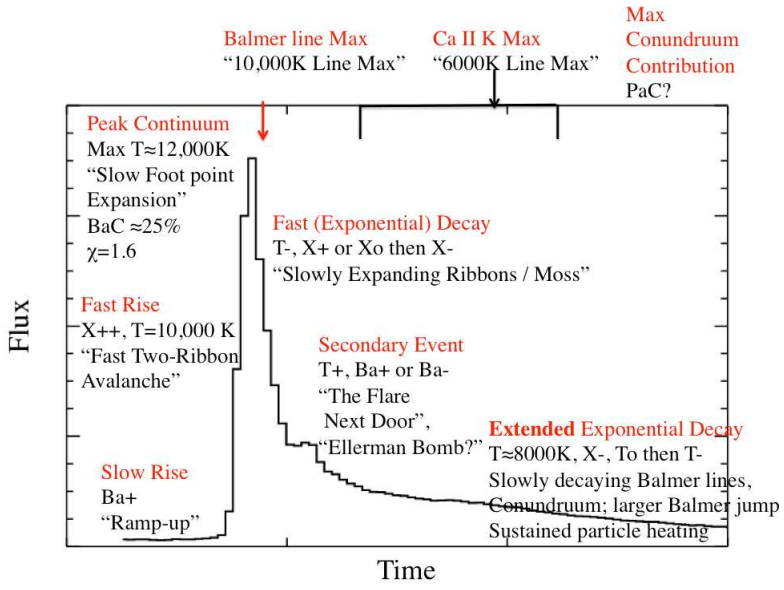

Figure 9.2 The u-band light curve of IF3 smoothed to 1 minute. Phases of the light curve are labeled according to continuum and line properties. The solar analogy is given in quotation marks. T refers to $T_{\rm BB}$, X refers to $X_{\rm BB}$. $+$ indicates an increase, $-$ indicates a decrease, o indicates a constant level.

BIBLIOGRAPHY

Abbett, W. P., & Hawley, S. L. 1999, ApJ, 521, 906

Abdul-Aziz, H., et al. 1995, A&AS, 114, 509

Abranin, E. P., et al. 1997, Ap&SS, 257, 131

Aller, L. H. 1965, American Journal of Physics, 33, 353

Allred, J. C., Hawley, S. L., Abbett, W. P., & Carlsson, M. 2005, ApJ, 630, 573

Allred, J. C., Hawley, S. L., Abbett, W. P., & Carlsson, M. 2006, ApJ, 644, 484

Andrews, A. D., Corvan, P., Hardy, B., Johnston, P., Johnston, W., & Perrott, J. 1969, Information Bulletin on Variable Stars, 325, 1

Aschwanden, M. J. 2011, Sol. Phys., 274, 119

Balasubramaniam, K. S., et al. 2010, ApJ, 723, 587

Baranovsky, E. A., & Kurochka, E. V. 1997, Astronomical and Astrophysical Transactions, 13, 173

Berger, T. E., de Pontieu, B., Fletcher, L., Schrijver, C. J., Tarbell, T. D., & Title, A. M. 1999, Sol. Phys., 190, 409

Berlicki, A., Heinzel, P., & Avrett, E. H. 2010, Mem. Soc. Astron. Italiana, 81, 646

Berlicki, A., Schmieder, B., Vilmer, N., Aulanier, G., & Del Zanna, G. 2004, A&A, 423, 1119

Blinnikov, S. I., Novikov, I. D., Perevodchikova, T. V., & Polnarev, A. G. 1984, Pis ma Astronomicheskii Zhurnal, 10, 422

Bohlin, R. C. 2007, in Astronomical Society of the Pacific Conference Series, Vol. 364, The Future of Photometric, Spectrophotometric and Polarimetric Standardization, ed. C. Sterken, 315

Böhm-Vitense, E. 1989, Introduction to stellar astrophysics. Vol. 2. Stellar atmospheres.

Brown, J. C. 1971, Sol. Phys., 18, 489

Brown, J. C., Turkmani, R., Kontar, E. P., MacKinnon, A. L., & Vlahos, L. 2009, A&A, 508, 993

Bruzek, A. 1972, Sol. Phys., 26, 94

Butler, C. J., Rodono, M., & Foing, B. H. 1988, A&A, 206, L1

Canfield, R. C., et al. 1993, ApJ, 411, 362

Canfield, R. C., Gunkler, T. A., & Ricchiazzi, P. J. 1984, ApJ, 282, 296

Carlsson, M. 1998, in Lecture Notes in Physics, Berlin Springer Verlag, Vol. 507, Space Solar Physics: Theoretical and Observational Issues in the Context of the SOHO Mission, ed. J. C. Vial, K. Bocchialini, & P. Boumier, 163

Carlsson, M., & Leenaarts, J. 2012, A&A, 539, A39

Carlsson, M., & Stein, R. F. 1994, in Chromospheric Dynamics, ed. Carlsson, M. (Oslo: University), 47

Carlsson, M., & Stein, R. F. 1995, ApJ, 440, L29

Carlsson, M., & Stein, R. F. 1997, ApJ, 481, 500

Carlsson, M., & Stein, R. F. 2002, ApJ, 572, 626

Carrington, R. C. 1859, MNRAS, 20, 13

Castelli, F., & Kurucz, R. L. 2004, ArXiv Astrophysics e-prints

Charbonneau, P., McIntosh, S. W., Liu, H.-L., & Bogdan, T. J. 2001, Sol. Phys., 203, 321

Christian, D. J., Mathioudakis, M., Jevremović, D., Dupuis, J., Vennes, S., & Kawka, A. 2003, ApJ, 593, L105

Connolly, A. J., Szalay, A. S., Bershady, M. A., Kinney, A. L., & Calzetti, D. 1995, AJ, 110, 1071

Covey, K. R., et al. 2008, AJ, 136, 1778

Cox, D. P., & Tucker, W. H. 1969, ApJ, 157, 1157

Cram, L. E., & Woods, D. T. 1982, ApJ, 257, 269

Crespo-Chacón, I., Montes, D., García-Alvarez, D., Fernández-Figueroa, M. J., López-Santiago, J., & Foing, B. H. 2006, A&A, 452, 987

Cully, S. L., Fisher, G. H., Abbott, M. J., & Siegmund, O. H. W. 1994, ApJ, 435, 449

Dal, H. A., & Evren, S. 2010, AJ, 140, 483

de Jager, C., et al. 1989, A&A, 211, 157

de La Beaujardiere, J.-F., Canfield, R. C., & Leka, K. D. 1993, ApJ, 411, 378

Dennis, B. R., & Zarro, D. M. 1993, Sol. Phys., 146, 177

Dhillon, V. S., et al. 2007, MNRAS, 378, 825

Donati-Falchi, A., Falciani, R., & Smaldone, L. A. 1985, A&A, 152, 165

Dorfi, E. A., & Drury, L. O. 1987, Journal of Computational Physics, 69, 175

Doyle, J. G., Butler, C. J., Bryne, P. B., & van den Oord, G. H. J. 1988, A&A, 193, 229

Drake, S. A., & Ulrich, R. K. 1980, ApJS, 42, 351

Eason, E. L. E., Giampapa, M. S., Radick, R. R., Worden, S. P., & Hege, E. K. 1992, AJ, 104, 1161

Ellerman, F. 1917, ApJ, 46, 298

Emslie, A. G. 1978, ApJ, 224, 241

Emslie, A. G., Dennis, B. R., Holman, G. D., & Hudson, H. S. 2005, Journal of Geophysical Research (Space Physics), 110, 11103

Fang, C., Tang, Y. H., Xu, Z., Ding, M. D., & Chen, P. F. 2006, ApJ, 643, 1325

Filippenko, A. V. 1982, PASP, 94, 715

Fisher, G. H., Bercik, D. J., Welsch, B. T., & Hudson, H. S. 2012, Sol. Phys., 277, 59

Fisher, G. H., Canfield, R. C., & McClymont, A. N. 1985, ApJ, 289, 425

Fletcher, L., et al. 2011, Space Sci. Rev., 159, 19

Fletcher, L., Hannah, I. G., Hudson, H. S., & Metcalf, T. R. 2007, ApJ, 656, 1187

Fletcher, L., & Hudson, H. 2001, Sol. Phys., 204, 69

Fletcher, L., & Hudson, H. S. 2008, ApJ, 675, 1645

Fletcher, L., Pollock, J. A., & Potts, H. E. 2004, Sol. Phys., 222, 279

Fuhrmeister, B., Lalitha, S., Poppenhaeger, K., Rudolf, N., Liefke, C., Reiners, A., Schmitt, J. H. M. M., & Ness, J. . 2011, ArXiv e-prints

Fuhrmeister, B., Liefke, C., Schmitt, J. H. M. M., & Reiners, A. 2008, A&A, 487, 293

Fuhrmeister, B., Schmitt, J. H. M. M., & Hauschildt, P. H. 2010, A&A, 511, A83

García–Alvarez, D., Jevremović, D., Doyle, J. G., & Butler, C. J. 2002, A&A, 383, 548

Georgoulis, M. K., Rust, D. M., Bernasconi, P. N., & Schmieder, B. 2002, ApJ, 575, 506

Gershberg, R. E. 1972, Ap&SS, 19, 75

Giampapa, M. S. 1983, in Astrophysics and Space Science Library, Vol. 102, IAU Colloq. 71: Activity in Red-Dwarf Stars, ed. P. B. Byrne & M. Rodono, 223

Gizis, J. E., Reid, I. N., & Hawley, S. L. 2002, AJ, 123, 3356

Guedel, M., Benz, A. O., Schmitt, J. H. M. M., & Skinner, S. L. 1996, ApJ, 471, 1002

Gurzadian, G. A. 1988, ApJ, 332, 183

Hartigan, P., Hartmann, L., Kenyon, S., Hewett, R., & Stauffer, J. 1989, ApJS, 70, 899

Hawley, S. L., et al. 2003, ApJ, 597, 535

Hawley, S. L., & Fisher, G. H. 1992, ApJS, 78, 565

Hawley, S. L., & Fisher, G. H. 1994, ApJ, 426, 387

Hawley, S. L., et al. 1995, ApJ, 453, 464

Hawley, S. L., & Pettersen, B. R. 1991, ApJ, 378, 725

Hawley, S. L., Walkowicz, L. M., Allred, J. C., & Valenti, J. A. 2007, PASP, 119, 67

Herczeg, G. J., & Hillenbrand, L. A. 2008, ApJ, 681, 594

Hertzsprung, E. 1924, Bull. Astron. Inst. Netherlands, 2, 87

Hessman, F. V., & Guenther, E. W. 1997, A&A, 321, 497

Hessman, F. V., Robinson, E. L., Nather, R. E., & Zhang, E.-H. 1984, ApJ, 286, 747

Hiei, E. 1982, Sol. Phys., 80, 113

Hilton, E. J., Hawley, S. L., Kowalski, A. F., & Holtzman, J. 2011, in Astronomical Society of the Pacific Conference Series, Vol. 448, Astronomical Society of the Pacific Conference Series, ed. C. Johns-Krull, M. K. Browning, & A. A. West, 197

Hilton, E. J., West, A. A., Hawley, S. L., & Kowalski, A. F. 2010, AJ, 140, 1402

Holman, G. D. 2012, ApJ, 745, 52

Holman, G. D., Sui, L., Schwartz, R. A., & Emslie, A. G. 2003, ApJ, 595, L97

Holtzman, J. A., Harrison, T. E., & Coughlin, J. L. 2010, Advances in Astronomy, 2010

Houdebine, E. R. 1992, Irish Astronomical Journal, 20, 213

Hudson, H., Fletcher, L., & Krucker, S. 2010, ArXiv e-prints

Hudson, H. S., Acton, L. W., Hirayama, T., & Uchida, Y. 1992, PASJ, 44, L77

Hudson, H. S., Wolfson, C. J., & Metcalf, T. R. 2006, Sol. Phys., 234, 79

Hurford, G. J., Krucker, S., Lin, R. P., Schwartz, R. A., Share, G. H., & Smith, D. M. 2006, ApJ, 644, L93

Hurley, K., et al. 2005, Nature, 434, 1098

Inglis, A. R., & Dennis, B. R. 2012, ApJ, 748, 139

Irwin, J., Berta, Z. K., Burke, C. J., Charbonneau, D., Nutzman, P., West, A. A., & Falco, E. E. 2011, ApJ, 727, 56

Isobe, H., et al. 2007, PASJ, 59, 807

Jefferies, J. T., & Orrall, F. Q. 1961a, ApJ, 133, 946

Jefferies, J. T., & Orrall, F. Q. 1961b, ApJ, 134, 747

Jess, D. B., Mathioudakis, M., Browning, P. K., Crockett, P. J., & Keenan, F. P. 2010a, ApJ, 712, L111

Jess, D. B., Mathioudakis, M., Christian, D. J., Keenan, F. P., Ryans, R. S. I., & Crockett, P. J. 2010b, Sol. Phys., 261, 363

Jess, D. B., Mathioudakis, M., Crockett, P. J., & Keenan, F. P. 2008, ApJ, 688, L119

Jevremovic, D., Butler, C. J., Drake, S. A., O'Donoghue, D., & van Wyk, F. 1998, A&A, 338, 1057

Johns-Krull, C. M., Hawley, S. L., Basri, G., & Valenti, J. A. 1997, ApJS, 112, 221

Johns-Krull, C. M., & Valenti, J. A. 1996, ApJ, 459, L95

Johnson, H. L. 1966, ARA&A, 4, 193

Kahler, S., et al. 1982, ApJ, 252, 239

Katsova, M. M. 1990, Soviet Ast., 34, 614

Katsova, M. M., Boiko, A. Y., & Livshits, M. A. 1997, A&A, 321, 549

Katsova, M. M., Livshits, M. A., Butler, C. J., & Doyle, J. G. 1991, MNRAS, 250, 402

Kašparová, J., Varady, M., Heinzel, P., Karlický, M., & Moravec, Z. 2009, A&A, 499, 923

Keys, P. H., Jess, D. B., Mathioudakis, M., & Keenan, F. P. 2011, A&A, 529, A127

Kosovichev, A. G., & Zharkova, V. V. 2001, ApJ, 550, L105

Kouveliotou, C., Meegan, C. A., Fishman, G. J., Bhat, N. P., Briggs, M. S., Koshut, T. M., Paciesas, W. S., & Pendleton, G. N. 1993, ApJ, 413, L101

Koval, A. N., & Severny, A. B. 1970, Sol. Phys., 11, 276

Kowalski, A. F., Hawley, S. L., Holtzman, J. A., Wisniewski, J. P., & Hilton, E. J. 2010, ApJ, 714, L98

Kowalski, A. F., Hawley, S. L., Holtzman, J. A., Wisniewski, J. P., & Hilton, E. J. 2011a, in Choudhary, D.P., Strassmeier, K.G. (eds.) Physics of Sun and Star Spots, 6, 261

Kowalski, A. F., Hawley, S. L., Holtzman, J. A., Wisniewski, J. P., & Hilton, E. J. 2012, Sol. Phys., 277, 21

Kowalski, A. F., Mathioudakis, M., Hawley, S. L., Hilton, E. J., Dhillon, V. S., Marsh, T. R., & Copperwheat, C. M. 2011b, ArXiv e-prints

Kretzschmar, M. 2011, A&A, 530, A84

Krucker, S., Hudson, H. S., Jeffrey, N. L. S., Battaglia, M., Kontar, E. P., Benz, A. O., Csillaghy, A., & Lin, R. P. 2011, ApJ, 739, 96

Kunkel, W. E. 1969, Nature, 222, 1129

Kunkel, W. E. 1970, ApJ, 161, 503

Kurochka, L. N., & Maslennikova, L. B. 1970, Sol. Phys., 11, 33

Kurokawa, H., Kawaguchi, I., Funakoshi, Y., & Nakai, Y. 1982, Sol. Phys., 79, 77

Lacy, C. H., Moffett, T. J., & Evans, D. S. 1976, ApJS, 30, 85

Leka, K. D., Canfield, R. C., McClymont, A. N., de La Beaujardiere, J.-F., Fan, Y., & Tang, F. 1993, ApJ, 411, 370

Linsky, J. L., Glackin, D. L., Chapman, R. D., Neupert, W. M., & Thomas, R. J. 1976, ApJ, 203, 509

Linton, M. G., & Longcope, D. W. 2006, ApJ, 642, 1177

Lites, B. W., Meidig, D. F., & Trujillo Bueno, J. 1986, in The lower atmosphere of solar flares; Proceedings of the Solar Maximum Mission Symposium, Sunspot, NM, Aug. 20-24, 1985 (A87-26201 10-92). Sunspot, NM, National Solar Observatory, 1986, p. 101-116., ed. D. F. Neidig, 101

Liu, W., Petrosian, V., & Mariska, J. T. 2009, ApJ, 702, 1553

Livshits, M. A., Badalian, O. G., Kosovichev, A. G., & Katsova, M. M. 1981, Sol. Phys., 73, 269

Lovell, B. 1969, Nature, 222, 1126

Lu, E. T., & Hamilton, R. J. 1991, ApJ, 380, L89

Magain, P. 1986, A&A, 163, 135

Maíz Apellániz, J. 2006, AJ, 131, 1184

Martens, P. C. H., & Kuin, N. P. M. 1989, Sol. Phys., 122, 263

Mauas, P. J. D., & Gomez, D. O. 1997, ApJ, 483, 496

Maurya, R. A., & Ambastha, A. 2009, Sol. Phys., 258, 31

Metcalf, T. R., Alexander, D., Hudson, H. S., & Longcope, D. W. 2003, ApJ, 595, 483

Mihalas, D. 1970, Stellar atmospheres

Milligan, R. O., Chamberlin, P. C., Hudson, H. S., Woods, T. N., Mathioudakis, M., Fletcher, L., Kowalski, A. F., & Keenan, F. P. 2012, ApJ, 748, L14

Mochnacki, S. W., & Zirin, H. 1980, ApJ, 239, L27

Moffett, T. J. 1974, ApJS, 29, 1

Moffett, T. J., & Bopp, B. W. 1976, ApJS, 31, 61

Moore, R. L., Sterling, A. C., Hudson, H. S., & Lemen, J. R. 2001, ApJ, 552, 833

Mullan, D. J. 1990, ApJ, 361, 215

Mullan, D. J., Mathioudakis, M., Bloomfield, D. S., & Christian, D. J. 2006, ApJS, 164, 173

Nakar, E. 2007, Advances in Space Research, 40, 1224

Nakariakov, V. M., & Zimovets, I. V. 2011, ApJ, 730, L27

Neidig, D. F. 1983, Sol. Phys., 85, 285

Neidig, D. F., Grosser, H., & Hrovat, M. 1994, Sol. Phys., 155, 199

Neidig, D. F., Kiplinger, A. L., Cohl, H. S., & Wiborg, P. H. 1993, ApJ, 406, 306

Neidig, D. F., Wiborg, P. H., & Gilliam, L. B. 1993, Sol. Phys., 144, 169

Neidig, D. F., & Wiborg, P. H., Jr. 1984, Sol. Phys., 92, 217

Nelson, G. J., Robinson, R. D., Slee, O. B., Ashley, M. C. B., Hyland, A. R., Tuohy, I. R., Nikoloff, I., & Vaughan, A. E. 1986, MNRAS, 220, 91

Neupert, W. M. 1968, ApJ, 153, L59

Nishizuka, N., Asai, A., Takasaki, H., Kurokawa, H., & Shibata, K. 2009, ApJ, 694, L74

Oke, J. B. 1990, AJ, 99, 1621

Orrall, F. Q., & Zirker, J. B. 1976, ApJ, 208, 618

Osten, R. A., et al. 2004, ApJS, 153, 317

Osten, R. A., et al. 2010, ApJ, 721, 785

Osten, R. A., Hawley, S. L., Allred, J., Johns-Krull, C. M., Brown, A., & Harper, G. M. 2006, ApJ, 647, 1349

Osten, R. A., Hawley, S. L., Allred, J. C., Johns-Krull, C. M., & Roark, C. 2005, ApJ, 621, 398

Osterbrock, D. E. 1977, ApJ, 215, 733

Palmer, D. M., et al. 2005, Nature, 434, 1107

Paulson, D. B., Allred, J. C., Anderson, R. B., Hawley, S. L., Cochran, W. D., & Yelda, S. 2006, PASP, 118, 227

Payne, T. E. W. 1993, Ph.D. thesis, New Mexico State Univ.

Pettersen, B. R., Coleman, L. A., & Evans, D. S. 1984, ApJS, 54, 375

Phillips, K. J. H., Bromage, G. E., Dufton, P. L., Keenan, F. P., & Kingston, A. E. 1988, MNRAS, 235, 573

Puetter, R. C., Smith, H. E., Willner, S. P., & Pipher, J. L. 1981, ApJ, 243, 345

Qiu, J., Ding, M. D., Wang, H., Denker, C., & Goode, P. R. 2000, ApJ, 544, L157

Qiu, J., Liu, W., Hill, N., & Kazachenko, M. 2010, ApJ, 725, 319

Raymond, J. C., Cox, D. P., & Smith, B. W. 1976, ApJ, 204, 290

2005, New light on dark stars : red dwarfs, low-mass stars, brown dwarfs, ed. Reid, I. N. & Hawley, S. L.

Reid, I. N., Hawley, S. L., & Gizis, J. E. 1995, AJ, 110, 1838

Ricchiazzi, P. J., & Canfield, R. C. 1983, ApJ, 272, 739

Robinson, R. D., Linsky, J. L., Woodgate, B. E., & Timothy, J. G. 2001, ApJ, 554, 368

Rodono, M., et al. 1984, in ESA Special Publication, Vol. 218, Fourth European IUE Conference, ed. E. Rolfe, 247

Rodono', M., et al. 1989, in Solar and Stellar Flares. Poster Papers, 53P

Rosner, R., Tucker, W. H., & Vaiana, G. S. 1978, ApJ, 220, 643

Rust, D. M., & Hegwer, F. 1975, Sol. Phys., 40, 141

Rutten, R. J. 2003, Radiative Transfer in Stellar Atmospheres

Saar, S. H., & Linsky, J. L. 1985, ApJ, 299, L47

Scharmer, G. B., & Carlsson, M. 1985, Journal of Computational Physics, 59, 56

Schmidt, S. J., Kowalski, A. F., Hawley, S. L., Hilton, E. J., Wisniewski, J. P., & Tofflemire, B. M. 2012, ApJ, 745, 14

Schmitt, J. H. M. M., Reale, F., Liefke, C., Wolter, U., Fuhrmeister, B., Reiners, A., & Peres, G. 2008, A&A, 481, 799

Schrijver, C. J., Hudson, H. S., Murphy, R. J., Share, G. H., & Tarbell, T. D. 2006, ApJ, 650, 1184

Severny, A. B. 1968, in Mass Motions in Solar Flares and Related Phenomena, ed. Oehman, Y. (Stockholm: Almqvist and Wiksell), 71

Severnyi, A. B., Steshenko, N. P., & Khokhlova, V. L. 1960, Soviet Ast., 4, 19

Share, G. H., Murphy, R. J., Smith, D. M., Schwartz, R. A., & Lin, R. P. 2004, ApJ, 615, L169

Simnett, G. M., & Strong, K. T. 1984, ApJ, 284, 839

Sutton, K. 1978, J. Quant. Spec. Radiat. Transf., 20, 333

Tofflemire, B. M., Wisniewski, J. P., Kowalski, A. F., Schmidt, S. J., Kundurthy, P., Hilton, E. J., Holtzman, J. A., & Hawley, S. L. 2012, AJ, 143, 12

Uitenbroek, H. 2001, ApJ, 557, 389

Uitenbroek, H., & Criscuoli, S. 2011, ApJ, 736, 69

Štepán, J. Å., Kašparová, J., Karlický, M., & Heinzel, P. 2007, A&A, 472, L55

Švestka, Z. 1972, Sol. Phys., 24, 154

Valenti, J. A., Basri, G., & Johns, C. M. 1993, AJ, 106, 2024

van den Oord, G. H. J. 1988, A&A, 207, 101

van den Oord, G. H. J., et al. 1996, A&A, 310, 908

Wang, L. 2009, ApJ, 694, 247

Wang, L., Fang, C., & Ming–DeDing. 2007, , 7, 721

Wisniewski, J. P., Clampin, M., Grady, C. A., Ardila, D. R., Ford, H. C., Golimowski, D. A., Illingworth, G. D., & Krist, J. E. 2008, ApJ, 682, 548

Woodgate, B. E., Robinson, R. D., Carpenter, K. G., Maran, S. P., & Shore, S. N. 1992, ApJ, 397, L95

Woods, T. N., et al. 2004, Geophys. Res. Lett., 31, 10802

Worden, S. P., Schneeberger, T. J., Giampapa, M. S., Deluca, E. E., & Cram, L. E. 1984, ApJ, 276, 270

Zharkova, V. V., & Zharkov, S. I. 2007, ApJ, 664, 573

Zhilyaev, B. E., et al. 2007, A&A, 465, 235

Zhou, A. H., Li, J. P., & Wang, X. D. 2011, ApJ, 727, 42

Appendix A

DATA REDUCTION

In this Appendix, we describe in detail the procedure for data reduction and flux calibration.

A single fixed extraction aperture was used for all spectra in one night. The width was calculated as $\pm 2.25\times$ the median seeing in the night (the seeing was estimated at every spectrum using an automatic routine). As there were as many as 2000 spectra obtained per night, we verified by eye that the trace worked on every $\sim$25th image. As the spectrum of an M dwarf varies in peak counts by a factor of 10 from 3800Å to 4800Å, we extracted the counts using a variance weighting, which we found has much higher signal to noise than a unweighted aperture for very large extraction widths. The variance weighting was robust for extremely large apertures, but the larger the aperture, the larger chance for including cosmic rays. The DIS blue has an asymmetric, low-level flux excess (possibly a reflection) in the far blue. There are also low-lying, extended wings at all pixels in the blue. These far wings not included in the aperture extraction contain about 4% of the total flux.

The widths of the apertures were typically $\pm 5-8$ pixels. The data for IF1 was extracted with a larger aperture (± 10 pixels) in order to account for the very bright flare emission lines which appeared at low levels farther from the spectrum than the continuum. An effect which I never could explain was that an extraction with a smaller aperture divided by an extraction with a wider aperture counterintuitively resulted in a larger line-to-continuum ratio for emission lines (e.g., Hγ) and a smaller line-to-continuum ratio for absorption lines (e.g., Ca I 4026). One would think that a larger aperture would have a larger line-to-continuum ratio (for emission lines) because the larger aperture accounts for the line flux (spatial) wings at larger distances from the spectrum.

Cosmic ray rejection was not applied to the data. Because of the short integration times, they rarely affected spectra. The IRAF tool in apall (clean) often mistook flare emission

lines for cosmic rays and was not used. We experimented with lacosmic, which has a well-developed algorithm for cosmic ray rejection; however, the processing takes a long time and was not a realistic

A wavelength solution for the blue chip was determined using a HeNeArHg lamp obtained at the beginning of the night combined with a constant offset (usually $2-3$Å) determined from a HeNeAr taken on sky at the target. The Hg lamp provided additional lines in the blue, including the blue-most line at 3650Å (which is blended with a low-level Mercury line). We verified the wavelength solution to being accurate to 1Å down to 3300Å using three O III lines obtained from a deep exposure of the planetary nebula NGC 7009. The wavelength solution for the red chip was determined in a similar way with a HeNeAr lamp, but we refit the entire solution as there are far more lines in the red.

Ideally, one wants a standard star with a small Balmer jump, bright blue flux ($U < 10$), narrow Hydrogen lines, no nearby companions with $\sim$5", taken at similar airmass (or over a range of airmasses), time, and transparency as the flare observations. However, this is not always (and almost never) possible especially with the limited number of high-quality spectrophotometric sdO standard stars available. We at least tried to obtain a flux standard at the beginning and end of the observations (and possibly in the middle of the night if a flare already occurred). The standard stars were used together to assess the sensitivity trends in the night. The best standard star observation was used to flux calibrate the data. If several observations were combined to create the sensitivity curve, they were shifted (using a grey offset) to the observation with highest sensitivity. The atmospheric extinction curve from the SDSS project was converted to magnitudes/airmass and used to correct the target observations at a different airmass than the standard star. There are many atmospheric bands in the red, and the extinction curve was fit with a low-order polynomial to interpolate over the atmospheric bands. The standard star data (binned to 15Å) from Oke (1990) was used because it it better accounts for the height of the Balmer jump. The blue chip target spectra were split into two sections and were used to derive independent sensitivities, each with $\sim$7th order spline functions. For the red, we used a 6th order spline function. The standard star observations of Feige 110 seem to be anomalous at $\lambda = 7800 - 8300$Å, and these points were not used in the fit to the sensitivity function.

We investigated the possibility of applying a second order airmass correction to the data, but it was rarely unambiguous using the available IRAF tools if the extinction residuals were significant. Comparing the observed fluxes from other standard stars (that were *not* used in generating the master sensitivity) from the same night to the published fluxes from Oke (1990) gave us an estimate on the absolute and relative (color) accuracy of the flux calibration. The red spectra were calibrated with the same standard star exposure as the blue spectra, and therefore were joined at 5500Å.

In Figure A.1 (top), we show the observations of the standard star G191B2B obtained on various nights over several years. In In Figure A.1 (middle), we bin the observations from 24 Feb 2011 into $\Delta\lambda$ =35Åbins and divide by the accepted flux from Oke (1990). Note that the G191B2B exposure was taken at an airmass of 1.06 and the Feige 34 observation (which was used to calibrate the data) was taken at an airmass of 1.35. There is a grey offset due to transparency variations during this night. There appears to be a $3-5\%$ color change in the spectral region from $\lambda = 4000-4800$Å (where the blackbody fitting was done in Section 6; indicated by the vertical lines). Note that the airmass difference between the peak flare spectra for this night and the standard star is much less than 0.3 and so the error should be smaller (although there was a dust spike during the peak). For this night, we tried a second order extinction correction, which is possible when there is a large enough spread in airmasses of the standard stars, irrelevant of whether you use the same standard star. and the corrected flux is shown as the dashed line, which takes the On some nights, there clearly was not evidence for a second order correction, but on some nights there is a marked difference between the accepted color and the observed color of the standard. In this same figure, we show the flux ratio of a different star (Feige 34) from a different night (08 Feb 2011) compared to the accepted flux from Oke (1990). This shows much less variation with color and also less grey extinction. In both cases, the flux is more uncertain from $\lambda = 3750-4100$Å because of the broad Hydrogen lines and blending of these lines near the Balmer jump. However, it's worse in G191B2B than Feige 34 because of the broader line profiles in the former. The error in the Balmer jump ratio resulting from not applying a second order correction is $\sim$5% (at this airmass).

In Figure A.1 (bottom), we show the flux ratio (observed flux/accepted flux) for the

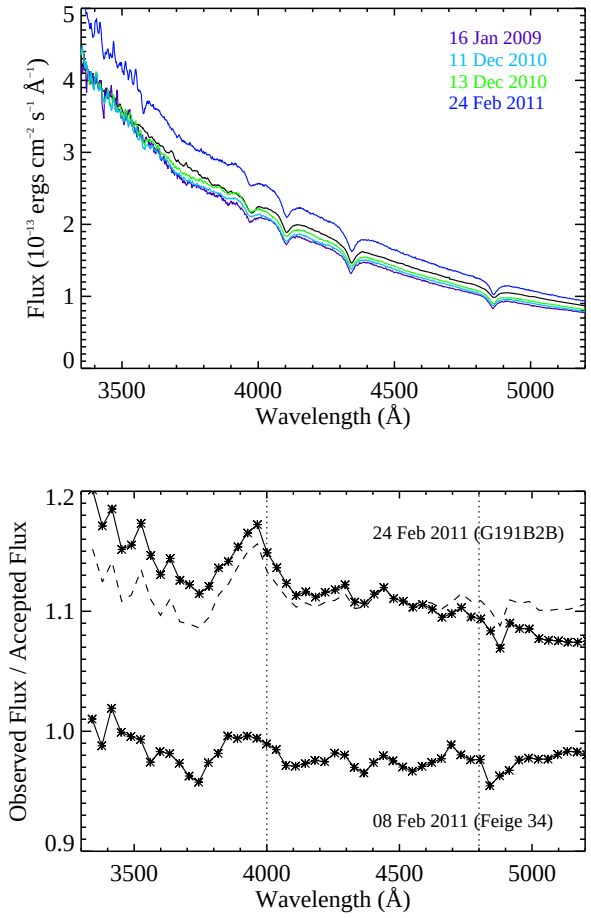

Figure A.1

entire wavelength range of DIS. The color of the red spectrum is very accurate (in this case), and the flux is much more uncertain near the dichroic ($\lambda \sim 5500$Å) and near the atmospheric bands in the red. Note that the relative flux experiences little color variation in the regions chosen to minimize the subtraction residuals (Appendix B).

A.1 Flux Calibrating the Data from 01 October 2008

An extra step was taken to flux-calibrate the spectra from 01 Octoer 2008 because the main flare event was observed at high airmass (≥ 1.9) and the slit was positioned across both flare stars EQ Peg A and B and not at the parallactic angle. First, we calibrated all spectra

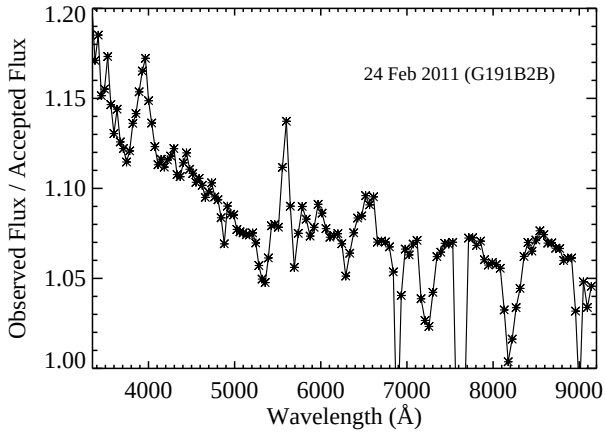

Figure A.2

with the standard star G191B2B at an airmass of 1.07 Then, we used the quiescent spectra from immediately before each flare (IF4 and HF4) and divided by a quiescent spectrum at an airmass of $\sim$1, when the slit loss from differential refraction is negligible. This resulted in a second order color correction that we multiplied by the flare data. The scaling with the molecular features in the blue was then applied.

Appendix B

SCALING SPECTRA USING MOLECULAR FEATURES

We tested the scaling algorithm's accuracy by adding simple, model blackbody flare SED's to the quiescent spectrum and multiplying by a constant factor that simulates slit-loss and/or weather-induced flux variations. First, a quiescent spectrum from YZ CMi was multiplied by $d^2/R^2_{\rm star}$ to convert flux to surface flux. Three blackbody temperatures were used to simulate the flare SED, $T = 5000, 10\,000$, and $50\,000$ K, to sample a large range of possible SED shapes. The flare surface flux was multiplied by a filling factor to simulate the surface coverage. Finally, we multiplied the total resultant flare+quiescent spectrum by a factor ranging from 0.7 to 1.3 to simulate the non-flare flux variations. The "observed" spectrum was then run through the scaling algorithm to determine the artificial factor (0.7 – 1.3) applied initially.

The largest flares on dM stars have factors of ∼100 enhancements in the U-band flux. The filling factors necessary to produce this enhancement of $T_{BB} = 5000, 10\,000$,and $50\,000$ K are 0.76, 0.016, and 0.0004 respectively. The smallest flares in our sample increase the U-band by a factor of ∼2. The filling factors necessary for this enhancement are 0.015, 0.0003, and 8×10^{-6} for these temperatures, respectively.

The results of running this range of flare sizes through the algorithm are given in the Table H.1 (first and third row for each temperature). They indicate that for small flares, the algorithm determines precisely the correct predetermined multiple (0.7-1.3) that was applied to the total spectrum. At the other extreme, for the largest possible flares, there are large errors (all overestimations) for the 5000 K flare, 10% errors for the $10\,000$ K flare, and 3% errors for the $50\,000$ K flare. However, none of the flares in our sample are this large ($I_{f,U} + 1$ ∼100; and further it is unlikely that 76% of the surface is flaring at 5000 K!) but this does tell us to use a large slit width (and hope for photometric conditions!) for data of large flares. We note that the corrections for the data of IF3 - the largest flare in

the sample (with peak coverage) - are very minimal ($< 2\%$), consistent with having robust flux measurements via the use of a wide slit and clear conditions. We note that when the algorithm errs, it always overestimates the scaling factor.

Finally, we determine the flare amplitude at which the algorithm begins to show noticeable errors (second row of the table). This occurs only for the 5000 K flare with an amplitude $\Delta U = 4$ mags; for this amplitude flare, the hotter temperatures give scalings $<3\%$ different from the predetermined values.

In Figure B.1, we show the result of scaling the spectral fluxes for a night with occasional cloud cover. This figure shows the corrected and uncorrected fluxes for synthetic U and B fluxes obtained from the spectra.

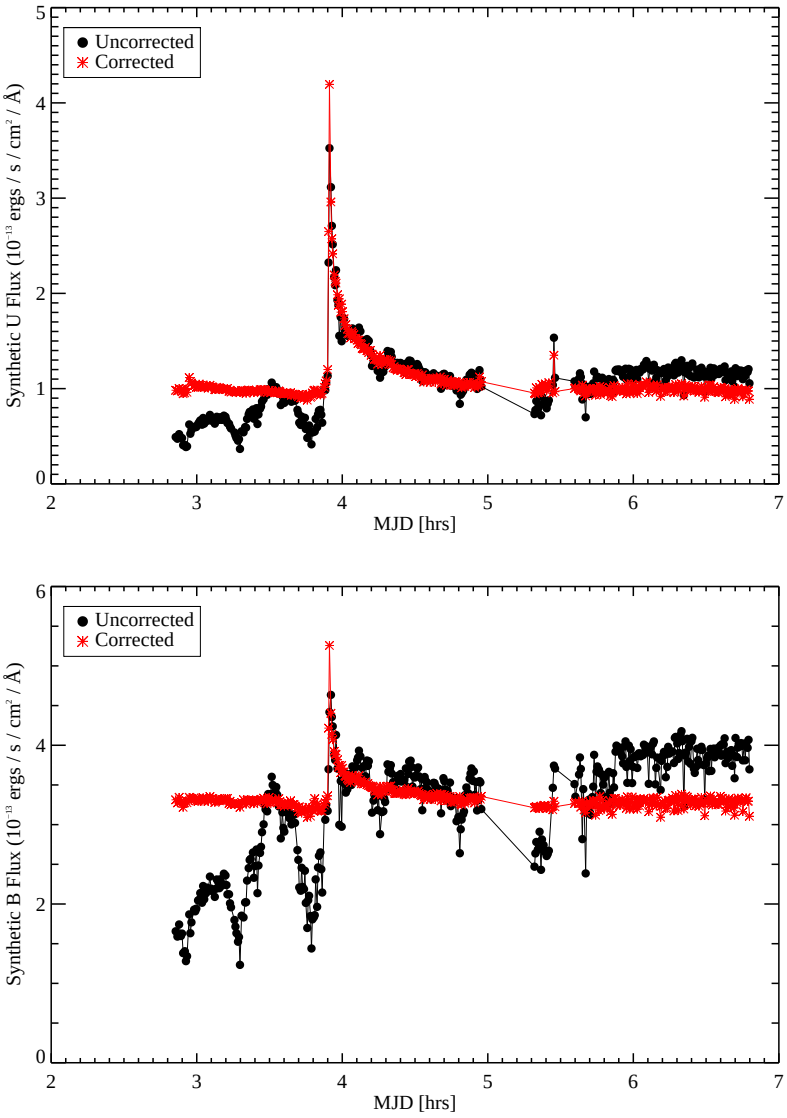

Figure B.1 Variations due to occasional cloud cover are apparent in the raw fluxes from the spectra obtained on 03 April 2010 (IF9). Our simple algorithm predicts corrections that adjust for these variations, allowing the flare to be characterized at wavelengths redder than the U-band, as apparent in the synthetic B-band flux in the bottom panel.

Appendix C

INTEGRATION TIMES OF THE SPECTRA

In this Appendix, we show the photometry light curves and the integration times of the simultaneous spectra (Figures C.1 – C.19). The grey shaded vertical bars show the integration time windows, and the S# is given at the bottom of each grey bar. The vertical dashed red line indicates the time at which the gradual phase emission is analyzed (Table 4.2).

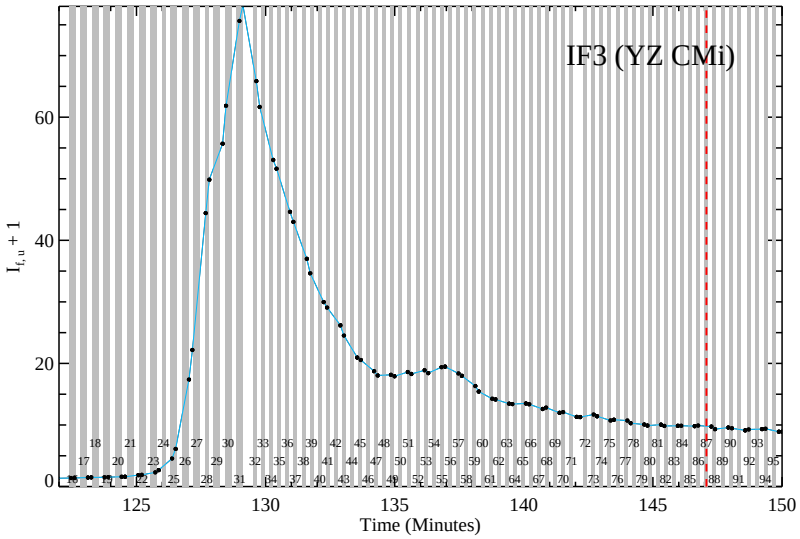

Figure C.1 The U-band (or u-band) photometry (blue line, black circles) for IF1 and the spectral integration times given as shaded bars; the S#'s are indicated at the bottom, and the vertical red dashed line indicates the time at which gradual phase emission is analyzed. The gradual phase spectra in Figures 6.21 – 6.25 are averaged over three spectra around the red line.

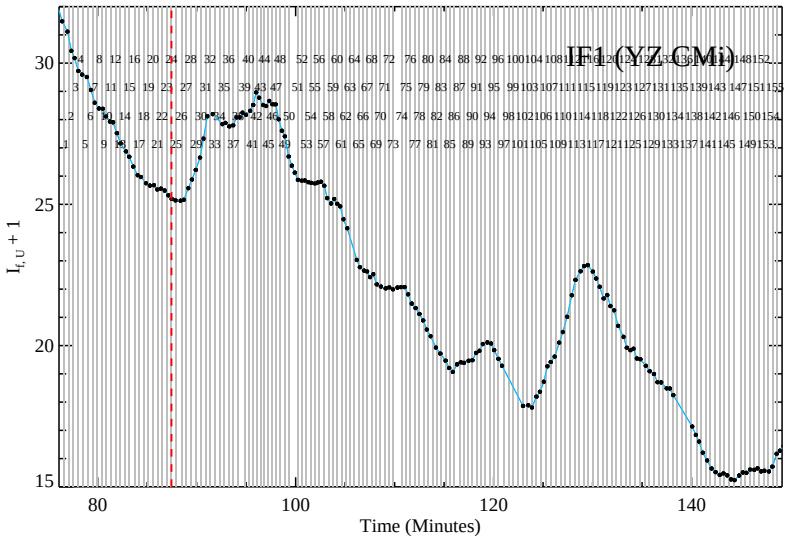

Figure C.2 Same as Figure C.1 but for IF1.

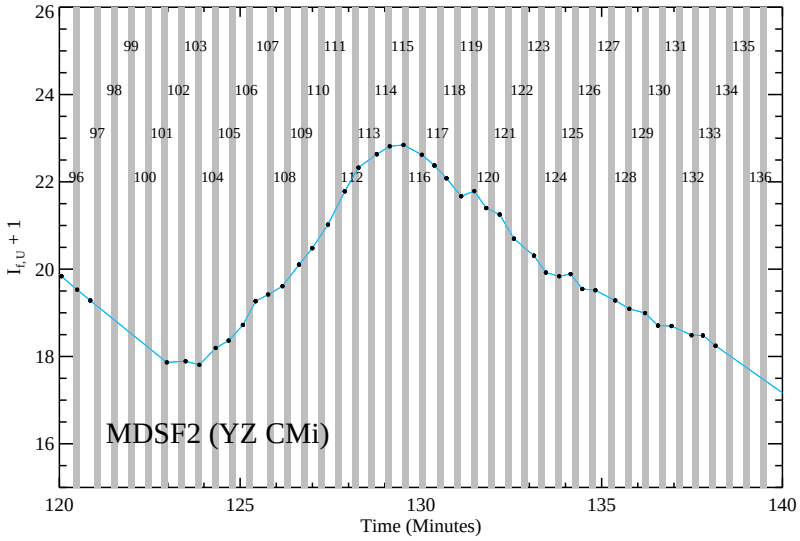

Figure C.3 Same as Figure C.1 but for MDSF2.

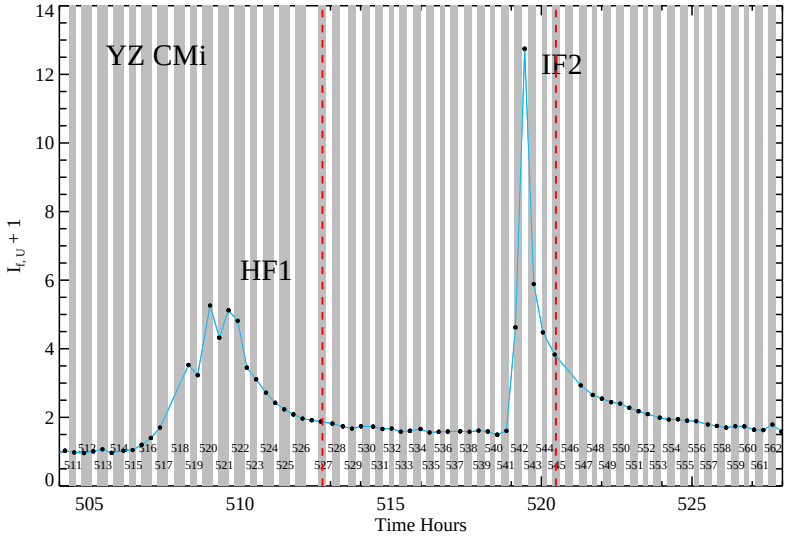

Figure C.4 Same as Figure C.1 but for HF4 and IF2.

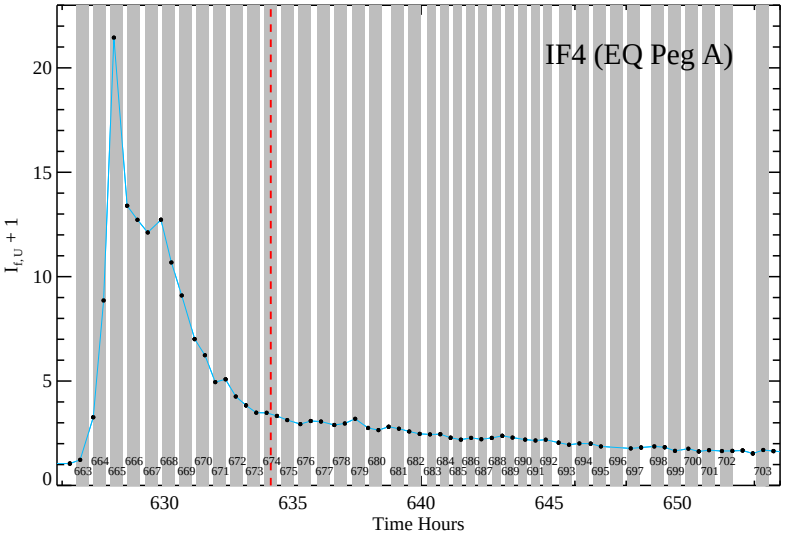

Figure C.5 Same as Figure C.1 but for IF4.

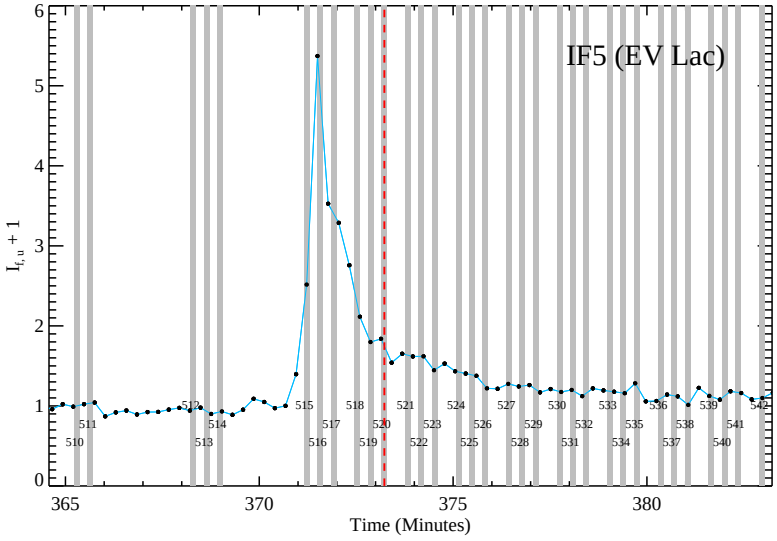

Figure C.6 Same as Figure C.1 but for IF5.

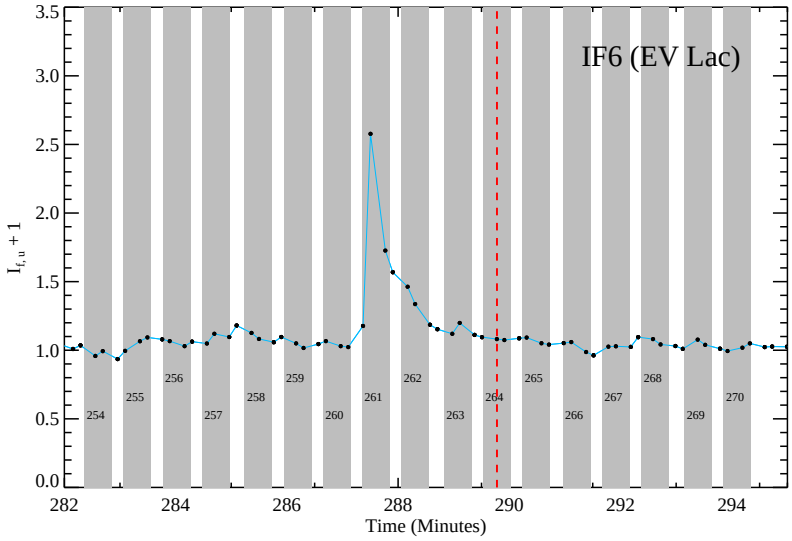

Figure C.7 Same as Figure C.1 but for IF6.

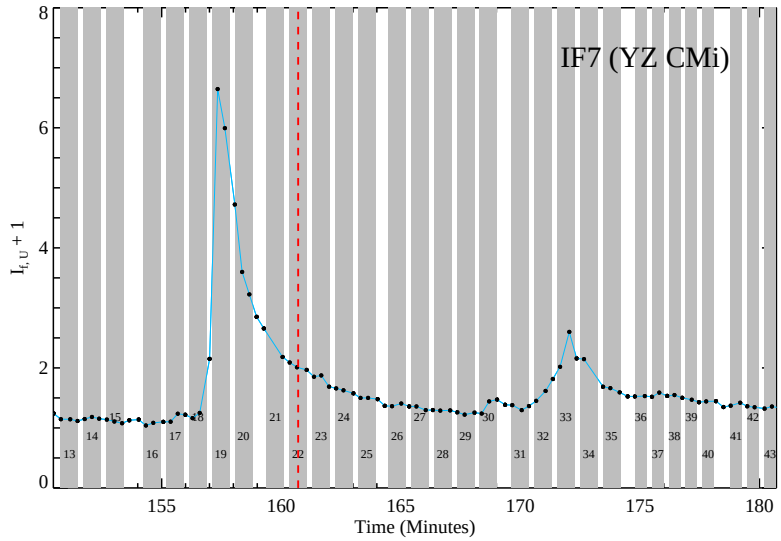

Figure C.8 Same as Figure C.1 but for IF7.

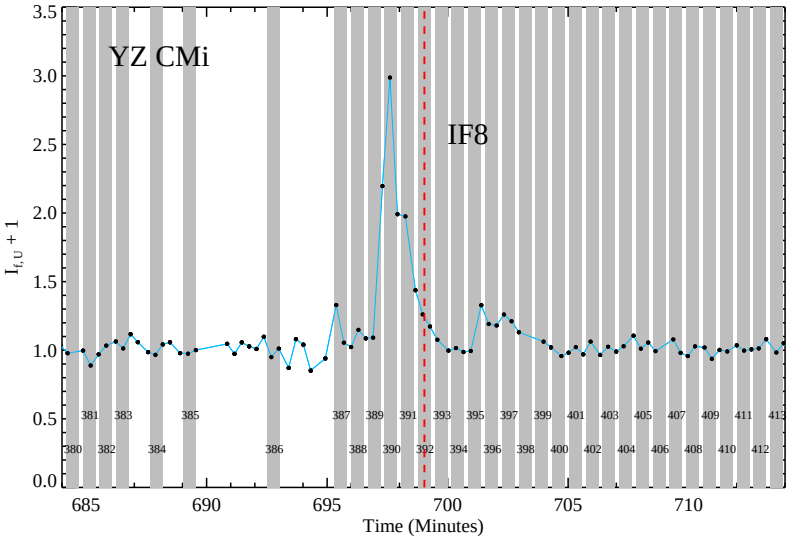

Figure C.9 Same as Figure C.1 but for IF8.

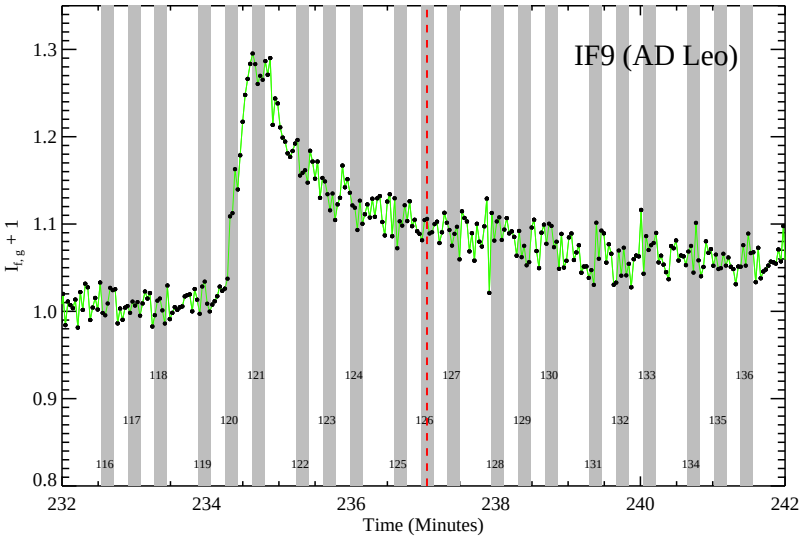

Figure C.10 Same as Figure C.1 but for IF9.

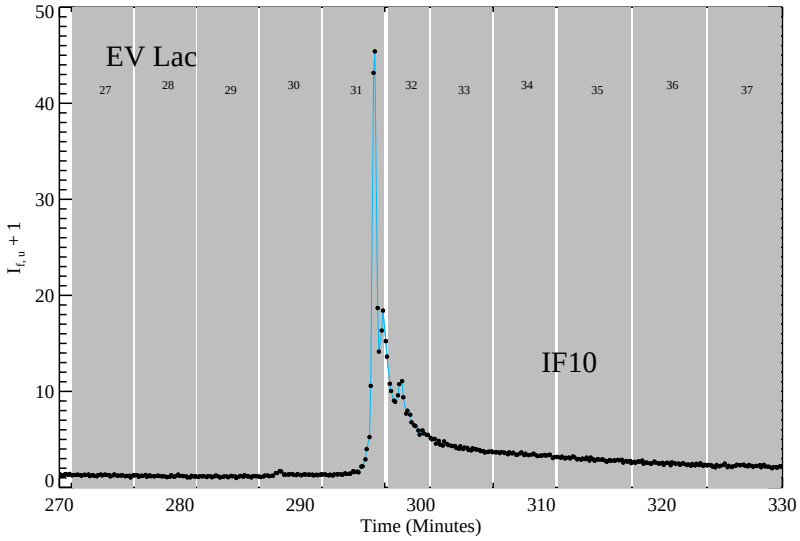

Figure C.11 Same as Figure C.1 but for IF10.

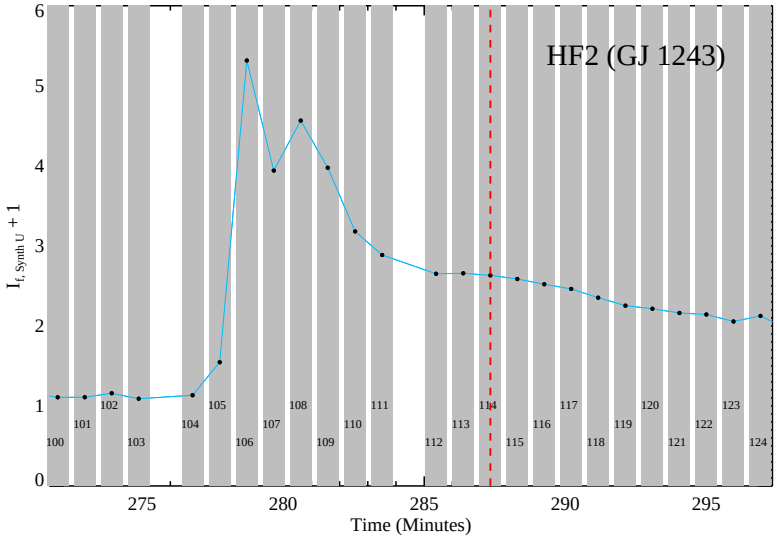

Figure C.12 Same as Figure C.1 but for HF2.

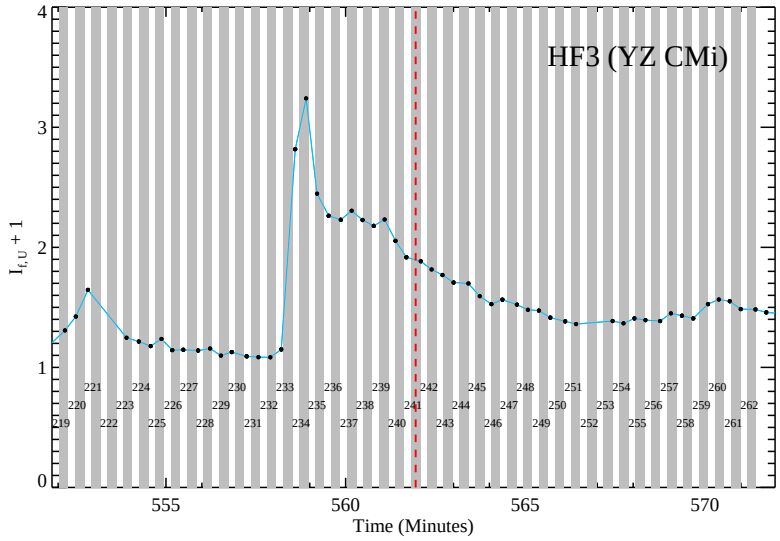

Figure C.13 Same as Figure C.1 but for HF3.

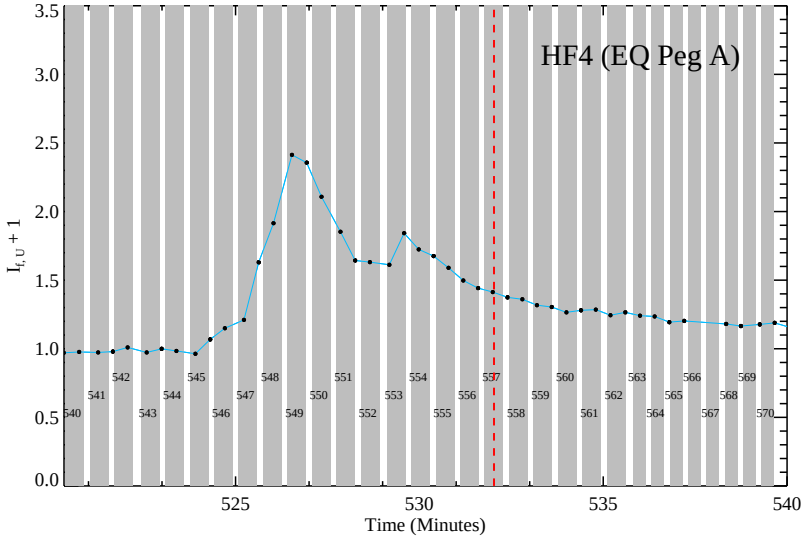

Figure C.14 Same as Figure C.1 but for HF4.

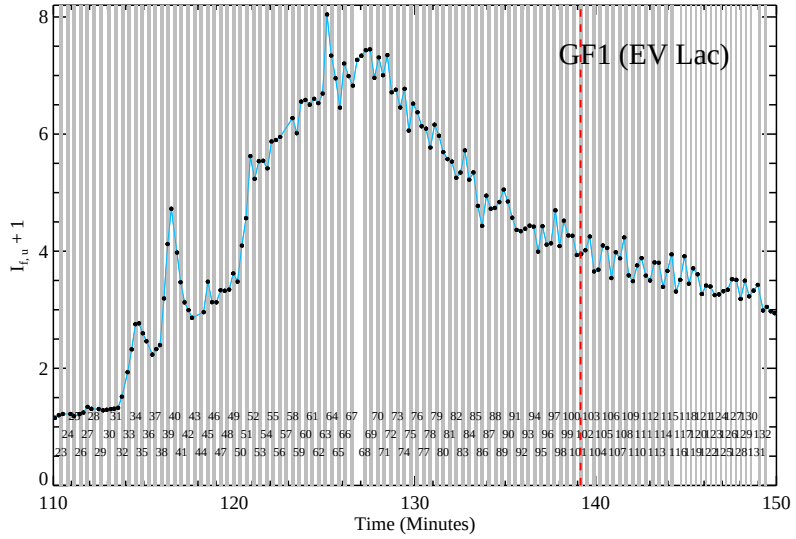

Figure C.15 Same as Figure C.1 but for GF2.

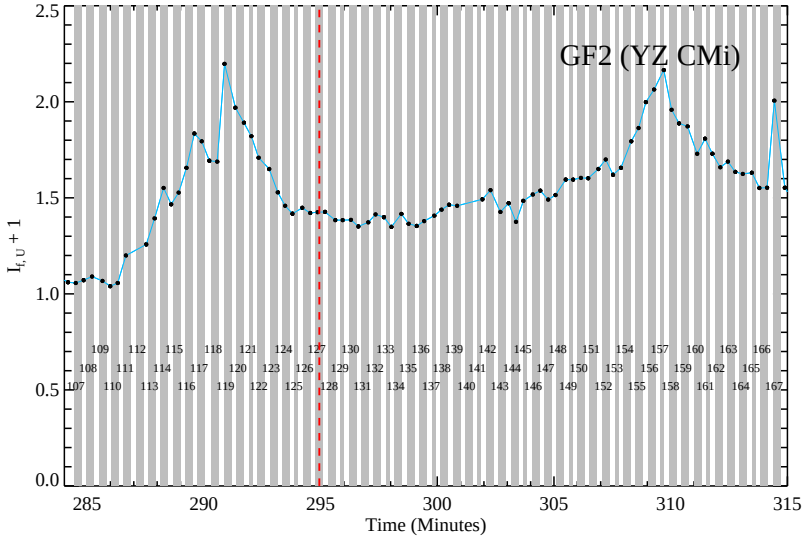

Figure C.16 Same as Figure C.1 but for GF2.

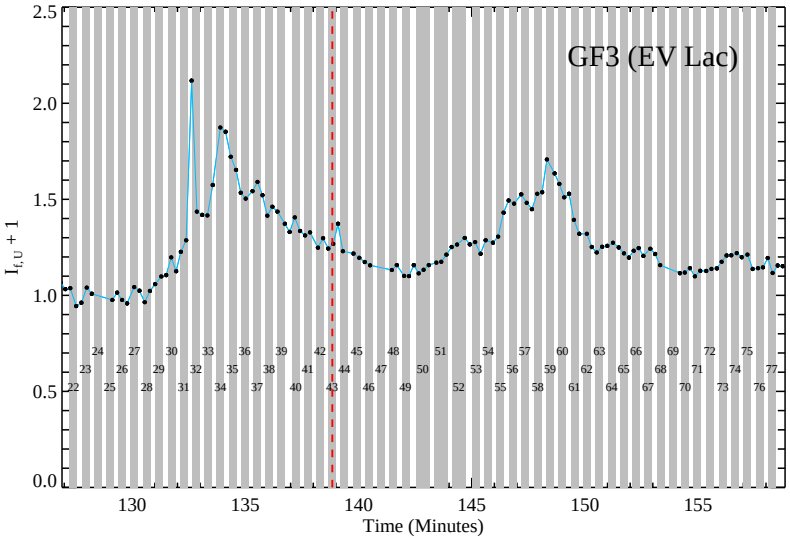

Figure C.17 Same as Figure C.1 but for GF3.

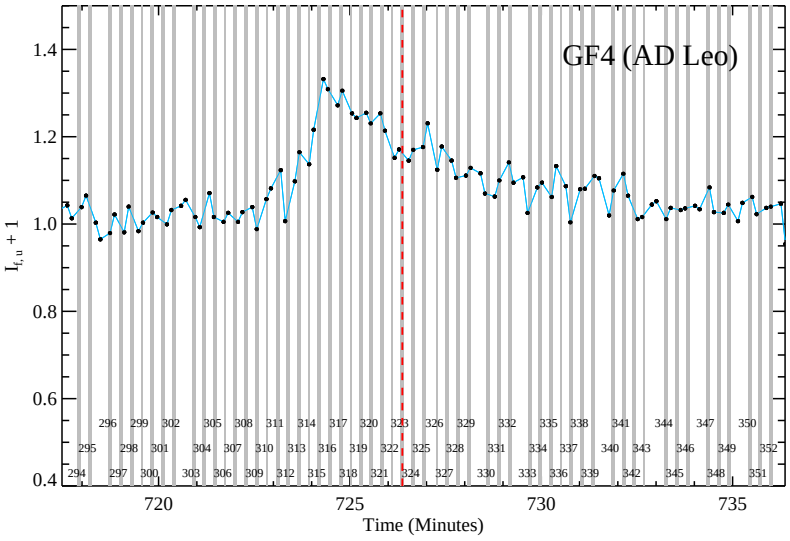

Figure C.18 Same as Figure C.1 but for GF4.

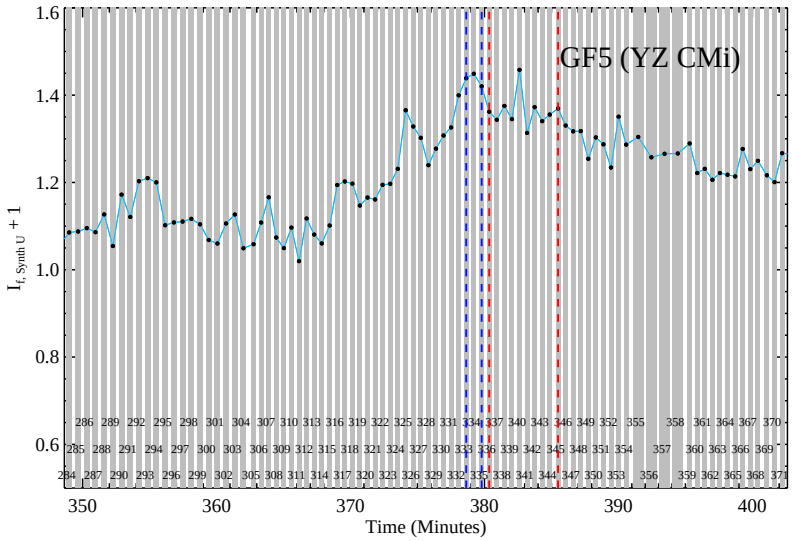

Figure C.19 Same as Figure C.1 but for GF5. The red lines indicate the ten spectra used for the gradual phase spectrum. The purple vertical lines indicate the four spectra averaged for the peak spectrum.

Appendix D

EMISSION LINES

D.1 Calculating Line Widths with Low-Resolution Spectra

We choose to analyze the flare-only emission profiles for calculating line widths 0.0, 0.05, and 0.1. To calculate 0.5 width, we use the flare+quiescent profile. When the emission is low, such as near the beginning of the flare, the line width can artificially appear to be large, if we use the flare-only profiles. If we use the flare+quiescent profiles, then the molecular features can affect the line width estimation as it contributes to varying levels of the peak flux as the line emission changes.

To illustrate the line broadening effects, we show the broadening in IF9 for the Hγ line in Figure D.1 (left panel). This flare had higher resolution data (1.5" slit) and we analyze in detail in this appendix. It is difficult to tell where the line begins and flare continuum ends; vertical grey lines denote where I would draw the beginning and end by eye in the total emission ($\pm$20Å, corresponding to about 0.05 of the peak). This selects most of the profile but misses some low-lying line emission. In the right panel of this figure, we zoom in on the line and show the same black and red curves. An inactive M3.5 is overplotted to show that identifying bona-fide wings (and line-fluxes) can be ambiguous due to molecular features that blend near the line wings. The FWHM broadens and the molecular features near the line change their relative depths [adam-gedanken] Notice at +15Å, there is veiling from continuum emission and from broad line emission. Subtracting the quiescent therefore reveals more about the wing shape, whereas the line width can be estimated by using the total flux. Note that the detailed core shape of the subtracted profile should not be trusted because the quiescent subtraction of the line affects the core shape.

There are no strong secondary events in this flare; therefore, we study the line broadening evolution of IF9 as a representative standard, large flare. In Figure D.3, we show the emission lines in the blue-optical normalized to peak (continuum subtracted) for the max

continuum time of IF9 (purple) and the beginning of the extended gradual phase (red). In this figure one can observe the relative evolution in the line fluxes of Helium I, the line width change in the Balmer lines from peak to decay, and also the greater change in the red wing of Hδ, which gives rise to its apparently larger width compared to Hγ. Finally, note the extremely broad wings of a low-lying component in the Hγ line (relative flux <0.04 extending 150Å. This is approximately symmetric, is present in both peak and decay, and is also a feature seen in other flares in the sample. There are known to be a pileup of metallic lines centered at 4300Å during flares (Paulson et al., 2006).

In Figure D.4 (left panel), we show the line profiles for IF9 at the time of peak flux in Hγ (one spectrum after the peak in the continuum emission for this flare). An estimate of the "pure" Hγ line in quiescence is shown in red (subtracting an inactive template). The three Hydrogen lines' broadening are very similar in this flare. The time profile of the Hγ broadening is given in the right panel for various measures of the width. The horizontal dashed lines on the right are the quiescent values for each measure. For the FWHM, the flare+quiescent emission was used so as not to bias the line profile. The line profile undergoes a significant obvious broadening during the flare, which is evident in all measures of the line width. Although not significant within the errors (given by the resolution, $\sim$ 3.5Å), the maximum line width occurs at the continuum peak of the flare, unlike IF4. At the time of maximum line emission, the widths are 103Å, 43Å, 34Å, and 10 Å($\pm$3.5Å). The light curve for the Hγ line is shown in red to illustrate the differences in the flux evolution compared to the broadening evolution.

At first sight, it appears that the broadening doesn't exhibit as large percentage changes as the line emission, However, if the *excess* broadening is plotted using the quiescent level as the zero level, the fractional changes in the broadening are *larger* than the total flux. In Figure D.5, we show the evolution of the four main Hydrogen line fluxes (left panel) and widths (right panel). In the right panel, the evolution of the Hβ, Hγ, and H δ widths are shown. Here, 14Å is the zero level for the Hγ width, and the flux is overplotted as a black line, normalized to the peak of Hγ width. The fast evolution of the widths is apparent during the impulsive phase. Furthermore, the evolution of the width of Hγ more closely matches the BaC3615 flux evolution (red crosses) than the Hγ flux evolution.

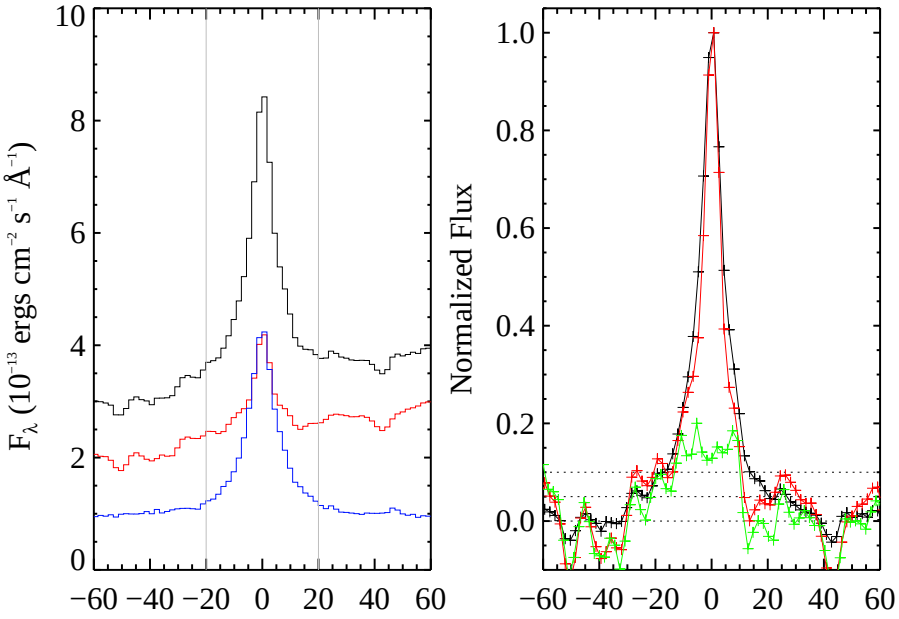

Figure D.1 (Left panel) Line widths of Hγ for AD Leo during flare (black), quiescence (red), and flare-only (blue). (Right panel) Inactive template shown in green, quiescent AD Leo shown in red, total flare+quiescent emission at line emission peak of IF9 shown in black (with continuum level subtracted). The continuum veiling by emission wings and continuum is evident (compare black and red). The difficulty in isolating pure emission due to line is due to the molecular features that blend together near the base of the Hydrogen line.

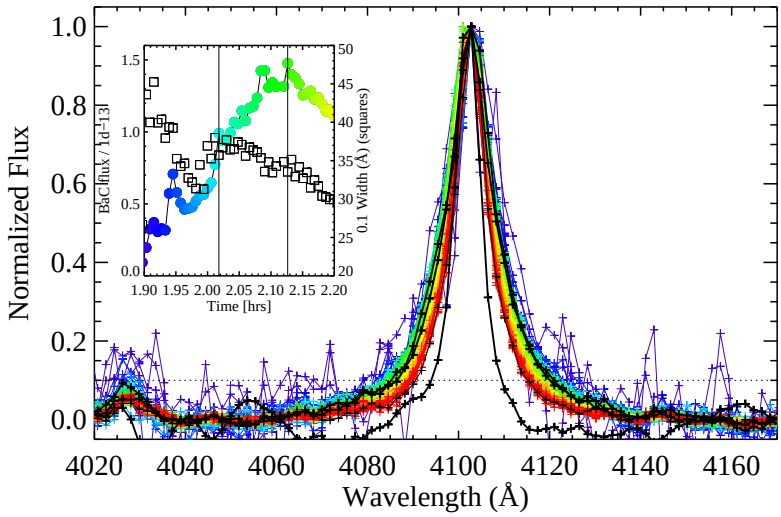
Normalized Flux
Wavelength (Å)
1.0
0.8
0.6
0.4
0.2
0.0
4020
4040
4060
4080
4100
4120
4140
4160
BaC flux / 1d−13
0.1 Width (Å) (squares)
Time [hrs]
1.90 1.95 2.00 2.05 2.10 2.15 2.20

Figure D.2

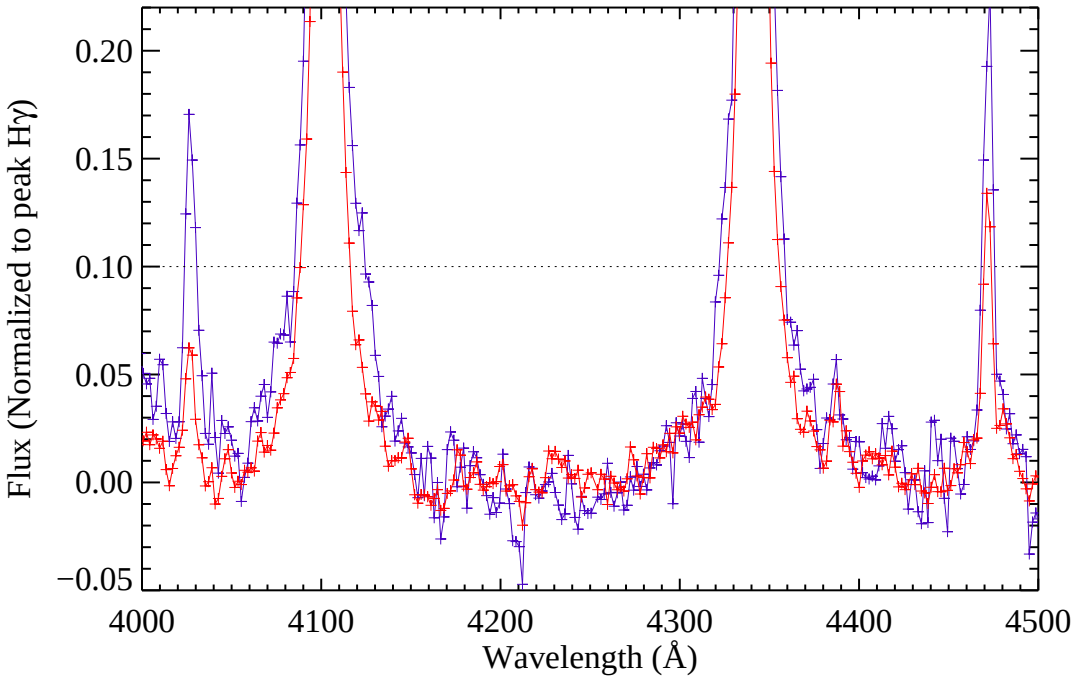

Figure D.3 A close inspection of the line profiles in IF9 at peak line emission (purple) and an average during the extended gradual phase (red). The 0.1 max of Hγ is 35Å, but they appear to extend $>$ 100Å at 0 level. Extreme broadening is also noticeable in the red wing of Hδ. Also, note the more impulsive behavior of He I λ4026 compared to He I λ4471. Helium I λ4387 can also be seen.

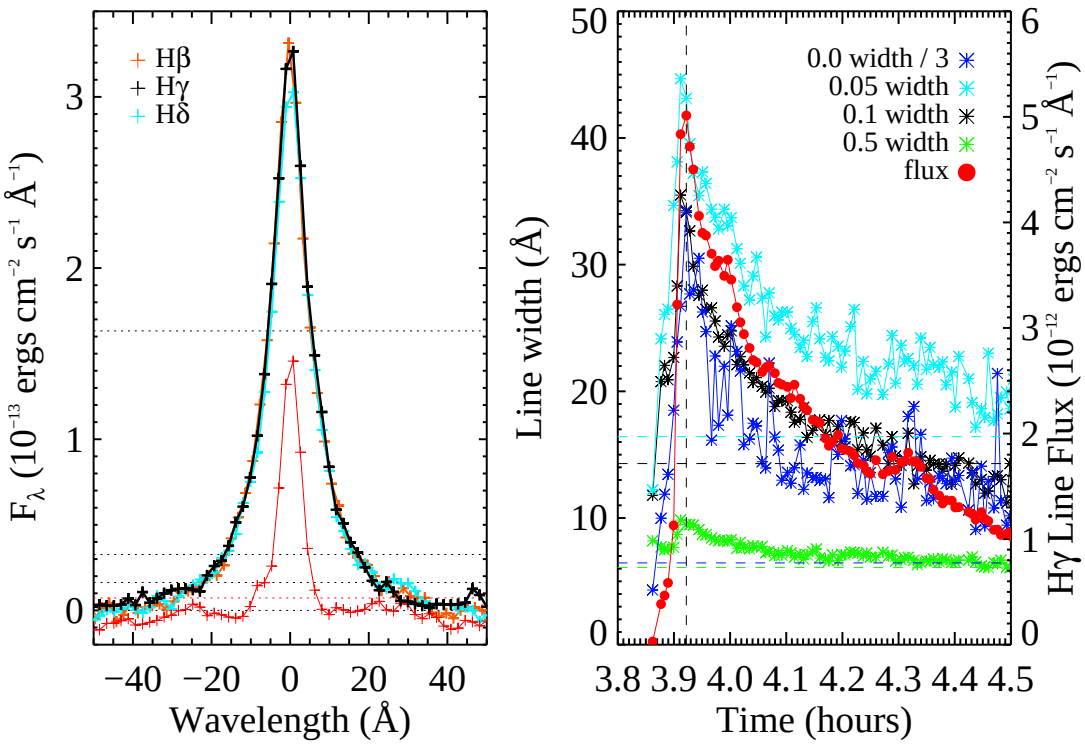

Figure D.4 (Left) The line profile of Hγ, Hβ, and Hδ at peak Hγ flux for IF9. The horizontal lines indicate the three line widths that are measured. (Right) The line flux of Hγ compared to the line width at 0.05, 0.1 and 0.5 maximum flux.

D.2 A detailed study of HF2 line emission

HF2 allows us to study line evolution during a flare that deviates from the classical morphology by possessing a double peak and a highly elevated decay phase. The double peak of HF2 is similar to impulsive phase of IF0, IF4, and the flare in García–Alvarez et al. (2002). Using HF2, we analyze Figure 4.10, and we show how to search for evidence of A star emission in the secondary continuum spikes of flares. In Figure 4.10, the emission lines for HF2 are shown. The lines peak ∼3 minutes after the first continuum spike, and one spectrum after the second continuum spike. Note the varying degrees of "response" to the secondary spike in this flare, and also the smoothly varying light curve slopes ($dflux/dt$) at the first continuum peak, in the order of Hα (positive slope), Hβ (positive slope), Hγ (zero slope), Hδ (negative slope), PseudoC (negative slope), BaC (negative slope), and C4170 (most negative slope). This behavior is likely the fact that the lower energy transitions decay slowest and continua the fastest; therefore, the continua decay fast enough that the emission generated by the second spike doesn't cause the total emission to increase above the first spike.

The relative peak heights of each component is calculated and displayed in Figure D.6, showing that the peaks become equal for the H10 line. The values for C4170 and C3615 are also shown in red; the continua react the strongest to the first spike. The BaC3615 contributes to C3615, which brings it down compared to C4170. We predict that the total in each component at their peak flux is a combination of the decay rate (from the first event) and the time-lag to the beginning of the secondary spike event. The time-lag is difficult to constrain precisely with these data, which have an integration times of 45 sec.

We compare the ratio of the total flux at peak 1 and 2 and the ratio of the new increase at peak 1 and 2, and show this is consistent with forming a hot star spectrum during the second spike. The C4170 responds relatively more in the first peak but absolutely less (compared to the C3615), which is related to the decay rate of C4170 being faster than C3615, as we have seen for IF3 and IF9 in Figures 4.8 and 4.9. The ratio of the total fluxes is therefore dependent on the timing of the two peaks and thereby how the new emission adds to the previously decaying emission. Whereas the ratio for the total emission

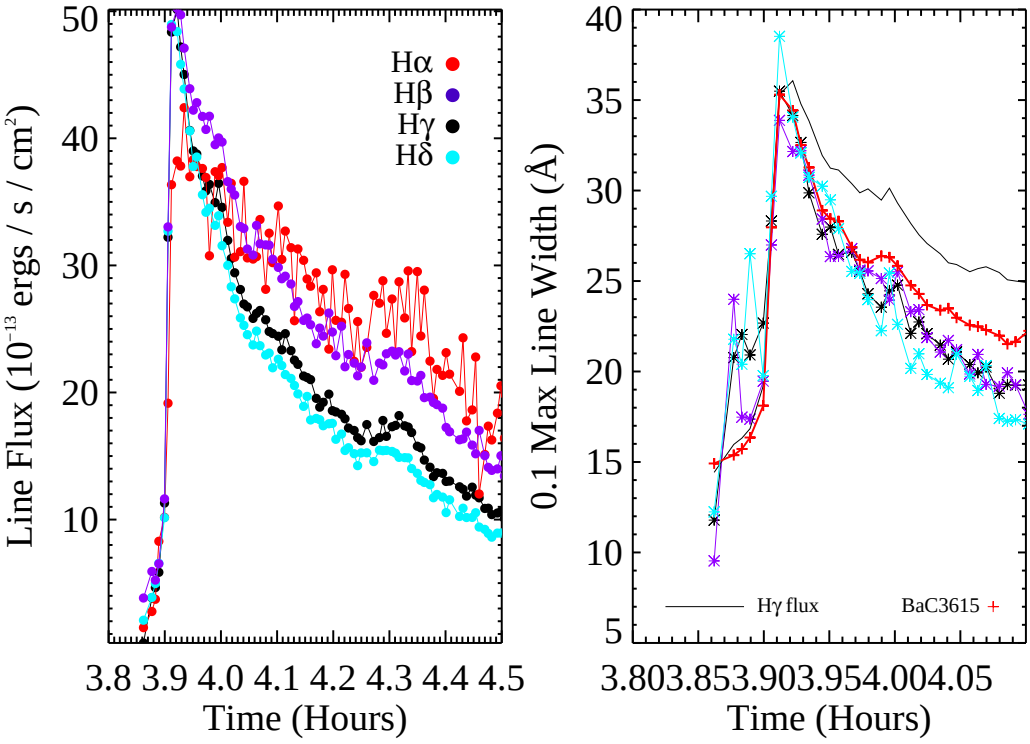

Figure D.5 Flux of Hδ, Hγ, and Hβ over time (left) and the widths at 0.1 maximum of the profile for each of the lines (right). On the right, the widths are all equal within the error bars but the trends are slightly suggestive of larger widths for the higher order lines. On the left, the different evolution in the four Hydrogen lines after the fast rise are evident. The horizontal line in the right figure corresponds to the 0.1 width in the quiescent (red) in Figure D.4 (14Å). The line width evolution is faster ending at about 4.3 hours, than the line flux decrease. At peak the Hδ line has the appearance of becoming the broadest but not within uncertainties. Hα widths are difficult to calculate so are not included in the right-side figure. The fluxes for Hβ and Hδ were calculated after subtracting the quiescent whereas the Hγ line was calculated before subtraction.

is greater in the C4170 ($C4170_{peak1}/C4170_{peak2}$ compared to the same quantity in C3615), the ratio of the newly formed emission, $C4170_{peak1}/(C4170_{peak2}\text{-}C4170_{trough})$, is *less* than that same quantity for C3615, indicating that the first and second peaks produce different relative amounts of C3615 and C4170. The ratio of new emission fluxes is shown in Figure D.6. This quantity is low, 2-3, for the Balmer lines.

There is a trend where the new emission produced in peak #2 is relatively lower in the higher order lines. The new emission in the *secondary* event is one that responds strongly in C4170 and also stronger in the *lower* order events. The BaC3615 follows the same trend as the Balmer lines. This scenario is consistent with the formation of a small amount of hot-star material on that star; the additional chromospheric radiation and this hot star radiation add together (since they are spatially unresolved) to produce the above trends. The decrements for an A star (Vega, Bohlin (2007)) are Hδ : Hγ : Hβ : Hα = is 1.10: 1.0 : 0.72 : 0.22. Therefore, if this type of absorption forms on the star, and emission from the chromosphere with a flat decrement (see Section Decrements) of $\sim$1 also develops, the larger amount of absorption in the higher order lines would add to give an apparent increase in the higher order lines that is not as much as one would expect from a purely chromospheric increase. This effect is consistent with Figure D.6.

D.3 Mg ib / *Fe* ii *at* $\lambda \sim$*5170Å*

There are three prominent emission lines in the spectra of flares at $\lambda \sim 4923, 5018, 5170$Å. These features are likely blends of He I, Fe II, and the Mg Ib lines. The Mg Ib 5183Å line is seen as a smaller feature just redward of $\lambda = 5170$Å, which is the brightest line in the region from $\lambda = 4900 - 5870$Å. The 5170Å and 5183Å features appear elevated on a "pedestal" of flux features, which may be smaller blended lines of Fe I and Fe II. The 5170Å line was identified as Mg Ib by Moffett & Bopp (1976), but Abdul-Aziz et al. (1995) identified these three lines as part of an Fe II (42) triplet ($\lambda = 4924, 5018, 5169$Å) in stellar flare spectra, which also appear strongly in solar flares (Severnyi et al., 1960). Ultimately, higher spectral resolution data should be obtained to determine the identification, time-evolution, and origin of these lines. Fe II lines are seen copiously in the NUV flare spectrum (Hawley et al., 2007) as nearly 80 lines have been observed in a flare, equaling the energy released

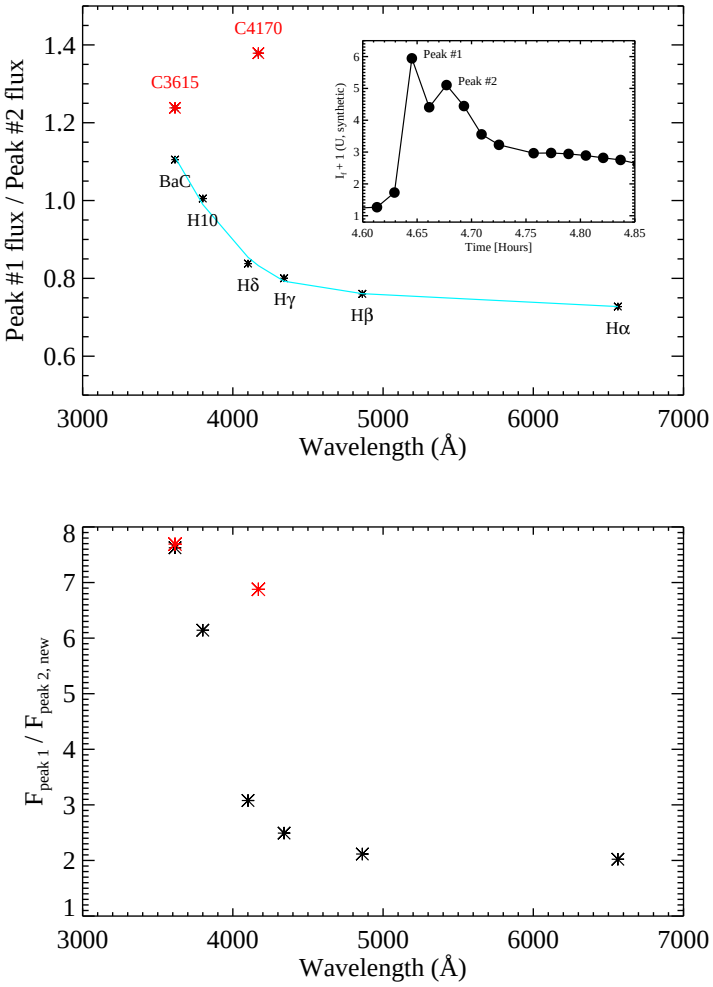

Figure D.6 (Top panel) The ratio of first and second peak (*total*) fluxes for the Balmer series during HF2 forms a λ^{-3} relationship. The C3615 and C4170 show the largest relative response. The inset displays the synthetic U-band calculated from the spectra of HF2. (Bottom panel) Given that peak#2 is a new event, this is the ratio of new emission formed in the peak. The relation is similar to the top panel, but the gradient is much stronger going from higher order to lower order. The ordering of the continuum points, C4170 and C3615, is reversed.

in Mg II h and k. In our spectral range, we note that several of the lines appear broader at times, indicating they are likely blends with the He I and/or Mg I. The third member of the Mg I b triple is resolved as a separate line just redward of the large feature that could be Mg I b or Fe II. It is not well-known where Fe II forms, but Baranovsky & Kurochka (1997) claim they are of photospheric origin and Fuhrmeister et al. (2010) claim an origin of Fe II λ3227 distributed throughout layers with a temperature range of $8000 - 14\,000$ K.

For sake of continuity, we will call it Mg Ib. In Figure D.7, we show the evolution of this line compared to Ca II K and Ca II 8542 for the IF3 flare. The general evolution of the three are very similar, with a fast rise, a slow rise and a late phase peak. The $t_{1/2}$ values of Ca II K, Mg Ib, and Ca II 8542 are 62, 63 and 69 minutes, respectively. However, the rise phase of Mg Ib is not as delayed as for the Ca II lines, and by the end of the fast rise, it is closer to the level of peak emission. However, both Mg Ib and Ca II 8542 show longer fast rise phase to $\sim$ 70% of peak emission, but Ca II K begins the slow rise at 50% the peak emission. The Mg Ib is slightly more impulsive than the Ca II lines (see the larger relative emission at $t = 2.3$ hours) and doesn't respond as strongly to the peak in the late decay at $t = 2.65$ hours. Note the slightly faster decay of Ca II K that eventually catches up to the Mg Ib line. The slowest decay of the three lines is the Ca II 8542 line. The peak flux and time-integrated energy ratios of Ca II K to Mg Ib in the IF3 flare are both 1.5.

The megaflare (IF1) decay shows a more contrasting evolution in the Mg Ib evolution compared to the Ca II lines. The Mg Ib exhibits a monotonic decline with no response to the secondary peaks. The flux in the triplet decreases by about 40% over the 1.3 hours of spectral observations, with a decay constant of 3 hours. The lack of substructure in Mg Ib is similar to what was found in IF3; we speculate that Mg Ib peaked earlier in this flare, similar to the Mg Ib peak in IF3. In the two flares, Ca II K shows some low-level substructure. The Mg Ib in IF9 appears more impulsive than Ca II K. In GF1, the overall morphology, especially the late peak, is similar but the detailed substructure of Ca II K is not evident. Similar to IF3, the rise phase of Mg Ib is not delayed relative to the Hydrogen lines whereas the Ca II K rise is delayed. In summary, the Mg Ib line is a cool line with a late peak, a rise phase in sync with the rise phase of Hydrogen, and a lack of substructure in the decay phase.

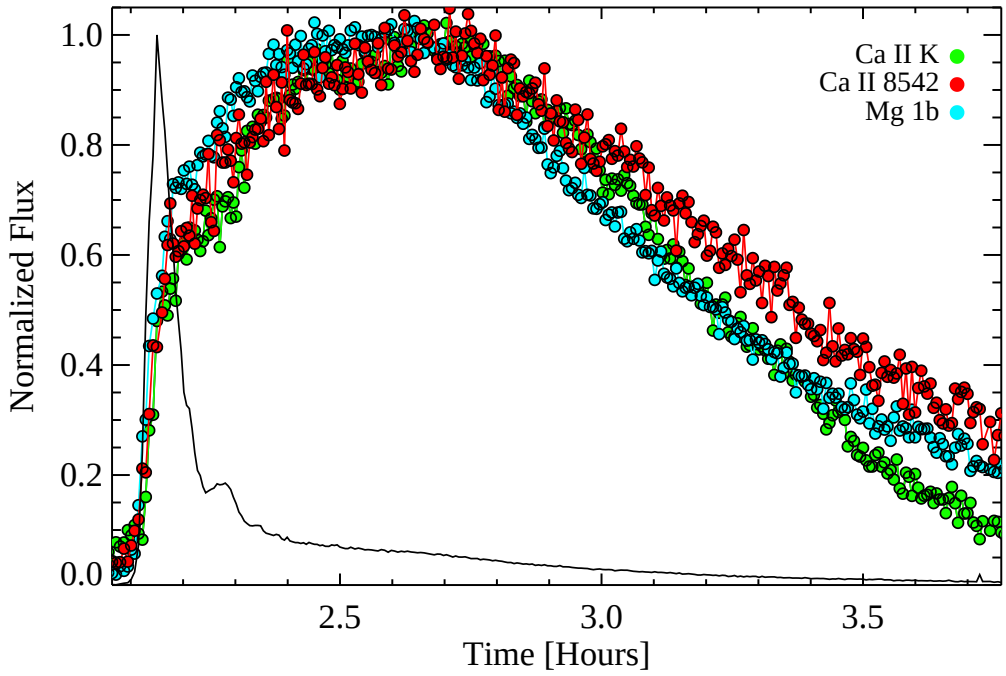

Figure D.7 The Mg I b evolution compared to the Ca II features. The fluxes are normalized to peaks, which are in the ratio of 1.5 : 1.0 : 1.0 for Ca II K : Ca II 8542 : Mg I b. The solid line is the C4170 normalized flux.

D.4 Helium i

We present the He I evolution in detail in Figure 4.8-Figure 4.10. The time-resolved properties of Helium I λ4471 was presented in Schmidt et al. (2012) for the IF10 flare.

Because λ4471 is the brightest Helium I line in the blue-optical, we study it in detail. The striking characteristic of the Helium I emission is the impulsive time evolution, with obviously the fastest $t_{1/2}$ of all the lines, and even faster than the BaC3615. We find that the total energy of this flare correlate more strongly with the energy of Hγ than the energy in the C4170 over the flares in our sample. Therefore, it is unlikely that the continuum is related to Helium λ4471.

We consider several possibilities for the source of the fast evolution of He I λ4471. First, it could originate from a region of the atmosphere with a rapid excitation time profile, e.g., from rapid beam heating of the transition region as the beam passes to the chromosphere, and as material is quickly ablated from transition region temperatures to coronal temperatures in the chromospheric evaporation material. Unfortunately, the He I lines are not included in the detailed radiation calculations in RADYN, but we can study the formation height with static modeling via the RH code. Second, it could originate from a region of high electron density, higher than the Hydrogen lines, thereby having a short cooling timescale. Third, because this line is optically thin (the ratio at peak with the 4026 line is $\sim$0.5, the optically thin ratio (Giampapa, 1983) it produces radiation that escapes quickly from the atmosphere.

The formation of this line is discussed by Lites. Finally, we posit that the rapid evolution of this line is related to being formed in the transition region, at T$\sim$ 20 000 K. These temperatures lie between 10K and 50K, which are the plateaus of sustained cooling from Hydrogen and singly ionized Helium Allred et al. (2006). When plasma is struck by beam heating, material quickly passes through the temperature of Helium I excitation. In other words, flare heated material cannot be sustained at these temperatures for long before they reach the "Helium II plateau".

He I λ4026 is blended with Mn I in the decay phase (excited by Mg II k Doyle 1992) and also apparently in the peak spectrum, such as in IF7. He I 4471 has Mg II at 4481,

such as in IF7 peak. In the Megaflare decay, the two lines are resolved, and we estimate that the flux in the Mg II line is 25% of the flux in He I 4471.

D.5 Line Asymmetries

Line asymmetries are observed in IF9 at peak continuum in Hδ, in Hβ at peak line emission during IF4 and also in the megaflare. Beyond the scope of this work.

D.6 Doppler Shifts

Wavelength stability of DIS not possible with this. Beyond the scope of this work.

Appendix E

FAST DECAY FITS

I fit the IF event from August 10, 2008 EQ Peg A using ULTRACAM NBF3500 data. I first binned by two observations (∼0.7 second cadence). The rise phase may be bursty and not very well represented by an 1-exponential function. Does an exponential rise of avalanche and 1-exponential of equilibrium result in a more linear looking rise? The $t_{\rm rise} = 8.1$ seconds, $\tau_{\rm rise} = 8.3$ seconds; the $t_{\rm decay} = 27$ seconds, $\tau_{\rm decay} = 11.8$ seconds. The $t_{\rm rise}$, $\tau_{\rm rise}$, and $\tau_{\rm decay}$ are all about equal, and the $t_{\rm decay} \sim 2.3 \times \tau_{\rm decay}$. In IF1, there is a similar relation, with $t_{\rm decay} \sim 2.1 \times \tau_{\rm decay}$. In both cases, the fast decay is followed by a secondary event (also, see IF3).

Appendix F

DETAILED TEMPERATURE FITTING

F.1 Temperature Errors

Mochnacki & Zirin (1980) quoted errors on temperatures of ∼200-700 K; we find that our errors, despite having much higher quality, higher time-resolution data are not better. Isolating flare emission in the blue-optical regime is difficult considering the quickly rising contribution from the quiescent background.

We consider several case studies of errors: using a different quiescent spectrum for IF1 decay; the detailed temperature fitting of IF9 (using different types of scaling); and the choice of windows for IF2.

F.1.1 The Conundruum

The data for IF2 flare is very low resolution since it was taken with the 5 arcsec slit. It has has the broadest Hydrogen lines, which makes it an extreme case for testing the effect on the lines on the choice of continuum fitting windows. In Figure F.1 we show the results of fitting the peak spectrum (S#542) without BW1 and BW2 (purple line) compared to using the windows in Chapter 6. Note that in high-gravity hot stars, BW1 is probably affected by Hydrogen opacity of the far wings (but, really, what isn't affected by Hydrogen opacity in the blue?). The results indicate a stunning difference in the inferred temperature of nearly 2500 K lower and surface area coverage 70% larger. Furthermore, the excess continuum at red wavelengths appears to be accounted for in this flare by using the cooler blackbody.

IF2 is an extreme case and we also test it for IF7, data with much higher resolution. The results are shown in Figure F.2, indicating a lower temperature by about 1000 K. In this case, the excess red flux is not completely accounted for by the lower temperature blackbody.

Finally, we show the same comparison for IF3, the flare which was fit in detail in Chapter

6. The results are shown in Figure F.1.1, indicating that the excess flux at 5000Å is more accounted for, but the new fits don't account for all of the red flux, nor do they appear to do a good job of handling the blue-optical shape.

For each of these two cases, the prediction for BaC3615 is noticeably different also. Note that a line extrapolation is used to estimate BaC3615, and it falls between the two blackbody fits in these figures; the line vastly underpredicts the red flux.

In summary, the temperatures are found to be systematically lower by about 1000 K in data without extreme line broadening; the nature of the apparent excess continuum flux at 5000 Å should be investigated further, as it is accounted for by varying degrees depending on how you fit the blue-optical blackbody. This same result has been reached by fitting hot star spectra. In Figure F.1.1, we show the same tests for the peak of the secondary flare in the Megaflare decay; the excess continuum at 5000 Å remains after changing the fitting windows; indeed, in some flares, it is more apparent than others.

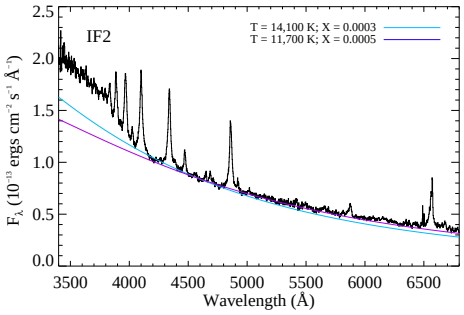

Figure F.1 Peak spectrum from IF2; detailed blackbody fitting tests, indicating 1000 K uncertainties in some flares but larger 2500 K uncertainties for flares with extreme broadening in the Hydrogen lines.

F.1.2 IF3

Here, we show the many possibilities for fitting the peak of IF3 with blackbody models.

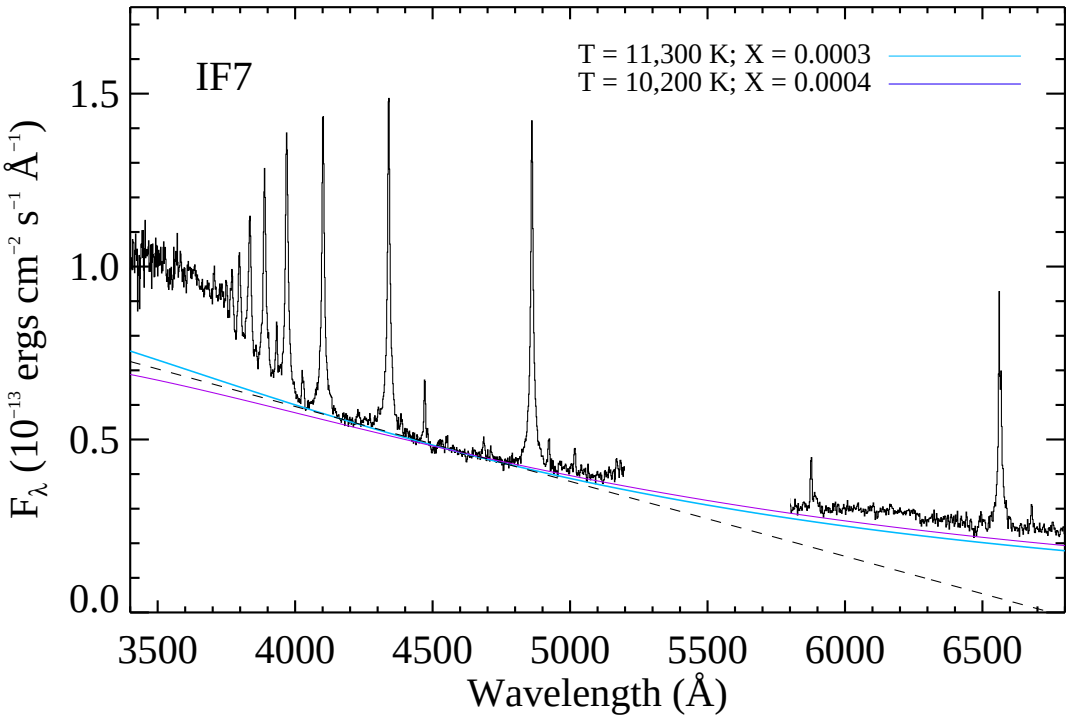

Figure F.2 Peak spectrum from IF7; detailed blackbody fitting tests.

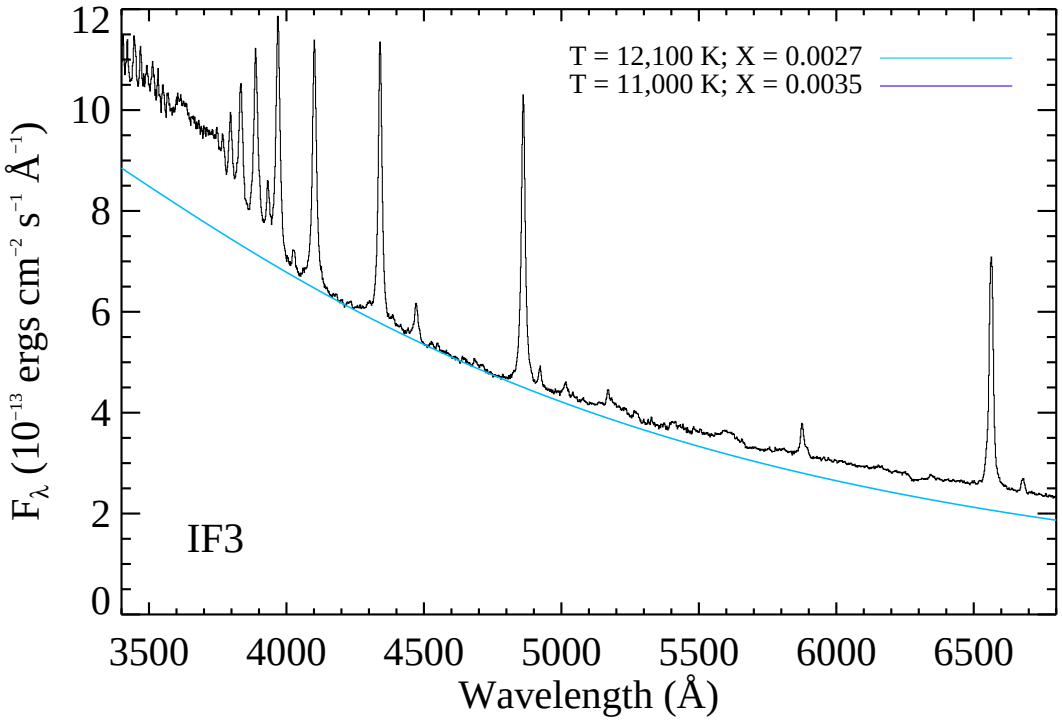

Figure F.3 Peak spectrum from IF7; detailed blackbody fitting tests.

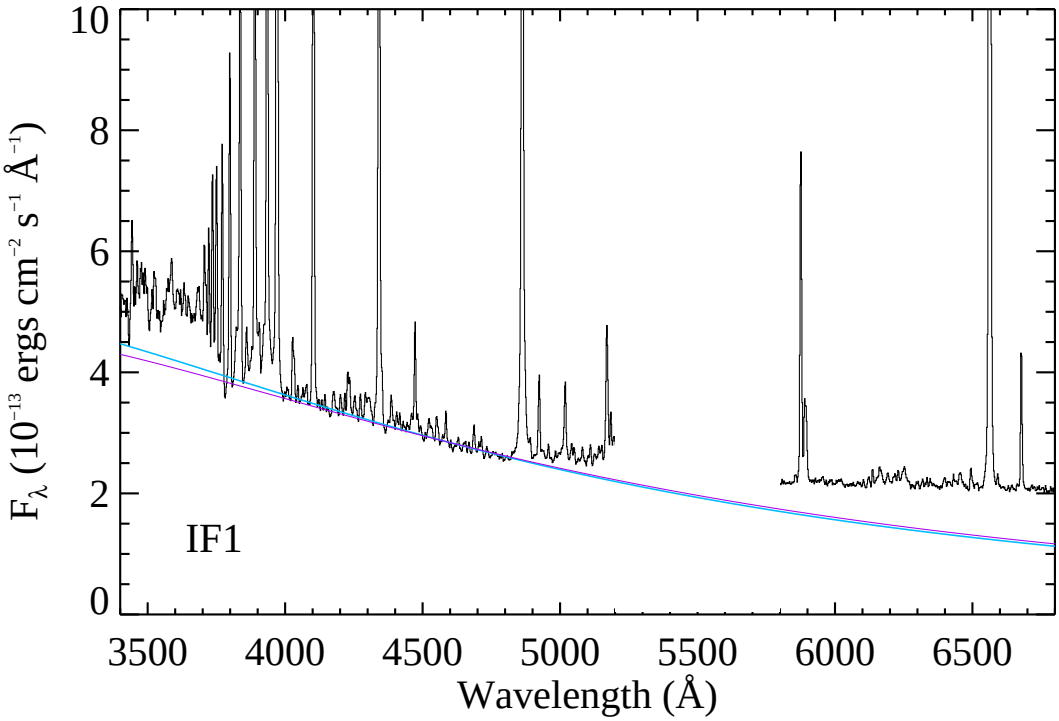

Figure F.4 Peak spectrum from IF1; detailed blackbody fitting tests.

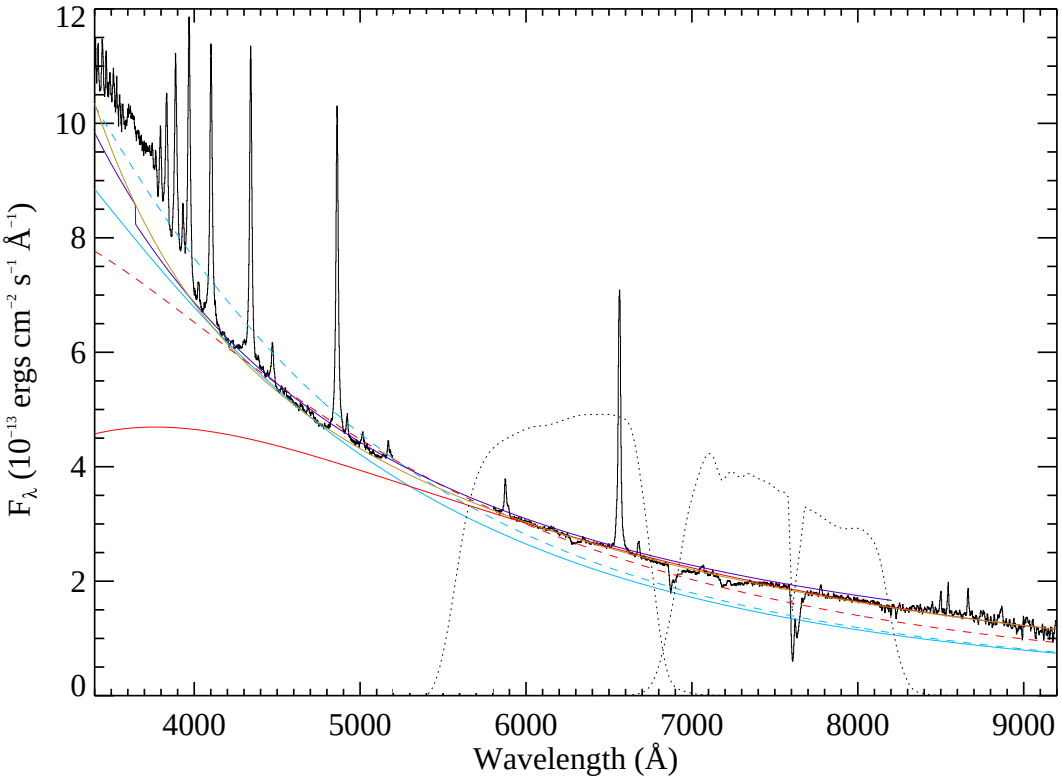

Figure F.5 The peak spectrum of IF3 from 3400 – 9200Å. The region from 5200 – 5800Å has been whited out because the dichroic affects the flux calibration here. The best-fit blackbody (T= 12 100K to the blue-optical is shown in light blue, and excess emission is apparent above an extrapolation to the redder wavelengths (e.g., at λ = 6000Å). Other possible fits are shown as a blue dashed line (fit to near-UV, blue-optical, and red-optical zones) and a red dashed line (to the blue-optical and red-optical continua). The red dashed line ($T \sim 10\,200$ fits the red continuum well, but misses on the detailed shape of the blue-optical. The solid red line is a Planck function fit to the red side only, and reveals a cooler slope, $\sim$ 7700 K. A double-blackbody fit gives the best match to the optical with temperatures of 163,800 K and 6369 K (maze line). A bf+ff fit with $T = 10^6$ K produces a $\chi_{flare} \sim 1.4$ and a decent match to the optical also; however this is inconsistent with previous observations of flares that show the SED peaks between 2000 – 3000Å.

F.1.3 Subtracted Flare Spectra

In Section 6.6.1, we found the newly formed flare emission (the flux in spectrum S#113 with the flux from spectrum S#102 subtracted) during MDSF2 resembles the spectra of a hot star, like Vega. It is a concern, however, whether the decay emission (S#102) continues to evolve (e.g., decrease) during the rise phase of the secondary flare thereby resulting in an *oversubtraction* of flare flux. In this section, we show how our results change if we estimate the amount by which the previously decaying flare emission decreases over the course of the rise phase.

We estimate the decay phase timescale using a double exponential fit to the overall decay trend of the U band. We then scale this fit by 90% to match the underlying level of the troughs in the decay phase. We predict that the U band of the previously decaying emission would decrease by 5% from S#102 to S#113 and by 2.5% from S#102 to S#108 if the secondary flare (MDSF2) were not present. Figure F.6 shows the results of subtracting these adjusted decay phase spectra. Qualitatively, our conclusions are the same. However, there are significant temperature differences between the unadjusted subtractions and the adjusted subtractions: For the unadjusted rise and peak phase spectra, $T_{\rm BB}$is 14 884 K and 17 651 K, respectively. For the adjusted rise and peak phase spectra, $T_{\rm BB}$is 13 144 and 15 021 K, respectively. Adjusting for decaying emission decreases the derived temperatures by $\sim$1800 – 2500 K. The detection of the Balmer continuum and lines in absorption is, however, robust.

F.1.4 Flare Velocities

In this section we show the expanding blackbody speed of IF3 using the uncorrected areas. The results are shown in Figure F.7.

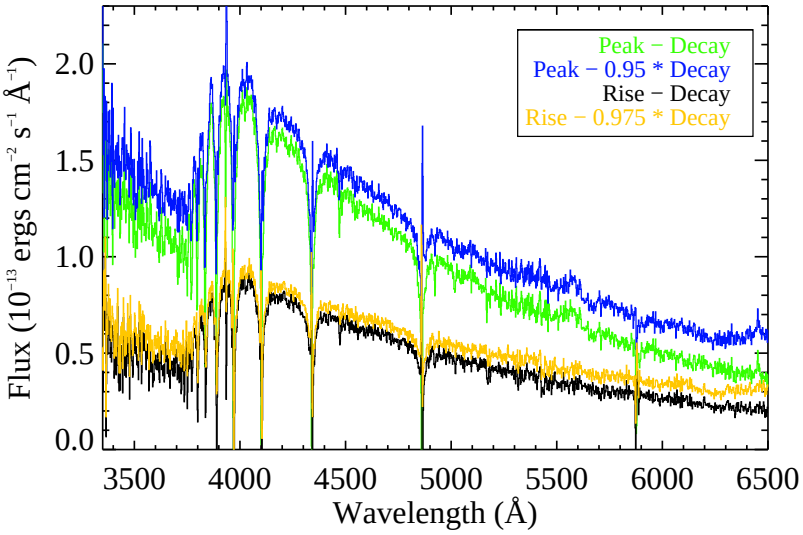

Figure F.6 The flare-only spectra during MDSF2 rise (black) and peak (green), which are the same as in Figure 6.12. We adjust for an approximate amount by which the previously decaying emission evolves to the rise phase time (yellow) and peak time (blue).

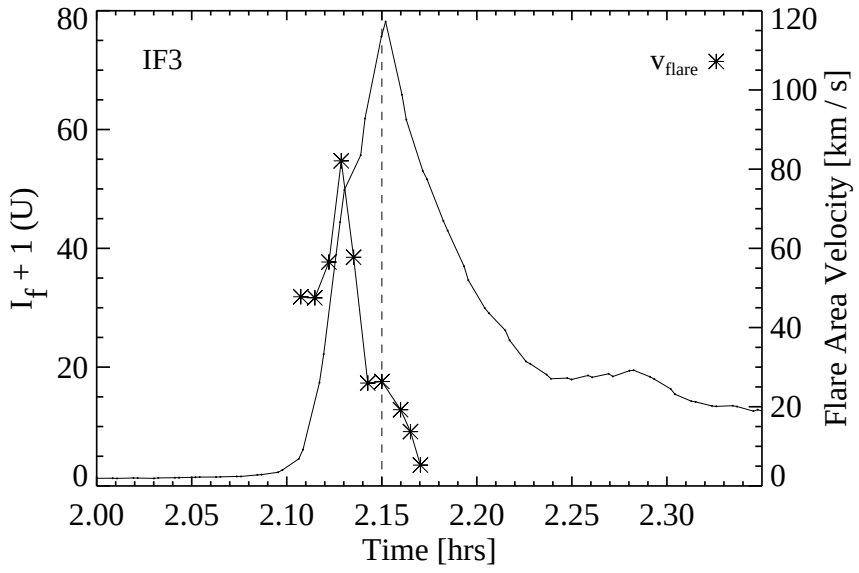

Figure F.7 SDSS u band and derived speed of the expanding flare area during the rise phase using the Planck areas.

Appendix G

ISOTHERMAL MODELS

In this section, we show the predicted $\chi_{\rm flare}$ values for isothermal models in Figure G.1. We also give the equations for the bf and ff isothermal, optically thin spectra in the Figure. The spectra from these slab models were presented in Kunkel (1970), but the equations were not given. We caution the use of these simplistic slab equations, which assume that

$$\frac{dI_\nu}{dz} = j_\nu \tag{G.1}$$

In a future document, I will summarize recombination processes. Following Aller (1965), we derive the following emission coefficients. We confirm that the equations match those in Jefferies & Orrall (1961a,b); Hiei (1982).

The emission coefficient for bound free emission (assuming that $n_e = n_i$) and that gII is near unity, is the following:

$$j_{\lambda,bf} = 6.48 \times 10^{-14}/(\lambda^2 4\pi) n_e^2 T_e^{-1.5}/n^3 exp((1.58 \times 10^5/(n^2 T_e)) - 1.44 \times 10^8/(\lambda T_e)) \tag{G.2}$$

in units of ergs s^{-1} cm^{-3} Å^{-1} s.r.$^{-1}$ where n is the level number of hydrogen and λ is in units of Å.

The emission coefficient for free-free emission is

$$j_{\lambda,ff} = 1.634 \times 10^{-28} n_e^2 T_e^{-0.5} \lambda^{-2} exp(-1.439/(\lambda T_e)) \times 10^{-8} \tag{G.3}$$

in units of ergs s^{-1} cm^{-3} Å^{-1} s.r.$^{-1}$ where λ is in units of cm.

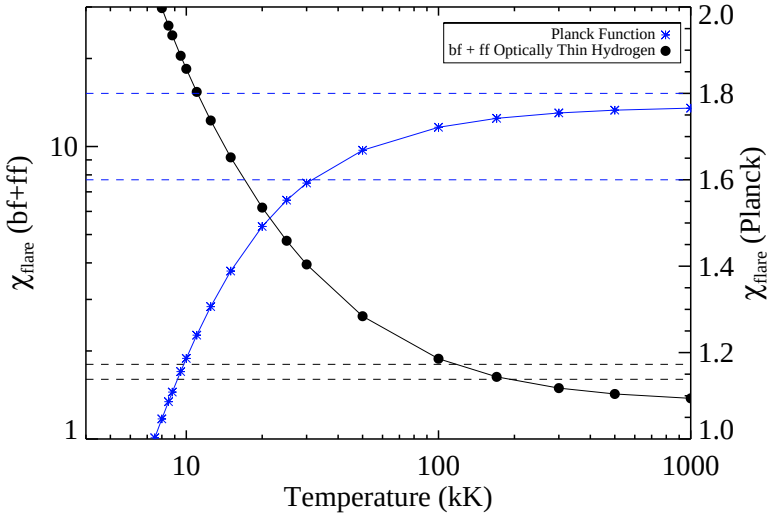

Figure G.1 The predicted $\chi_{\rm flare}$ for isothermal continuum models. The black circles are the predictions for a bf+ff optically thin Hydrogen model (left axis) and the dark blue are the predictions for an optically thick blackbody (right axis). The horizontal dashed lines indicate the range of peak $\chi_{\rm flare,peak}$ $1.6-1.8$.

Appendix H

BEAM EQUILIBRIUM PROCESSES

Exponential functions are expected to be the solution to the non-equilibrium rate equation for a given level. Considering a two-level + continuum Hydrogen atom,

$$\frac{Dn_1}{Dt} = n_2 P_{21} - n_1 P_{12} \tag{H.1}$$

Following Carlsson & Stein (2002), this has the solution

$$n_1(t) = n_1(inf) + [n_1(0) - n_1(inf)] \times exp(-t(P_{21} + P_{12})) \tag{H.2}$$

Considering the population density of the $n = 2$ level as a function of time when the beam is turned on, the solution becomes

$$n_{n=2}(t) = n_{n=2,\text{beam on}}(inf) - C \times exp(-t/\tau(t)) \tag{H.3}$$

during the rise phase where $C = |n_{n=2}(0) - n_{n=2,\text{beam on}}(inf)|$. Therefore, given that the population density of $n = 2$ is related to the recombination rate to $n = 2$, we may expect the recombination radiation to follow a similar exponential rise in the beginning of the flare. Of course, the rise of the total flare emission at $\lambda = 3550$Å is the sum of this process occuring at many depths of the atmosphere, each with different timescales.

Table H.1. Appendix Table: Scaling Spectra

$T_{\rm BB}$ (K)	$X_{\rm BB}$*	Algorithm's Prediction**
5000	0.015	(0.70, 0.95, 1.05, 1.30)
···	0.3	(0.73, 0.99, 1.1, 1.35)
···	0.76	(0.82, 1.11, 1.23, 1.52)
10 000	0.0003	(0.70, 0.95, 1.05, 1.30)
···	0.0062	(0.71, 0.97, 1.08, 1.33)
···	0.016	(0.75, 1.02, 1.14, 1.43)
50 000	8×10^{-6}	(0.70, 0.95, 1.05, 1.30)
···	0.00015	(0.70, 0.96, 1.06, 1.32)
···	0.0004	(0.72, 0.93, 1.08, 1.33)

Note. — *The $X_{\rm BB}$ are for a $I_{f,U}+1 \sim 2, 40, 100$ flare given each $T_{\rm BB}$. **Scaling algorithm's prediction for a set of scale factors: (0.70, 0.95, 1.05, 1.30).

Curriculum Vitae

Education

B.A., Physics with Honors, University of Chicago, 2006 (thesis advisor: Dietrich Muller)
M.S., Astronomy, University of Washington, 2008
Ph.D., expected August 17th, 2012 (thesis advisor: Suzanne L. Hawley)

Employment History

2007 - present : Research Assistant, University of Washington
2006 - 2007, 2009, 2010 : Teaching Assistant, University of Washington
2004 : Research Experience for Undergraduates, University of Toledo
2003 : Research Assistant, VERITAS project, University of Chicago

Grant and Award Summary

2011	Kepler Cycle 3 GO-0002 (Co-I); $37,809
2011	Kepler Cycle 3 GO-0015 (Co-I)
2010-present	Chandra GO0-11032B (Co-I); $30,556
2011	Herschel OT1 shawley_2 (Co-I); $119,900 upon completion of observations
2011	GSFEI Graduate Student Travel Grant (PI); $500
2011	Theodor Jacobsen Fund (PI); $1150
2010	Theodor Jacobsen Fund (PI); $850
2010-present	Kepler Cycle 2 GO-0016 (Co-I); $37,659
2010-2011	Kepler Cycle 2 GO-0035 (Co-I)
2009	Sigma Xi Grant-in-Aid of Research (PI); $1200
2009	AAS International Travel Grant; $850
2008-present	NSF Grant AST 0807205 (Co-I); $34,409

Ground-based Observing Experience

Telescope	Instrument	Number of nights or hours
ARC 3.5m at APO	DIS	57 half nights***
ARC 3.5m at APO	ARCES	6 half nights
ARCSAT 0.5m at APO	Flarecam	26 half nights***
Dunn Solar Telescope	ROSA + IBIS	26 days
Dunn Solar Telescope	HSG + IBIS	9 days
WHT at La Palma	ISIS	2 nights
WHT at La Palma	ULTRACAM	2 nights
NTT at La Silla	ULTRACAM	3 nights
Subaru	IR Coronagraph	3 nights
UKIRT	IR Coronagraph	4 nights
2.1m and 0.9m at KPNO	IR and optical phot	8 nights
1.8m at DAO	Spectrograph	11 nights
SALT	RSS	8.5 hours, pending

***14 of these half-nights involved operating the 3.5m and 0.5m simultaneously

Refereed Publications

(1) **Kowalski, A.F.**, Hawley, S.L., Holtzman, J.A., Wisniewski, J.P., Hilton, E.J. 2012, "The Multiple Continuum Components in the White Light Flare of 16 January 2009 on the dM4.5e Star YZ CMi", *Solar Physics* 277, 21-29

(2) **Kowalski, A.F.**, Hawley, S.L., Holtzman, J.A., Wisniewski, J.P., Hilton, E.J. 2010, "A White Light Megaflare on the dM4.5e Star YZ CMi", *Astrophysical Journal Letters*, 714L, 98-102

(3) **Kowalski, A.F.**, Hawley, S.L., Hilton, E.J., Becker, A.C., West, A.A., Bochanski, J.J., Sesar, B. 2009, "M Dwarfs in Sloan Digital Sky Survey Stripe 82: Photometric Light Curves and Flare Rate Analysis", *Astronomical Journal*, 138, 633-648

(4) Schmidt, S. J., **Kowalski, A. F.**, Hawley, S. L., Hilton, E. J., Wisniewski, J. P., Tofflemire, B. M., 2012, "Probing the Flare Atmospheres of M Dwarfs using Infrared Emission Lines", *Astrophysical Journal* 745-754, 14

(5) Tofflemire, B. M., Wisniewski, J. P., **Kowalski, A. F.**, Schmidt, S. J., Kundurthy, P., Hilton, E. J., Holtzman, J. A., Hawley, S. L., 2012, "The Implications of M Dwarf Flares on the Detection and Characterization of Exoplanets at Infrared Wavelengths", *Astronomical Journal* 143-154, 12

(6) Becker, A. C., Bochanski, J. J., Hawley, S. L., Ivezić, Ž., **Kowalski, A. F.**, Sesar, B., West, A. A. 2011, "Periodic Variability of Low-mass Stars in Sloan Digital Sky Survey Stripe 82", *Astrophysical Journal*, 731, 17-33

(7) West, A.A., Morgan, D.P., Bochanski, J.J., Andersen J.M., Bell, K.J., **Kowalski, A.F.**, Davenport, J.R.A., Hawley, S.L., Schmidt, S.J., Bernat, D., and 10 coauthors 2011, "The Sloan Digital Sky Survey Data Release 7 Spectroscopic M Dwarf Catalog. I. Data", *Astronomical Journal*, 141, 97-108

(8) Hilton, E.J., West, A.A., Hawley, S.L., **Kowalski, A.F.** 2010, "M Dwarf Flares from Time-resolved Sloan Digital Sky Survey Spectra", *Astronomical Journal*, 140, 1402-1413

(9) Bond, N.A., Ivezić, Z., Sesar, B., Jurić, M., Munn, J.A., **Kowalski, A.F.**, Loebman, S., Roškar, R., Beers, T.C., Dalcanton, J., and 47 coauthors, 2010, "The Milky Way Tomography with SDSS. III. Stellar Kinematics", *Astrophysical Journal*, 715, 1-29

(10) Wisniewski, J.P., Draper, Z.H., Bjorkman, K.S., Meade, M.R., Bjorkman, J.E., **Kowalski, A.F.** 2010, "Disk-Loss and Disk-Renewal Phases in Classical Be Stars. I. Analysis of Long-Term Spectropolarimetric Data", *Astrophysical Journal*, 709, 1306-1320

(11) Parker, A.; Ivezić, Ž.; Jurić, M.; Lupton, R.; Sekora, M. D.; **Kowalski, A.F.** 2008, "The size distributions of asteroid families in the SDSS Moving Object Catalog 4",

Icarus, 198, 138-155

(12) Wisniewski, J. P., **Kowalski, A. F.**, Bjorkman, K. S., Bjorkman, J. E., Carciofi, A. C. 2007, "Toward Mapping the Detailed Density Structure of Classical Be Circumstellar Disks", *Astrophysical Journal*, 656, 21-24

(13) Milligan, R. O., Chamberlin, P. C., Hudson, H. S., Woods, T. N., Mathioudakis, M., Woods, Fletcher, L., **Kowalski, A. F.**, Keenan, F. P., "Observations of Enhanced Free-Bound Continua During an X-Class Solar Flare Using SDO/EVE", *Astrophysical Journal Letters in press, http://arxiv.org/abs/1202.1731*

(14) Davenport, J. R. A., Becker, A. C., **Kowalski, A.F.**, Hawley, S.L., Schmidt, S.J., Hilton, E.J., Sesar, B., Cutri, R. "Multi-wavelength characterization of stellar flares on low-mass stars using SDSS and 2MASS time domain surveys", *Astrophysical Journal* in press, *http://arxiv.org/abs/1202.1902*

Selected Conference Proceedings and White Papers

(1) **Kowalski, A.F.**, Hawley, S.L., Holtzman, J.A., Wisniewski, J.P., Hilton, E.J. 2011, "An 'A Star' on an M Star during a Flare within a Flare", Proceedings of IAU Symposium 273: "Physics of Sun and Star Spots", August 22-26, 2010, D.P. Choudhary and K.G. Strassmeier (eds.), Vol. 6., 261-264, DOI: 10.1017/S1743921311015341, arXiv: 1010.0452

(2) **Kowalski, A.F.**, Mathioudakis, M.; Hawley, S. L.; Hilton, E. J.; Dhillon, V. S.; Marsh, T. R.; Copperwheat, C. M., 2011, "White Light Flare Continuum Observations with ULTRACAM", Proceedings of the 16th Workshop on Cool Stars, Stellar Systems, and the Sun (PASP conference series, in press), arXiv:1103.0822

(3) **Kowalski, A.F.**, Wisniewski, J.P.; Clampin, M.; Grady, C. A.; Sitko, M. L.; Bjorkman, K. S.; Fukagawa, M.; Hines, D. C.; Katoh, E.; Whitney, B. A. 2009, "Diagnosing the Structure of the HD 163296 Protoplanetary Disk via Coronagraphic Imaging Polarimetry", Cool Stars, Stellar Systems, and the Sun: Proceedings of the 15th Cambridge Workshop on Cool Stars, Stellar Systems and the Sun. AIP Conference Proceedings, 1094, 393

(4) Fletcher, L.; Turkmani, R.; Hudson, H. S.; Hawley, S. L.; **Kowalski, A.F.**; Berlicki, A.; Heinzel, P. 2010, "Solar Flares and the Chromosphere", A white paper prepared for the Space Studies Board, National Academy of Sciences (USA), for its Decadal Survey of Solar and Space Physics (Heliophysics), arXiv1011.4650F

(5) LSST Science Collaborations; Abell, Paul A.; Allison, Julius; Anderson, Scott F.; Andrew, John R.; Angel, J. Roger P.; Armus, Lee; Arnett, David; Asztalos, S. J.; Axelrod, Tim S.; and 238 coauthors including **Kowalski, A.F.**, "LSST Science Book, Version 2.0", arXiv0912.0201L

(6) Browning, Matthew K.; Walkowicz, Lucianne M.; West, Andrew A.; Basri, Gibor; Browning, Matthew K.; **Kowalski, Adam F.**, Hilton, Eric; Bochanski, John J. 2009, "Understanding Activity in Low Mass Stars", Astro2010: The Astronomy and Astrophysics Decadal Survey, Science White Papers

Non-Refereed (Submitted/In Preparation) Articles

(1) **Kowalski, A. F.**, Hawley, S. L., Holtzman, J. A., Hilton, E. J., Wisniewski, J. P., Schmidt, S. J., Davenport, J. R. A., Ule, N., Covey, K. 2012, "An Atlas of dMe Optical Flare Spectra", in preparation for *Astrophysical Journal Supplements*

Selected Abstracts

(1) **Kowalski, A. F.**, Osten, R. A.; Sahu, K. C.; Hawley, S. L. 2011, "An Optical Flare Rate Census of Galactic Bulge Dwarf Stars", AAS Meeting #217, #342.07; Bulletin of the American Astronomical Society, 43, 2011

(2) **Kowalski, A.F.**; Hawley, S. L.; Holtzman, J. A.; Wisniewski, J. P.; Hilton, E. J. 2010, "A White Light Megaflare on the dM4.5e Star YZ CMi", AAS Meeting #215, #424.11; Bulletin of the American Astronomical Society, 42, 332

(3) **Kowalski, A.F.**, Hawley, S. L.; Hilton, E. J.; Becker, A. C.; Bochanski, J. J.; West, A. A. 2009, "M Dwarf Flare Rate Analysis of SDSS Stripe 82", American Astronomical Society, AAS Meeting #213, #434.02; Bulletin of the American Astronomical Society, 41, 303

Co-Author on 25 Other Conference Proceedings and Abstracts

Invited Talks

- "Time-Resolved Properties of White Light Emission During Stellar Flares", University of Wisconsin-Madison, November 22nd 2011

- "Time-Resolved Properties of White Light Emission During Stellar Flares", National Solar Observatory Colloquium, Sac Peak, August 11th 2011

- "UV Spectroscopy of Stellar and Solar Flares", AAS Meeting #218, Meeting-in-a-Meeting "What's New Under the Suns", Boston MA, May 24th, 2011

- "Time-Resolved Properties of White Light Emission During Stellar Flares", ING/NOT La Palma Colloquium, February 17th, 2011

- "Overview of Stellar Flare Observations", 16th Workshop on Cool Stars, Stellar Systems, and the Sun, 'Solar and Stellar Flares' Splinter Session, August 29, 2010

- "Towards Understanding White Light Emission in Stellar Flares", IAUS 273, Physics of Sun and Star Spots, Ventura, California 22-26 August 2010

- "Towards Understanding White Light Emission in Stellar Flares", 'The Origin, Evolution, and Diagnosis of Solar Flare Magnetic Fields and Plasmas: Honoring the Contributions of Dick Canfield', 9 – 11 August 2010 at HAO/NCAR in Boulder, CO

- "A White Light Megaflare on the dM4.5e Star YZ CMi", CTIO Colloquium, Chile, May 18th 2010

- "M Dwarfs in Sloan Digital Sky Survey Stripe 82: Photometric Light Curves and Flare Rate Analysis", Gemini North Observatory Colloquium, Hawaii, July 24th 2009

Referee Experience

- 1 article for PASJ, 1 article for AN

Current Participation in Collaborations

- Young Scientist participant in 'Solar Chromospheric Flares' Workshop at the International Space Science Institute (ISSI) in Bern, Switzerland; November 2009, June 2010, March 2011

- Member of LSST Transients Working Group

- Co-I on SDSS-III BOSS Ancillary guest observer program

Outreach Activities

- Public talk on stellar flares at the Tacoma Astronomical Society meeting, July 2010.

- Press release on `Optical Flares on Dwarf Stars: Implications for Exoplanet Habitability' at the 2011 Winter American Astronomical Society meeting in Seattle, WA, January 10. Our press release resulted in articles in *National Geographic* (http://news.nationalgeographic.com/news/2011/01/110124-stars-eruptions-alien-life-planets-earthlike-science-space/), the *BBC* (http://www.bbc.co.uk/news/science-environment-12184029), *Astronomy* magazine (http://www.astronomy.com/en/News-Observing/News/2011/01/Hubble%20finds%20stellar%20flares.aspx), *NASA*'s website (http://www.nasa.gov/mission_pages/hubble/science/big-punch.html), and *Hubblesite* (http://hubblesite.org/newscenter/archive/releases/2011/02/full/)

- Developed curricular material on accessing and using Sloan Digital Sky Survey (SDSS) spectra for the graduate Astronomy class, ASTR 581. I taught this tutorial (a 3-hour session) in 2010 and 2011.

- Interviewed by and appeared on local news channel about flares during the upcoming solar Cycle 24, Cool Stars 16, August 2010